Physics of the Solid State, Vol. 46, No. 12, 2004, pp. 2185–2190. Translated from Fizika Tverdogo Tela, Vol. 46, No. 12, 2004, pp. 2113–2118.

METALS AND SUPERCONDUCTORS

Long-Wavelength Static Atomic Displacements in γ-FeNi Alloys

Yu. N. Mikhaĭlov and S. F. Dubinin

Institute of Metal Physics, Ural Division, Russian Academy of Sciences, ul. S. Kovalevskoĭ 18, Yekaterinburg, 620219 Russia
e-mail: mikhailov@uraltc.ru

Received February 26, 2004

Abstract—The temperature dependences of the intensity of elastic diffuse neutron scattering from γ-Fe_xNi_{100-x} (x = 57 and 68 at. %) alloy single crystals near basic reciprocal-lattice sites in the (110) plane are measured using a triaxial neutron spectrometer. New effects of instability of the γ-phase lattice with respect to long-wavelength (transverse and longitudinal) static atomic displacements have been detected. The displacements are found to depend on the iron concentration in the alloys and on temperature. The relations of these structural distortions to premartensitic phenomena and the invar effect in γ-FeNi alloys are discussed © *2004 MAIK "Nauka/Interperiodica".*

1. INTRODUCTION

It is well-known that, depending on their composition, γ-Fe_xNi_{100-x} ($x \geq 50$ at. %) alloys have elinvar or invar properties and undergo a martensitic transformation in which their fcc structure transforms into a less dense bcc lattice as the temperature decreases. The concentration range of the invar properties (anomalous behavior of the thermal expansion coefficient $\alpha(T)$) and that of the fcc ⟶ bcc transformation partially overlap, which makes it difficult to interpret experimental results and to create adequate theoretical models.

Recently, theoretical studies have been published (see, e.g., [1–3]) in which the band structure of the alloys is calculated to explain these physical phenomena. As follows from those calculations, the existence of high-spin (HS) and low-spin (LS) states in fcc lattices is conditioned by the degree of filling of electron subbands with different t_{2g} and e_g symmetries depending on the number of electrons per atom and on temperature. According to this theory, the invar properties and phase transformations in FeNi alloys are two different effects caused by magnetic volume instability. Moreover, Moruzzi [1] found that the transformation temperatures in FeNi alloys and pure Fe are related to the difference in energy between the HS and LS states. However, in the context of the model developed in [1–3], the roles of structural [4, 5] and magnetic [6–8] states and dynamic [9–11] and static [12–14] atomic displacements in the initial alloys remain unclear. These displacements are important for establishing the mechanisms of the appearance of the invar properties and the martensitic transformation.

In this work, we studied the instability of the crystal lattice of γ-FeNi alloys with respect to static atomic displacements. Earlier, these alloys were studied using x-ray and electron diffraction [12–14]; these methods cannot resolve the scattering effects induced by static and dynamic atomic displacements. We also performed measurements near the martensitic transformation temperatures using elastic nuclear diffuse neutron scattering, which gives information on purely static atomic displacements in the bulk of massive samples. Such neutron scattering data on static atomic displacements over a wide temperature range covering both the ferromagnetic and paramagnetic states of alloys are given in [15]. In that study, elastic nuclear diffuse neutron scattering from a γ-$Fe_{68}Ni_{32}$ single crystal ($T_C \cong 380$ K) was detected in the vicinity of the Curie temperature in the (001) plane of the reciprocal lattice. This scattering was assumed to be due to long-wavelength longitudinal static atomic displacements in the alloy that occur during transformation into a magnetically ordered state. Since the measurements were carried out on a single crystal of one composition and in one plane of the reciprocal lattice, it is of interest to continue that investigation.

Therefore, in this work, we investigated the temperature dependences of the intensity of elastic diffuse neutron scattering near the basic reciprocal lattice sites for the same γ-$Fe_{68}Ni_{32}$ single crystal but in the (110) plane. To compare experimental results obtained for alloys with significantly different compositions, we also studied a γ-$Fe_{57}Ni_{43}$ single crystal ($T_C \cong 695$ K), which, contrary to the γ-$Fe_{68}Ni_{32}$ single crystal ($T_{\gamma\to\alpha} \cong$ 200 K), does not undergo the structural fcc ⟶ bcc transformation.

2. EXPERIMENTAL

The γ-FeNi single crystals were balls 1.2×10^{-2} m in diameter grown using the Bridgman crystal growth technique. The misorientation angles of mosaic blocks in the single crystals did not exceed 30′. The samples were fixed in a high-temperature chamber so that the [110] direction was normal to the plane in which neutron-scattering measurements were performed.

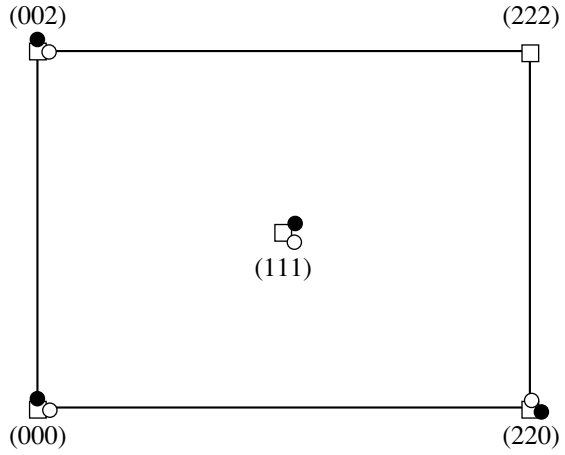

Fig. 1. Schematic diagram of the reciprocal lattice (squares) of γ-FeNi alloys in the (110) plane and the sites (filled and open circles) at which the temperature dependence of nuclear diffuse neutron scattering was determined.

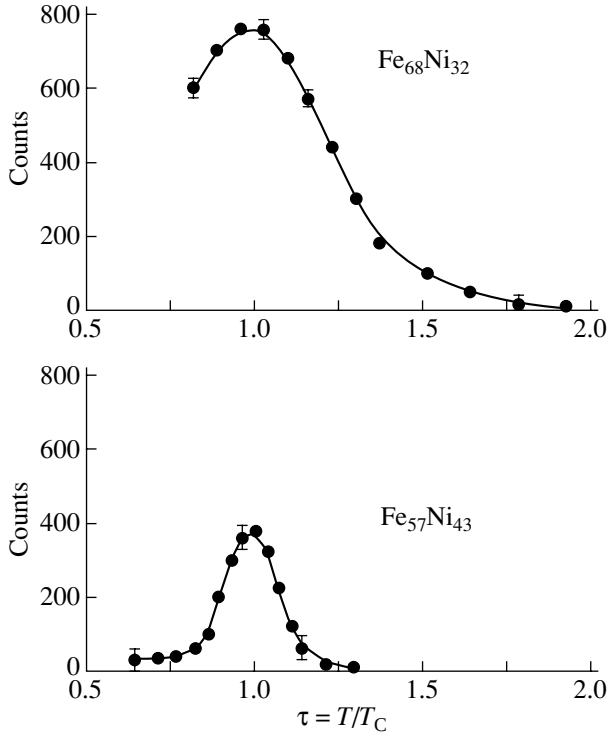

Fig. 2. Magnetic critical neutron scattering in γ-FeNi alloys depending on the reduced temperature near the (000) reciprocal lattice site.

The intensity of scattered neutrons was measured using a triaxial neutron spectrometer. The incident-neutron wavelength was controlled by a double-crystal monochromator made of pyrolytic graphite with a (004) reflection plane and was equal to $\lambda = 1.490$ Å. As an analyzer, we used the (111) plane of a deformed germanium single crystal. Since the total diffuse neutron scattering cross section near nonzero reciprocal lattice sites can consist of elastic nuclear, magnetic critical, and inelastic (phonon and spin-wave) scattering cross sections, the spectrometer analyzer was set at the energy of the primary neutron beam to eliminate the inelastic components of neutron scattering. Therefore, hereafter, we will discuss only elastic neutron scattering.

Magnetic critical scattering (MCS) near nonzero reciprocal lattice sites was calculated from the formula

$$I_M(T, \mathbf{k} = \boldsymbol{\tau}_{hkl} + \mathbf{q}) = I_M(T, \mathbf{q})F^2(\mathbf{k}), \qquad (1)$$

where $\mathbf{k}$ is the scattering vector, $\boldsymbol{\tau}_{hkl}$ is a reciprocal lattice vector, $\mathbf{q}$ is the wave vector, $I_M(T, \mathbf{q})$ is the MCS near the (000) site, and $F(\mathbf{k})$ is the magnetic form factor. The temperature dependences of the neutron MCS intensity near the (000) site were experimentally measured at the same values of $\mathbf{q}$ that were used for measurements near nonzero reciprocal lattice sites, and the magnetic form factors for the alloys were determined according to their compositions. The values of $F(\mathbf{k})$ for Fe and Ni atoms were taken from [16].

A comparison of the experimental neutron scattering intensities as functions of temperature near nonzero reciprocal lattice sites with the corresponding calculated MCS contributions can give information on the nature of the effects observed. If the difference in the intensities measured at different temperatures exceeds the value given by Eq. (1), the extra contribution to the intensity is due solely to nuclear diffuse neutron scattering related to static atomic displacements.

3. EXPERIMENTAL RESULTS

The temperature dependence of diffuse neutron scattering in the γ-FeNi alloys was measured in the (110) plane of the reciprocal lattice (Fig. 1). The filled and open circles show the reciprocal lattice points at which experimental data were obtained. The scattering vectors corresponding to all the points are

$$\boldsymbol{\kappa} = \boldsymbol{\tau}_{hkl} + \mathbf{q}, \qquad (2)$$

where the magnitude of the wave vector is $|\mathbf{q}| = 0.07(2\pi/a)$.

First, we give the results of MCS measurements in the γ-FeNi alloys. Uncombined scattering of this type in ferromagnets will be observed near the (000) site if, as in our case, inelastic contributions are eliminated. Figure 2 shows the dependences of the MCS intensity near the (000) site on reduced temperature for the γ-$Fe_{57}Ni_{43}$ and γ-$Fe_{68}Ni_{32}$ alloys. The MCS intensities in Fig. 2 are averaged over two directions ([001], [110]) of the wave vector, since this scattering is isotropic. MCS is known to be caused by short-range magnetic-order fluctuations in the vicinity of the Curie temperature. The width of the temperature range of MCS characterizes the degree of inhomogeneity of the magnetic state in the alloy. The more inhomogeneous the magnetic structure of an alloy, the larger the range where MCS is

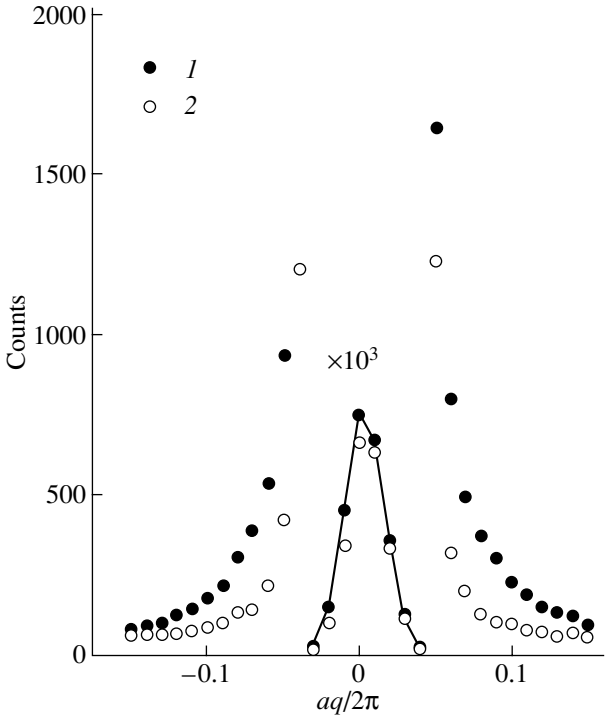

Fig. 3. Intensities of scattered neutrons in the γ-$Fe_{68}Ni_{32}$ alloy in the case of longitudinal scanning of the (002) reciprocal lattice site at (*1*) 300 and (*2*) 550 K.

observed near the phase transition point. This is clearly visible in Fig. 2. In the γ-$Fe_{57}Ni_{43}$ alloy, MCS is retained up to a reduced temperature $\tau \cong 1.25$, and in the γ-$Fe_{68}Ni_{32}$ alloy, up to $\tau \cong 1.9$.

Neutron diffraction patterns from the γ-FeNi alloys provide information on nuclear diffuse neutron scattering only near nonzero reciprocal lattice sites. Therefore, we performed measurements in the vicinity of the (111), (002), and (220) reciprocal lattice sites of both single crystals. At temperatures below and above the corresponding Curie points, scanning was carried out both perpendicular and parallel to the scattering vectors

$$\boldsymbol{\kappa} = \boldsymbol{\tau}_{hkl} + \mathbf{q} \quad (\boldsymbol{\tau}_{hkl} \perp \mathbf{q}), \tag{3}$$

$$\boldsymbol{\kappa} = \boldsymbol{\tau}_{hkl} + \mathbf{q} \quad (\boldsymbol{\tau}_{hkl} \parallel \mathbf{q}), \tag{4}$$

respectively. The intensity profiles below and above T_C are different because of the differences in composition, in the indices of reciprocal lattice sites, and in the scanning directions between the single crystals studied. As an example, Fig. 3 shows the scattering intensity profiles of the (002) site for the γ-$Fe_{68}Ni_{32}$ alloy ($T_C \cong 380$ K) measured parallel to the scattering vector at 300 and 550 K. The intensities are seen to be different at these temperatures up to $aq/2\pi \cong \pm 0.15$. It should be noted that, in this particular case, the neutron scattering intensity in the paramagnetic state is lower than that in the magnetically ordered state.

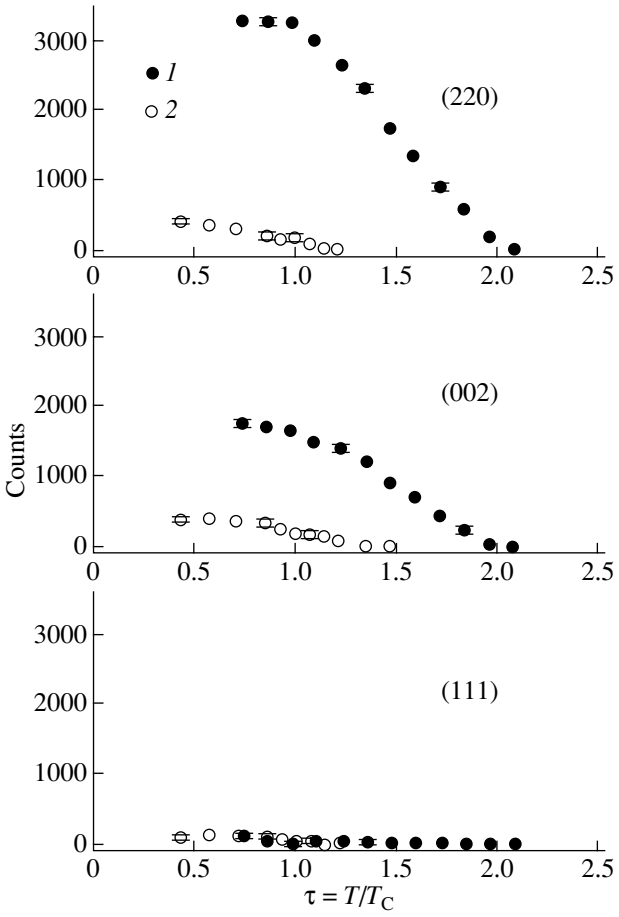

Fig. 4. Nuclear diffuse neutron scattering in the (*1*) γ-$Fe_{57}Ni_{43}$ and (*2*) γ-$Fe_{68}Ni_{32}$ alloys as a function of the reduced temperature at the reciprocal lattice sites satisfying condition (3).

To study diffuse scattering, we measured the temperature dependences of the neutron scattering intensities near basic nonzero sites in both alloys, γ-$Fe_{57}Ni_{43}$ and γ-$Fe_{68}Ni_{32}$. Measurements were performed only at the reciprocal lattice sites (indicated in Fig. 1) that satisfy Eqs. (3) and (4) at the same wave vector, $|\mathbf{q}| = 0.07(2\pi/a)$.

The measured diffuse scattering intensities at reciprocal lattice points defined by Eq. (3) are shown in Fig. 4 as functions of the reduced temperature. These data correspond only to nuclear diffuse scattering, since the background and the contributions due to MCS calculated using Eq. (1) were subtracted from the experimental intensities. According to Fig. 4, the basic specific features of nuclear diffuse scattering in the γ-$Fe_{57}Ni_{43}$ and γ-$Fe_{68}Ni_{32}$ alloys are the following. The maximum intensities are observed in the γ-$Fe_{68}Ni_{32}$ alloy, i.e., at a higher iron concentration. The reduced-temperature ranges of the scattering above the Curie point also widen as the iron concentration in the alloys is increased. In the γ-$Fe_{57}Ni_{43}$ alloy, nuclear diffuse scattering appears below $\tau \cong 1.25$, and in the γ-$Fe_{68}Ni_{32}$

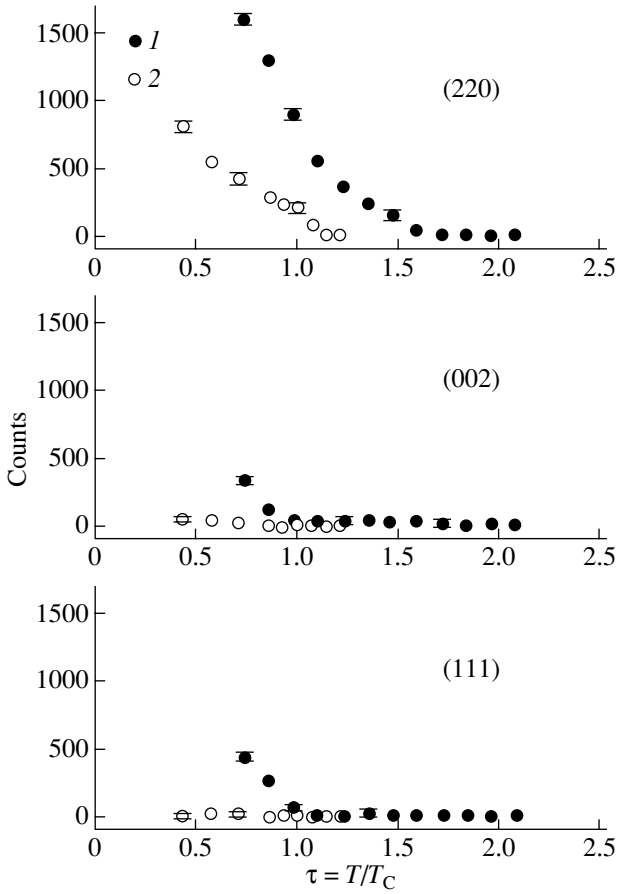

Fig. 5. Nuclear diffuse neutron scattering in (*1*) the γ-$Fe_{57}Ni_{43}$ and (*2*) γ-$Fe_{68}Ni_{32}$ alloys as a function of reduced temperature at the reciprocal lattice sites satisfying condition (4).

alloy, below $\tau \cong 2.0$. This scattering is virtually absent near the (111) reciprocal lattice site in both alloys. Based on the experimental data, we can state that, in both alloys under study, long-wavelength transverse static atomic displacements appear at different reduced temperatures depending on the alloy compositions.

Now, we present the results of studying the temperature dependence of diffuse neutron scattering in the γ-$Fe_{57}Ni_{43}$ and γ-$Fe_{68}Ni_{32}$ alloy single crystals at reciprocal lattice points defined by Eq. (4). The background and the contributions due to MCS were also subtracted from the experimental scattering intensities. The remaining intensities of nuclear diffuse scattering are shown in Fig. 5 as functions of the reduced temperature. The situation is seen to be simplest in the γ-$Fe_{57}Ni_{43}$ alloy near the (111) and (002) sites. At these reciprocal lattice sites, the intensities of nuclear diffuse scattering are temperature-independent. However, near the (220) site of this alloy, nuclear diffuse scattering appears slightly above the Curie temperature. A more complex pattern of nuclear diffuse neutron scattering is observed in the γ-$Fe_{68}Ni_{32}$ single crystal, where this scattering occurs near all reciprocal lattice sites. Near the (111) and (002) sites, this scattering appears in the vicinity of the Curie temperature ($\tau \cong 1.0$). Near the (220) site, the nuclear diffuse scattering is more intense and appears well above the Curie temperature ($\tau \cong 1.5$). These data indicate that long-wavelength longitudinal static atomic displacements in the γ-$Fe_{57}Ni_{43}$ appear only in the [110] direction. In the γ-$Fe_{68}Ni_{32}$ single crystal, this type of atomic displacement exists along all symmetry axes.

Thus, our experimental results reveal the effects of instability of the fcc lattices of γ-$Fe_{57}Ni_{43}$ and γ-$Fe_{68}Ni_{32}$ alloys with respect to long-wavelength (transverse and longitudinal) static atomic displacements. Displacements of these two types and the temperatures of their appearance increase with the iron concentration in the alloys, i.e., with the degree of inhomogeneity of the magnetic order in them.

4. DISCUSSION OF THE RESULTS

The purpose of this work was not only to reveal different types of instability of the fcc lattice of FeNi alloys (long-wavelength transverse and longitudinal static atomic displacements) but also to find their relations to the anomalous behavior of the thermal expansion coefficient $\alpha(T)$ and to the fcc ⟶ bcc martensitic transformation.

4.1. Long-Wavelength Transverse Static Atomic Displacements in γ-FeNi Alloys

Before discussing this type of static atomic displacement, let us dwell on the phase diagram of pure iron and correlate it with the phase transitions in the FeNi alloys. In the temperature range 1663–1183 K, pure iron is known to be in an fcc phase [17]. Below the temperature $T_{\gamma\to\alpha}$ = 1183 K, transformation into a bcc phase occurs, and at T_C = 1043 K, into the ferromagnetic state. The distinctive property of phase transitions in FeNi alloys consists in the fact that, as the temperature decreases, a ferromagnetic order first appears in them and then the fcc ⟶ bcc transformation occurs (at an iron concentration $x \gtrsim 66$ at. %).

We believe that there is a close relation between the structural fcc ⟶ bcc transformation in pure Fe and those in FeNi alloys. This assumption is supported by the data from [3, Fig. 6]. That figure gives the experimental temperatures of the onset of martensitic transformations in pure iron and in a number of alloys of iron and transition metals as functions of the electron concentration per atom and of the atomic volume. In these coordinates, pure iron corresponds to the vertex of the three-dimensional region of the bcc phase of some of these alloys (FePt, FeNiPt, FeNi, FeNiCo). This experimental finding indicates that the structural fcc ⟶ bcc transformations in all of these materials (including pure iron) are of the same nature. Moreover, according to [18, 19], the crystalline modifications of iron and FeNi alloys depend substantially on their mag-

netic states. In particular, the authors of [18] showed that only the appearance of ferromagnetic ordering makes the bcc phase of iron stable down to very low temperatures. The existence of the bcc phase of iron in the range between the structural transformation temperature and the Curie point was explained in [18] by the retention of a short-range ferromagnetic order. This assumption was then experimentally confirmed by the authors of [20, 21], who detected spatial spin correlations by measuring paramagnetic neutron scattering in α-Fe and γ-Fe (below and above the structural transformation).

Hence, the difference between the fcc ⟶ bcc transformations in pure Fe and in FeNi alloys consists in the fact that, in the former case, a short-range ferromagnetic order is sufficient to cause this transformation, whereas in the latter case the magnetically ordered state is required for this transition to occur. These features are also likely to determine the kinetics of the structural transformations. In pure iron, the transformation proceeds through the formation of microscopic nucleation centers of the new phase and their subsequent growth with decreasing temperature [17], that is, in the presence of a short-range ferromagnetic order. In FeNi alloys with a low nickel content, the structural transformation occurs much in the same way as the transformation in pure iron. However, as the nickel concentration increases, the transformation kinetics in FeNi alloys becomes explosive. Based on these experimental facts, we can conclude that nickel atoms in these alloys create energy barriers that hinder the transformation when their content is low and make the martensitic transformation in the alloys impossible at a certain critical concentration (~34 at. %).

Our experimental results indicate that the fcc lattice of the alloys under study becomes unstable with respect to long-wavelength transverse static atomic displacements near the temperature range where a short-range ferromagnetic order occurs (Figs. 2, 4). Based on this experimental fact, we can assume that, just as in pure γ-Fe, the cause of structural lattice distortions in γ-FeNi alloys at $T > T_C$ is a short-range ferromagnetic order. As the temperature decreases, these structural distortions in pure γ-Fe result in the fcc ⟶ bcc transformation even in the paramagnetic state; in γ-FeNi alloys, the transformation into this state turns out to be incomplete. In the γ-$Fe_{57}Ni_{43}$ alloy, this transformation manifests itself in long-wavelength transverse static atomic displacements (down to very low temperatures), while in the γ-$Fe_{68}Ni_{32}$ alloy the martensitic transformation occurs, but only at temperatures below T_C. Therefore, we assume that the instability of the fcc lattices of the alloys that arises at $T > T_C$ with respect to transverse static atomic displacements is a premartensitic phenomenon. This assumption is also supported by the absence of nuclear diffuse neutron scattering in the vicinity of the (111) site in both alloys (Fig. 4), which is consistent with the orientation relationship

$$\tau(111)_\gamma = \tau(110)_\alpha, \quad (5)$$

relating the crystal lattices of the initial and final phases. All other reciprocal lattice sites of the fcc phase differ from the corresponding sites of the bcc phase. Therefore, near these sites, nuclear diffuse scattering will appear in diffraction patterns in the premartensitic (incomplete) stage of the structural transformation.

The pattern of transverse atomic displacements can roughly be described using the results of the experimental [15] and theoretical [22] studies dealing with nuclear diffuse neutron scattering in the (001) reciprocal lattice plane of γ-FeNi alloys. It was shown that nuclear diffuse neutron scattering induced by long-wavelength transverse static atomic displacements is absent in this plane. Therefore, we can assume that the vectors of transverse static atomic displacements lie mainly in the {110} reciprocal lattice planes or near them.

4.2. Long-Wavelength Longitudinal Static Atomic Displacements in γ-FeNi Alloys

The fcc lattice of a γ-FeNi alloy become unstable with respect to longitudinal static atomic displacements predominantly in the magnetically ordered state (Fig. 5). Instability above T_C occurs only along the [110] direction, near the (220) site. It is well known that longitudinal distortions directly affect the lattice parameter of alloys and result in volume effects. Moreover, the anomalous behavior of the thermal expansion coefficient $\alpha(T)$ in the γ-FeNi alloys under study occurs in the same temperature range (see, e.g., [23]). Hence, we may assume that long-wavelength longitudinal static atomic displacements detected in our experiments are involved in the formation of the invar effect in γ-FeNi alloys.

The origin of the longitudinal atomic displacements can be explained in terms of a phenomenological theory [22]. According to this theory, longitudinal static atomic displacements appear due to a magnetoelastic interaction related to magnetization fluctuations of an inhomogeneous ferromagnet in the vicinity of the Curie temperature. The calculations performed in [22] show that the intensity of nuclear diffuse neutron scattering induced by longitudinal atomic displacements depends on the degree of inhomogeneity of the magnetic structure. The results given in Figs. 2 and 5 agree well with the predictions from the phenomenological theory. However, as seen from Fig. 5, the nuclear diffuse neutron scattering intensity continues to increase when the temperature decreases well below T_C. Therefore, we assume that the long-wavelength longitudinal static atomic displacements increase with the spontaneous magnetization of the alloy.

5. CONCLUSIONS

Two types of long-wavelength (transverse and longitudinal) static atomic displacements have been detected in γ-$Fe_{57}Ni_{43}$ and γ-$Fe_{68}Ni_{32}$ alloys. These displacements have been related to the following different physical phenomena in the alloys.

(1) Since the temperature of the appearance of transverse static atomic displacements in the alloys correlates with the temperature of the appearance of a short-range ferromagnetic order in them, we believe that such atomic displacements are related to the instability of the fcc lattice belonging to premartensitic phenomena in γ-FeNi alloys.

(2) Longitudinal static atomic displacements in these alloys appear near the temperature range where the behavior of the thermal expansion coefficient $\alpha(T)$ begins to deviate from its purely lattice behavior (Fig. 5, (220) site). Therefore, we believe that this type of atomic displacement favors the invar effect.

(3) Since both transverse and longitudinal static atomic displacements have been detected at $T < T_C$, the premartensitic phenomena and invar behavior can be interrelated or even compete with each other in the ferromagnetic state.

ACKNOWLEDGMENTS

This work was supported by the Ministry of Industry, Science, and Technology of the Russian Federation (project no. 40.012.1.1.1150), the Department of Physical Sciences of the Russian Academy of Sciences (project no. 14), and the Russian Foundation for Basic Research (project no. 02-02-17849).

REFERENCES

1. V. L. Moruzzi, Phys. Rev. B **41** (10), 6939 (1990).
2. P. Entel, E. Hoffmann, P. Mohn, K. Schwarz, and V. L. Moruzzi, Phys. Rev. B **47** (14), 8706 (1993).
3. *The Invar Effect: A Centennial Symposium*, Ed. by J. Wittenauer (Minerals, Metals, and Materials Society, Warrendale, PA, 1997), p. 51.
4. Yu. D. Tyapkin, V. G. Pushin, R. R. Romanova, and N. N. Buĭnov, Fiz. Met. Metalloved. **41** (5), 1040 (1976).
5. V. L. Sedov and L. V. Solomatina, Phys. Status Solidi A **50** (2), 757 (1978).
6. V. E. Arkhipov, A. Z. Men'shikov, and S. K. Sidorov, Pis'ma Zh. Éksp. Teor. Fiz. **12** (7), 356 (1970) [JETP Lett. **12**, 243 (1970)].
7. V. I. Goman'kov, I. M. Puzeĭ, V. N. Sigaev, E. V. Kozis, and E. I. Mal'tsev, Pis'ma Zh. Éksp. Teor. Fiz. **13** (11), 600 (1971) [JETP Lett. **13**, 428 (1971)].
8. S. Komura, G. Lippmann, and W. Schmatz, J. Magn. Magn. Mater. **5** (2), 123 (1977).
9. Y. Endoh and Y. Noda, J. Phys. Soc. Jpn. **46** (3), 806 (1979).
10. Yu. N. Mikhaĭlov, Fiz. Met. Metalloved. **77** (4), 56 (1994).
11. P. J. Brown, B. Roessli, J. G. Smith, K.-U. Neumann, and K. R. A. Ziebeck, J. Phys.: Condens. Matter **8** (10), 1527 (1996).
12. V. G. Pushin, R. R. Romanova, Yu. D. Tyapkin, N. N. Buĭnov, and V. V. Kondrat'ev, Fiz. Met. Metalloved. **43** (4), 826 (1977).
13. V. V. Kondrat'ev and V. G. Pushin, Fiz. Met. Metalloved. **60** (4), 629 (1985).
14. R. J. Comstock, J. B. Cohen, and H. R. Harrison, Acta Metall. **33** (3), 423 (1985).
15. Yu. N. Mikhaĭlov and S. F. Dubinin, Fiz. Met. Metalloved. **68** (2), 310 (1989).
16. C. G. Schull and Y. Yamada, J. Phys. Soc. Jpn. **17** (Suppl. B-III), 1 (1962).
17. V. L. Sedov, *Antiferromagnetism of Gamma Iron: The Problem of Invar* (Nauka, Moscow, 1987), pp. 7–8 [in Russian].
18. R. J. Weiss and K. J. Tauer, Phys. Rev. **102** (6), 1490 (1956).
19. L. F. Skorentsev and V. S. Demidenko, Fiz. Met. Metalloved. **83** (5), 18 (1997) [Phys. Met. Metallogr. **83**, 471 (1997)].
20. P. J. Brown, H. Capellmann, J. Deportes, D. Givord, and K. R. A. Ziebeck, J. Magn. Magn. Mater. **30** (3), 335 (1983).
21. P. Boni, G. Shirane, J. P. Wicksted, and C. Stassis, Phys. Rev. B **31** (7), 4597 (1985).
22. É. Z. Valiev, Fiz. Met. Metalloved. **62** (2), 228 (1986).
23. A. I. Zakharov, A. Z. Men'shikov, and A. S. Uralov, Fiz. Met. Metalloved. **36** (6), 1306 (1973).

Translated by K. Shakhlevich

Physics of the Solid State, Vol. 46, No. 12, 2004, pp. 2191–2195. Translated from Fizika Tverdogo Tela, Vol. 46, No. 12, 2004, pp. 2119–2123.

METALS AND SUPERCONDUCTORS

Formation and Structure of Nanocrystals in Bulk $Zr_{50}Ti_{16}Cu_{15}Ni_{19}$ Metallic Glass

G. E. Abrosimova*, A. S. Aronin*, D. V. Matveev*, and V. V. Molokanov**

**Institute of Solid State Physics, Russian Academy of Sciences, Chernogolovka, Moscow oblast, 142432 Russia*
e-mail: matveev@issp.ac.ru
***Baĭkov Institute of Metallurgy and Materials Sciences, Russian Academy of Sciences, Leninskiĭ pr. 49, Moscow, 117911 Russia*

Received April 13, 2004

Abstract—The possible formation of a nanocrystalline structure in controlled crystallization of a bulk $Zr_{50}Ti_{16}Cu_{15}Ni_{19}$ amorphous alloy has been studied using differential scanning calorimetry, transmission and high-resolution electron microscopy, and x-ray diffraction. It was established that crystallization of the alloy at temperatures above the glass formation point occurs in two stages and brings about the formation of a nanocrystalline structure consisting of three phases. Local spectral x-ray analysis identified the composition and structure of the phases formed. © *2004 MAIK "Nauka/Interperiodica".*

1. INTRODUCTION

Amorphous alloys have recently been shown to exist in many metallic systems [1]. Nanocrystalline alloys with a variety of characteristics have been prepared by partial crystallization of the amorphous phase in a number of rapidly quenched alloys, such as Fe–Nb–B [2–4], Fe–Si–B–Nb–Cu [5], Fe–(Zr, Nb)–B [6], and Al–*Ln*–TM (here, *Ln* stands for a lanthanide and TM, for a transition metal) [7]. While the nanocrystalline alloys prepared exhibited high mechanical and magnetic characteristics, they could be produced only in the form of ribbons 30- to 50-μm thick, which limited their application potential. Quite recently, bulk metallic glasses appeared [8–12]. They form at substantially lower chilling rates (~100 K/s); have, as a rule, a complex chemical composition; and consist (by the rule of Inoue [11]) of no less than four components. Melts of such compositions exhibit a high viscosity and a low solidification temperature. The glass transition temperature for these alloys usually lies below the crystallization point; therefore, they pass through a broad temperature region of supercooled liquid before the onset of crystallization. Among these metallic glasses, Zr-based alloys are of particular interest, because they feature a very broad supercooled-liquid temperature region, which is in excess of 100 K for many alloys [13]. These alloys have unique mechanical properties. For instance, some zirconium-based alloys exhibit a high yield point (840–2100 MPa), an elastic strain of ~4%, high plasticity, and good resistance to corrosion [14]. These alloys also attract attention because one can obtain a nanocrystalline structure in them under thermal treatment. Earlier studies have shown that crystallization of Zr-based alloys sometimes gives rise to the formation not only of various crystalline phases but of quasicrystals as well [15], but the chemical composition of the crystalline phases, their mutual arrangement, and the degree of perfection have not been studied in considerable detail in the majority of cases. However, this information is needed to understand the processes occurring in the crystallization of amorphous alloys. Our preceding publication [16] reported on a study of the mechanical properties of bulk $Zr_{50}Ti_{16}Cu_{15}Ni_{19}$ amorphous alloy samples at room and elevated temperatures and the correlation of these properties with the sample structure. We determined the structural type of the phases formed, but their chemical composition remained unknown. The purpose of this study was to establish the conditions under which a nanocrystalline structure forms and to determine the composition of the phases precipitating in the crystallization of a bulk $Zr_{50}Ti_{16}Cu_{15}Ni_{19}$ amorphous alloy, their mutual arrangement, and the degree of perfection.

2. EXPERIMENTAL TECHNIQUE

Bulk samples of the $Zr_{50}Ti_{16}Cu_{15}Ni_{19}$ amorphous alloy were prepared by quenching a melt in a quartz capillary. The samples were rod-shaped with a diameter of ~4 mm. The starting materials were more than 99.8% pure. The composition was taken to be that of the batch. Samples prepared for electron microscopy and electron diffraction studies were ribbons ~0.3×3.0 mm in cross section. The temperatures of glass transition (T_g) and nucleation (T_x) and the alloy crystallization enthalpy ΔH were determined using differential scanning calorimetry on a SETARAM DSK-7 calorimeter at a heating rate of 10 K/min.

Phase transformations were analyzed on samples annealed in vacuum at a pressure of 10^{-3} Pa in the tem-

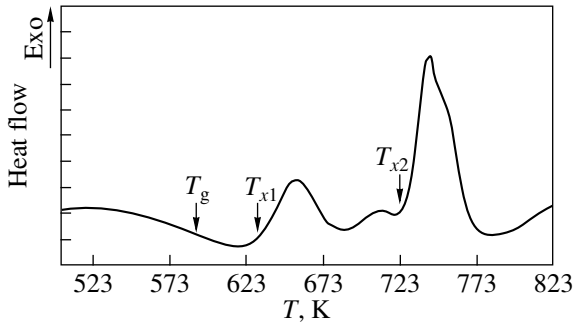

Fig. 1. Thermogram of a bulk amorphous $Zr_{50}Ti_{16}Cu_{15}Ni_{19}$ alloy.

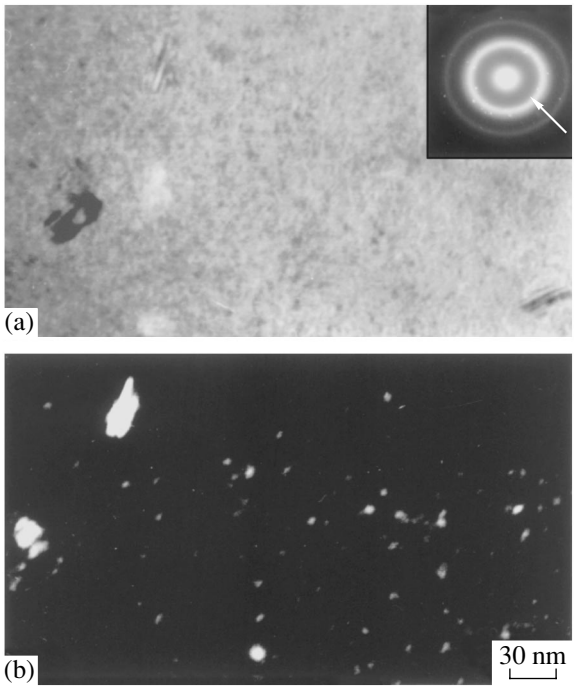

Fig. 2. Microstructure of the $Zr_{50}Ti_{16}Cu_{15}Ni_{19}$ alloy obtained after thermal treatment at 685 K. (a) Bright-field image and (b) dark-field image.

perature interval from 293 to 823 K over 10–90 min. The samples were annealed in a resistance furnace.

The structure and phase composition of the starting and annealed samples were studied using x-ray diffraction and transmission electron microscopy. X-ray measurements were performed on a SIEMENS D-500 diffractometer with CuK_α radiation. Electron microscopic studies were carried out on JEOL-100 CX and JEOL-2010FX transmission electron microscopes equipped with an attachment for local x-ray spectral analysis. The latter technique was employed to probe the chemical composition of individual crystals directly in the column of the transmission electron microscope.

3. EXPERIMENTAL RESULTS AND THEIR DISCUSSION

The as-prepared samples were amorphous. The diffractogram of the starting alloy contains only broad diffuse maxima characteristic of an amorphous structure. We determined the glass transition temperature T_g and the temperature of the onset of alloy crystallization T_x by means of differential scanning calorimetry (DSC). The thermogram exhibits two broad peaks (Fig. 1). They overlap partially, thus demonstrating the existence of a temperature interval within which several phases form simultaneously. It was found that $T_g \sim 590$ K, $T_{x1} \sim 630$ K, and $T_{x2} \sim 725$ K. The maxima of the peaks are at ~655 and ~740 K, and the enthalpies of crystallization ΔH are ~8 and ~20.5 J/g for the first and second peaks, respectively. This pattern of the DSC curve suggests that, in the first stage, the crystallization proceeds by the primary mechanism (this transformation is identified by the first exothermal peak), after which crystals of the other phases precipitate out of the remaining amorphous matrix, whose composition changed as a result of the primary crystallization.

Prolonged annealing of the samples performed at 575 K (below the glass transition temperature) did not drive crystallization of the amorphous phase.

To reveal the phase transformation sequence and study the structure of the forming phases, thermal treatment was carried out at temperatures corresponding to the first and second maxima on the DSC curve.

Figure 2 presents the microstructure and an electron diffraction pattern (see inset) after thermal treatment performed at 685 K (the region of the first peak). The electron diffraction pattern contains a diffuse halo and a few reflections due to crystalline phases. The dark-field image obtained for one of the reflections (identified by an arrow in the diffraction pattern) reveals crystal precipitates up to 10 nm in size.

An analysis of high-resolution images of such crystals and of the corresponding Fourier transforms of the direct lattice images obtained revealed that, in the first stage, where the primary crystallization occurs, a phase precipitated with a Zr_6CoAl_2-type lattice having hexagonal structure (space group $P62m$). Figure 3 displays a high-resolution image of a nanocrystal of the phase with a Zr_6CoAl_2-type lattice surrounded by the amorphous matrix. The inset to Fig. 3 shows an image of a section of the reciprocal lattice of this crystal obtained by Fourier transform. Note that such nanocrystals have no defects.

Thus, after thermal treatment, a sample consists mostly of an amorphous phase with a few nanocrystalline precipitates with a Zr_6CoAl_2-type lattice.

Figure 4 presents a diffraction pattern of a sample obtained after thermal treatment at 773 K (completion of the crystallization process). The observed diffraction reflections correspond to three phases: the already mentioned Zr_6CoAl_2-type structure with lattice parameters $a = 0.793$ nm and $c = 0.331$ nm (hexagonal lattice,

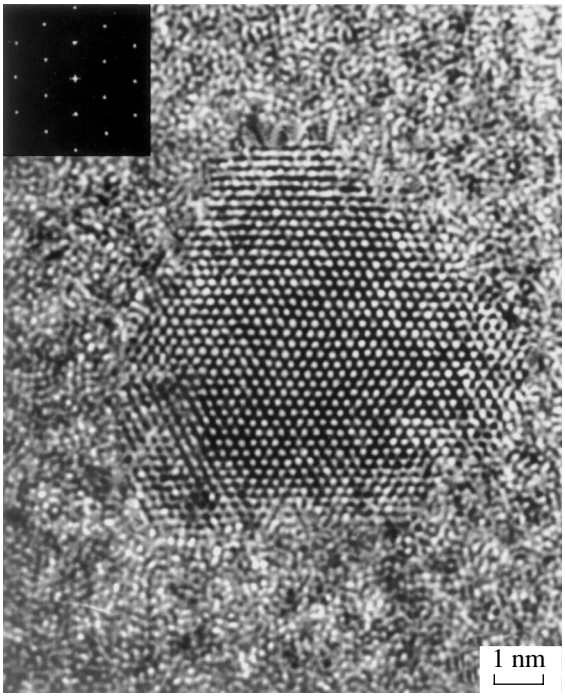

Fig. 3. Direct resolution of a nanocrystal of the Zr_6CoAl_2-structure phase embedded in an amorphous matrix.

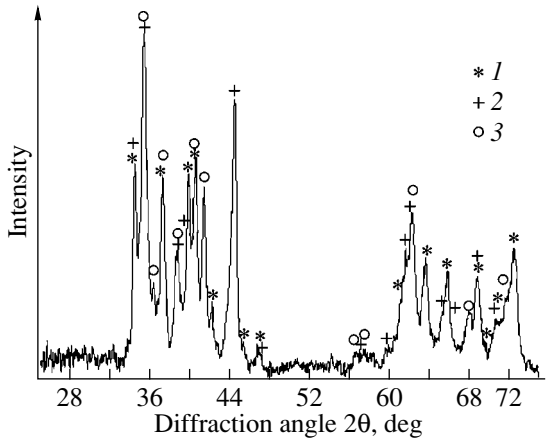

Fig. 4. Diffraction pattern of the $Zr_{50}Ti_{16}Cu_{15}Ni_{19}$ alloy obtained following thermal treatment at 773 K. (*1*) $MgZn_2$-structure phase, (*2*) Zr_6CoAl_2-structure phase, and (*3*) quasicrystalline phase.

space group $P62m$), a hexagonal phase with a $MgZn_2$ structure (space group $P6_3/mmc$) and lattice parameters $a = 0.524$ nm and $c = 0.854$ nm, and a quasicrystalline phase with $a_0 = 0.254$ nm. The Cahn system [17] was used for indexing the quasicrystalline phase.

The Zr_6CoAl_2-structure phase was observed earlier after crystallization of the amorphous phase [18], as well as following mechanoactivation [19]. The hexagonal phase with a $MgZn_2$-type structure is usually referred to in the literature as ZrTi(Ni,Cu); this phase was observed in the crystallization of bulk Zr-based amorphous alloys [20]. Its lattice parameters differ only slightly, which may be due to differences in the chemical composition, but the chemical composition of the phase was not discussed in the literature. The formation of quasicrystalline phases in the course of crystallization of zirconium-based amorphous alloys was also seen to occur earlier. For instance, a quasicrystalline phase with $a_0 = 0.253$ nm was detected in the $Zr_{69.5}Cu_{12}Ni_{11}Al_{7.5}$ alloy in [21].

Figure 5 displays an image of the microstructure of a sample obtained after subjecting it to thermal treatment at 773 K. The nanocrystals formed during annealing at this temperature are seen to be 25–35 nm in size. Some of them contain twins and stacking faults. Figure 6 shows the area specified in Fig. 5 at a high magnification. The image was obtained by high-resolution electron microscopy. It features two crystals of the Zr_6CoAl_2- and $MgZn_2$-structure phases, which have different orientations and are separated by a boundary.

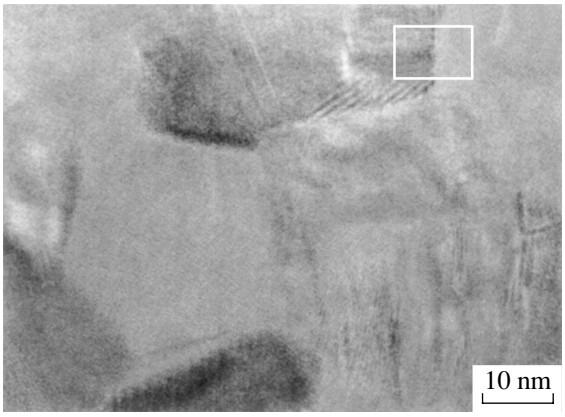

Fig. 5. Microstructure of a $Zr_{50}Ti_{16}Cu_{15}Ni_{19}$ alloy sample obtained after thermal treatment at $T = 773$ K.

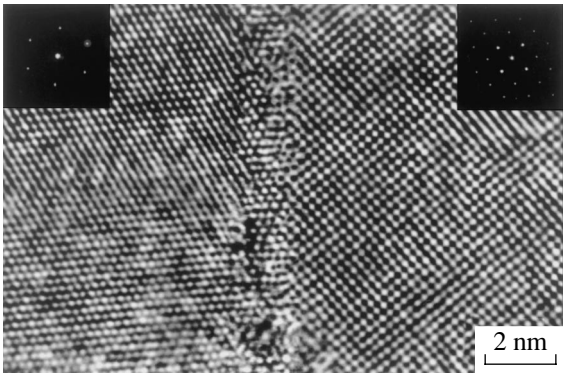

Fig. 6. High-resolution image of a $Zr_{50}Ti_{16}Cu_{15}Ni_{19}$ alloy obtained after thermal treatment at $T = 773$ K.

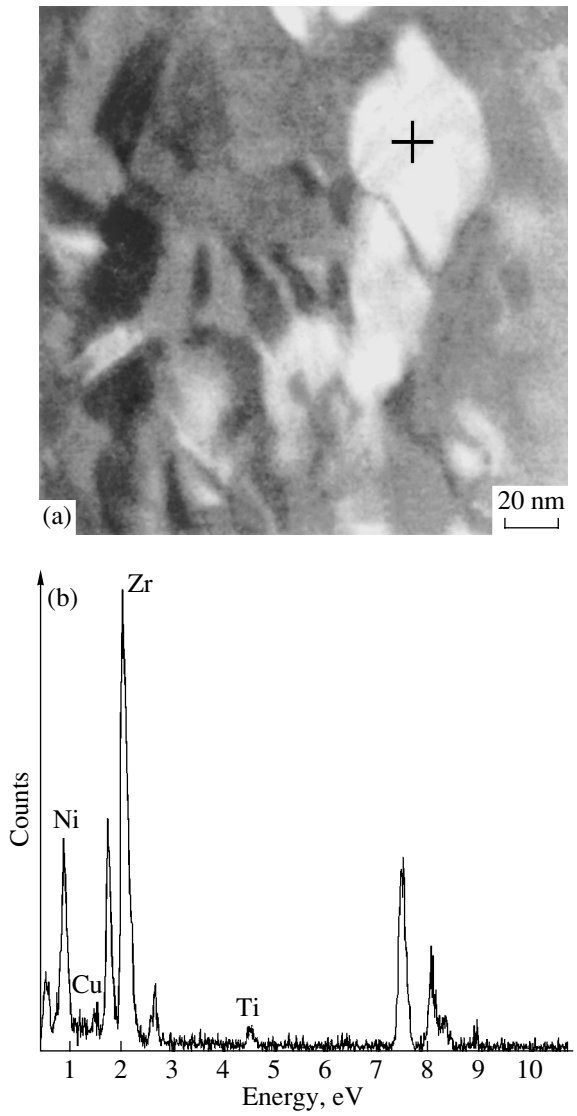

Fig. 7. (a) Photomicrograph of a $Zr_{50}Ti_{16}Cu_{15}Ni_{19}$ alloy sample obtained after isothermal annealing at 773 K and (b) the corresponding elemental spectrum.

The insets show sections of the reciprocal lattice of these phases obtained by Fourier transform of a direct lattice resolution.

Note that a nanocrystalline structure was observed to form only during thermal treatment at temperatures above the glass transition point, i.e., from the supercooled liquid state. This observation is in full agreement with the available information on the formation of a nanocrystalline structure occurring primarily above the glass transition temperature. For Cu–Ti alloys, it was found earlier that, as the transformation temperature crosses the glass transition point, the kinetic characteristics of the transformation change sharply; indeed, the rate of crystal nucleation begins to increase faster than the growth rate does [22] and a break appears in the plot relating the nucleation rate to temperature. A sharp increase in the transformation temperature (above T_g) in Fe–B alloys also stimulates the formation of a nanocrystalline structure [23]. At the same time, crystallization of these alloys below the glass transition temperature does not lead to the formation of a nanocrystalline structure.

To determine the chemical composition of the phases, local x-ray analysis was carried out directly in the electron microscope column. Figure 7 presents a photomicrograph of a sample made by transmission scanning electron microscopy following isothermal treatment at 773 K (the cross identifies the spot where the analysis was performed), as well as the corresponding spectrum. The chemical composition of the three different phases averaged over several measurements yielded the following formulas: (1) $Zr_{49}Ti_7Cu_{12}Ni_{32}$, (2) $Zr_{47}Ti_{18}Cu_{16}Ni_{19}$, and (3) $Zr_{65}Ti_4Cu_{12}Ni_{21}$. To identify these compositions with the relevant phases formed in the crystallization, computer modeling and calculation of the scattering intensity were performed for the crystalline phases, with subsequent collation of the calculated with experimental diffraction patterns. The choice of the atomic positions was made with due account of the atomic radii of the components.

The calculations showed that the best fit between the experimental and calculated diffractograms was obtained when the Zr_6CoAl_2-structure phase was assigned the composition $Zr_{47}Ti_{18}Cu_{16}Ni_{19}$. In this case, the Zr positions are occupied by Zr atoms (R = 0.16 nm) and Ti atoms, which are the closest in size (R = 0.145 nm), while the atoms of copper (R = 0.1278 nm) and nickel (R = 0.1245 nm) occupy the positions of Al (R = 0.1431 nm) and Co (R = 0.1253 nm) in the Zr_6CoAl_2 structure. The $MgZn_2$-structure phase has the chemical composition $Zr_{49}Ti_7Cu_{12}Ni_{32}$.

It was shown in [24] that crystallization of the amorphous $Zr_{66.4}Cu_{10.5}Ni_{8.7}Al_8Ti_{6.4}$ alloy brings about the formation of a quasicrystalline phase and that only this phase forms in the crystallized sample; i.e., its chemical composition is actually that of the alloy. This composition is close to the third composition observed by us ($Zr_{65}Cu_{12}Ni_{21}Ti_4$), thus giving us grounds to suggest that it is this composition that corresponds to the quasicrystalline phase.

4. CONCLUSIONS

We have shown that crystallization of the bulk amorphous $Zr_{50}Ti_{16}Cu_{15}Ni_{19}$ alloy takes place in two stages; more specifically, the first to form is a hexagonal phase with a Zr_6CoAl_2 structure, followed by parallel precipitation of a hexagonal phase with a $MgZn_2$ structure and a quasicrystalline phase. The Zr_6CoAl_2-structure phase has the $Zr_{47}Ti_{18}Cu_{16}Ni_{19}$ composition, and it has maximum content in the alloy; the composition of the $MgZn_2$-structure phase is $Zr_{49}Ti_7Cu_{12}Ni_{32}$, and that of the quasicrystalline phase is $Zr_{65}Ti_4Cu_{12}Ni_{21}$. A nanocrystalline structure forms at temperatures above the

glass transition point; the first to appear are $Zr_{47}Ti_{18}Cu_{16}Ni_{19}$ nanocrystals up to 10 nm in size, and then, as the temperature is increased, a nanocrystalline structure consisting of three phases forms with grain sizes of 25–35 nm.

ACKNOWLEDGMENTS

This study was supported by the Russian Foundation for Basic Research (project no. 03-02-17227), the program of the Presidium of the RAS "Fundamental Problems in the Physics and Chemistry of Nanosized Systems and Nanomaterials," and the program of the Department of Physical Sciences of the RAS "New Materials and Structures."

REFERENCES

1. *Amorphous Metal Alloys*, Ed. by F. E. Lyuborskiĭ (Metallurgiya, Moscow, 1987), p. 584 [in Russian].
2. J. J. Croat, J. F. Herbst, R. W. Lee, and F. E. Pinkerton, J. Appl. Phys. **55**, 2078 (1984).
3. R. Coehoorn, D. B. de Mooij, and C. De. Waard, J. Magn. Magn. Mater. **80**, 101 (1989).
4. A. Inoue, A. Takeuchi, A. Makino, and T. Masumoti, Mater. Trans., JIM **36**, 676 (1995).
5. Y. Yoshizawa, S. Ogume, and K. Yamaguchi, J. Appl. Phys. **64**, 6044 (1988).
6. K. Suzuki, N. Kataoka, A. Inoue, A. Makino, and T. Masumoti, Mater. Trans., JIM **31**, 743 (1990).
7. Y. H. Kim, A. Inoue, and T. Masumoti, Mater. Trans., JIM **31**, 747 (1990).
8. A. Inoue, T. Zhang, and T. Masumoti, Mater. Trans., JIM **33**, 177 (1990).
9. A. Inoue, T. Zhang, N. Nishiyama, K. Ohba, and T. Masumoti, Mater. Trans., JIM **34**, 1234 (1993).
10. A. Peker and W. L. Johnson, Appl. Phys. Lett. **63**, 2342 (1993).
11. A. Inoue, Mater. Trans., JIM **36**, 866 (1995).
12. A. Inoue, T. Zhang, and T. Itoi, Mater. Trans., JIM **38**, 359 (1997).
13. T. Zhang, A. Inoue, and T. Masumoto, Mater. Trans., JIM **32**, 1005 (1991).
14. L. Q. Xing, D. M. Herlach, M. Cornet, C. Bertrand, J.-P. Dallas, M.-H. Trichet, and J.-P. Chevalier, Mater. Sci. Eng. A **226–228**, 874 (1997).
15. A. Inoue, T. Zhang, M. W. Chen, T. Sakurai, J. Saida, and M. Matsushita, Appl. Phys. Lett. **76** (8), 967 (2000).
16. G. Abrosimova, A. Aronin, D. Matveev, I. Zverkova, V. Molokanov, S. Pan, and A. Slipenyuk, J. Mater. Sci. **36** (16), 3933 (2001).
17. J. W. Cahn, D. Shechtman, and D. Gratias, J. Mater. Res. **1**, 13 (1986).
18. J. Eckert, N. Mattern, M. Zinkevitch, and M. Seidel, Mater. Trans., JIM **39**, 623 (1998).
19. J. Saida, M. S. El-Eskandarany, and A. Inoue, Scr. Mater. **48**, 1397 (2003).
20. S. Spiriano, C. Antonione, R. Doglione, L. Battezzati, S. Cardoso, J. C. Soares, and M. F. Da Silva, Philos. Mag. B **76** (4), 529 (1997).
21. U. Köster, J. Meinhardt, S. Roos, and H. Liebertz, Appl. Phys. Lett. **69** (2), 179 (1996).
22. U. Köster, J. Meinhardt, A. Aronin, and Y. Birol, Z. Metallkd. **86**, 171 (1986).
23. G. E. Abrosimova, A. S. Aronin, and V. A. Stel'mukh, Fiz. Tverd. Tela (Leningrad) **33**, 3570 (1991) [Sov. Phys. Solid State **33**, 2006 (1991)].
24. G. He, W. Löser, and J. Eckert, Scr. Mater. **48**, 1531 (2003).

Translated by G. Skrebtsov

Physics of the Solid State, Vol. 46, No. 12, 2004, pp. 2196–2200. Translated from Fizika Tverdogo Tela, Vol. 46, No. 12, 2004, pp. 2124–2128.

SEMICONDUCTORS AND DIELECTRICS

Electron Spin Orientation under Optically Stimulated Radiative Recombination

A. I. Grachev

Ioffe Physicotechnical Institute, Russian Academy of Sciences, Politekhnicheskaya ul. 26, St. Petersburg, 194021 Russia
e-mail: grach.shuv@mail.ioffe.ru

Received December 30, 2003; in final form, April 26, 2004

Abstract—Optical spin orientation of electrons (holes) in radiative transitions stimulated by circularly polarized photons is considered. It is shown that this effect can be used to advantage in developing an optical generator of spin-polarized carriers operating on a principle similar to that of a semiconductor laser. © *2004 MAIK "Nauka/Interperiodica".*

1. INTRODUCTION

Development of efficient methods for injecting spin-polarized carriers is a major problem in spintronics. Methods based on optoelectronic effects may provide a viable alternative to the various proposals envisaging the use of ferromagnetic materials as sources of polarized carriers (see, e.g., review [1]). Until recently, the best known of the former methods was electron (hole) spin orientation through asymmetric direct optical transitions induced by circularly polarized photons [2–4]. A new method of generating spin-polarized current was demonstrated in [5] through the specific example of a semiconductor heterostructure with an asymmetric quantum well (QW). This method is based on the fact that the spontaneous radiative recombination of carriers with oppositely directed spins becomes asymmetric when an electric current is passed in the QW plane. One readily sees an intimate connection between this mechanism and the microscopic processes that underlie the circular photogalvanic effect [6, 7] and related phenomena [8–10]. A feature common to all these effects is the asymmetry of the elementary electronic processes (scattering, optical excitation, or radiative recombination of charge carriers) stemming from the electron having a spin degree of freedom. The possible electron spin polarization in a sample carrying a current was also treated in [9, 10], but in the latter publications, in contrast to [5], the appearance of polarization was a consequence of the asymmetry intrinsic in spin-dependent carrier scattering.

Here, we consider carrier spin orientation, which is based, like that in [5], on the asymmetry of spin-dependent recombination but is a process of radiative recombination stimulated by circularly polarized light. As in the traditional method of optical orientation [2], we propose illuminating a crystal (a heterostructure, etc.) by circularly polarized light, but its spectral composition, the direction of its propagation, and the sign of circular polarization should now coincide with those of the photons emitted spontaneously in the recombination of carriers with a given spin direction. Thus, the proposed method is based not on the photoexcitation of, for example, electron–hole pairs but rather on the process of their optically stimulated recombination. We will also discuss the concept of an optical generator of spin-polarized carriers, which, by analogy with a laser, has been termed a "soser" (spin orientation by stimulated emission of radiation).

2. MECHANISM OF ELECTRIC CURRENT–INDUCED SPIN POLARIZATION

Consider first the essence of the mechanism of spin polarization described in [5]; to make its comparison with the one we are proposing more revealing, we also analyze a heterostructure containing a QW that provides an inverse band population. In contrast to [5], however, we assume that the spin splitting of the valence and conduction bands of the QW is a consequence of spin–orbital interaction (irrespective of its origin). In this case, the effective Hamiltonian describing the QW energy spectrum contains not only the conventional parabolic contribution

$$E_{c,v}(k) = \hbar^2 k^2/2m^*_{c,v} \quad (1)$$

(m_c^* and m_v^* are the effective electron and hole masses, respectively) but also spin-dependent terms linear in the wave vector **k**, including those of the type

$$H_{c,v} = \beta_{c,v}\sigma_z k_x, \quad (2)$$

where σ_z is a Pauli matrix and the z and x axes are assumed to be directed along and perpendicular to the QW growth axis, respectively. Linear-in-**k** terms for bulk materials can exist only if the materials belong to one of the gyrotropic symmetry classes [11]. The necessary condition for the existence of a term similar to that in Eq. (2) for heterostructures based, for instance,

on zinc blende semiconductors, is the lowering of QW symmetry to C_s [11].

We introduce the following simplifying assumptions, which do not influence the generality of our consideration noticeably: (i) only spin polarization of the conduction electrons will be taken into account, because the valence band holes are assumed to have a considerably lower mobility and a much shorter spin relaxation time (τ_s^h); (ii) the spin splitting of the conduction band is markedly smaller than that of the valence band, so we neglect it in drawing a schematic band structure (Fig. 1), although spin degeneracy near the conduction band bottom is assumed to be lifted completely for electrons with $s_z = \pm 1/2$; and (iii) the states prevailing near the valence band top are those with an angular momentum projection $m_z = \pm 3/2$, which appears to be quite reasonable for states below the Fermi level for holes (μ_h) in the heavy-hole subband (Fig. 1), provided the condition $\mu_h < \Delta$ is met, where Δ is the spin–orbital splitting of the valence band.

For definiteness, we will consider only the region of sufficiently low temperatures in what follows.

Although lifting of the valence-band spin degeneracy does bring about an asymmetry in **k** space of the spontaneous radiative recombination of electrons with oppositely directed spins, this is certainly insufficient for the onset of spin polarization [5]. Indeed, because the distribution of electrons and holes in **k** space, $f_{c,v}(\mathbf{k})$, is symmetric, the filling of the pairs of states (*1*, *2*) and (*1*', *2*') with a given magnitude of the wave vector $|k_x|$ (Fig. 1a) involved in spontaneous radiative transitions allowed by optical selection rules does not depend on the sign of k_x. Therefore, although the recombination asymmetry will produce more electrons with $s_z = +1/2$ in the $k_x > 0$ region, the number of electrons with $s_z = -1/2$ in the $k_x < 0$ region will increase by the same amount.

Generation of spin polarization becomes possible if $f_{c,v}(\mathbf{k})$ is anisotropic; one of the ways to make this distribution anisotropic is to apply a transverse electric field $\mathbf{E}_t$ in order to produce an electric current in the QW plane [5]. The drift of carriers in field $\mathbf{E}_t$ will impart to them an additional momentum, which will be different in magnitude for the electrons and holes because of their assumed difference in mobility. As a result, a relative band offset will appear in **k** space (Fig. 1b) by an amount $\delta\mathbf{k} = m_c^* \mu_e \mathbf{E}_t/\hbar$ (where μ_e is the electron mobility), which will provide the required anisotropy of $f_{v,c}(\mathbf{k})$.

In our case, in order for electron spin polarization to appear along the *z* axis, the field $\mathbf{E}_t$ should be applied along the QW axis *x*. Now, the filling of valence band states *2* and *2*' by holes is different (Fig. 1b); therefore, the rates of radiative transitions $1 \longrightarrow 2$ for electrons with $s_z = +1/2$ ($R_{z\uparrow}$) and of transitions $1' \longrightarrow 2'$ for electrons with $s_z = -1/2$ ($R_{z\downarrow}$) will no longer be equal. Because $R_{z\uparrow} < R_{z\downarrow}$, a nonequilibrium spin polarization

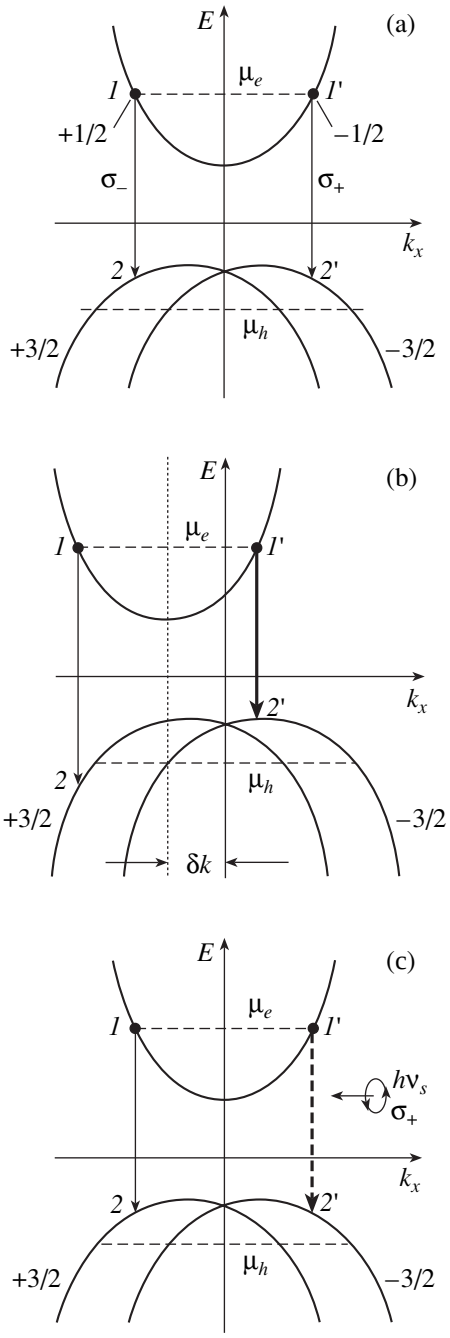

Fig. 1. (a) Schematic diagram of the quantum-well energy structure forming under band splitting due to spin–orbit coupling and of spontaneous radiative transitions involved in recombination of electrons with oppositely directed spins. (b) Recombination mechanism of spin polarization based on the difference between the rates of spin-dependent spontaneous transitions, arising as a transverse electric current is passed along the *x* axis. (c) Recombination mechanism of spin polarization based on the difference between the rates of spontaneous and stimulated radiative transitions stimulated by σ_+-polarized photons. Spontaneous and stimulated transitions are identified by solid and dashed arrows, respectively. The difference in the thickness of the arrows specifying the radiative transitions indicates the difference in the recombination rates between electrons with oppositely directed spins.

associated with the dominant concentration of electrons with $s_z = +1/2$ will appear in the conduction band. (Injection of spin-polarized electrons can now be attained, for instance, by applying a longitudinal electric field to the QW [5].)

The degree of the electron spin polarization P produced by the above mechanism is determined by the parameter

$$P_z = (R_{z\uparrow} - R_{z\downarrow})/(R_{z\uparrow} + R_{z\downarrow}) = \Delta R/(R_{z\uparrow} + R_{z\downarrow}), \quad (3)$$

which can be written in the form

$$P_z = [\tau_r(\uparrow)^{-1} - \tau_r(\downarrow)^{-1}]/[\tau_r(\uparrow)^{-1} + \tau_r(\downarrow)^{-1}], \quad (4)$$

where $\tau_r(\uparrow)$ and $\tau_r(\downarrow)$ are the times of spontaneous radiative recombination of electrons. For the spin polarization of electrons to be efficient, the difference between these times should be as large as possible. The difference between $R_{z\uparrow}$ and $R_{z\downarrow}$ arising under transverse-current generation is mainly due to the growth of $\tau_r(\uparrow)$; the variation in $\tau_r(\downarrow)$ may be neglected in a first approximation. The growth of $\tau_r(\uparrow)$ can be provided by increasing $\mathbf{E}_t$ [5], but with this one may meet with the problem of competition between the radiative transitions and the processes of nonradiative recombination and spin relaxation. Indeed, the degree of spin polarization in this method is also governed by the quantum yield of luminescence [5]:

$$\eta_l = \tau_{nr}/(\tau_{nr} + \tau_r), \quad (5)$$

where τ_{nr} is the nonradiative recombination time of an electron–hole pair. One should also take into account the dependence of P on the electron spin-relaxation time τ_s^e [12] determined by the parameter

$$\eta_s = \tau_s^e/(\tau_s^e + \tau), \quad (6)$$

where $\tau = \tau_{nr}\tau_r/(\tau_{nr} + \tau_r)$. Obviously enough, growth of $\tau_r(\uparrow)$ will inevitably bring about an increase in the total radiative recombination time, which, in turn, may give rise to an undesirable decrease in the quantities η_l and η_s. Below, we consider the mechanism of optical electron spin orientation involving the process of stimulated radiative recombination. This mechanism is not only free of the above shortcoming but also offers a number of new possibilities, which is a more important feature.

3. SPIN ORIENTATION IN STIMULATED RADIATIVE TRANSITIONS

It thus follows that, in order for the recombination mechanism of spin polarization to operate, two conditions have to be fulfilled. First, the spontaneous radiative transitions involved in electron–hole pair recombination should feature a spin-dependent asymmetry, and second, these transitions should occur at different rates (which in the above method is a consequence of an electric current–induced anisotropy in the distribution of electrons and holes in **k** space). Radiative recombination stimulated optically by circularly polarized light can meet both of the above conditions simultaneously. Realization of this mechanism will also be illustrated in the specific example of a QW.

Spontaneous radiative recombination in a QW is accompanied by emission of circularly polarized photons, whose sign of circular polarization, in accordance with the optical selection rules, is negative (σ_-) for $1 \longrightarrow 2$ transitions but positive (σ_+) for $1' \longrightarrow 2'$ transitions. We assume, for the sake of simplicity, that the emission spectrum with a bandwidth $\Delta\nu_r$ is practically the same for photons of both types, both with and without the field $\mathbf{E}_t$ applied. Now, let a beam of circularly polarized light whose frequency ν_s is confined in this spectral band strike the QW surface along the z axis. Depending on the actual sign of polarization, the incident light beam is capable of stimulating recombination events for one of the transitions, thus increasing or decreasing the current-induced difference ΔR. We assume the direction of light propagation to be such that photons of σ_- polarization stimulate additional transitions $1' \longrightarrow 2'$ (Fig. 1c). This will give rise to a further growth of ΔR, which will favor the growth of P_z. Note that the total rate of radiative recombination should increase in these conditions; hence, the parameters η_l and η_s will also increase.

The rate of stimulated radiative recombination is directly proportional to the intensity of incident light I (which is assumed to be too weak to give rise to effects associated with the variation of state population in the bands). Therefore, as I increases, a time will come when the rate of spontaneous transitions $1' \longrightarrow 2'$ can be neglected compared to that of the stimulated transitions. In this case, the electron spin polarization will be determined almost completely by the higher rate of the optically stimulated $1' \longrightarrow 2'$ transitions (compared to the rate of spontaneous transitions $1 \longrightarrow 2$). Clearly enough, the presence or absence of current in the QW plane is inessential in these conditions; i.e., the mechanism of spin polarization becomes purely optical. However, in contrast to the traditional optical spin polarization of electrons that is achieved in direct optical transitions resulting, in particular, in the formation of electron–hole pairs, here we have used optically stimulated recombination of these pairs. Because stimulated radiative transitions obey the same selection rules as direct optical transitions, the electron spin polarization **S** produced in recombination emission can be described phenomenologically in a similar way [12]:

$$\mathbf{S}_k = i\gamma_{kl}[\mathbf{E}\mathbf{E}^*]_l, \quad (7)$$

where **E** is the complex amplitude of the electric field of light and γ_{kl} is a material parameter, which is a function of the frequency of light. Note that the polarizations **S** that are produced by direct and radiative transitions induced by photons with the same sign of circular polarization and direction of propagation are opposite

in sign. It should also be stressed that, although the band structure scheme in Fig. 1 corresponds, as already mentioned, to one of the gyrotropic classes of symmetry, our mechanism of optical orientation, just as the traditional one, is applicable in any case of lifting (partial or complete) of band spin degeneracy in a semiconductor [2, 5, 12].

The degree of carrier spin orientation obtainable with this mechanism is naturally governed by the specific features of the semiconductor structure under study. A requirement common for all structures, however, is the generation and/or support of the inverse population of electronic levels by electrical or optical pumping. The value of P can be found, for instance, with the use of standard rate equations describing the operation of an optical semiconductor amplifier (see, e.g., [13]). We employ here, however, a simpler method to evaluate P, which will also permit us to compare the proposed and traditional methods of optical orientation.

We assume the levels μ_e and μ_h in the QW under study (Fig. 1c) to be located near the bottom of the conduction band and the top of the valence band, respectively. We illuminate the QW with a light pulse of σ_- polarization with the appropriate photon energy $h\nu_s$ and parameters satisfying the following conditions: $\tau_s^h \ll \Delta t_p \ll (\tau_s^e, \tau_r)$ and $(h\nu_s/\Delta t_p\sigma_p) < I_p < (h\nu_s/\tau_s^h\sigma_p)$, where Δt_p and I_p are the pulse duration and intensity, respectively, and σ_p is the photon capture cross section for the optical transitions under consideration. In this case, the population variation kinetics of the spin-split band branches can be adequately described by two pairs of levels, (*1*, *2*) and (*1*', *2*') (Fig. 1c). We readily see that, under these conditions, the electrons originally populating level *2*' (population $N_{in}(2')$) will become distributed by the end of the pulse between this level and levels *1*' and *1*, with the population of level *2* remaining practically unchanged, $N_{in}(2) = N_{in}(2')$. As a result, the degree of electron spin polarization will be 50%. Assuming now that, with all other conditions being equal, the semiconductor is intrinsic, i.e., only the valence band states are filled originally and, hence, optical orientation is attained by the traditional method, we obtain in this case $P = 100\%$. Thus, the efficiency of our method of spin polarization is only half that of the traditional approach, which should be ascribed to the fact that the populations of levels *2*' and *1*' are equal for an arbitrarily high power of illumination. (Note that the theoretical estimate of P and the corresponding experimental value obtained under spin injection into a semiconductor from ferromagnetic contacts are ~50 and ~30%, respectively [1].) This shortcoming could possibly be counterbalanced by invoking the concept of a spin-polarized carrier generator combining the electrical method of pumping with the mechanism of optical spin orientation in the absence of external illumination.

We assume that the QW considered by us is employed as an active layer, for instance, in a VCSEL. We next assume that we have succeeded in reaching a lasing regime in which photons propagating in the optical resonator of the laser in opposite directions along the z axis have polarizations σ_+ and σ_-. In this case, as follows from Eq. (6), photons will stimulate radiative recombination of electrons only with one (given) sign of the spin; hence, the spin polarization effect will take place. Obviously enough, this (spin-dependent) asymmetry in stimulated transitions is undesirable from the standpoint of the conversion efficiency of supplied electric power to optical radiation. Assuming the internal quantum efficiency η_i of the laser to be close to unity in standard conditions, generation of one circular mode could reduce η_i, in the limit, by one-half. Indeed, about 50% of all electrons supplied from the source of current to the laser active region can escape from this region without becoming involved in radiative transitions. This is exactly what is needed to convert a laser to a generator of spin-polarized electrons. Moreover, both optical resonator mirrors should have as high a reflection coefficient as possible, because the generated radiation is no longer an output signal for such a device, which, as already mentioned, may be called, by analogy with a laser, a soser.

The regime that is required for soser operation and in which only one of the two circularly polarized degenerate laser modes is amplified, can be attained in different ways, three of which are considered below.

(1) One method consists in introducing elements into the laser optical resonator that are capable of suppressing one of the above modes. For instance, a plate (layer) of a ferromagnetic material featuring circular birefringence can be placed between the VCSEL active region and one of the resonator mirrors. In this case, the effective resonator length will be different for oppositely polarized circular modes. Therefore, by choosing the parameters of this ferromagnetic material such that the active region of the laser falls into the antinode of the electric-field standing wave corresponding to only one of the circular polarizations, we will be able to almost completely suppress amplification of the wave with the opposite sign of polarization.

(2) The idea underlying the second approach follows logically from the above mechanism of current-induced spin polarization. By applying a transverse electric field to a QW (acting as an active laser region), we produce conditions favoring preferential generation of one of the circular modes (for instance, of σ_+) because of the rates of the corresponding spontaneous transitions becoming different. As a result, the generation threshold (determined, for instance, by the magnitude of the longitudinal threshold current) for one mode will be lower than that for the other. After the onset of generation of the σ_+ mode, we might expect this mode to be additionally amplified through suppression of the

σ_- mode due to spin relaxation of the polarized electrons.

(3) To illustrate the essence of the third method, we consider the recent publications [14, 15] dealing with the effect of electron spin polarization on the lasing conditions in a VCSEL. Optical pumping of a laser by linearly and circularly polarized beams revealed a decrease in the lasing threshold by 50% in the latter case [14]. This result is explained in [14] as being due to the fact that circular optical pumping induces electron spin polarization (accompanied by an increase in the inverse band population) and, as a consequence, increases the efficiency of emission of circularly polarized photons with the corresponding sign of the circular polarization. The hope was expressed in [14] that a similar result could be obtained by electrically injecting spin-polarized carriers. Thus, the desired generation regime can be obtained by injecting spin-polarized carriers into the laser active region by an optical or electrical pulse. This method could be called spin laser triggering.

Certainly, the above methods do not exhaust all possible schemes for realizing the proposed generator. Solving this problem, as well as developing effective means of injecting spin-polarized carriers from the active region, would require, however, consideration of the physics underlying the operation of the concrete semiconducting structures of interest.

ACKNOWLEDGMENTS

The author expresses gratitude to B.B. Krichevtsov for useful discussions and valuable comments.

REFERENCES

1. B. T. Jonker, Proc. IEEE **91**, 727 (2003).
2. *Optical Orientation*, Ed. by F. Meier and B. P. Zakharchenya (Elsevier, Amsterdam, 1984).
3. J. M. Kikkawa and D. D. Awschalom, Nature **397**, 139 (1999).
4. J. M. Kikkawa and D. D. Awschalom, Phys. Rev. Lett. **80**, 4313 (1998).
5. A. G. Mal'shukov and K. A. Chao, Phys. Rev. B **65**, 241308 (2002).
6. E. L. Ivchenko and G. E. Pikus, Pis'ma Zh. Éksp. Teor. Fiz. **27**, 640 (1978) [JETP Lett. **27**, 604 (1978)].
7. V. I. Belinicher, Fiz. Tverd. Tela (Leningrad) **20** (10), 2955 (1978) [Sov. Phys. Solid State **20**, 1706 (1978)].
8. S. D. Ganichev, E. L. Ivchenko, V. V. Bel'kov, S. A. Tarasenko, M. Solinger, D. Weiss, W. Wegscheider, and W. Prettl, Nature **417**, 153 (2002).
9. A. G. Aronov and Yu. B. Lyanda-Geller, Pis'ma Zh. Éksp. Teor. Fiz. **50**, 398 (1989) [JETP Lett. **50**, 431 (1989)].
10. V. M. Edelstein, Solid State Commun. **73**, 233 (1990).
11. E. L. Ivchenko and G. E. Pikus, *Superlattices and Other Heterostructures. Symmetry and Optical Phenomena* (Springer, Berlin, 1997).
12. M. I. D'yakonov and V. I. Perel', Zh. Éksp. Teor. Fiz. **60**, 1954 (1971) [Sov. Phys. JETP **33**, 1053 (1971)].
13. H. J. S. Dorren, D. Lenstra, Y. Liu, M. T. Hill, and G. D. Khoe, IEEE J. Quantum Electron. **39**, 141 (2003).
14. J. Rudolph, D. Hangle, H. M. Gibbs, G. Khitrova, and M. Oestreich, Appl. Phys. Lett. **82**, 4516 (2003).
15. M. Oestreich, M. Bender, J. Hubner, D. Hagele, W. W. Ruhle, Th. Hartmann, P. J. Klar, W. Heimbordt, M. Lampalzer, K. Volz, and W. Stolz, Semicond. Sci. Technol. **17**, 285 (2002).

Translated by G. Skrebtsov

Physics of the Solid State, Vol. 46, No. 12, 2004, pp. 2201–2206. Translated from Fizika Tverdogo Tela, Vol. 46, No. 12, 2004, pp. 2129–2134.

SEMICONDUCTORS AND DIELECTRICS

Afterglow of GaN Wurtzite-Structure Crystals Doped by Rare-Earth Metals

V. V. Krivolapchuk and M. M. Mezdrogina

Ioffe Physicotechnical Institute, Russian Academy of Sciences, Politekhnicheskaya ul. 26, St. Petersburg, 194021 Russia
e-mail: vlad.krivol@mail.ioffe.ru, margaret.m@mail.ioffe.ru

Received April 26, 2004

Abstract—The effect of impurity distribution and total defect concentration on the transport of nonequilibrium carriers has been estimated and specific features of afterglow in GaN and GaN⟨Eu, Sm, Er⟩ crystals revealed by measuring delayed near-edge photoluminescence spectra. A decrease in the total carrier concentration is shown to correlate with the afterglow in GaN wurtzite-structure crystals. The influence of additional illumination at a wavelength of 5145 Å on the evolution of delayed near-edge photoluminescence spectra was estimated in crystals with different Fermi level positions. *© 2004 MAIK "Nauka/Interperiodica".*

1. INTRODUCTION

Intense studies of InGaN/GaN-based quantum-well heterostructures culminated in the development of various light-emitting diodes. To improve the efficiency of these devices, one has to estimate the efficiency of nonequilibrium carrier transport depending on the presence of various defects and impurities and their inhomogeneous spatial distribution in an epitaxial GaN layer.

Interaction of impurities and defects is a major issue in the physics of semiconductors. The inhomogeneity of impurity and defect distribution in semiconductors with a spatially nonuniform structure, to which epitaxial GaN layers belong, can be varied by gettering with the use of rare-earth (RE) metals. However, when only steady-state near-edge photoluminescence (NEPL) spectra were measured, the problem of spatial defect ordering remained unsolved. To tackle it, we studied both stationary and delayed NEPL spectra of GaN crystals, undoped and RE doped, by properly varying the time delay.

Our earlier studies [1, 2] dealing with the variation of photoluminescence (PL) spectra of bulk GaN crystals doped by rare-earth metals, GaN⟨RE⟩, revealed the effect of defect gettering. This effect most probably originates from a decrease in the number of dangling bonds and a transformation of deep to shallow states and from the inverse process of conversion of shallow to deep states in the original *n*-GaN matrix, which are initiated by the formation of acceptor states. The considerable decrease in the intensity and FWHM of the emission line observed in GaN⟨RE⟩ samples can be traced to the fact that an RE metal acts here as a deep trapping level, thus interfering with carrier transport to the radiating states that determine the intensity and width of the emission lines. Thus, the issue of increasing the emission efficiency reduces to the problem of excitation (and, in particular, nonequilibrium-carrier) transport to the corresponding centers, which makes it dependent on their spatial distribution.

Estimation of the kinetic parameters of carrier transport in wide-bandgap semiconductors is notoriously a complex problem in connection with the need of obtaining contacts with the required barrier height. The presently available technologies of deposition of multilayer contacts are complex and do not take into account the change in barrier height induced by a change in defect concentration in the semiconductor matrix. Furthermore, the microstructure of bulk crystals, as a rule, is highly heterogeneous, which greatly complicates the interpretation of the results obtained. In this study, we employed contact-free methods of estimating both the total concentration and the spatial heterogeneity of defects.

Our goal was to determine the effect of spatial correlation between the RE states and defects of the original GaN matrix on the nonequilibrium-carrier kinetics in GaN⟨RE⟩ crystals, which is due to carrier transport in doped and undoped crystals. Furthermore, we addressed the question of the potential of contact-free optical methods in estimating the carrier concentration and transport in the wide-bandgap GaN matrix. To solve these problems, the evolution of delayed near-edge PL spectra was studied (by properly varying the gating time).

2. EXPERIMENTAL

RE metals were doped into GaN crystals, as in [1], by diffusion to reduce the concentration of additionally generated defects, which can appear both in the course of crystal growth and during dopant implantation. Sm, Eu, and Er were introduced into each group of crystals under identical conditions (film deposition and subsequent annealing in an ammonium environment at a tem-

1063-7834/04/4612-2201$26.00

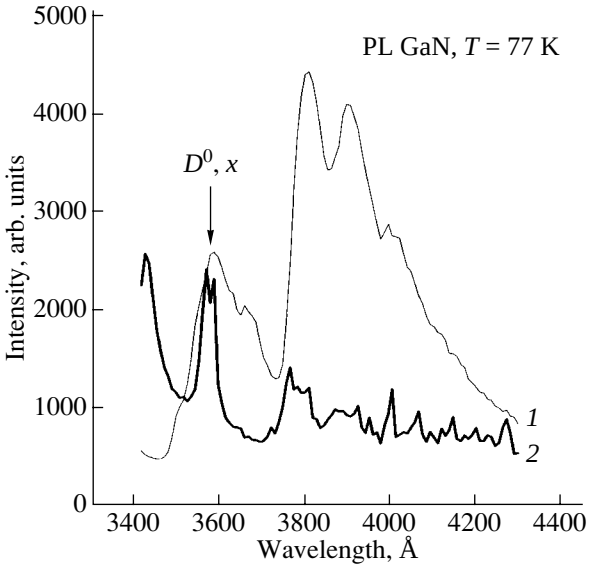

Fig. 1. Typical photoluminescence spectra of GaN crystals of (*1*) type 1 and (*2*) type 2.

perature of 1000–1050°C for 1.0–1.5 h were carried out in one technological run). As in [2], to ensure the possibility of a broader variation of defect concentration in the original semiconductor matrix, we used crystals prepared by two different techniques, namely, chloride–hydride epitaxy in an open system (HVPE, samples of the first type) and MOCVD (hydride technology, samples of the second type).

Most of the information on carrier and defect concentrations in the original crystals was extracted (as in [1]) from PL spectra, carrier concentration measurements carried out using the van der Pauw method (the Hall effect), determination of the Fermi level position in undoped and erbium-doped crystals, study of the surface morphology by electron microscopy, and the diffraction curve width (derived from x-ray data). In addition, the carrier and total defect concentrations in the original and doped crystals were estimated from optical measurements (PL spectra), namely, the intensity and position of the emission lines, the FWHM of lines, and the evolution of this parameter determined from delayed spectra by properly varying the gating time and excitation intensity. RE metals can reside in a semiconductor matrix in different charge states. The Er ion is in one charge state only (3+), and the two others (Eu, Sm) can be in two states each, 2+ and 3+. The charge state of the Eu impurity ion was determined using Mössbauer spectroscopy.

A study of the effect of RE doping on the photoluminescence spectra of GaN crystals performed in [3] showed that the method of doping employed governs the pattern of a PL spectrum. Indeed, the emission lines observed when doping during the growth are characteristic of NEPL and the *f–f* transition in the RE ion. When an RE metal is doped by implantation, no NEPL is observed and the only emission lines seen are typical of the *f–f* transitions in the RE ion (which may imply a large number of defects generated by implantation).

We report here on a study of stationary and delayed PL spectra. An analysis of GaN PL spectra places major attention on the position and intensity of the NEPL line and its FWHM. To be able to compare the emission spectra of different GaN samples, the controllable parameters, namely, the angle of beam incidence, the pump light intensity, and the temperature (300, 77 K), were maintained constant.

Optical measurements were conducted on an SDL-2 diffraction spectrometer with a reciprocal linear dispersion of 1.3 nm/mm in the GaN edge luminescence region. Several types of lasers were employed for photoluminescence excitation. Photoluminescence in stationary conditions was excited by a He–Cd cw laser operating at a wavelength $\lambda = 3250$ Å with an output power of 5 mW (interband GaN excitation). The delayed PL spectra and the decay process were studied with an LGI-21 pulsed nitrogen laser producing pulses $\tau \approx 10$-ns long (FWHM) at a wavelength $\lambda = 3371$ Å. The delayed PL pulses were recorded in a time gate 5- to 10-μs long. A cw argon laser provided illumination.

3. EXPERIMENTAL RESULTS AND DISCUSSION

Zero-delay NEPL spectra (stationary measurements) of the bulk original GaN crystals of different types are displayed in Fig. 1, where curve *1* is a spectrum of type-1 (HVPE-grown) samples and curve *2* refers to a spectrum of type-2 (MOCVD-grown) samples. Note that the carrier concentration in samples of the first type, obtained by Hall measurements using the van der Pauw method, is higher than 10^{18} cm^{-3} and is almost independent of temperature. The Fermi level at $T = 77$ K lies 23 meV above the conduction band bottom.

The spectra of type-1 samples contain an asymmetric emission line (the line FWHM was tentatively determined as 120–200 meV) peaking at $E = 3.463$ eV (358.1 nm), which can be identified with an exciton bound to a shallow donor (D^0, x) [4], and a band (3.27–3.18 eV), which corresponds to donor–acceptor recombination (*D–A* PL) involving shallow donors and acceptors. Note that the presence of the *D–A* PL band is evidence for the existence of shallow acceptor levels.

Curve *2* in Fig. 1 illustrates a PL spectrum of samples of the second type. The carrier concentration in these samples at $T = 77$ K is an order of magnitude lower than that in samples of type 2. The Fermi level at $T = 77$ K lies below the conduction band bottom, and the carrier concentration depends on temperature. The spectra of such samples also contain an emission line with a maximum at $E = 3.463$ eV (358.1 nm), but this line is symmetric in shape and its FWHM is 30–50 meV. This NEPL linewidth in *n*-GaN crystals at $T = 77$ K is determined by carrier concentration [4, 5], among other factors, and should be not less than 30 meV for the sam-

ples under study ($N_d - N_a > 10^{17}$ cm^{-3}). No emission is observed in the region 3.27–3.18 eV corresponding to donor–acceptor recombination (*D–A* PL), but a band is seen in the yellow–green spectral region (2.2–2.5 eV).

Major attention in the analysis of PL spectra of GaN crystals is focused on the position of the (D^0, x) line, its FWHM, and the intensity relation between this line and the *D–A* PL band. Note that, in real crystals, the (D^0, x) line has an inhomogeneous width. The inhomogeneous broadening is due to the fact that the radiations emitted in radiative recombination of carriers bound to various shallow centers differ somewhat in wavelength. The reason for this difference lies in the dispersion of the thermal activation energy E_{LT} of shallow donors. The E_{LT} dispersion itself arises because of the different local potentials V_{loc} at the shallow-impurity locations. This means that various defects lying close to shallow impurities affect the magnitude of the crystal field and thus influence the wavelength dispersion within the emission line profile. One should also bear in mind that this effect originates from a disordered distribution of defects over the emitting region of the sample. The radiation intensity of the (D^0, x) line and its FWHM depend on the concentration of radiative and nonradiative states and carrier transport to them. Whence it follows that, other conditions being equal, samples with different PL intensities and different values of the FWHM differ in terms of their total defect concentration. The defects are responsible both for the deep levels (which reduce the free carrier lifetime considerably) and for band density-of-states fluctuations. Furthermore, the defects may contain states with longer lifetimes of the photoexcited carriers they capture. It is this situation that is realized in epitaxial *n*-GaAs layers. The existence of metastable states in *n*-GaAs brings about a noticeable modification of both stationary and transient emission spectra [6–9]. Therefore, we studied the evolution of delayed NEPL spectra by properly varying the delay time in order to understand the role played by correlation between metastable states and other defects of the original GaN matrix in the nonequilibrium carrier kinetics in GaN⟨RE⟩ crystals and compare the mechanisms governing carrier transport in doped and undoped crystals.

Figure 2 illustrates the pattern of gated PL spectra (measured at different delay times Δt_d) of type-1 (HVPE-grown) GaN crystals, which had a width of 120–200 meV for zero delay. Note the following characteristic features of these spectra: (i) a sharp (by a factor of 3) decrease in the FWHM of the (D^0, x) line in type-1 samples (primarily on the long-wavelength side of the profile) with increasing delay time (Fig. 2a) and (ii) a considerable decrease (compared with the (D^0, x) line) in the intensity of the *D–A* PL band with increasing gating time Δt_d.

Considered from the phenomenological standpoint, the mechanism of appearance of such a long-lived (D^0, x) line afterglow is similar to that in the case of *n*-GaAs having metastable states (N_{MS}) [9]. There are, however, noticeable differences in the specific features of the long-lived afterglow between *n*-GaAs and *n*-GaN. In samples of *n*-GaAs (in contrast to *n*-GaN), the presence of the *D–A* PL band leads to disappearance of the long-lived kinetics in the (D^0, x) line. In *n*-GaAs epitaxial layers, this fact is a consequence of the material being topologically singly connected, so that shallow acceptor states in it trap photoexcited holes, thus competing with metastable centers and reducing the population of the metastable states substantially.

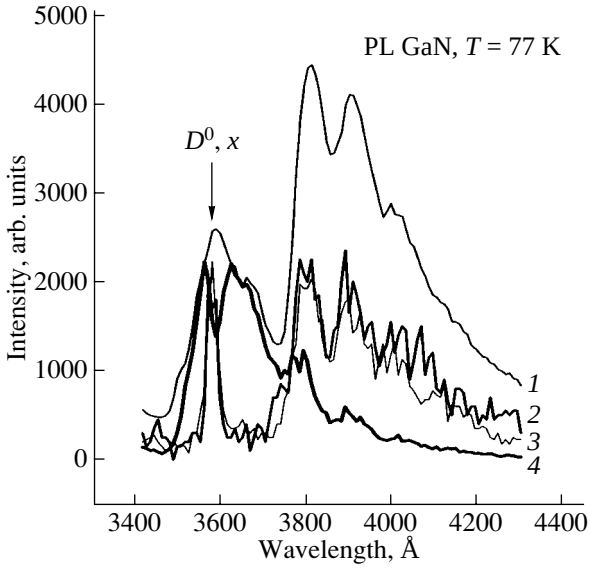

Fig. 2. Photoluminescence spectra of type-1 GaN crystals for different values of the delay time Δt_d: (*1*) 0, (*2*) 20, (*3*) 40, and (*4*) 60 μs.

The presence of the *D–A* PL band in the delayed PL spectra of GaN implies that the near-edge emission in epitaxial layers of *n*-GaN derives from two different "reservoirs" of holes. Holes localized at shallow acceptor levels (reservoir I) recombine (within a topologically singly connected region) with shallow-donor electrons to produce the *D–A* PL band. The intensity of this band falls off in a time characteristic of this recombination mechanism ($t_{DA} \approx 10^{-5}$ s). The long-lived afterglow of the (D^0, x) line is fed by another hole source (reservoir II), consisting of metastable states (N_{MS}) inhomogeneously distributed over the emitting region of the sample.

Turning now to an analysis of the reasons accounting for the line broadening, we note that the emission line profile in type-2 samples is asymmetric and has a noticeable feature on the long-wavelength side, which implies that the line is not elemental. Therefore, in order to unravel the nature of the emission line, one has to take into account not only the inhomogeneous broadening but also the contribution from radiation (other lines) of another origin. The first to come to mind in this

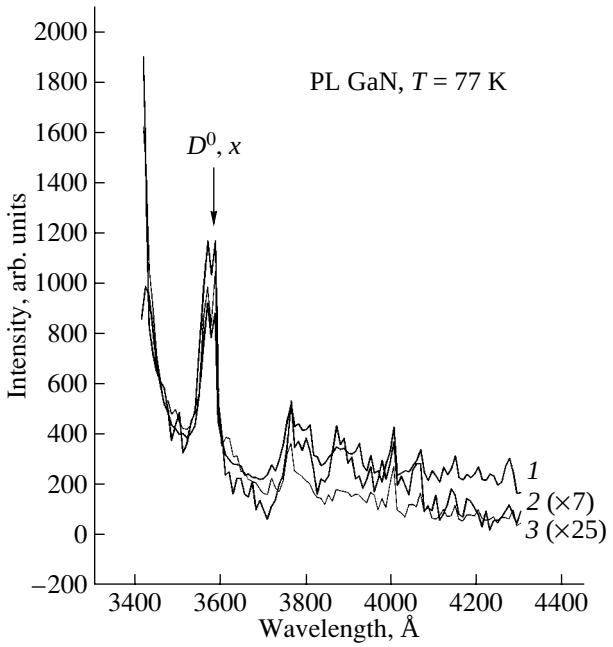

Fig. 3. Photoluminescence spectra of type-2 GaN crystals for different values of the delay time Δt_d: (*1*) 0, (*2*) 20, and (*3*) 40 μs.

respect is the emission of excitons bound to shallow neutral acceptors of various natures (A^0, x) [10].

The concentration of shallow donors in *n*-type crystals, N_d, is substantially higher than that of shallow acceptors, N_a ($N_d > N_a$). As the delay time increases to $\Delta t_d \approx 15$ μs, the holes bound to shallow acceptors recombine with the donor electrons (*D–A* PL band). As a result, the contribution of these excitons (A^0, x) to the long-wavelength wing of the emission line profile decreases, thereby causing a considerable decrease in the *D–A* PL band intensity. The line acquires a symmetric shape determined by the donor distribution, which is nonuniform, as considered above. As the delay time is increased still more ($\Delta t_d > 20$ μs), the FWHM of the (D^0, x) line decreases, thus indicating a contraction of the emitting region that contains shallow donors. This contraction is caused by constrained transport of free holes (ejected from metastable states into the valence band) to the emitting centers (D^0), as a result of which a noticeable part of the donors become excluded from the (D^0, x) line formation. This situation is realized in the case where the delay time Δt_d is longer than the free-hole lifetime τ_p. As the delay time is increased even further ($\Delta t_d > 40$ μs), the line FWHM does not change, which implies that, for $\Delta t_d > \tau_p$, carriers are no longer transported to the emitting centers.

It is essential that, in contrast to type-1 samples (where the FWHM decreases by a factor of 3), the half-width in type-2 samples is comparatively small and varies only very slightly with time (Fig. 3). This means that type-2 samples typically have a more homogeneous distribution of spatially correlated metastable states (N_{MS}) and shallow donors, thus providing better conditions for carrier transport. We see that these samples, which are more perfect in terms of both the concentration of residual shallow impurities ($N_d - N_a \approx 10^{17}$ cm^{-3}) and the homogeneity of their spatial distribution, exhibit (just as type-1 samples) long-lived emission of the (D^0, x) line. Thus, a comparison of the (D^0, x) emission line decay in type-1 and type-2 samples, which differ in degree of homogeneity, suggests that the boundaries between domains (mosaic pattern) do not play a noticeable part in the formation and distribution of metastable states and, hence, are not responsible for the long-lived afterglow of this line. A better understanding of the differences in the temporal evolution of the FWHM between samples of different types can be gained by considering the quantity $N_d - N_a$, which determines the position of the quasi-Fermi level. Indeed, the radiation intensity of the delayed PL spectra $I(E, t)$ is proportional to $N(E, t) = D(E)f(E, \mu, T)$, where $D(E)$ is the density of radiating states (which depends on spatial coordinates) and $f(E, \mu, T)$ is the Fermi–Dirac distribution function. For a fixed temperature, the quantity μ is determined by the carrier concentration. For long enough delay times, $\Delta t_d > 40$ μs, the evolution of the intensity of the emission line and of its half-width actually reflects the variation of the population of radiating states $N(E, t)$ with time.

Questions may arise in this connection as to the nature and spatial and energy position of the long-lived states and their origin and effect on the radiation intensity decay and the carrier transport parameters. To determine the energy position of the metastable levels (reservoir II), measurement of the delayed PL spectra was accompanied by simultaneous cw illumination by an argon laser. We used both single lines (487.9 and 514.5 nm) and a combination of all lines present in the laser output spectrum. It was found that delayed PL spectra undergo the largest changes under illumination with a photon energy $E = 2.409$ eV (514.5 nm). The actual pattern of the variation is determined by the sample type; namely, the largest changes are seen to occur in type-1 samples, whose (D^0, x) line with a comparatively small FWHM (51 meV) was the strongest in the continuous spectrum ($\Delta t = 0$). In these samples, the (D^0, x) line intensity in delayed PL spectra decreases by an order of magnitude. In type-1 samples with a large FWHM and a strong *D–A* PL band, illumination brings about a 30% increase (by a factor of 1.3) in the (D^0, x) line intensity in delayed PL spectra. In type-2 samples, the (D^0, x) line intensity varies within 10–20%. In view of the fact that illumination (at a photon energy coinciding with the characteristic excitation energy of metastable centers) changes the population of these centers, one has to assume the existence of different types of centers with substantially different parameters in the samples.

Thus, a comparison of the radiation intensity decay between samples differing in terms of their degree of homogeneity suggests that the boundaries separating

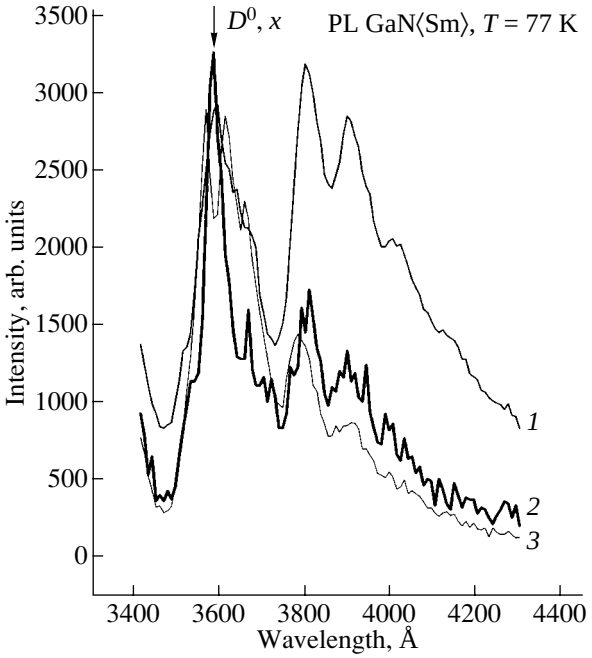

Fig. 4. Photoluminescence spectra of doped type-1 GaN⟨Sm⟩ crystals for different values of the delay time Δt_d: (*1*) 0, (*2*) 20, and (*3*) 40 μs.

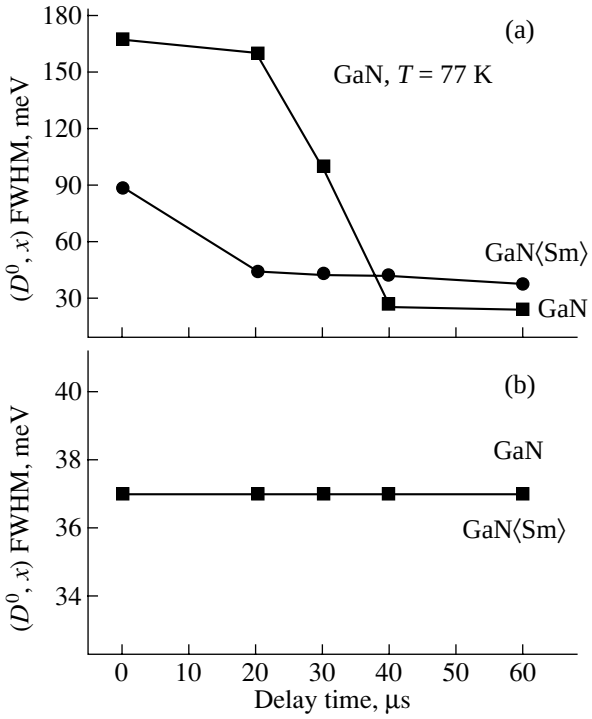

Fig. 5. FWHM as a function of delay time for undoped GaN crystals and crystals doped with samarium (GaN⟨Sm⟩) of (a) type 1 and (b) type 2.

domains (mosaic spread) do not play a noticeable role in the formation and distribution of metastable states and, hence, are not responsible for the long-lived afterglow. At the same time, the degree of homogeneity most likely exerts an influence on the transport parameters of nonequilibrium carriers in GaN. This influence is accounted for by the fact that the hole transport parameters are closely related to the existence of potential barriers in *n*-GaN, which has, in contrast to the homogeneous *n*-GaAs, a heterogeneous (domain, mosaic spread) microstructure. Indeed, epitaxial GaN layers have a mosaic structure made up of domains of a fairly good material (with a lower defect concentration); the domains are separated by boundaries formed of isolated hexagons [11, 12], so the boundaries are actually not topologically singly connected regions. The presence of barriers at domain boundaries gives rise to a spatial inhomogeneity in the distribution of both acceptors and donors, so the afterglow pattern in *n*-GaN may be a characteristic of topological disorder (connectivity) in this material. To shed light on the character of the spatial distribution of long-lived states and carrier transport to them, GaN crystals were doped by RE metals. When doping GaN crystals with RE metals, rare-earth atoms (ions) are prone to being incorporated into interdomain regions; therefore, part of the RE impurity atoms will act as getters, as a result of which the carrier concentration will decrease and the variation of the FWHM in delayed GaN⟨RE⟩ spectra will be weaker. The evolution of the PL spectrum of GaN⟨Sm⟩ type-1 crystals is displayed in Fig. 4. We see that the variation of the spectra with delay time Δt_d varying from zero to 40 μs differs from that in the case presented in Fig. 2.

Figure 5a illustrates the variation of the FWHM with time delay for undoped GaN and doped GaN⟨Sm⟩ type-1 crystals. The delayed PL spectra of RE-doped GaN crystals (GaN⟨Sm⟩) exhibit a considerably weaker variation of FWHM than those of the undoped crystals. The smaller variation of the FWHM with time may be accounted for both by an improved spatial homogeneity in the defect distribution and by the defect gettering that takes place when RE metals are inserted into the original GaN semiconductor matrix [1, 2]. The FWHM variation in both undoped and doped (GaN⟨Sm⟩) crystals of type 2 is displayed graphically in Fig. 5b. We immediately see that, in contrast to type-1 crystals, doping did not bring about any change in the FWHM under variation of the delay time, which can be attributed to a higher degree of ordering in the original semiconductor matrix.

4. CONCLUSIONS

To sum up, an analysis of delayed PL spectra of epitaxial *n*-GaN layers suggests that, irrespective of the growth method employed, there is a metastable level that supplies holes to the valence band in epitaxial lay-

ers. It has also been shown that combined measurements of the carrier concentration and kinetics offer the possibility of obtaining reliable estimates of the parameters of wide-bandgap crystals by using optical contact-free methods. The results of the present study suggest the operation of a process of spatial defect ordering in RE-doped GaN crystals.

ACKNOWLEDGMENTS

The authors are indebted to V.V. Lundin and S.N. Rodin for providing the samples for the study.

This study was supported by the program of the Presidium of the Russian Academy of Sciences "Low-Dimensional Quantum Structures."

REFERENCES

1. V. V. Krivolapchuk, M. M. Mezdrogina, A. V. Nasonov, and S. V. Rodin, Fiz. Tverd. Tela (St. Petersburg) **45** (9), 1556 (2003) [Phys. Solid State **45**, 1634 (2003)].
2. V. V. Krivolapchuk, V. V. Lundin, M. M. Mezdrogina, A. V. Nasonov, S. V. Rodin, and N. M. Shmidt, Fiz. Tverd. Tela (St. Petersburg) **46** (5), 814 (2004) [Phys. Solid State **46**, 836 (2004)].
3. S. Kim, R. L. Henry, A. E. Wicken, D. E. Koleske, S. J. Rhee, and J. O. White, J. Appl. Phys. **90** (1), 252 (2001).
4. E. Iliopoulos, D. Doppalapudi, H. M. Ng, and T. D. Moustakas, Appl. Phys. Lett. **73**, 377 (1998).
5. R. Dingle, D. D. Seil, S. E. Stakowsky, and M. Ilegems, Phys. Rev. B **4**, 1211 (1971).
6. V. V. Krivolapchuk, N. K. Poletaev, and L. M. Fedorov, Fiz. Tekh. Poluprovodn. (St. Petersburg) **28**, 310 (1994) [Semiconductors **28**, 188 (1994)].
7. V. V. Krivolapchuk and N. K. Poletaev, Fiz. Tekh. Poluprovodn. (St. Petersburg) **32**, 307 (1998) [Semiconductors **32**, 277 (1998)].
8. V. V. Krivolapchuk, M. M. Mezdrogina, and N. K. Poletaev, Fiz. Tverd. Tela (St. Petersburg) **45** (1), 29 (2003) [Phys. Solid State **45**, 28 (2003)].
9. V. Kiroilyuk, P. H. Hageman, and M. Zielenski, Appl. Phys. Lett. **75**, 4109 (1999).
10. R. A. Zauner, P. C. M. Christianen, J. L. Weyher, P. R. Hageman, and P. K. Larsen, Appl. Phys. Lett. **76**, 2355 (2000).
11. B. K. Meyer, Mater. Res. Soc. Symp. Proc. **449**, 497 (1997).
12. N. M. Schmidt, A. N. Besyl'kin, M. S. Dunaevsky, A. G. Kolmakov, A. V. Sakharov, A. S. Usikov, and E. E. Zavarzin, J. Phys. C **14**, 13025 (2002).

Translated by G. Skrebtsov

Physics of the Solid State, Vol. 46, No. 12, 2004, pp. 2207–2212. Translated from Fizika Tverdogo Tela, Vol. 46, No. 12, 2004, pp. 2135–2138.

SEMICONDUCTORS AND DIELECTRICS

A Simple Model for Calculating the Height of Schottky Barriers at Contacts of Transition Metals with Silicon Carbide Polytypes

S. Yu. Davydov

Ioffe Physicotechnical Institute, Russian Academy of Sciences, Politekhnicheskaya ul. 26, St. Petersburg, 194021 Russia
e-mail: Sergei.Davydov@mail.ioffe.ru

Received May 18, 2004

Abstract—The heights of Schottky barriers at contacts of Ag, Au, Pd, Pt, Ti, Ru, Ni, Cr, Al, Mg, and Mn metals with different polytypes of silicon carbide SiC are self-consistently calculated in the framework of a simple model proposed earlier. The results of calculations performed for contacts of transition metals with silicon carbide polytypes are in quite reasonable agreement with experimental data under the assumption that silicon vacancies with an energy $E_d = E_V + 2.1$ eV make a dominant contribution to the Schottky barrier height. © *2004 MAIK "Nauka/Interperiodica".*

1. The effect of polytypism of silicon carbide SiC on the Schottky barrier height Φ_b has been noted in a number of papers [1–6]. To the best of my knowledge, the first attempt to relate the Schottky barrier height Φ_b to a particular characteristic of polytypes was made by Verenchikova *et al.* [1]. By using the example of chromium contacts with 4*H*-SiC, 6*H*-SiC, 8*H*-SiC, 10*H*-SiC, 15*R*-SiC, 21*R*-SiC, and 27*R*-SiC polytypes with electron conduction, those authors demonstrated that the Schottky barrier height obeys the relationship $\Phi_b^n \propto D$, where $D = N_h/(N_h + N_k)$ is the degree of hexagonality (N_h and N_k are the numbers of hexagonal and cubic sites occupied by atoms, respectively). Since the degree of hexagonality of silicon carbide is proportional to the vacancy concentration N_{Si} in the silicon sublattice [7, 8], it can easily be shown that the Schottky barrier height satisfies the following relationship: $\Phi_b^n \propto N_{Si}^s \propto D$. Here, N_{Si}^s is the silicon vacancy concentration calculated for the two-dimensional case: $N_{Si}^s = (N_{Si})^{2/3}$. The above dependence is adequately described by the simple model proposed in our earlier work [9]. This model is a slightly modified Ludeke model of surface defects [10]. In [9], it was assumed that the Fermi level E_F for a contact of chromium with silicon carbide coincides with the energy level E_d for a surface defect of the system. Under this assumption, the surface concentration of defects N_d was calculated from the experimental values of Φ_b^n. Moreover, it was found that the ratios N_{Si}^s/N_d and Φ_b^n/N_d remain approximately constant in the series 8*H*–6*H*–15*R*–27*R*–4*H*. On this basis, we made the inference that silicon vacancies have a dominant effect on the Schottky barrier height Φ_b^n for contacts of different SiC polytypes with the same metal.

In [9], it was also assumed that the electron affinity χ for all polytypes is identical and equal to 4.4 eV, as is the case with the 6*H*-SiC polytype[1] [11]. On the other hand, Bazack [6] obtained the electron affinity $\chi = 3.3$–3.7 eV for the 6*H*-SiC polytype and $\chi = 4.0$ eV for the 3*C*-SiC polytype, whereas the reference book edited by Grigor'ev and Meĭlikhov [12] gives an electron affinity $\chi = 4.8$ eV for the 3*C*-SiC polytype and $\chi = 4.1$ eV for the 2*H*-SiC polytype. In the present work, the model proposed in [9] was analyzed on the basis of the experimental data taken from [1] without recourse to the simplifying assumption that $E_F = E_d$.

According to the model proposed in [9], the energy level of a surface defect in a semiconductor substrate lies in the band gap and is characterized by an energy E_d (hereafter, the energy will be reckoned from the valence band top). The occupation number n_d of this level is defined by the self-consistent equation

$$\begin{aligned} n_d &= \pi^{-1}\operatorname{arccot}[(E_d - E_F)/\Gamma], \\ E_F &= \chi + E_g - \phi_m - \Delta\phi, \\ \Delta\phi &= -4\pi e^2 \lambda N_d q_d. \end{aligned} \quad (1)$$

Here, E_F is the energy of the system at the Fermi level, E_g is the band gap, ϕ_m is the work function of the metal, e is the elementary charge, 2λ is the thickness of the dipole layer at the contact, Γ is the half-width of the quasi-level of the defect, and N_d is the surface concentration of defects. When the energy level of the defect before its contact with the metal is not occupied, the charge of this defect after the contact can be written in

[1] As a rule, the electron affinity χ for the 6*H*-SiC polytype lies in the range from 3.5 to 4.4 eV [5, 6, 12]. It should be emphasized that the problem of determination of the electron affinity for silicon carbide polytypes will likely remain quite unpopular with both experimenters and theorists.

Table 1. Calculated occupation numbers n_d of vacancies and Schottky barrier heights Φ_b^n for Ag/3*C*-SiC, Au/3*C*-SiC, Ag/6*H*-SiC, and Au/6*H*-SiC contacts

	Parameter	3*C*-SiC		6*H*-SiC	
		Ag	Au	Ag	Au
Calculation for variant *a*	n_d	0.44	0.21	0.545	0.32
	Φ_b^n, eV	0.40	0.96	0.93	1.32
Calculation for variant *b*	n_d	0.31	0.15	0.30	0.16
	Φ_b^n, eV	0.64	1.29	1.36	1.91
Experiment	Φ_b^n, eV	0.40	0.87	0.97	1.14

Note: In variant *a*, electron affinity χ = 4.4 eV for 3*C*-SiC and 6*H*-SiC; in variant *b*, electron affinity χ = 4.0 eV for 3*C*-SiC and χ = 3.5 eV for 6*H*-SiC.

the form $q_d = -n_d$. If this level prior to contact of the defect with the metal is occupied, the charge of the defect after contact takes the form $q_d = 1 - n_d$. The Schottky barrier height Φ_b^n for a contact with an *n*-type semiconductor can be represented by the expression

$$\Phi_b^n = \phi_m - \chi + \Delta\phi. \quad (2)$$

Now, we assume that the defect concentration N_d affects only the charge q_d. Then, it can easily be shown that the following expression holds:

$$\frac{d\Phi_b^n}{dN_d} = -\frac{4\pi e^2 \lambda q_d}{1 + 4\pi e^2 \lambda N_d \rho_d}, \quad (3)$$

where the density of states at the energy level of the defect has the form

$$\rho_d = \frac{1}{\pi}\frac{\Gamma}{(E_d + \phi_m + \Delta\phi)^2 + \Gamma^2}. \quad (4)$$

Therefore, as the defect concentration N_d increases, the Schottky barrier height Φ_b^n increases in the case when the energy level of the defect is not occupied before its contact with the metal ($q_d = -n_d$) and decreases when the energy level of the defect is occupied before its contact with the metal ($q_d = 1 - n_d$). According to the experimental data obtained in [1], the Schottky barrier height Φ_b^n increases with an increase in the degree of hexagonality *D*. Taking into account these findings, we made the inference (in the framework of a simplified model) in [9] that the difference between the Schottky barrier heights for different polytypes is determined by the concentration N_{Si}^s of initially empty surface vacancies in the silicon sublattice.

2. Let us start with a revision of the results obtained in our previous work [13], in which the heights of Schottky barriers at silver and gold contacts with 3*C*-SiC and 6*H*-SiC polytypes were calculated in the framework of the self-consistent approach. As before, we set Γ = 0.5 eV and λ = 2 Å for both polytypes[2] (the value of λ is close both to the distance between the nearest neighbor atoms in the structure of silicon carbide (1.88 Å) [14] and to half the lattice constants for single crystals of silver and gold [15]) and $q_n = -n_d$. The band gaps E_g and the work functions ϕ_m were taken from [16] and [12], respectively. In particular, we used ϕ_m = 4.26 eV for silver and ϕ_m = 5.10 eV for gold. In contrast to the calculations performed in [13], we assumed that the surface concentration of defects N_d is equal to N_{Si}^s; i.e., we have 3.42×10^{13} cm^{-2} for 3*C*-SiC and 4.20×10^{13} cm^{-2} for 6*H*-SiC. We consider two variants of the calculation. For variant *a*, we used the electron affinity χ = 4.4 eV for the 3*C*-SiC and 6*H*-SiC polytypes. For variant *b*, the electron affinity χ = 4.0 eV for the 3*C*-SiC polytype and χ = 3.5 eV for the 6*H*-SiC polytype were taken from [6]. The energy E_d = 2.1 eV was determined by fitting the calculated Schottky barrier height Φ_b^n for the Ag/3*C*-SiC system to the experimental value (0.4 eV) [2]. Then, reasoning from the results obtained in [17], we assumed that the corresponding energy levels of vacancies for all other polytypes (i.e., the energy levels of vacancies in the same charge state) are equidistant from the valence band top. Since the shift of the energy level E_d due to the interaction of the defect with the metal was ignored within the models used in [9, 10, 13], it was assumed that E_d = 2.1 eV for all the metal/SiC polytype systems. The results of our calculations are presented in Table 1. It can be seen from this table that, compared to variant *b*, the calculation for variant *a* leads to better agreement with the experimental data. Therefore, the electron affinity χ = 4.4 eV (variant *a*) will be used in subsequent calculations for all the polytypes under consideration.

Now, we calculate the heights of Schottky barriers at palladium and platinum contacts with the 6*H*-SiC, 15*R*-SiC, and 4*H*-SiC polytypes studied in [18]. As before, we set λ = 2 Å, which is close to half the lattice constants for bulk crystals of palladium and platinum (3.89 and 3.92 Å, respectively [15]), and Γ = 0.5 eV. Moreover, we assume that the energy level of the vacancy before contact with the metal is not occupied; i.e., $q_d = -n_d$. According to the data obtained by Lebedev [8], the defect concentrations for the 15*R*-SiC and 4*H*-SiC

[2] There are no strong grounds to believe that the parameter λ depends on the polytype. Indeed, according to the estimates made in [9], we have $\lambda \approx 2$–3 Å. Since all the polytypes under investigation differ from each other only in the arrangement of the third neighbors, there is no reason to think that the dipole layers can have significantly different thicknesses. The half-width of the quasi-level obeys the relationship $\Gamma \propto \exp(-2\gamma\lambda)$, where $\gamma \sim 1$ Å^{-1}; consequently, this parameter can also be considered to be identical for different polytypes. Note that, in [9], we used the parameter λ = 3 Å. For λ = 2 Å, the quantities listed in the table should be recalculated as follows: the surface concentrations of defects N_d should be multiplied by 1.5, and the ratios next after the values of N_d should be divided by 1.5.

polytypes are equal to 6.30×10^{13} and 8.11×10^{13} cm^{-2}, respectively. The results of our calculations are compared with the experimental data in Table 2. The Schottky barrier heights for the Pd/3*C*-SiC system considered in [2] are also given in Table 2.

Table 3 presents the results of our calculations for titanium and aluminum contacts with the 3*C*-SiC and 6*H*-SiC polytypes studied in [2, 3, 19]. In these calculations, we used the work function $\phi_m = 4.33$ eV for titanium [2] and $\phi_m = 4.25$ eV for aluminum [12]. As before, we set $\lambda = 2$ Å, $\Gamma = 0.5$ eV, and $q_d = -n_d$. It should be noted that, in this case, we considered the Schottky barrier at the interface between a simple (rather than transition) metal, namely, aluminum, and silicon carbide for the first time. The calculated Schottky barrier height Φ_b^n for the Al/3*C*-SiC system is 2.5 times greater than the experimental value. For magnesium ($\phi_m = 3.83$ eV) in contact with the 6*H*-SiC polytype, the Schottky barrier height was calculated to be $\Phi_b^n = 0.725$ eV ($n_d = 0.66$), whereas the experimental value falls in the range 0.79–0.96 eV [3]. For the Mg/6*H*-SiC system ($\phi_m = 3.64$ eV) with a band gap $E_g = 3.1$ eV [16], we found that the Schottky barrier height Φ_b^n is equal to 0.61 eV ($n_d = 0.70$). This value is nearly twice as large as the experimental barrier height (0.30–0.34 eV [3]). By assuming that $E_g = 2.86$ eV (as in [3]), we obtained $\Phi_b^n = 0.51$ eV ($n_d = 0.65$), which is in closer agreement with the experimental result. Moreover, we attempted to calculate the barrier height for the Cs/6*H*-SiC system studied in [20] and obtained a negative sign for Φ_b^n. However, according to the experimental data, we have $\Phi_b^n = 0.57$ eV. Therefore, the Schottky barriers arising at contacts of simple metals with silicon carbide polytypes are less adequately described by the proposed model than those of transition metals.

In order to verify the validity of our model further, we calculated the heights of Schottky barriers at the cobalt and terbium contacts with the 3*C*-SiC polytype and at the ruthenium and nickel contacts with the 6*H*-SiC polytype. The experimental data for these systems are presented in [2–5]. By setting $\phi_m = 4.41$ eV for cobalt [12], we obtained the Schottky barrier height $\Phi_b^n = 0.49$ eV ($n_d = 0.385$). For the work function $\phi_m = 5$ eV [2], the Schottky barrier height was calculated to be $\Phi_b^n = 0.88$ eV ($n_d = 0.225$), whereas the experimental value was equal to 0.69 eV [2]. The calculation performed for terbium ($\phi_m = 3.15$ eV) gave a negative sign for Φ_b^n, whereas the barrier height determined from the experiment by Waldrop and Grant [2] is a positive quantity, i.e., $\Phi_b^n = 0.35$ eV.[3] For ruthenium ($\phi_m = 4.60$ eV) with a band gap $E_g = 3.1$ eV, the barrier height Φ_b^n was calculated to be 1.08 eV, which considerably exceeds the experimental value of 0.67 eV [21]. By assuming again that the band gap E_g is equal to 2.86 eV, we obtained the barrier height $\Phi_b^n = 0.95$ eV ($n_d = 0.38$). This result is in better agreement with the experimental data. In the case of nickel ($\phi_m = 4.50$ eV), the calculations gave $\Phi_b^n = 1.04$ eV. However, according to the experimental data taken from [4, 5], the barrier height falls in the range $\Phi_b^n = 1.17$–1.68 eV.

Now, we turn to the calculations of the heights of Schottky barriers at chromium contacts with silicon carbide polytypes. As before, the calculations were per-

Table 2. Calculated occupation numbers n_d of vacancies and Schottky barrier heights Φ_b^n for Pd/3*C*-SiC, Pd/6*H*-SiC, Pd/15*R*-SiC, Pd/4*H*-SiC, Pt/3*C*-SiC, Pt/6*H*-SiC, Pt/15*R*-SiC, and Pt/4*H*-SiC contacts

Metal	Parameter	Polytype			
		3*C*	6*H*	15*R*	4*H*
Pd	n_d	0.27	0.39	0.35	0.35
	Φ_b^n, eV (calculation)	1.07	1.17	1.21	1.42
	Φ_b^n, eV (experiment)	0.95	1.27	1.22	1.56
Pt	n_d	–	0.27	0.245	0.25
	Φ_b^n, eV (calculation)	–	1.45	1.48	1.66
	Φ_b^n, eV (experiment)	–	1.34	–	1.58

Note: The Schottky barrier heights Φ_b^n used as the experimental data are taken from [18] (these values are closest to the results of the calculations).

Table 3. Calculated occupation numbers n_d of vacancies and Schottky barrier heights Φ_b^n for Ti/3*C*-SiC, Ti/6*H*-SiC, Al/3*C*-SiC, and Al/6*H*-SiC contacts

Parameter	3*C*-SiC		6*H*-SiC	
	Ti	Al	Ti	Al
n_d	0.41	0.44	0.525	0.55
Φ_b^n, eV (calculation)	0.44	0.40	0.96	0.925
Φ_b^n, eV (experiment)	0.53 [2]	0.16 [3]	0.98 [2]	0.98 [19]

Note: The mean barrier height obtained for annealed samples in [3] is used as the experimental value of Φ_b^n for the Ti/6*H*-SiC contact.

[3] It seems likely that the proposed model is not applicable to the description of silicon carbide contacts with rare-earth metals; however, a strict conclusion, of course, cannot be drawn from a single estimate.

Table 4. Calculated occupation numbers n_d of vacancies and Schottky barrier heights Φ_b^n for chromium contacts with SiC polytypes

Parameter	Polytype					
	3*C*	8*H*	6*H*	15*R*	27*R*	4*H*
N_{Si}^s, 10^{13} cm^{-2}	3.42	4.78	5.70	6.87	7.27	7.96
n_d	0.33	0.40	0.42	0.37	0.39	0.40
Φ_b^n, eV (calculation)	0.59	0.87	1.05	1.10	1.18	1.33
Φ_b^n, eV (experiment)	0.40	0.80–0.95	1.1–1.2	1.1–1.2	1.20–1.35	1.4–1.6

Note: The value of Φ_b^n for the Cr/3*C*-SiC contact was obtained in [1] using extrapolation.

formed for $\lambda = 2$ Å, $\Gamma = 0.5$ eV, and $q_d = -n_d$. The results given in Table 4 were calculated according to the data taken from [1] for the band gap E_g and the defect concentration N_{Si}. In these calculations, we used the work function $\phi_m = 4.58$ eV. Note that the band gap $E_g = 3.125$ eV for the 27*R*-SiC polytype was taken from the theoretical work by Dubrovskiĭ and Lepneva [22].

3. The results of the calculations performed for metal contacts with silicon carbide polytypes are in quite reasonable agreement with experimental data (see Tables 1–4), because the fitting of the calculated Schottky barrier height Φ_b^n to the experimental value was carried out for only one system (Ag/3*C*-SiC). Therefore, we can draw the conclusion that the decisive role in the formation of the Schottky barriers initially (before contact with a metal) is played by silicon vacancies (not occupied by electrons) with an energy $E_d = E_V + 2.1$ eV (where E_V is the energy at the valence band top). It should be emphasized that the energy E_d is identical for all polytypes with the same electron affinity $\chi = 4.4$ eV.

The calculated dependences of the Schottky barrier height Φ_b^n on the surface concentration of silicon vacancies N_{Si}^s are depicted in Figs. 1 and 2. It can be seen from these figures that the Schottky barrier height

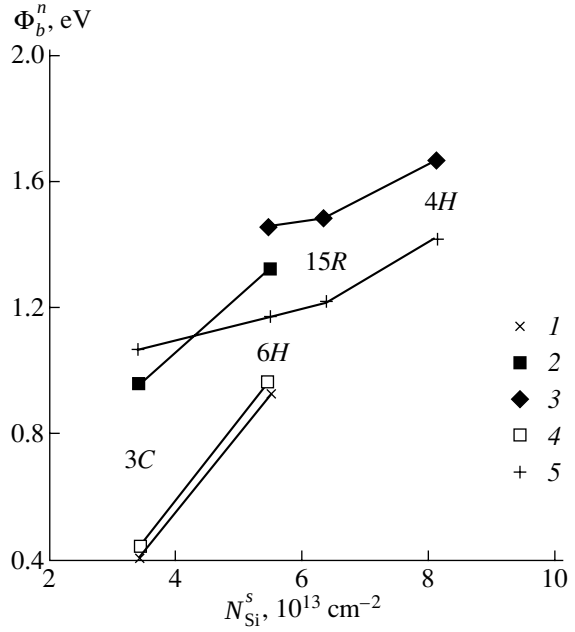

Fig. 1. Dependences of the Schottky barrier height Φ_b^n on the surface concentration N_{Si}^s of silicon vacancies in contacts between metals and silicon carbide polytypes: (*1*) Ag and Al, (*2*) Au, (*3*) Pt, (*4*) Ti, and (*5*) Pd.

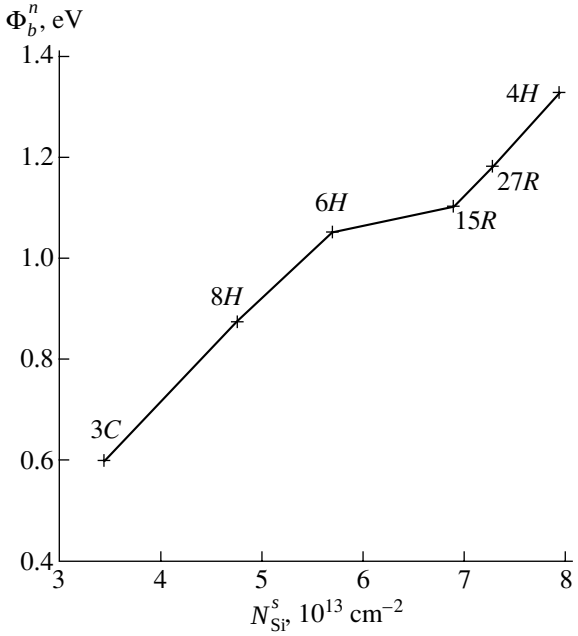

Fig. 2. Dependence of the Schottky barrier height Φ_b^n on the surface concentration N_{Si}^s of silicon vacancies for the Cr/SiC polytype system.

Φ_b^n increases with an increase in the surface concentration N_{Si}^s. This is supported by the experimental data in all the cases under consideration, with one exception: in the series of palladium contacts with 3*C*-SiC, 6*H*-SiC, 15*R*-SiC, and 4*H*-SiC polytypes, the Schottky barrier height for the 15*R*-SiC polytype is less than that for the 6*H*-SiC polytype [18]. Thus, we confirmed the conclusions drawn in [9, 13] that the silicon vacancies make a dominant contribution to the Schottky barrier height.

As was shown by Waldrop [5] for Pd, Ni, Au, Ag, Mg, Ti, and Al contacts with the 6*H*-polytype (see also the paper by van Elsbergen *et al.* [20], who studied the Cs/6*H*-SiC contact), in the case when the samples with *n*- and *p*-type conductivities are prepared according to the same procedure, the Schottky relationship $\Phi_b^n + \Phi_b^p = E_g$ can be considered to be exact to within 10%. Consequently, the proposed model is also valid for the calculation of the Schottky barrier height Φ_b^p. In this respect, we should also note the following circumstance. Waldrop [5] analyzed the Schottky barrier heights Φ_b^n and Φ_b^p for contacts of the aforementioned metals both with the (0001) surface containing silicon atoms and with the $(000\bar{1})$ surface involving carbon atoms. It was found that the difference between the corresponding barrier heights $\delta = \Phi_b^n(\mathrm{Si}) - \Phi_b^n(\mathrm{C})$ has a negative sign for all metals except gold. In the framework of our model, we can assume that the sign of the difference δ is governed by the decrease in the parameter λ when changing over from the (0001) surface to the $(000\bar{1})$ surface, because the atomic radii of silicon and carbon are equal to 0.77 and 1.18 Å, respectively [12]. Under the assumption that the half-width of the quasi-level of the defect satisfies the relationship $\Gamma \propto \exp(-2\gamma\lambda)$, where $\gamma \sim 1$ Å^{-1} [23], we obtain

$$\frac{d\Phi_b^n}{d\lambda}[1 + 4\pi e^2 N_d \lambda \rho_d] = A,$$
$$A = 4\pi e^2 N_d n_d - 2\gamma\rho_d \Phi_b^n. \quad (5)$$

Here, the density of states ρ_d is given by expression (4). The calculation performed with theoretical values of n_d and Φ_b^n (at $N_d = N_{\mathrm{Si}}^s$) leads to $A < 0$ for all transition metals. Consequently, an increase in the parameter λ should result in a decrease in the Schottky barrier height Φ_b^n. This dependence was observed in the experiment by Waldrop [5] (the origin of the difference in sign for gold remains unclear). As a result, we also obtain $A < 0$ for aluminum but $A > 0$ for magnesium. This difference is not surprising, because the calculated Schottky barrier height is twice as large as the experimental value (see above).

4. It is well known that, in the framework of the model allowing for the interaction of the $|sp^3\rangle$ orbitals of the next-to-nearest neighbors, the quadruply degenerate level of the vacancy in a tetrahedral crystal is split into one *s*-type nondegenerate level and three *p*-type degenerate levels lying above the *s* level [24]. Therefore, within our model, in which only one level, namely, E_d, is considered for simplicity, it is reasonable to assign the initially unoccupied level to a *p*-type level and the initially occupied level to an *s*-type level. Levels of the *p* type also undergo a spin splitting that is independent of the polytype for singly positively charged, neutral, and singly negatively charged silicon vacancies [17]. For example, the energy levels of silicon vacancies in the band gaps of the 3*C*-SiC and 4*H*-SiC polytypes are closely located with respect to the valence band top. Moreover, the energy of these levels in the 4*H*-SiC polytype does not depend on the type of site (hexagonal or cubic) occupied by the vacancy. These circumstances also confirm the approximation $E_d = \mathrm{const}$ used in our calculations.

ACKNOWLEDGMENTS

This work was supported in part by the Russian Foundation for Basic Research (project no. 03-02-16054b), the International Association of Assistance for the promotion of cooperation with scientists from the New Independent States of the Former Soviet Union (project no. INTAS 01-0603), and the "Science for Peace" NATO program (grant no. SiP 978 011).

REFERENCES

1. R. G. Verenchikova, V. I. Sankin, and E. I. Radovanova, Fiz. Tekh. Poluprovodn. (Leningrad) **17** (10), 1757 (1983) [Sov. Phys. Semicond. **17**, 1123 (1983)].
2. J. R. Waldrop and R. W. Grant, Appl. Phys. Lett. **56** (6), 557 (1990).
3. J. R. Waldrop, R. W. Grant, Y. C. Wang, and R. F. Davis, J. Appl. Phys. **72** (10), 4757 (1992).
4. J. R. Waldrop and R. W. Grant, Appl. Phys. Lett. **62** (21), 2685 (1993).
5. J. R. Waldrop, J. Appl. Phys. **75** (9), 4548 (1994).
6. M. J. Bozack, Phys. Status Solidi B **202** (3), 549 (1997).
7. N. D. Sorokin, Yu. M. Tairov, V. F. Tsvetkov, and M. A. Chernov, Kristallografiya **28** (5), 910 (1983) [Sov. Phys. Crystallogr. **28**, 539 (1983)].
8. A. A. Lebedev, Fiz. Tekh. Poluprovodn. (St. Petersburg) **33** (7), 769 (1999) [Semiconductors **33**, 707 (1999)].
9. S. Yu. Davydov, A. A. Lebedev, O. V. Posrednik, and Yu. M. Tairov, Fiz. Tekh. Poluprovodn. (St. Petersburg) **35** (12), 1437 (2001) [Semiconductors **35**, 1375 (2001)].
10. R. Ludeke, Phys. Rev. B **40** (3), 1947 (1989).
11. A. N. Andreev, A. S. Tregubova, M. P. Shcheglov, V. P. Rastegaev, S. I. Dorozhkin, and V. E. Chelnokov, Fiz. Tekh. Poluprovodn. (St. Petersburg) **29** (10), 1828 (1995) [Semiconductors **29**, 955 (1995)].

12. *Physical Quantities: A Handbook*, Ed. by I. S. Grigor'ev and E. Z. Meĭlikhov (Énergoatomizdat, Moscow, 1991) [in Russian].
13. S. Yu. Davydov, A. A. Lebedev, O. V. Posrednik, and Yu. M. Tairov, Fiz. Tekh. Poluprovodn. (St. Petersburg) **36** (6), 690 (2002) [Semiconductors **36**, 652 (2002)].
14. W. A. Harrison, *Electronic Structure and the Properties of Solids: The Physics of the Chemical Bond* (Freeman, San Francisco, 1980; Mir, Moscow, 1983), Vol. 1.
15. C. Kittel, *Introduction to Solid State Physics*, 5th ed. (Wiley, New York, 1976; Nauka, Moscow, 1978).
16. V. I. Gavrilenko, A. M. Grekhov, D. V. Korbutyak, and V. G. Litovchenko, *Optical Properties of Semiconductors: A Handbook* (Naukova Dumka, Kiev, 1987) [in Russian].
17. F. Bechstedt, A. Fissel, J. Furtmuller, U. Grossner, and A. Zywietz, J. Phys.: Condens. Matter **13** (15), 9027 (2001).
18. H.-J. Im, B. Kaczer, J. P. Pelz, and W. J. Choyke, Mater. Sci. Forum **264–268**, 813 (1998).
19. C.-M. Zetterling, F. Dahlquist, N. Lundberg, M. Östling, K. Rottner, and L. Ramberg, Solid-State Electron. **42** (9), 1757 (1998).
20. V. van Elsbergen, T. U. Kampen, and W. Mönch, J. Appl. Phys. **79** (1), 316 (1996).
21. M. E. Samiji and E. van Wyk, Mater. Sci. Forum **353–356**, 607 (2001).
22. G. B. Dubrovskiĭ and A. A. Lepneva, Fiz. Tverd. Tela (Leningrad) **19** (5), 1252 (1977) [Sov. Phys. Solid State **19**, 729 (1977)].
23. R. Brako and D. M. Newns, Rep. Prog. Phys. **52** (3), 655 (1989).
24. M. Lannoo and J. Bourgoin, *Point Defects in Semiconductors* (Springer-Verlag, 1981; Mir, Moscow, 1984).

Translated by O. Borovik-Romanova

Physics of the Solid State, Vol. 46, No. 12, 2004, pp. 2213–2216. Translated from Fizika Tverdogo Tela, Vol. 46, No. 12, 2004, pp. 2139–2142.

SEMICONDUCTORS AND DIELECTRICS

Giant Piezoelectric and Dielectric Enhancement in Disordered Heterogeneous Systems

A. V. Turik[1, 2], A. I. Chernobabov[2], G. S. Radchenko[1], and S. A. Turik[1]

[1] *Rostov State University, ul. Zorge 5, Rostov-on-Don, 344007 Russia*

e-mail: turik@phys.rsu.ru

[2] *Pyatigorsk State Technological University, Pyatigorsk, 357500 Russia*

Received May 11, 2004

Abstract—Effective complex piezoelectric and dielectric constants of disordered heterogeneous systems, such as statistical mixtures consisting of spheroidal particles of the same orientation but with random distribution in space, are studied. It is found for the first time that, in such systems, there exists giant piezoelectric enhancement accompanied by giant relaxation of piezoelectric coefficients and permittivity. The piezoelectric and dielectric spectra differ considerably from the Debye spectra and have a Cole–Cole character. The dependence of the effects considered on the aspect ratios of the spheroids is investigated. The physical mechanisms responsible for the anomalous behavior of the piezoelectric coefficients and permittivity are considered. © *2004 MAIK "Nauka/Interperiodica".*

1. INTRODUCTION

In connection with the numerous applications of heterogeneous systems (composites) in modern engineering, the problem arises of fabricating and using materials with very large (giant) piezoelectric coefficients d^* and permittivities ε^*. A promising way to realize this is through the use of Maxwell–Wagner relaxation in heterogeneous systems containing components with substantially different piezoelectric coefficients d_{ij}, permittivities ε_i, and electrical conductivities γ_i. These systems include composites with connectivity of the 0–3 type (following the classification developed in [1]) in the form of a matrix containing isolated inclusions and so-called statistical mixtures [2], whose components are randomly distributed in space. However, to date, some problems related both to the theoretical description and applications of such composites remain poorly studied. In this study, we consider the piezoelectric and dielectric properties of two-component statistical mixtures with particles of spheroidal form.

2. DISORDERED HETEROGENEOUS SYSTEMS: THEORETICAL DESCRIPTION

Giant dielectric enhancement caused by Maxwell–Wagner relaxation has been repeatedly observed experimentally and studied theoretically in ordered (2–2 composites [3]) and disordered (two-component statistical mixtures [4], ferroelectric ceramics [5, 6]) heterogeneous systems with strongly different permittivities ($\varepsilon_1/\varepsilon_2 \gg 1$) and conductivities ($\gamma_1/\gamma_2 \ll 1$) of the components. Giant piezoelectric enhancement has been much less investigated; it has been described only for the 2–2 composites consisting of a ferroelectric with large piezoelectric coefficients and a polymer with intentionally increased conductivity [3]. Giant piezoelectric enhancement in disordered heterogeneous materials has not been considered in the literature. To date, not only the physical mechanism, but even the actual possibility of obtaining giant piezoelectric coefficients in disordered systems has not been studied.

The aim of this study is to consider giant piezoelectric and dielectric enhancement in two-component disordered heterogeneous systems of the type of statistical mixtures. We assume that each component of the composite consists of spheroidal inclusions of the same orientation polarized along the c axis with the aspect ratio $\xi = c/a$ ($a = b \neq c$ are the spheroid semiaxes) either equal to unity (spheres) or considerably differing from unity. For a combined description with allowance for mutual effects of the dielectric, piezoelectric, and elastic properties and conductivities, the self-consistent effective-medium method [7, 8] was used. Previously, this method was employed to jointly consider only the permittivity and conductivity (the Bruggeman method [7, 8]) or the permittivities, piezoelectric coefficients, and elastic compliances (the Marutake method [9]). In the latter case, one cannot obtain analytical expressions for the physical constants of a heterogeneous system and the problem needs to be solved iteratively.

In order to take the conductivities into account in the Marutake method [9], one must use the complex permittivities $\varepsilon^{(1, 2)} = \varepsilon_{1, 2} - i\gamma_{1, 2}/\omega$ for each of the components of the mixture and for the composite as a whole: $\varepsilon^* = \varepsilon'^* - i\varepsilon''^* = \varepsilon'^* - i\gamma^*/\omega$ (ω is the angular frequency of a harmonic electric field). This circumstance significantly complicates the constitutive equations and com-

Elastic compliances s_{ij}^E (10^{-12} Pa^{-1}), piezoelectric coefficients d_{ki} (pC N^{-1}), and permittivities $\varepsilon_{33}^\sigma/\varepsilon_0$ of the PCR-73 ferroelectric ceramics [11] and polyethylene [12] at 25°C

	s_{11}^E	s_{12}^E	s_{13}^E	s_{33}^E	d_{31}	d_{33}	$\varepsilon_{33}^\sigma/\varepsilon_0$
PCR-73	17.9	−6.8	−9.6	23.5	−380	860	6000
Polyethylene	1370	−630	−630	1370	0	0	2.5

putational procedures used. To solve this problem, we developed a special program that allowed us to calculate simultaneously the frequency dependences and magnitudes of the piezoelectric coefficients, permittivities, elastic compliances, and conductivities of statistical mixtures. The program allowed us to vary over a wide range the bulk concentrations θ_i and the aspect ratio ξ, which determines the depolarization and stress relaxation factors [10] for the components of a mixture of spheroids. Using the effective-medium method, we calculated the internal electric fields, electric displacements, stresses, and strains for each spheroid, which was assumed to be immersed in a homogeneous environment with physical constants to be defined. By averaging the internal fields (electric displacements) and internal stresses (strains) over the ensemble with the required absence of scattering fields (which is standard for the effective-medium method) [10], we could obtain self-consistent equations for the piezoelectric coefficients, permittivities, elastic compliances, and conductivities. Since the equations are very bulky and are solved by the iteration method, they are not written out here.

3. RESULTS AND DISCUSSION

We considered a statistical mixture consisting of a piezoelectric component (a polarized soft ferroelectric PCR-73 piezoceramic [11] with conductivity $\gamma_1 = 10^{-13}$ Ω^{-1} m^{-1}) and a nonpiezoelectric component (polyethylene [12] with an intentionally increased conductivity $\gamma_2 = 10^{-10}$ Ω^{-1} m^{-1}) with spheroidal particles whose *c* axes were oriented along the direction of the residual polarization of the piezoceramic. The physical constants of both components are listed in the table. Typical simulation results are shown in Figs. 1–3. The behavior of ε^* differs only slightly from that obtained using the corresponding formula from [7] with complex permittivities in the absence of piezoelectricity [13]. As $\omega \longrightarrow 0$, the real part of the complex permittivity of the composite ε_{33}^* becomes very high, exceeding the permittivity $\varepsilon_{33}^\sigma = 6000$ of the PCR-73 piezoceramic by an order of magnitude or greater, and has a maximum near the conductivity percolation threshold corresponding to

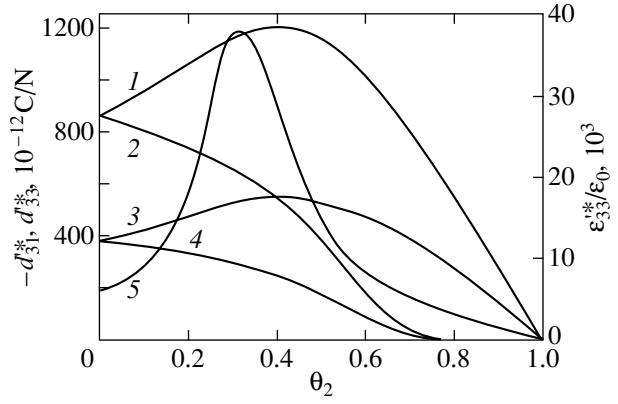

Fig. 1. Concentration dependence of (*1*, *3*) the (quasi)static and (*2*, *4*) high-frequency piezoelectric coefficients (*1*, *2*) d_{33}^* and (*3*, *4*) $-d_{31}^*$ and (*5*) static permittivity ε_{33}^* of a two-component statistical mixture of PCR-73 and polyethylene with spherical particles for $c/a = 1$, $\varepsilon_1' = 6000$, $\varepsilon_2' = 2.5$, $\gamma_1 = 10^{-13}$ Ω^{-1} m^{-1}, and $\gamma_2 = 10^{-10}$ Ω^{-1} m^{-1}.

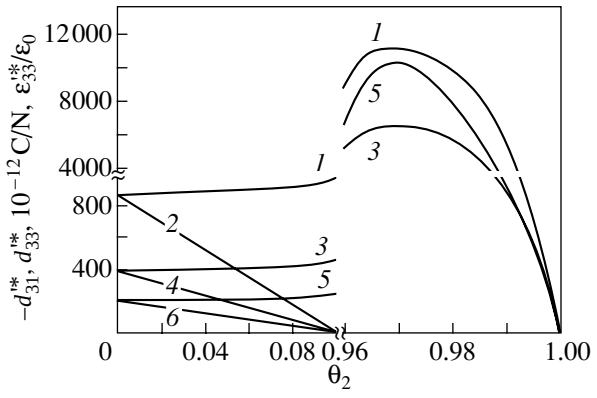

Fig. 2. Concentration dependence of (*1*, *3*, *5*) the (quasi)static and (*2*, *4*, *6*) high-frequency piezoelectric coefficients (*1*, *2*) d_{33}^* and (*3*, *4*) $-d_{31}^*$ and (*5*, *6*) permittivity $\varepsilon_{33}^*/30\varepsilon_0$ of a two-component statistical mixture of PCR-73 and polyethylene with spheroidal particles for $c/a = 0.02$, $\varepsilon_1' = 6000$, $\varepsilon_2' = 2.5$, $\gamma_1 = 10^{-13}$ Ω^{-1} m^{-1}, and $\gamma_2 = 10^{-10}$ Ω^{-1} m^{-1}.

the bulk concentration of the conducting polymer $\theta_2 = \theta_{2c} = 1/3$ for spheres and $\theta_2 = 0.969$ for oblate spheroids with $\xi = 0.02$. The result obtained for spheres was known earlier [4], while the result for spheroids was obtained for the first time. The high-frequency permittivity (for $\omega \longrightarrow \infty$) is shown in Fig. 2 to monotonically decrease with increasing θ_2 for oblate spheroids.

The behavior of (quasi)static (for $\omega \longrightarrow 0$) piezoelectric coefficients d_{33}^* and $-d_{31}^*$ is much more interesting and unexpected to a certain extent. In the case of spherical inclusions, their real parts pass through broad maxima at values of θ_2 slightly exceeding $\theta_{2c} = 1/3$ for spheres. For oblate spheroids, the effective piezoelectric coefficients d_{33}^* and $-d_{31}^*$ near $\theta_{2c} = 0.969$ are very high and exceed the corresponding values of piezoelectric coefficients for the ferroelectric PCR-73 ceramics by an order of magnitude or greater. The high-frequency ($\omega \longrightarrow \infty$) piezoelectric coefficients d_{33}^* and $-d_{31}^*$ decrease monotonically with increasing θ_2 and vanish at the concentration θ_2 corresponding to the percolation threshold of the high-frequency permittivity ($\omega \longrightarrow \infty$). As to the permittivity ε_{11}^* and the piezoelectric coefficient d_{15}^* of the statistical mixture, their behavior in the case of spherical particles quantitatively differs only slightly (and qualitatively does not differ at all) from the behavior of the permittivity ε_{33}^* and piezoelectric coefficient d_{33}^* in Fig. 1. It is also clear that, in the case of spheroidal particles with a small aspect ratio $\xi = 0.02$ (Fig. 2), the piezoelectric and dielectric properties of the composite are strongly anisotropic; indeed, the (quasi)static ε_{11}^* and d_{15}^* decrease rapidly with an increase in θ_2 and practically disappear already for $\theta_2 \approx 0.1$.

Turning to the nature of the giant dielectric and giant piezoelectric enhancement, we note that the physical reason for the divergence of the static permittivity is known. It is related to the formation of an infinite conducting cluster at the percolation threshold θ_{2c}; the cluster consists of closely spaced particles with high conductivity, at the boundaries of which electric charge is accumulated (the Maxwell–Wagner polarization related to the Maxwell–Wagner relaxation). The thickness of nonconducting (or poorly conducting) layers between the conducting particles is almost zero, and a situation similar to that observed in layered structures occurs [14].

The physical mechanism of the appearance of giant piezoelectric coefficients differs from that described above and is related to the specific features of the piezoelectric effect in heterogeneous systems. As shown in [3, 14], in the case of 2–2 composites, the main contribution to giant piezoelectric enhancement comes from

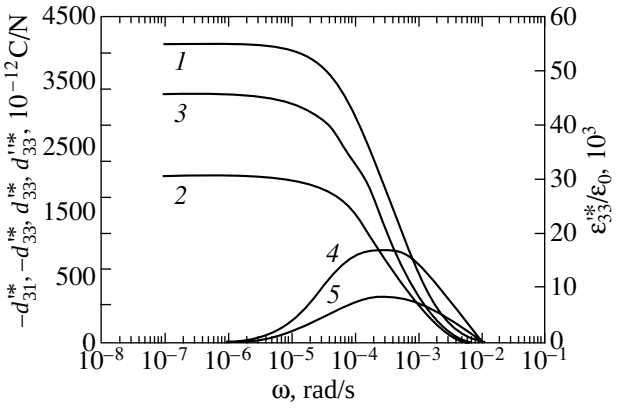

Fig. 3. Frequency dependence of (*1–3*) the real and (*4, 5*) imaginary parts of the piezoelectric coefficients (*1, 4*) d_{33}^* and (*2, 5*) $-d_{31}^*$ and (*3*) permittivity ε_{33}^* of a two-component statistical mixture of PCR-73 ($\theta_1 = 0.15$) and polyethylene ($\theta_2 = 0.85$) with spheroidal particles for $c/a = 0.02$, $\varepsilon_1' = 6000$, $\varepsilon_2' = 2.5$, $\gamma_1 = 10^{-13}\ \Omega^{-1}\ m^{-1}$, and $\gamma_2 = 10^{-10}\ \Omega^{-1}\ m^{-1}$.

the terms proportional to $\gamma_1 d_{31}^{(2)} - \gamma_2 d_{31}^{(1)}$; i.e., the transverse piezoelectric response is very large. This contribution is due to the external electric field E_3^* inducing internal electric fields $E_3^{(1)} \longrightarrow \infty$ (in the case $\gamma_1/\gamma_2 \ll 1$) and large internal mechanical stresses $\sigma_1^{(1)} = \sigma_1^{(2)}$, which occurs in the case of a small thickness of the piezoelectric layer, $\theta_1 \longrightarrow 0$.

It is seen in Fig. 2 that the described mechanism of giant piezoelectric enhancement also occurs in disordered heterogeneous systems with spheroidal particles. To obtain giant piezoelectric coefficients d_{33}^* and $-d_{31}^*$, a large concentration of the polymer with increased conductivity is required, which favors the appearance of very large fields $E_3^{(1)}$ in the piezoelectric component. It is also obvious that strong fields $E_3^{(1)}$ in disordered systems should arise near the percolation threshold, where very thin plates of the piezoelectric component with low conductivity are located between thick polymer layers with increased conductivity. As the aspect ratio $\xi = c/a$ increases, the spheroid depolarization factor decreases and the conductivity percolation threshold is shifted to lower values of θ_2 (Figs. 1, 2); simultaneously, the fields $E_3^{(1)}$ and the stresses $\sigma_1^{(1)} = \sigma_1^{(2)}$ related to them decrease substantially. Indeed, for $\gamma_1/\gamma_2 \ll 1$ and $\theta_2 \approx \theta_{2c}$, we have $E_3^{(1)}/E_3^* \longrightarrow \infty$ as $\xi \longrightarrow 0$, whereas $E_3^{(1)}/E_3^* \longrightarrow 3/2$ as $\xi \longrightarrow 1$ [2, 7, 8]. In the latter case, the transverse piezoelectric response

decreases sharply, which leads to a significant decrease in the quasistatic piezoelectric coefficients of the composite near the percolation threshold. Therefore, for spheres, diffuse maxima are observed instead of sharp and high maxima of d_{33}^* and $-d_{31}^*$; i.e., plateau-like dependences of the quasistatic piezoelectric coefficients on θ_2 take place in a wide interval of concentrations of the conducting component, $0 < \theta_2 < 0.7$. The dependences of the high-frequency piezoelectric coefficients and permittivities of composites on θ_2 are qualitatively different in character, because the distribution of internal electric fields at high frequencies is determined by the permittivity tensor; d^* and ε^* decrease monotonically and vanish at the value of θ_2 corresponding to the permittivity percolation threshold [7, 8].

It is seen from Figs. 1–3 that giant piezoelectric and dielectric enhancement must be accompanied by giant relaxations of the piezoelectric coefficients and permittivity. The depth of these relaxations is minimum at low polymer concentrations ($\theta_2 \longrightarrow 0$) and is maximum near the percolation threshold θ_{2c}. Both the dielectric and piezoelectric relaxation have a non-Debye character because of a wide distribution of relaxation times (especially near the percolation threshold). The reason for the non-Debye character of the spectra is obvious: the physical constants of the effective medium that surrounds chaotically distributed spheres or spheroids of the first and second components of the mixture depend on the frequency ω of the electric field.

The spectra of piezoelectric coefficients d_{33}^* and $-d_{31}^*$ and of the permittivity ε_{33}^*, shown in Fig. 3, can be fitted by the Cole–Cole formula [15]; e.g., for ε_{33}^*, we have

$$\varepsilon^* = \varepsilon_\infty + \frac{\varepsilon_s - \varepsilon_\infty}{1 + (i\omega\tau)^{1-\alpha}},$$

where ε_s and ε_∞ are the static ($\omega\tau \ll 1$) and high-frequency ($\omega\tau \gg 1$) permittivities, respectively. The average relaxation time τ and the Cole–Cole parameter α depend strongly on the ratio of bulk concentrations of the components of the mixture and are especially large near the conductivity percolation threshold ($\alpha = 0.3$–0.4 for $\theta \approx \theta_{2c}$). The average relaxation frequency $\omega_r = 1/\tau$ is very sensitive to the ratios γ_1/γ_2, $\xi = c/a$, and θ_1/θ_2 and can change by several orders of magnitude as these ratios vary.

4. CONCLUSIONS

Thus, we have established for the first time that, for a statistical mixture of spherical particles, the difference between the average relaxation time of the permittivity τ_ε, on the one hand, and the average relaxation times of the piezoelectric coefficients and constants of elasticity, τ_d and τ_s, on the other hand, is large (an order of magnitude or greater): $\tau_\varepsilon \gg \tau_d = \tau_s$. This result indicates a very slow accumulation of free charges and faster rates of mechanical processes related to variations in stress (strain). For strongly oblate spheroids, the difference between τ_ε and τ_d decreases (Fig. 3), since the relaxation of large internal stresses is slower. Giant quasistatic (at $\omega = 10^{-7}$–10^{-5} rad/s) permittivity and piezoelectric coefficients of the composite relax at frequencies $\omega = 10^4$–10^{-3} rad/s and reduce to values of order unity for $\omega > 10^{-2}$ rad/s.

Giant piezoelectric enhancement in the infralow-frequency range should be taken into account in designing devices with heterogeneous piezoelectric elements. Our analysis has shown that a piezoelectric element used as a sensor may have much greater piezoelectric coefficients than the same material used in an actuator.

REFERENCES

1. R. E. Newnham, D. P. Skinner, and L. E. Cross, Mater. Res. Bull. **13** (5), 525 (1978).
2. V. I. Odelevskiĭ, Zh. Tekh. Fiz. **21** (6), 678 (1951).
3. G. S. Radchenko and A. V. Turik, Fiz. Tverd. Tela (St. Petersburg) **45** (9), 1676 (2003) [Phys. Solid State **45**, 1759 (2003)].
4. A. L. Efros and B. I. Shklovskii, Phys. Status Solidi B **76** (2), 475 (1976).
5. V. V. Lemanov, A. V. Sotnikov, E. P. Smirnova, and M. Weihnacht, Fiz. Tverd. Tela (St. Petersburg) **44** (11), 1948 (2002) [Phys. Solid State **44**, 2039 (2002)].
6. P. Lunkenheimer, V. Bobnar, A. V. Pronin, A. Ritus, A. A. Volkov, and A. Loidl, Phys. Rev. B **66** (5), 052105 (2002).
7. D. A. G. Bruggeman, Ann. Phys. (Leipzig) **24** (5), 636 (1935).
8. J. A. Reynolds and J. M. Hough, Proc. Phys. Soc. London, Sect. B **70** (452), 769 (1957).
9. M. Marutake, J. Phys. Soc. Jpn. **11** (8), 807 (1956).
10. A. P. Vinogradov, *Electrodynamics of Composite Materials* (Éditorial URSS, Moscow, 2001) [in Russian].
11. A. Ya. Dantsiger, O. N. Razumovskaya, L. A. Reznichenko, and S. I. Dudkina, *High-Efficient Piezoceramics: Search Optimization* (Paĭk, Rostov-on-Don, 1995) [in Russian].
12. F. Levassort, M. Lethiecq, C. Millar, and L. Pourcelot, IEEE Trans. Ultrason. Ferroelectr. Freq. Control **45** (6), 1497 (1998).
13. A. V. Turik and G. S. Radchenko, Izv. Vyssh. Uchebn. Zaved. Sev.-Kavk. Reg., Tekh. Nauki, Special Issue, 100 (2004).
14. A. V. Turik and G. S. Radchenko, J. Phys. D **35** (11), 1188 (2002).
15. W. Brown, Jr., *Dielectrics* (Springer, Berlin, 1956; Inostrannaya Literatura, Moscow, 1961).

Translated by I. Zvyagin

Physics of the Solid State, Vol. 46, No. 12, 2004, pp. 2217–2221. Translated from Fizika Tverdogo Tela, Vol. 46, No. 12, 2004, pp. 2143–2147.

DEFECTS, DISLOCATIONS, AND PHYSICS OF STRENGTH

Phototransferred Thermoluminescence in Anion-Defect α-Al_2O_3 Crystals

V. S. Kortov, I. I. Milman, S. V. Nikiforov, E. V. Moiseĭkin, and M. M. Ovchinnikov

Ural State Technical University, ul. Mira 19, Yekaterinburg, 620002 Russia

e-mail: snik@dpt.ustu.ru

Received April 28, 2004

Abstract—Thermally stimulated migration of charge carriers from trapping centers responsible for the main thermoluminescence peak at 450 K to a deep trap was experimentally observed in anion-defect α-Al_2O_3 crystals. Optically induced transport of carriers from the deep trap to the main trap was also observed to cause phototransferred thermoluminescence at 450 K. The results obtained experimentally confirm the adequacy of the basic assumptions made in the model of interactive interaction between main and deep traps in the crystals under study, as well as substantiate the method of repeated obtaining of dosimetric data. © *2004 MAIK "Nauka/Interperiodica".*

1. INTRODUCTION

With the advent of anion-defect α-Al_2O_3 crystals and highly sensitive TLD-500K thermoluminescent detectors of ionizing radiation developed on their basis, the possibilities for personal and emergency dosimetry, environmental radiation monitoring, and detection of pulsed and low-dose radiations have significantly increased. Therefore, the luminescence and dosimetric properties of nominally pure anion-defect α-Al_2O_3 single crystals (α-Al_2O_3 : C) grown under reduction conditions to achieve a high content of F and F^+ centers continue to be actively studied [1–4].

Experimental studies of these crystals have detected a number of features that do not follow from the known models describing the kinetics of thermoluminescence (TL). The most significant features are the dependence of the TL yield on the crystal heating rate, the decrease in the average activation energy within the main peak measured by using the fractional TL method, and the quenching of photo- and radioluminescence of F centers in the temperature range of the main peak [5, 6].

Significant progress in interpreting the mechanisms of the observed phenomena came from the establishment of the fact that deep traps are involved in these processes. In particular, it has been experimentally substantiated that the degree of their filling with carriers is immediately associated with all the above-mentioned features. These results have been interpreted in terms of the model of an interactive system of traps, based on the assumption that the carriers released in the temperature range of the main TL peak are trapped by thermally stable deep traps. Calculations carried out according to such concepts allowed description of the entirety of experimentally observed TL features in these crystals as a function of the degree of filling of deep traps, namely, the shape and temperature position of the peak, the influence of the heating rate on the luminescence yield, the nonlinearity of the dose dependence, and the sensitivity change [7–12].

However, the basic assumptions made in this model, namely, that the carriers released during TL measurements from traps responsible for the main peak at 450 K can be trapped by deep traps and that the efficiency of this trapping depends on temperature, were made on the basis of indirect observations in which deep traps were preliminarily filled in an artificial way rather than immediately during TL measurements in the main peak [7–11]. Therefore, the existence of interactive coupling between the main and deep traps in anion-defect α-Al_2O_3 crystals calls for more detailed experimental confirmation. This model would be seriously confirmed if charge migration (when measuring TL in the main peak) to the deep trap and from the deep trap to the trap responsible for the main peak were to be observed directly. Experimental confirmation of such processes is the objective of this study.

2. SAMPLES AND EXPERIMENTAL TECHNIQUE

Samples of conventional TLD-500K thermoluminescent detectors based on nominally pure anion-defect α-Al_2O_3 single crystals were studied. Model concepts and numerical calculations of the TL features of the same crystals were discussed in [7–12].

In this study, two methods for filling the deep trap with charge carriers were used. In the first method, referred to as artificial, the deep trap corresponding to the TL peak at 730 K was filled by exposing samples (at 603 K) to the total spectrum of a DRT-240 mercury lamp for 2 min. In this case, the trap responsible for the main TL peak at 450 K remained unfilled. According to the second (natural) method, the deep trap was filled as

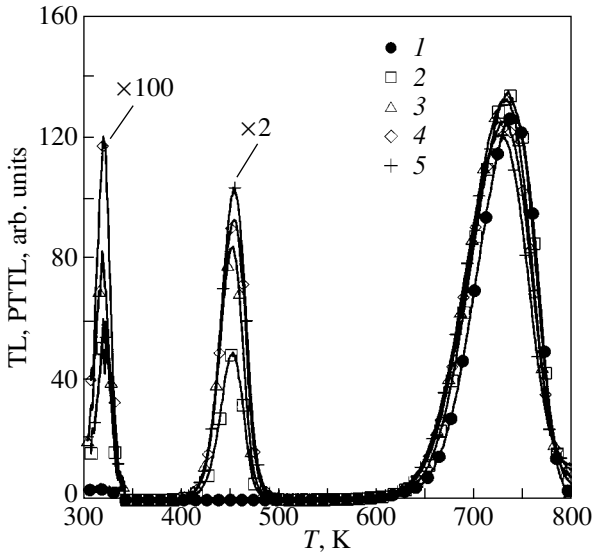

Fig. 1. (*1*) Thermoluminescence of α-Al_2O_3 with artificially filled deep traps and (*2–5*) the phototransferred thermoluminescence for various durations of stimulation by a light flux with a wavelength of 470 nm: (*1*) 0, (*2*) 2, (*3*) 3, (*4*) 4, and (*5*) 5 min.

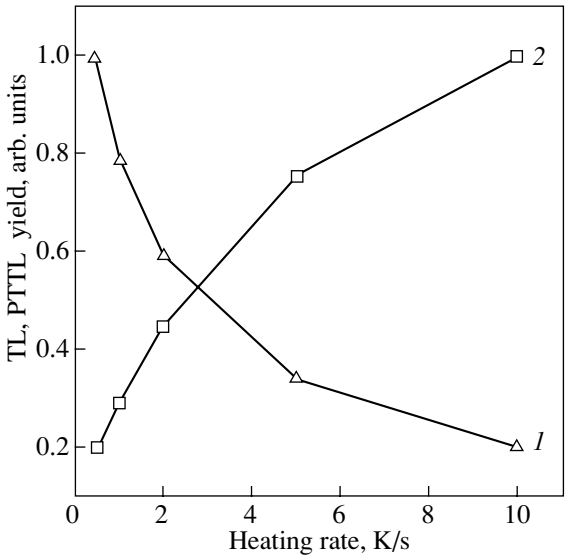

Fig. 2. Dependences of (*1*) the thermoluminescence and (*2*) phototransferred thermoluminescence yields in the peak at 450 K on the heating rate for α-Al_2O_3 samples (*1*) irradiated by a conventional radiation dose from a $^{90}Sr/^{90}Y$ source and (*2*) after their optical stimulation at a wavelength of 470 nm.

the samples, preliminarily irradiated at room temperature by a conventional dose of β radiation from a $^{90}Sr/^{90}Y$ source, were heated to 620 K at a rate of 0.5, 1, 2, 5, or 10 K/s and the main trap was emptied. Deep traps were emptied by 10-min heating of crystals at 1170 K.

Photostimulated migration of carriers from the deep to main traps was carried out using a light source with an increased spectral brightness at a wavelength of 470 nm, which consisted of an assembly of SDK-S469-5-10 light-emitting diodes and an objective with a focal length of ~2 cm for focusing a light flux on an area of ~2 cm^2. Phototransferred thermoluminescence (PTTL) in the main peak was measured using a conventional technique with a heating rate of 2 K/s.

3. RESULTS AND DISCUSSION

In the temperature range 300–900 K, at a heating rate of 2 K/s, the TL curve of anion-defect α-Al_2O_3 contains four TL peaks at 323, 450, 730, and 880 K. The peak at 323 K has not been thoroughly studied; its height depends on the elapsed time from irradiation to the measurement. The peak at 450 K is referred to as the main or dosimetric peak, since it stores the largest portion of the light yield in ordinary measurements. The peak at 730 K is not detected if the trap responsible for it (the first deep trap) is emptied, e.g., by annealing, and this peak manifests itself if the trap is filled by using the former of the above-described techniques. The TL peak at 880 K is caused by a second deep trap, and its role is not discussed in this paper.

According to the chosen study algorithm, we first observed PTTL from the samples prepared using the first of the above-described methods in order to experimentally confirm the possible optically stimulated charge transfer from a preliminarily filled deep trap to the basic trap, which remains empty as the deep trap is filled. Figure 1 shows PTTL curves of such samples in relation to the time of optical stimulation with 470-nm radiation. We can see that the optical stimulation causes charge transfer from the deep trap to the shallower traps responsible for the peaks at 450 and 323 K. The light yield stored in the deep trap decreases insignificantly as the stimulation time is increased, whereas the light yield in the peaks at 450 and 323 K increases significantly. The mere fact of PTTL excitation in the peak at 450 K is a direct confirmation of interactive interaction between the deep and main traps.

The dependences of the TL yield on the heating rate of irradiated samples were also measured. These dependences show that the TL signal in the main peak decreases as the heating rate is increased (curve *1* in Fig. 2). This dependence of the TL yield on the heating rate has been explained in terms of the model of interactive interaction of traps by the trapping of a portion of carriers released upon heating by the deep trap, which causes a decrease in the number of carriers involved in the recombination processes responsible for the luminescence [7, 11]. An alternative viewpoint is that the only cause of the decrease in the TL yield with increasing heating rate is the classical Mott–Seitz intracenter quenching of *F*-center luminescence, which takes place in the temperature range of the main peak [13]. If the former explanation is valid, the PTTL yield

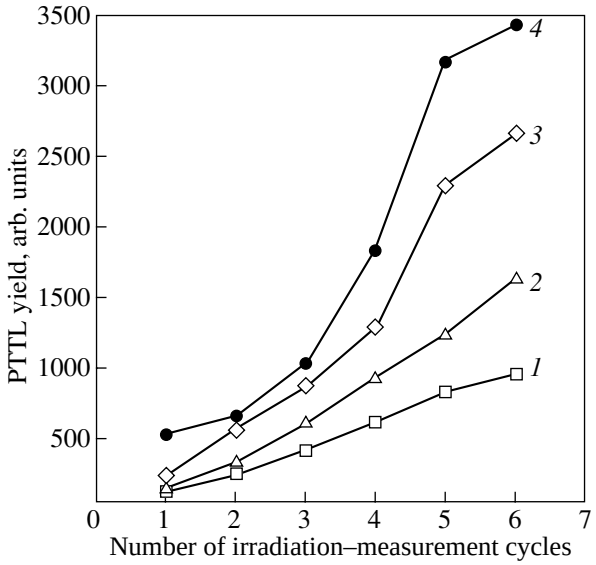

Fig. 3. Dependence of the phototransferred thermoluminescence yield of α-Al_2O_3 samples in the peak at 450 K on the number of irradiation–measurement cycles at heating rates of (*1*) 1, (*2*) 2, (*3*) 5, and (*4*) 10 K/s.

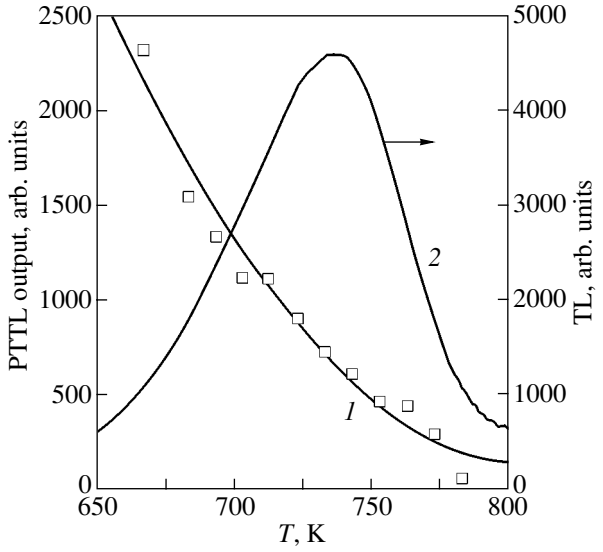

Fig. 4. (*1*) Dependence of the phototransferred thermoluminescence yield in the peak at 450 K on the temperature of preliminary heating of irradiated α-Al_2O_3 samples before optical stimulation and (*2*) the thermoluminescence curve.

in the main peak should, on the contrary, increase with the heating rate of the irradiated sample. Subsequent PTTL measurements confirmed this assumption (curve *2* in Fig. 2). A comparison of curves *1* and *2* in Fig. 2 shows good agreement with this assumption and allows the conclusion that the TL yield decreases with an increase in the heating rate because a portion of carriers is captured by the deep trap.

The concentration of carriers in the deep traps could be increased, all other factors being equal, by repeated TL measurements. Figure 3 shows the dependence of the PTTL yield in the peak at 450 K on the number of accumulation cycles of carriers in the deep traps at various heating rates for samples irradiated with identical doses. We can see that the charge is accumulated in the deep traps more efficiently as the number of irradiation–TL measurement cycles increases and also with an increase in the heating rate of irradiated samples. The experiments showed that carrier migration to the deep trap during TL measurements takes place even at crystal heating rates of 0.5–2.0 K/s, which are fairly low for dosimetric measurements. The latter observation became possible due to the extremely high sensitivity of the PTTL method used in this study.

The charge-exchange coupling of the dosimetric trap with the first deep trap, responsible for the TL peak at 730 K, was additionally examined. To eliminate the possibility of the PTTL observed in Figs. 2 and 3 being caused by carrier migration from other, still deeper trapping centers, the deep trap under study was filled, as is usually done, as the main trap was emptied (after irradiation of samples by the beta source) upon heating at a rate of 10 K/s. However, in this case, the final temperature was not limited to 620 K but was increased in each measurement cycle in steps of 10 up to 800 K. The PTTL was measured after each temperature step. The results of these measurements are shown in Fig. 4. We can see that the PTTL yield decreases when the temperature reaches the instability range (670–780 K) of the deep trap. The rate of this decrease is nonuniform; it is highest in the range 670–730 K, corresponding to the low-temperature region of the TL peak of the deep trap (where the largest portion of the stored light yield is concentrated), and decreases in the range 730–780 K, corresponding to the high-temperature portion of the peak (where the luminescence yield is relatively low). This allows us to argue that it is the deep trap with the TL peak at 730 K that was filled during thermally stimulated emptying of the main trap and from which photostimulated migration of the carriers responsible for the PTTL occurred. As follows from these results, the efficiency of filling of the deep trap is dependent on the temperature at which free carriers arise. Filling of the deep trap becomes more intense as this temperature approaches the range of temperature instability of the deep trap.

Thus, the TL yield decrease in the main peak and the simultaneous increase in the carrier concentration in the deep trap produced by an increase in the heating rate can be associated with the fact that the carriers released during TL measurement are captured by the deep trap. The prevalence of carrier trapping over carrier migration to radiative recombination centers results in the observed decrease in the luminescence yield, which can be intentionally varied or remain unchanged if the deep trap is preliminarily artificially filled, as was shown in [7, 11]. This feature was also observed in this

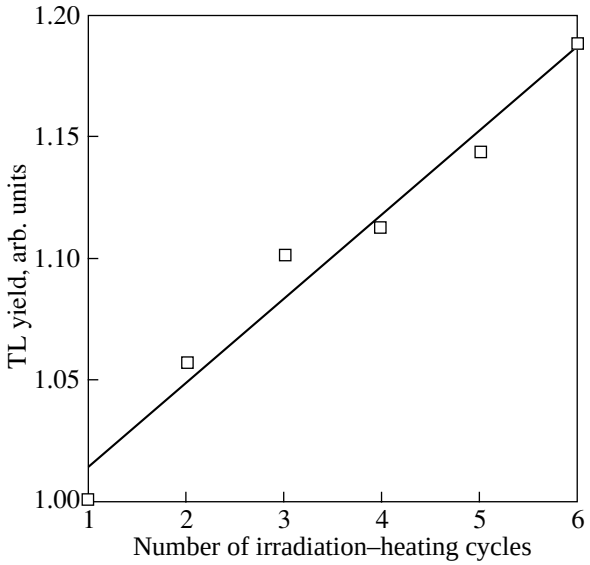

Fig. 5. Dependence of the thermoluminescence yield on the number of preliminary irradiation–heating cycles at a rate of 10 K/s.

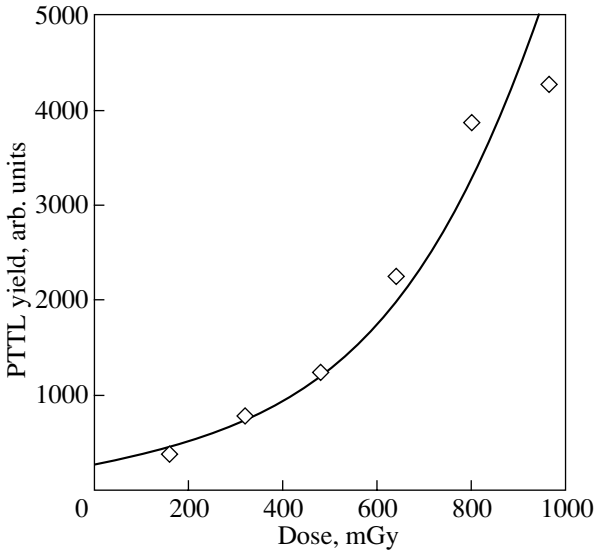

Fig. 6. Dependence of the phototransferred thermoluminescence yield on the irradiation dose of α-Al_2O_3-based detectors.

study. As carriers are accumulated in the deep trap due to repeated similar cycles of alternate irradiation and heating with measurement of the TL at a rate of 10 K/s, the yield in the main peak increases (Fig. 5). According to the data from Fig. 5 and the model concepts, the efficiency of free-carrier trapping by the deep trap decreases as the trap is filled. In the extreme case where the deep trap is artificially filled to saturation, the TL yield increases by a factor of 5 or greater and depends only weakly on the heating rate.

A practically important consequence of the observed features in charge exchange between traps of various energy depths in anion-defect α-Al_2O_3 crystals is the principal possibility of repeated measurements of the dose with the same detector using PTTL. It is believed that crystal heating during TL measurement results in an irreversible loss of dosimetric information. The results obtained in this study show that "reservation" of dosimetric information takes place during the first (after irradiation) TL measurement, because the carriers released during the TL measurement are captured by the deep trap. The number of such carriers is proportional to the radiation dose absorbed by the detector; therefore, the PTTL yield correlates with the dose. Figure 6 shows the dependence of the PTTL yield on the dose measured from the TL data. This dependence, found from the data on TL and PTTL, is a calibration curve and can be used to estimate the absorbed dose. The availability of a reserve channel for dose measurements in TL dosimetry significantly increases the reliability of measurements [14]. For detectors based on anion-defect α-Al_2O_3 crystals, this possibility has been shown for the first time in this study.

4. CONCLUSIONS

We have proposed a technique for studying the carrier transfer between the main dosimetric and deep traps in anion-defect α-Al_2O_3 crystals during photo- and thermostimulation and implemented it in this study. Direct experiments have confirmed the existence of interactive coupling between these traps. The dependences of PTTL on the heating rate and on the number of cycles of dosimetric information readout were studied. It has been shown that PTTL can be used as a reserve channel for obtaining dosimetric information.

ACKNOWLEDGMENTS

This study was supported in part by the Russian Ministry of Education and the U.S. Civilian Research and Development Foundation for the Independent States of the Former Soviet Union (Appendix 7 EK-005-X1, grant for young candidates of science no. Y1-EP-05-15).

REFERENCES

1. E. G. Yukihara, R. Gaza, S. W. S. McKeever, and C. G. Soares, Radiat. Meas. **38**, 59 (2004).
2. E. G. Yukihara, V. H. Whitley, J. C. Polf, D. M. Klein, S. W. S. McKeever, A. E. Akselrod, and M. S. Akselrod, Radiat. Meas. **37**, 627 (2003).
3. A. N. Yazici, S. Solak, Z. Ozturk, M. Topaksu, and Z. Yegingil, J. Phys. D: Appl. Phys. **36**, 181 (2003).
4. I. I. Milman, S. V. Nikiforov, and V. S. Kortov, Radiat. Meas. **33**, 561 (2001).
5. I. Tale, T. M. Piters, M. Barbosa-Flores, R. Peres-Salas, R. Aceves, and M. Springis, Radiat. Prot. Dosim. **65**, 235 (1996).

6. V. S. Kortov, I. I. Milman, V. I. Kirpa, and J. Lesz, Radiat. Prot. Dosim. **65**, 255 (1996).
7. I. I. Milman, V. S. Kortov, and S. V. Nikiforov, Radiat. Meas. **29** (3–4), 401 (1998).
8. V. E. Pelenyov, V. S. Kortov, and I. I. Milman, Radiat. Meas. **33**, 629 (2001).
9. V. S. Kortov, I. I. Milman, and S. V. Nikiforov, Radiat. Prot. Dosim. **100**, 75 (2002).
10. I. I. Milman, V. S. Kortov, and V. I. Kirpa, Fiz. Tverd. Tela (St. Petersburg) **37** (4), 1149 (1995) [Phys. Solid State **37**, 625 (1995)].
11. I. I. Milman, V. S. Kortov, and S. V. Nikiforov, Fiz. Tverd. Tela (St. Petersburg) **40** (2), 229 (1998) [Phys. Solid State **40**, 206 (1998)].
12. V. S. Kortov, I. I. Milman, S. V. Nikiforov, and V. E. Pelenev, Fiz. Tverd. Tela (St. Petersburg) **45** (7), 1202 (2003) [Phys. Solid State **45**, 1260 (2003)].
13. M. S. Akselrod, N. A. Larsen, V. Whitley, and S. W. S. McKeever, J. Appl. Phys. **84** (6), 3364 (1998).
14. J. L. Muciz, V. Correcher, and A. Delgado, Radiat. Prot. Dosim. **85**, 63 (1999).

Translated by A. Kazantsev

Physics of the Solid State, Vol. 46, No. 12, 2004, pp. 2222–2224. Translated from Fizika Tverdogo Tela, Vol. 46, No. 12, 2004, pp. 2148–2150.

MAGNETISM AND FERROELECTRICITY

Anomalies in the Magnetic and Magnetoelastic Properties of $Nd_{1-x}Ca_xMnO_3$ Single Crystals in Strong Magnetic Fields

Yu. F. Popov*, A. M. Kadomtseva*, G. P. Vorob'ev*, K. I. Kamilov*, A. A. Mukhin, V. Yu. Ivanov**, and A. M. Balbashov*****

** Moscow State University, Vorob'evy gory, Moscow, 119992 Russia*

e-mail: popov@plms.phys.msu.ru

*** General Physics Institute, Russian Academy of Sciences, ul. Vavilova 38, Moscow, 117942 Russia*

**** Moscow Power Institute, Krasnokazarmennaya ul. 14, Moscow, 111250 Russia*

Received March 9, 2004

Abstract—Measurements of the magnetic and magnetoelastic properties of $Nd_{0.5}Ca_{0.5}MnO_3$, $Nd_{0.55}Ca_{0.45}MnO_3$, and $Nd_{0.6}Ca_{0.4}MnO_3$ single crystals have revealed correlations between the observed anomalies in magnetization and magnetostriction associated with suppression of the antiferromagnetic phase and charge ordering by a strong magnetic field followed by transition to the ferromagnetic state. *H–T* phase diagrams are constructed. © *2004 MAIK "Nauka/Interperiodica".*

1. INTRODUCTION

The continuing interest in investigating the properties of rare-earth manganites can be traced not only to the discovery of colossal magnetoresistance in them [1] but also to the fact that these compounds possess a number of unique properties (including charge, orbital, and spin ordering) and intricate *T–x* phase diagrams originating from a difference in the tolerance factor and magnetic state of a rare-earth ion.

In contrast to the $La_{1-x}Ca_xMnO_3$ system, whose compositions remain in the ferromagnetic metallic state up to $x = 0.47$, the ferromagnetic state in $Nd_{1-x}Ca_xMnO_3$ persists up to $x = 0.35$ [2], while for $0.4 \le x \le 0.5$ an antiferromagnetic charge-ordered state is observed to exist (Néel temperature $T_N = 160$ K, charge-ordering temperature $T_{CO} = 160$ K) [3]. Application of a strong magnetic field can be used to suppress the charge-ordered and antiferromagnetic state and drive a ferromagnetic phase transition.

In [3–5], magnetization curves for polycrystalline $Nd_{1-x}Ca_xMnO_3$ samples ($x = 0.4$, 0.45, 0.5) were shown to exhibit anomalies in strong magnetic fields of ≈100 kOe (driving the phase transition to the ferromagnetic state) and *T–H* phase diagrams were constructed. It appeared of interest to check these measurements on $Nd_{1-x}Ca_xMnO_3$ single crystals and to study their magnetoelastic properties in strong magnetic fields, because no such information was available in the literature. It was believed that the anomalies in the magnetic and magnetoelastic properties should be clearly correlated, but no magnetostriction measurements have thus far been performed on single crystals of the $Nd_{1-x}Ca_xMnO_3$ system.

2. EXPERIMENTAL RESULTS AND THEIR DISCUSSION

Measurements of the magnetic and magnetoelastic properties of $Nd_{1-x}Ca_xMnO_3$ single crystals ($x = 0.3$, 0.4, 0.45, 0.5) were carried out in the temperature range 10–280 K in pulsed magnetic fields of up to 250 kOe, and thermal expansion was measured in the temperature interval 78–300 K. Single crystals were grown by cold-crucible zone melting under radiative heating.

$Nd_{0.7}Ca_{0.3}MnO_3$ is a ferromagnet for $T \le T_C = 120$ K (T_C is the Curie temperature) and a charge-ordered paramagnet for $T_C \le T \le T_{CO} = 240$ K [2]. Our studies of the magnetic properties of single crystals did not reveal any signs of charge ordering.

Figure 1 displays magnetization curves obtained for $Nd_{0.7}Ca_{0.3}MnO_3$ single crystals. It is seen that this composition is a ferromagnet at temperatures below T_C. As

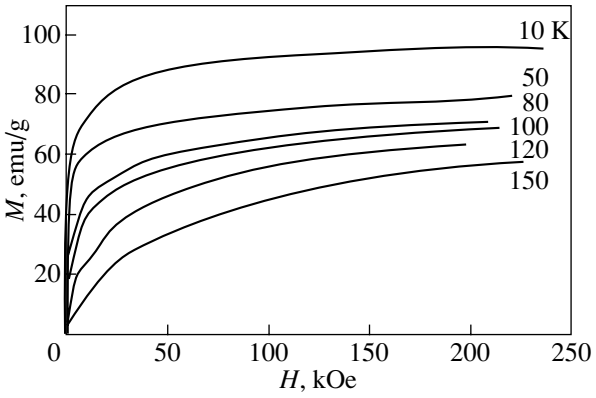

Fig. 1. Magnetization curves obtained on a $Nd_{0.7}Ca_{0.3}MnO_3$ single crystal.

1063-7834/04/4612-2222$26.00 © 2004 MAIK "Nauka/Interperiodica"

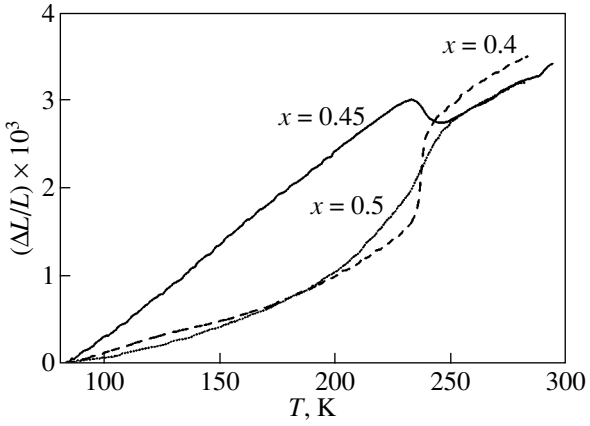

Fig. 2. Thermal expansion of $Nd_{1-x}Ca_xMnO_3$ single crystals.

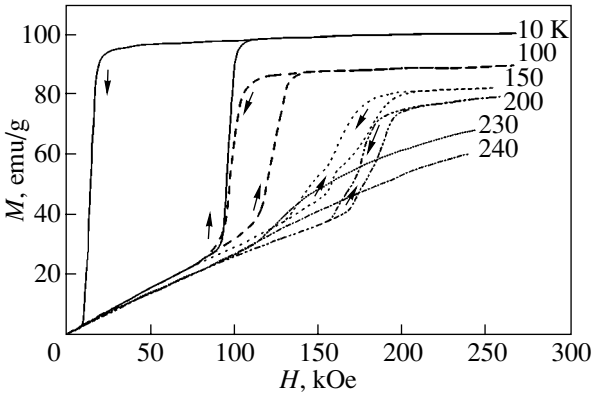

Fig. 3. Magnetization curves obtained on a $Nd_{0.55}Ca_{0.45}MnO_3$ single crystal.

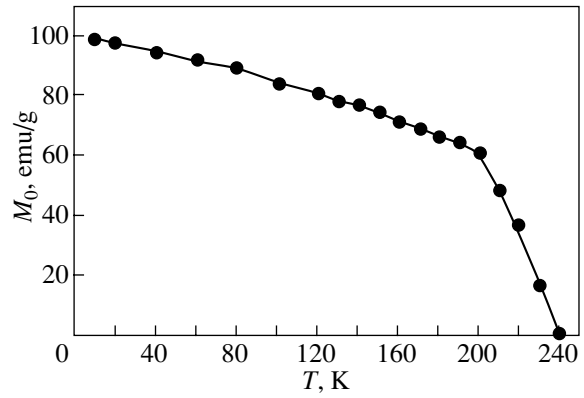

Fig. 4. Temperature dependence of the magnetic field–induced magnetization of $Nd_{0.55}Ca_{0.45}MnO_3$ extrapolated to zero field.

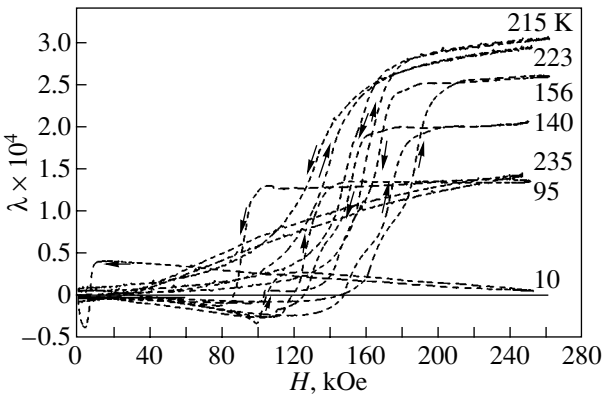

Fig. 5. Magnetostriction curves obtained on a $Nd_{0.55}Ca_{0.45}MnO_3$ single crystal.

the temperature is decreased, its magnetization increases because the ions of the Nd subsystem are magnetized by the Mn subsystem exchange field; this effect becomes particularly pronounced below 50 K [2]. It was demonstrated in [2–4, 6] that $Nd_{1-x}Ca_xMnO_3$ single crystals (x = 0.4, 0.45, 0.5) undergo charge ordering at a temperature T_{CO} = 250 K and antiferromagnetic ordering sets in as the temperature decreases to T_N = 160 K. Thermal-expansion measurements revealed an anomaly at the charge-ordering temperature T_{CO} = 235 K for all three compositions (Fig. 2). The difference in the magnitude and sign of this anomaly between different compositions (-10^{-4} for x = 0.45 and $+10^{-3}$ for x = 0.4, 0.5) originates from the fact that the measurements were performed along different crystallographic directions, more specifically, along the c axis for x = 0.4 and 0.5 and along the b axis for x = 0.45. In order to investigate magnetic field–induced phase transitions in $Nd_{1-x}Ca_xMnO_3$ single crystals (x = 0.4, 0.45, 0.5), we studied the magnetic and magnetoelastic properties in strong pulsed magnetic fields of up to 250 kOe.

Figure 3 shows magnetization curves for a crystal with x = 0.45 measured at different temperatures. It can be seen that this composition has zero spontaneous magnetization in a weak magnetic field. Increasing the magnetic field to $H_{Cr} \approx 100$ kOe gives rise to abrupt magnetization jumps, which are obviously caused by a phase transition to the ferromagnetic state. The temperature dependence of the magnetic field–induced magnetization, which was derived by extrapolating the magnetization isotherms to zero, is displayed in Fig. 4. As the temperature is increased, the magnetization is seen to decrease and vanish at the charge-ordering temperature, where the jumps on the magnetization curves disappear (Fig. 3).

To establish a correlation between anomalies in the magnetic and magnetoelastic properties at the phase transitions under study, the magnetostriction measurements were performed in strong magnetic fields. Figure 5 plots magnetostriction as a function of the magnetic field measured for a composition with x = 0.45 at different temperatures. As seen from Fig. 5, at tempera-

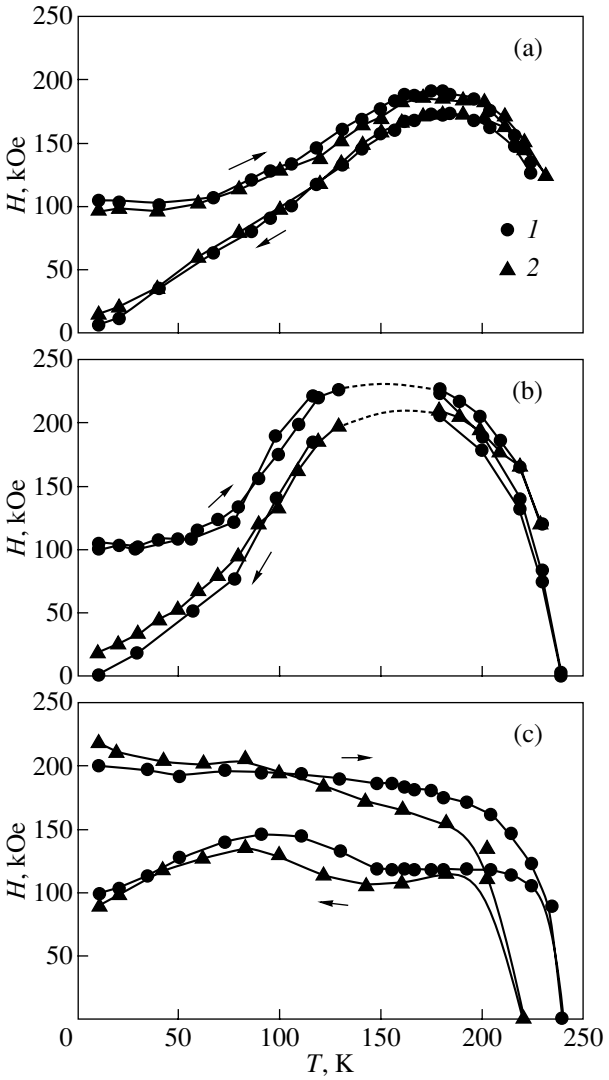

Fig. 6. *H–T* phase diagrams for $Nd_{1-x}Ca_xMnO_3$ single crystals derived from measurements of (*1*) magnetization and (*2*) magnetostriction for various values of *x*: (a) 0.45, (b) 0.4, and (c) 0.5.

tures from 10 K to the antiferromagnetic ordering point T_N = 160 K, a positive magnetostriction jump (associated with a transition to the ferromagnetic state) occurs at the threshold field against a background of comparatively weak negative magnetostriction existing in low magnetic fields. As the temperature is increased, the negative magnetostriction decreases and practically vanishes near T_N = 160 K. As the temperature is increased still further, up to T_{CO} = 235 K, only a positive magnetostriction jump is observed, which reaches a maximum value of 3×10^{-4} at 215 K, to vanish subsequently at 235 K near the charge-ordering temperature.

Our measurements of the magnetostriction suggest that the magnetostriction strains associated with suppression of antiferromagnetic ordering and of charge ordering are opposite in sign ($\lambda < 0$ for $T < T_N$ and $\lambda > 0$ for $T_N < T < T_{CO}$). The threshold fields driving the phase transition in the $Nd_{0.55}Ca_{0.45}MnO_3$ crystal to the ferromagnetic state were derived from magnetization and magnetostriction measurements performed at various temperatures and were used to construct *H–T* phase diagrams; they are depicted in Fig. 6a and are seen to be in good agreement. As is evident from Fig. 6a, the threshold fields obtained under increasing and decreasing temperature differ strongly; such a hysteretic behavior is characteristic of first-order phase transitions. The transitions to the ferromagnetic state observed to occur in the $Nd_{0.55}Ca_{0.45}MnO_3$ system are obviously associated with suppression of the antiferromagnetic charge ordering by a magnetic field.

Analogous measurements of magnetization and magnetostriction curves in strong magnetic fields were performed on compositions with $x = 0.4$ and 0.5, which also exhibited anomalies at the magnetic field–induced phase transition to the ferromagnetic state. *H–T* phase diagrams for these compositions are presented in Figs. 6b and 6c.

Note that the magnetization and magnetostriction jumps observed at the phase transition to the ferromagnetic state become less pronounced near T_N, which makes determination of the critical fields more difficult. This behavior manifests itself most clearly for the $x = 0.4$ composition (the critical fields in the range 130–180 K are shown for this case by dashed lines in Fig. 6b).

3. CONCLUSIONS

To sum up, our study on $Nd_{1-x}Ca_xMnO_3$ single crystals with $x = 0.4$, 0.45, and 0.5 has revealed a correlation between the variations in the magnetic and magnetoelastic properties that occur at the magnetic field–induced phase transitions associated with suppression of antiferromagnetic and charge ordering and transition to the ferromagnetic metallic state.

ACKNOWLEDGMENTS

This study was supported in part by the Russian Foundation for Basic Research, project no. 03-02-16445.

REFERENCES

1. Y. Tokura and Y. Tomioka, J. Magn. Magn. Mater. **200**, 1 (1999).
2. F. Dupont, F. Milange, S. de Brion, A. Janossy, and G. Chouteau, Phys. Rev. B **64**, 220403 (2001).
3. M. Tokunaga, N. Miura, Y. Tomioka, and Y. Tokura, Phys. Rev. B **57**, 5259 (1998).
4. F. Millange, S. de Brion, and G. Chouteau, Phys. Rev. B **62**, 5619 (2000).
5. M. Respaud, A. Llobet, C. Frontera, C. Ritter, J. M. Broto, H. Rakoto, M. Goiran, and J. L. Garcia-Munoz, Phys. Rev. B **61**, 9014 (2000).
6. T. Vogt, A. K. Cheetham, R. Mahendiran, R. Mahesh, and C. N. R. Rao, Phys. Rev. B **54**, 15303 (1996).

Translated by G. Skrebtsov

Physics of the Solid State, Vol. 46, No. 12, 2004, pp. 2225–2228. Translated from Fizika Tverdogo Tela, Vol. 46, No. 12, 2004, pp. 2151–2154.

MAGNETISM AND FERROELECTRICITY

Electron Transition in Intercalated Disulfide $CuCrS_2$

G. M. Abramova*, A. M. Vorotynov, G. A. Petrakovskiĭ**, N. I. Kiselev**, D. A. Velikanov**, A. F. Bovina**, R. F. Al'mukhametov***, R. A. Yakshibaev***, and É. V. Gabitov*****

**Krasnoyarsk State University, pr. Svobodnyĭ 79, Krasnoyarsk, 660041 Russia*

***Kirensky Institute of Physics, Siberian Division, Russian Academy of Sciences, Akademgorodok, Krasnoyarsk, 660036 Russia*

****Bashkortostan State University, ul. Frunze 32, Ufa, Bashkortostan, 450074 Russia*

e-mail: ovm@online.ru

Received March 9, 2004

Abstract—Electrical, resonant, and magnetic properties of intercalated copper chromium disulfide $CuCrS_2$ are studied. It is established that $CuCrS_2$ is an antiferromagnetic semiconductor with Néel temperature $T_N = 40.7$ K and an effective magnetic moment of $4.3\mu_B$. Anomalies in the electrical, magnetic, and resonant properties of $CuCrS_2$ are found at $T_c = 110$ K, which suggest an electron transition accompanied by alteration of the valences of the 3*d*-metal ions. © *2004 MAIK "Nauka/Interperiodica".*

1. INTRODUCTION

The properties of the crystal structure and chemical bonds of dichalcogenides of transitional metals MeX_2 (X = S, Se, Te; *Me* = Ti, Cr, Ta) make them a likely base for the development of promising materials for the electronic industry of the future. The basic atomic structure of these materials consists of series of *X–Me–X* trilayers within which atoms are coupled by ionic–covalent bonds and arranged with either trigonal prismatic or octahedral coordination [1, 2]. The trilayers are separated by tetrahedral hollows (a so-called van der Waals gap) and weakly coupled. Hollows of dichalcogenide lattices can be filled by auxiliary atoms (the process called intercalation) to create intercalated structures [1]. The physical properties of an intercalated structure can sometimes resemble those of multilayered thin-film materials. For example, structures consisting of a succession of magnetic and nonmagnetic, insulating and metallic, or magnetic and superconducting atomic layers can be created by intercalation [1, 3]. Due to a lack of experimental data, current notions of electron transport and magnetic ordering in intercalated structures (let alone the interrelation between the electrical and magnetic parameters) are semiempirical. Therefore, searching for intercalated compounds and complex study of their physical properties are highly topical.

According to the classification of layered disulfides of 3*d* metals by Wilson and Yoffe [1], copper chromium disulfide $CuCrS_2$ is an intercalated compound based on chromium disulfide CrS_2. Trilayers in the lattices of intercalated disulfides $MeCrS_2$ (*Me* = Na, Cu, Ag) are formed by S–Cr–S layers, and univalent ions of *Me* are located in between in the van der Waals gap. The $CuCrS_2$ compound has a rhombohedral unit cell of the α-$NaFeO_2$ type (*R*3*m* Fedorov symmetry group) [1, 4]. In this compound, sulfur atoms form a distorted cubic packing, which is often considered in hexagonal representation. Chromium atoms are located in the octahedral lattice sites, and copper atoms are in the tetrahedral sites. Half of the tetrahedral positions in the $CuCrS_2$ lattice are vacant; therefore, the structure of the disulfide is disordered and copper cations are mobile at high temperature. At the order–disorder structural phase transition temperature ($T \sim 670$ K), where the copper cation sublattice becomes disordered, copper chromium disulfide exhibits superionic properties [5]. We are unaware of any studies on the low-temperature electrical properties of this material. The magnetic properties of copper chromium disulfide were studied in [4, 5–7]. Intercalated disulfides $MeCrS_2$ are considered to be two-dimensional magnetic materials [4] whose magnetic properties are governed by ferromagnetic ordering of the magnetic moments of trivalent chromium ions in planes normal to the *c* axis and by antiferromagnetic ordering between the planes. Various authors report different values of the effective magnetic moment of $CuCrS_2$ in the paramagnetic state (for example, $5.5\mu_B$ [5], $3.985\mu_B$ [6], $3.8\mu_B$ [7]). The magnetic properties in the low-field region (below ~ 1 kOe) and the resonant properties of $CuCrS_2$ have not been studied previously. It is well known [8] that valuable information about free unpaired electrons, electron states, the interaction between them, and their interaction with the crystal lattice can be obtained by analyzing the temperature dependences of electron paramagnetic resonance (EPR). Further information about the electron states and charge transport mechanisms can be gained by simultaneously studying conductivity and magnetization in addition to EPR.

In the present paper, we report the results of studies on the structural, electrical, and magnetic properties and EPR spectra of layered intercalated copper chro-

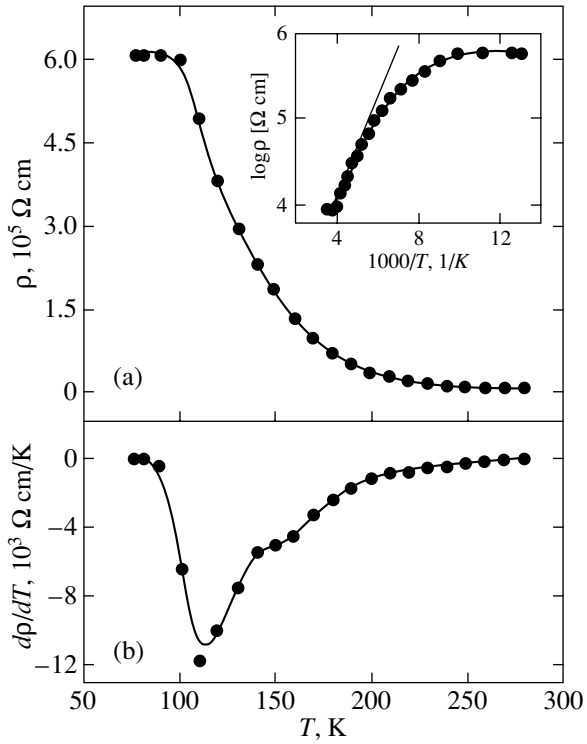

Fig. 1. Temperature dependences of (a) the resistivity ρ and (b) $d\rho/dT$ of $CuCrS_2$. Insert shows the resistivity in logarithmic scale, $\log\rho$ $(1000/T)$.

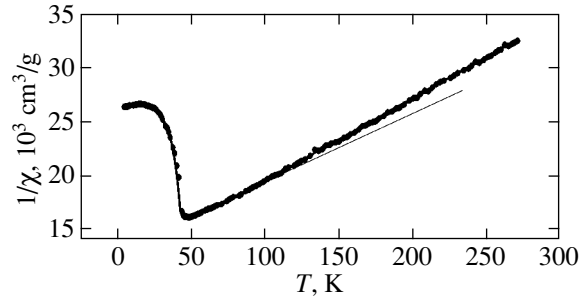

Fig. 2. Temperature dependence of the inverse magnetic susceptibility of $CuCrS_2$ in a magnetic field H = 50 Oe.

mium disulfide $CuCrS_2$, which were conducted in order to establish interrelation between the magnetic and electrical parameters.

2. EXPERIMENT

We studied polycrystalline samples of $CuCrS_2$. The sample preparation was described in detail in [5]. X-ray diffraction analysis was performed using a DRON-3M diffractometer (Cu–K_α radiation) at temperatures of 113 and 300 K. Electrical resistivity was measured using the standard dc four-probe technique (current of 1 μA) in the temperature range 77–300 K. We used rectangular samples with dimensions $1 \times 0.3 \times 0.5$ cm^3. Samples were molded from powders and annealed at 1000°C in evacuated quartz ampoules. The accuracy of voltage measurements was 10^{-4} mV, and the accuracy of resistance measurements was 2%. EPR spectra were studied using an EPR spectrometer in the 3-cm range at temperatures of 77 to 300 K. The magnetic properties of the samples were studied using a SQUID magnetometer in magnetic fields of up to 1 kOe in the temperature range 4.2–300 K.

3. RESULTS AND DISCUSSION

According to x-ray analysis, the polycrystalline samples we synthesized are single-phased with an α-$NaFeO_2$ structure, typical of $CuCrS_2$. At 300 K, the lattice parameters are $a = 3.48 \pm 0.01$ Å and $c = 18.705 \pm 0.005$ Å, which are close to those of single-crystal copper chromium disulfide (a = 3.482 Å, c = 18.686 Å [6]). As the temperature is lowered, the lattice is constricted mainly along the c axis without alteration of the crystal structure. At 113 K, the lattice parameters are $a = 3.47 \pm 0.01$ Å and $c = 18.608 \pm 0.005$ Å.

Figure 1 presents the temperature dependences of sample resistance $\rho(T)$ (Fig. 1a), its first derivative $d\rho/dT$ (Fig. 1b), and resistance in the logarithmic scale (insert). The dc resistivity of $CuCrS_2$ (current of 1 μA) at 300 K is 8.4×10^3 Ω cm and rises by two orders of magnitude as the temperature decreases, reaching 610×10^3 Ω cm at 77 K. At room temperature, samples are semiconductors with an activation energy of 0.12 eV. As the temperature is lowered, the activation energy decreases and nonlinear variation of $\log\rho$ $(1/T)$ is observed, which is typical of disordered Anderson semiconductors [9]. Below 110 K, almost no activation is observed in the conductivity of $CuCrS_2$ (inset to Fig. 1a). The activation energy for conductivity in the range 77–110 K is $\sim 3 \times 10^{-3}$ eV. The temperature dependence of the derivative $d\rho/dT$ exhibits an anomaly at T_c = 110 K, which suggests a phase transition in the electron subsystem of the material.

Figure 2 presents temperature dependences of the inverse magnetic susceptibility $\chi^{-1}(T)$ of $CuCrS_2$ samples measured with a SQUID magnetometer in a magnetic field of 50 Oe in the temperature range 4.2–270 K. The observed magnetic transition temperature T_N = 40.7 K, corresponding to a maximum in the temperature dependence of magnetic susceptibility, is close to the Néel temperature (T_N = 39 K) obtained for $CuCrS_2$ in [7]. The magnetic susceptibility $\chi(T_N)$ of the samples is 6.2×10^{-5} cm^3/g. Between 110 and 270 K, the inverse susceptibility $\chi^{-1}(T)$ follows the Curie–Weiss law (Fig. 2) with a negative paramagnetic Curie temperature Θ = –148 K and an effective magnetic moment $\mu_{eff} = 4.3\mu_B$. Around T_c = 110 K, where an anomaly in the resistivity of $CuCrS_2$ is observed, $\chi^{-1}(T)$ changes slightly in slope. Here, the paramagnetic Curie temperature changes to –176 K and the effective moment increases to $4.8\mu_B$.

In Fig. 3, the results of examining the resonant properties of $CuCrS_2$ at 9.4 GHz in the temperature range 77–300 K are presented. A single absorption line (*1*) is observed in the EPR spectrum at room temperature; its width is δH = 953 Oe, and the resonance field is H_r = 3349 ± 15 Oe. The *g* factor at 280 K is estimated to be $g = 1.90 \pm 0.01$. In the region of electrical and magnetic anomalies ($T_c \sim 110$ K), the width and intensity of resonance line *1* increase sharply and the value of the resonance field sharply drops to $H_r \sim 3270 \pm 15$ Oe. The *g* factor at 100 K is equal to $g = 1.94 \pm 0.01$ and is close to the value typical of chromium atoms. The second line (*2*) arising in the EPR spectrum (Fig. 3) is experimental evidence for reconstruction of the electron system of copper chromium disulfide at around T_c = 110 K. The resonance field and width of the second line at 100 K are H_r = 2911 Oe ($g = 2.184 \pm 0.002$) and δH = 178 Oe. The *g* factor of line *2* is typical of the bivalent Cu^{2+} ion ($3d^9$, S = 1/2) [8]. Therefore, we can assume that below T_c the electron configuration of the disulfide matches $Cu^{2+}Cr^{2+}S_2$. In this case, line *1* in the EPR spectrum at $T < T_c$ pertains to chromium ions Cr^{2+}. At room temperature, line *1* in the EPR spectrum has to correspond to trivalent chromium ions, since, according to [4, 5], copper ions at 300 K are in the nonmagnetic univalent state (electron configuration $Cu^{+}Cr^{3+}S_2$).

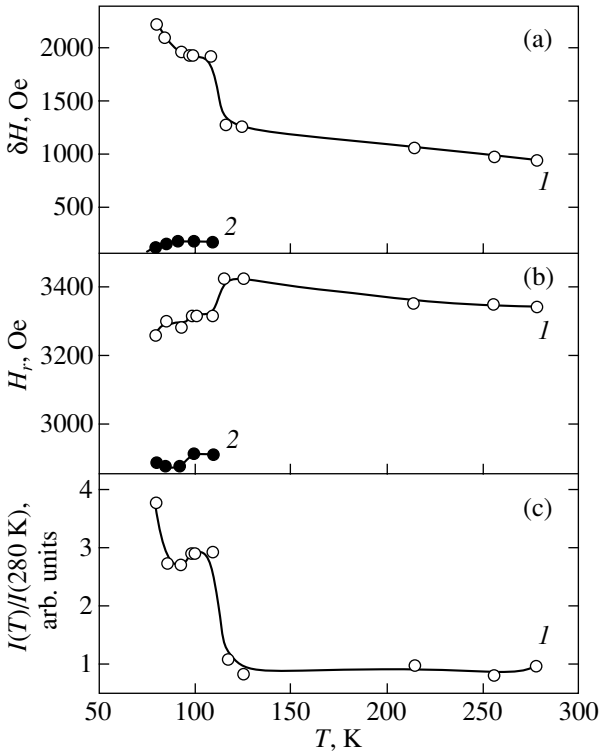

Fig. 3. Temperature dependences of (a) the EPR line width, (b) the resonance field, and (c) the normalized line intensity of $CuCrS_2$.

The anomalies and correlations found in the behavior of the magnetic, electrical, and resonant properties indicate that an electron phase transition takes place at T_c = 110 K in the paramagnetic state of $CuCrS_2$. The temperature dependence of resistivity typical of disordered semiconductors and the nonactivated type of conductivity despite the high values of resistivity (610×10^3 Ω cm) in the low-temperature phase at $T < T_c$ suggest that the transition found at T_c = 110 K in $CuCrS_2$ may be related to localization of the charge carriers, for example, to the formation of a Fermi glass (Anderson insulator) [9].

According to [5], the conductivity of $CuCrS_2$ is of hybrid electronic–ionic type in the temperature range from 300 to 670 K. The charge transfer in the insulating phase of disordered electronic–ionic semiconductors [10, 11] can be considered to be associated with a recharging of univalent ions, for example, of copper ions: $2Cu^{+} = Cu^{2+} + Cu^{0}$, where Cu^0 denotes a complex consisting of a univalent ion and a charged vacancy. It is generally accepted [11, 12] that, in copper compounds, the ionic part of the conductivity σ_i is determined by the diffusion of univalent copper ions over lattice vacancies. The electronic part of the conductivity, σ_{el}, is *p* type and is determined by holes hopping over univalent copper ions with the formation of Cu^{2+} ions.

In the temperature range $T \geq 300$ K, the activation energy of mobile copper ions, for instance, in $Cu_{2-x}Se$ [12], is 0.14 eV and their mobility at 673 K is 0.003 cm^2/V s. We measured the full dc conductivity σ_{tot}, which is equal to the sum of the ionic σ_i and electron σ_{el} conductivities. The activation energy for $CuCrS_2$ in the range 250–300 K is found to be 0.12 eV, which is close to the activation energy of mobile copper ions. No details are known of the charge transfer in $CuCrS_2$. At reduced temperatures, diffusion freezes out, because an activation energy is required for hopping of either electrons or ions in such materials [11]. The ensuing localization of the charge carriers, namely, the hole localization on the copper ions with the formation of bivalent ions Cu^{2+}, could well be the reason for the observed change in behavior of the conductivity of copper chromium disulfide at T_c = 110 K.

At least two different electron configurations of copper chromium disulfide (differing in magnetic moment) should be considered for recharging processes: $Cu^{2+}Cr^{2+}S_2$ (S = 5/2, $\mu_{eff} = 5.91\mu_B$) and $Cu^{+}Cr^{3+}S_2$ (S = 3/2, $\mu_{eff} = 3.87\mu_B$). In this case, the magnetic ground state of the compound would be determined by the recharging rate of copper ions and by the state of these ions in the "frozen" phase. The observed behavior and magnitude of the effective magnetic moment in the paramagnetic region, as well as the resonant properties of our samples, can be described well if one assumes that $CuCrS_2$ is a mixture of both electronic phases, $Cu^{2+}Cr^{2+}S_2$ and $Cu^{+}Cr^{3+}S_2$, with the proportion between them changing sharply at T_c. The behavior of the magnetic and resonant properties of the samples is correlated with the behavior of their electric properties

and shows evidence that the localization of charge carriers about T_c is related to the formation of bivalent copper ions. The anomalies observed in the parameters of absorption line *1* in the EPR spectrum of $CuCrS_2$ at 110 K suggest that the change in the valence of the copper ions is accompanied by a modification of the electronic state of the chromium ions. Therefore, the magnetic properties and the conductivity mechanism of the compound are interrelated. The dispersion of data on the effective moment of the paramagnetic state of $CuCrS_2$ presented by different authors could be explained by assuming there are fluctuations in the valences of the copper and chromium ions in the compound; the mechanism of these fluctuations is likely related to specific features of the transport properties.

4. CONCLUSIONS

To summarize, our study has shown that, at low temperatures, intercalated disulfide $CuCrS_2$ is an antiferromagnetic semiconductor with Néel temperature T_N = 40.7 K. In the paramagnetic semiconductor phase, the electrical and magnetic properties of $CuCrS_2$ are interrelated and the compound undergoes an electronic transition at T_c = 110 K, whose nature is likely associated with charge carrier localization and a change in the valences of the copper and chromium ions. The correlation of changes in spin and electronic states, as well as the observed magnetic state of the copper cations (Cu^{2+}), suggests that further study is needed into the mechanisms of electronic and ionic transport around T_c = 110 K and the nature of magnetic ordering at T_N = 40.7 K.

ACKNOWLEDGMENTS

This study was supported by the Ministry of Education of the Russian Federation, project no. E02-3.4-227.

REFERENCES

1. J. A. Wilson and A. D. Yoffe, Adv. Phys. **18**, 193 (1969).
2. G. B. Dubrovskiĭ, Fiz. Tverd. Tela (St. Petersburg) **45** (9), 1590 (2003) [Phys. Solid State **45**, 1669 (2003)].
3. M. Inoue, H. P. Hughes, and A. D. Yoffe, Adv. Phys. **38**, 565 (1989).
4. K. G. Nikiforov, *Multicomponent Magnetic Semiconductors* (KGPU im. K. É. Tsiolkovskogo, Kaluga, 2000) [in Russian].
5. R. F. Akmukhametov, R. A. Yakshibayev, E. V. Gabitov, A. R. Abdullin, and R. M. Kutusheva, Phys. Status Solidi B **236**, 29 (2003).
6. N. Le Nagard, G. Collin, and O. Gorochov, Mater. Res. Bull. **14** (11), 1411 (1979).
7. P. F. Bongers, C. F. van Bruggen, J. Koopstra, and W. P. A. M. Omloo, J. Phys. Chem. Solids **29**, 977 (1968).
8. S. A. Altshuler and B. M. Kozyrev, *Electron Paramagnetic Resonance in Compounds of Transition Elements* (Nauka, Moscow, 1972; Halsted, New York, 1975).
9. N. F. Mott and E. A. Davis, *Electronic Processes in Non-Crystalline Materials*, 2nd ed. (Clarendon, Oxford, 1979; Mir, Moscow, 1982).
10. V. L. Bonch-Bruevich and S. G. Kalashnikov, *Physics of Semiconductors* (Nauka, Moscow, 1977) [in Russian].
11. Yu. Ya. Gurevich and Yu. I. Kharkats, *Superionic Conductors* (Nauka, Moscow, 1992) [in Russian].
12. R. A. Yakshibaev, V. N. Konev, and M. Kh. Balapanov, Fiz. Tverd. Tela (Leningrad) **26** (12), 3641 (1984) [Sov. Phys. Solid State **26**, 2189 (1984)].

Translated by G. Tsydynzhapov

Physics of the Solid State, Vol. 46, No. 12, 2004, pp. 2229–2231. Translated from Fizika Tverdogo Tela, Vol. 46, No. 12, 2004, pp. 2155–2157.

MAGNETISM AND FERROELECTRICITY

Faraday Rotation and the Magnetocaloric Effect in the $Tb_3Ga_5O_{12}$ Terbium Gallium Garnet at Low Temperatures in Strong Magnetic Fields

V. I. Plis and A. I. Popov

Moscow State Institute of Electronic Engineering, Moscow, 124498 Russia

Received March 15, 2004

Abstract—The magnetocaloric effect and the Faraday rotation in a paramagnetic cubic crystal of terbium gallium garnet in strong magnetic fields oriented along different crystallographic directions are calculated theoretically. It is demonstrated that, in strong magnetic fields, the magnetocaloric effect and the Faraday effect are characterized by strong anisotropy, which disappears in weak magnetic fields. *© 2004 MAIK "Nauka/Interperiodica".*

1. INTRODUCTION

Rare-earth crystals with a garnet structure have cubic symmetry. The complex structure of these crystals is described by space group O_h^{10} [1, 2]. The garnet unit cell contains 160 atoms. It is significant that, in the garnet structure, the rare-earth ions are located in six nonequivalent dodecahedral positions whose environment has orthorhombic (lower than cubic) symmetry with point group D_2. For all the nonequivalent positions, the local symmetry axes can be oriented by rotating the crystal system of coordinates with respect to the crystallographic axes through angles of $\pm\pi/4$ measured from the [100], [010], and [001] axes. This circumstance is responsible for a number of specific features in the behavior of the magnetic, magnetoelastic, and magneto-optical properties of these compounds [2], which qualitatively differ from those of crystals with cubic symmetry of the environment of the magnetic ions. These differences most clearly manifest themselves in orientation dependences of the magnetostriction and the magnetic linear birefringence of rare-earth gallium garnets and aluminum garnets in strong magnetic fields [2, 3].

In the garnet structure, the low symmetry of the crystal environment of the rare-earth non-Kramers ion Tb^{3+} leads to total removal of the degeneracy of the energy levels. The low-energy part of the electronic spectrum of the Tb^{3+} ion consists of quasi-doublets: the ground state corresponds to a quasi-doublet with a gap of 2.5 cm^{-1}, the first excited quasi-doublet is located 34 cm^{-1} above the ground state, and the third excited quasi-doublet lies 43 cm^{-1} above the ground state [4]. The exchange interaction between rare-earth ions in gallium garnets is very weak (for the terbium gallium garnet, the Néel temperature T_N = 0.25 K [5]); therefore, this interaction can be disregarded when analyzing the behavior of these compounds in strong magnetic fields.

At present, there exist several sets of parameters of the crystal field acting on the Tb^{3+} ion in the gallium garnet [6, 7]. In our opinion, the most suitable set of parameters was proposed by Guillot *et al.* [6] (see table). This set of parameters allows one to describe quantitatively not only the crossing of the low-lying energy levels in the spectrum of the Tb^{3+} ion, which is experimentally observed in the $Tb_3Ga_5O_{12}$ compound in a magnetic field aligned parallel to the ⟨110⟩ direction, but also the magnetization curves [6] and the curves of the Faraday effect along this direction in magnetic fields up to 75 T [8].

Parameters of the crystal field in the terbium gallium garnet [6] (in cm^{-1})

B_{20}	B_{22}	B_{40}	B_{42}	B_{44}	B_{60}	B_{62}	B_{64}	B_{66}
–81	169	–2163	249	945	677	–155	1045	–4

It should be noted that superstrong magnetic fields, which are of particular interest to experimenters, can be generated only in a pulsed mode. These measurements are conducted under adiabatic conditions, which results in a strong magnetocaloric effect. The purpose of this study is to reveal the specific features in the behavior of the magnetocaloric and magneto-optical properties of the $Tb_3Ga_5O_{12}$ compound in strong magnetic fields when the magnetic field **B** is oriented along the [111] and [100] axes. In order to accomplish this, it is necessary to know the electronic structure of Tb^{3+} ions, which is formed both under the action of the ion environment described by the Hamiltonian of the crystal field and in response to a magnetic field. The actual Hamiltonian of the formulated problem can be represented in the following form:

$$H = H_{cr} + H_z, \quad (1)$$

1063-7834/04/4612-2229$26.00

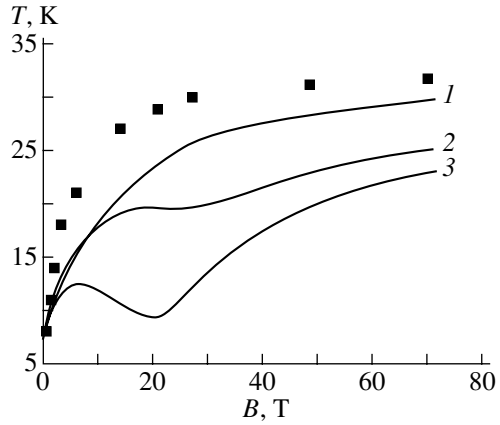

Fig. 1. Dependences of the temperature of the $Tb_3Ga_5O_{12}$ sample on the magnetic field at $T_0 = 6$ K. Points are the experimental values at $\mathbf{B} \parallel \langle 110 \rangle$ [8]. Solid lines are the theoretical dependences $T(B)$ calculated for the Debye temperature $\Theta_D = 500$ K: (*1*) $\mathbf{B} \parallel \langle 110 \rangle$, (*2*) $\mathbf{B} \parallel \langle 111 \rangle$, and (*3*) $\mathbf{B} \parallel \langle 001 \rangle$.

where

$$H_{cr} = \sum_{kqi} B_{kq}(C_q^k(i) + C_{-q}^k(i)), \quad (2)$$

C_q^k are the irreducible tensor operators [9] ($k = 2, 4, 6$; $q \le k$), and summation with respect to i is taken over all $4f$ electrons of the Tb^{3+} ion. In relationship (1), the term H_z is the Hamiltonian of the interaction between the Tb^{3+} ion and the magnetic field:

$$H_z = \mu_B(\mathbf{L} + 2\mathbf{S})\mathbf{B}. \quad (3)$$

In our calculations, we used a set of parameters of the crystal field proposed by Guillot *et al.* [6] (see table).

According to the above scheme, we calculated the energy levels E_n and determined the eigenfunctions for Tb^{3+} ions over a wide range of magnetic fields oriented along the [111] and [100] axes. In these calculations, we took into account the nonequivalent positions occupied by the Tb^{3+} ions in the crystal structure of the terbium gallium garnet.

2. THE MAGNETOCALORIC EFFECT

The change in the temperature due to adiabatic magnetization can be calculated by solving the adiabatic equation

$$S_M(T_0, 0) + S_P(T_0) = S_M(T, B) + S_P(T). \quad (4)$$

Here, $S_P = \int_0^T \frac{C_V dT}{T}$ is the phonon contribution to the entropy and C_V is the molar heat capacity, which, at low temperatures, can be approximately determined as

$$C_V = \frac{12}{5} R\pi^4 n (T/\Theta_D)^3, \quad (5)$$

where $n = 20$ is the number of atoms in the $Tb_3Ga_5O_{12}$ molecule, R is the universal gas constant, and Θ_D is the Debye temperature. The exact value of the Debye temperature for the $Tb_3Ga_5O_{12}$ compound is unknown. However, by comparing the available data on the Debye temperature for aluminum garnets [10], we estimated its value as $\Theta_D \approx 500$ K [8]. In expression (4), we have

$$S_M = -\frac{R}{2} \sum_{m=1}^{6} \sum_n \left(\exp\left(-\frac{E_n(m)}{T}\right) Z_m^{-1} \right) \times \ln\left(\exp\left(-\frac{E_n(m)}{T}\right) Z_m^{-1} \right), \quad (6)$$

where

$$Z_m = \sum_n \exp\left(-\frac{E_n(m)}{T}\right)$$

is the magnetic contribution [averaged over nonequivalent positions (index m)] to the entropy. The solution of Eq. (4) determines the magnetocaloric effect.

Figure 1 shows the dependences $T(B)$ thus calculated for $\mathbf{B} \parallel \langle 110 \rangle$, $\mathbf{B} \parallel \langle 111 \rangle$, and $\mathbf{B} \parallel \langle 001 \rangle$ at temperature $T_0 = 6$ K and Debye temperature $\Theta_D = 500$ K. It is worth noting that, for the $Tb_3Ga_5O_{12}$ compound in strong magnetic fields, the magnetocaloric effect is characterized by strong anisotropy.

3. THE FARADAY EFFECT

The angle of rotation of the plane of light polarization in the $Tb_3Ga_5O_{12}$ compound contains two contributions:

$$\alpha_F = \alpha(\mathrm{Tb}) + \alpha_D. \quad (7)$$

Here, α(Tb) is the contribution of Tb^{3+} paramagnetic ions and α_D is the contribution of the matrix formed by diamagnetic ions of gallium and oxygen. The term α_D does not depend on the temperature and is proportional to the magnetic field B up to $B \approx 10^9$ Oe:

$$\alpha_D = VB. \quad (8)$$

To a first approximation, the quantity V can be taken as the Verdet constant for yttrium gallium garnet: $V(\mathrm{YGG}) = 0.043$ min/(cm · Oe) [11].

In the visible and ultraviolet ranges, the contribution of rare-earth ions to the Faraday rotation is predominantly determined by *f–d* electric dipole transitions (except for narrow ranges in the vicinity of the reso-

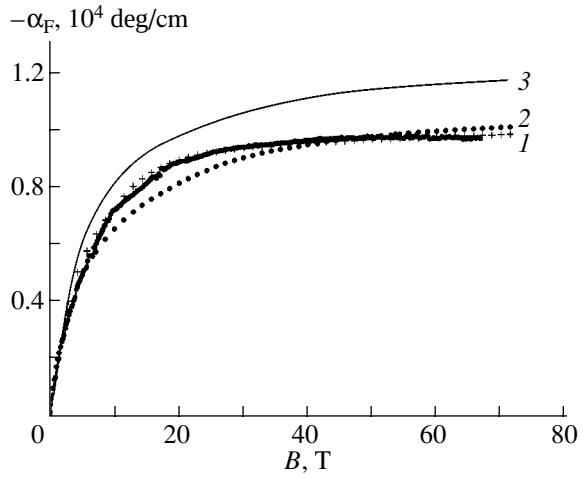

Fig. 2. Adiabatic curves for the Faraday effect at $T_0 = 6$ K according to the experimental data (**B** ∥ ⟨110⟩) taken from [8] (heavy line) and the results of calculations for (*1*) (**B** ∥ ⟨110⟩, (*2*) **B** ∥ ⟨001⟩, and (*3*) **B** ∥ ⟨111⟩.

nance frequencies of the forbidden *f–f* transitions). In the general case, the quantity α(Tb) includes three terms: the paramagnetic contribution, the mixing contribution, and the diamagnetic contribution. The diamagnetic contribution is linear with respect to the magnetic field *B*, reaches a significant value only in a narrow spectral range at resonance frequencies of the optical transitions, and can be reduced to the renormalization of the constant *V* in expression (2). According to Valiev *et al.* [12], the paramagnetic contribution and the mixing contribution can be represented as

$$\alpha(\mathrm{Tb}) = A\left(M_0 - \frac{g_{J_0}}{2 - g_{J_0}} M_{VV}\right), \qquad (9)$$

where M_0 is the magnetization related to the splitting of the levels of the $^7F_6$ fundamental multiplet, M_{VV} is the contribution to the magnetization due to the admixture of the first excited multiplet $^7F_5$ of the Tb^{3+} ion to the fundamental multiplet in the magnetic field, $g_{J_0} = 3/2$ is the Landé splitting factor of the fundamental multiplet of this ion, and *A* is a constant dependent on the frequency of incident radiation and on the oscillator strengths of the *f–d* transitions. Figure 2 presents the theoretical adiabatic curves for the Faraday effect calculated with the values of the magnetocaloric effect determined from the solution of Eq. (8) (Fig. 1) for the orientations **B** ∥ ⟨110⟩, **B** ∥ ⟨111⟩, and **B** ∥ ⟨001⟩ at $T_0 = 6$ K. This figure also shows the experimental dependence $\alpha_F(B)$ for **B** ∥ ⟨110⟩ and $T_0 = 6$ K [8]. It should be noted that the Faraday effect for the $Tb_3Ga_5O_{12}$ compound in strong magnetic fields is also characterized by a considerable anisotropy, even though it is substantially weaker than the anisotropy observed in the case of the magnetocaloric effect.

4. CONCLUSIONS

Thus, it has been shown that, for $Tb_3Ga_5O_{12}$ cubic crystals in strong magnetic fields, the Faraday rotation and the magnetocaloric effect exhibit considerable anisotropy, which disappears in weak magnetic fields.

ACKNOWLEDGMENTS

This work was supported by the Russian Foundation for Basic Research (project no. 03-02-17166) and the Foundation for Basic Research in the Field of Natural Sciences, Russian Ministry of Education (project no. E02-3.4-116).

REFERENCES

1. S. Krupička, *Physik der Ferrite und der Verwandten Magnetischen Oxide* (Academia, Prague, 1973; Mir, Moscow, 1976), Vol. 2.
2. A. K. Zvezdin, V. M. Matveev, A. A. Mukhin, and A. I. Popov, *Rare-Earth Ions in Magnetically Ordered Crystals* (Nauka, Moscow, 1985), p. 296 [in Russian].
3. N. F. Vedernikov, A. K. Zvezdin, R. Z. Levitin, and A. I. Popov, Zh. Éksp. Teor. Fiz. **93** (6), 2161 (1987) [Sov. Phys. JETP **66**, 1233 (1987)]; *Neutron Diffraction Analysis of Magnets* (Atomizdat, Moscow, 1981), p. 312 [in Russian].
4. J. A. Koningstein and C. J. Kaue-Maguire, Can. J. Chem. **52**, 3445 (1974).
5. F. Harbus and H. E. Stanly, Phys. Rev. B **8** (3), 1156 (1973).
6. A. Guillot, A. Marchand, V. Nekvasil, and F. Tcheou, J. Phys. C **18**, 3547 (1985).
7. V. Nekvasil and I. Veltruski, J. Magn. Magn. Mater. **86**, 315 (1990).
8. R. Z. Levitin, A. K. Zvezdin, M. von Ortenberg, V. V. Platonov, V. I. Plis, A. I. Popov, N. Puhlmann, and O. M. Tatsenko, Fiz. Tverd. Tela (St. Petersburg) **44** (11), 2013 (2002) [Phys. Solid State **44**, 2107 (2002)].
9. B. G. Wybourne, *Spectroscopic Properties of Rare Earths* (Wiley, New York, 1965).
10. B. Nagaian, M. Pam Babu, and D. B. Sirdeshmukh, Indian J. Pure Appl. Phys. **17**, 838 (1979).
11. U. V. Valiev, A. A. Klochkov, A. I. Popov, and B. Yu. Sokolov, Opt. Spektrosk. **66**, 613 (1989) [Opt. Spectrosc. **66**, 359 (1989)].
12. U. V. Valiev, A. K. Zvezdin, G. S. Krinchik, R. Z. Levitin, K. M. Mukimov, and A. I. Popov, Zh. Éksp. Teor. Fiz. **85** (7), 311 (1983) [Sov. Phys. JETP **58**, 181 (1983)].

Translated by O. Moskalev

Physics of the Solid State, Vol. 46, No. 12, 2004, pp. 2232–2237. Translated from Fizika Tverdogo Tela, Vol. 46, No. 12, 2004, pp. 2158–2163.

MAGNETISM AND FERROELECTRICITY

Effect of Thermal Treatment on the Microstructure and Magnetic Properties of a Bulk Amorphous $Fe_{72}Al_5P_{10}Ga_2C_6B_4Si_1$ Alloy

G. E. Abrosimova*, A. S. Aronin*, Yu. P. Kabanov*, D. V. Matveev*, V. V. Molokanov, and O. G. Rybchenko***

**Institute of Solid State Physics, Russian Academy of Sciences, Chernogolovka, Moscow oblast, 142432 Russia*
e-mail: matveev@issp.ac.ru
***Baĭkov Institute of Metallurgy and Materials Sciences, Russian Academy of Sciences, Leninskiĭ pr. 49, Moscow, 117911 Russia*

Received March 17, 2004

Abstract—The structure and chemical composition of the phases that form in the controlled crystallization of a bulk amorphous $Fe_{72}Al_5P_{10}Ga_2C_6B_4Si_1$ alloy are studied by differential scanning calorimetry, transmission electron microscopy, and x-ray diffraction. It was established that, when the alloy is annealed at a temperature above the glass transition point, a nanocrystalline structure consisting of three phases arises. The magnetic properties of amorphous and nanocrystalline samples were studied with a vibrating-sample magnetometer. The coercive force and saturation magnetization of amorphous samples were found to be 1 Oe and 130 emu/g, respectively. The structure and chemical composition of the forming phases and their correlation with the magnetic properties of the samples were determined. © *2004 MAIK "Nauka/Interperiodica".*

1. INTRODUCTION

Amorphous and nanocrystalline ferromagnetic alloys possess good magnetic properties and can find broad application in various electromagnetic devices. Of particular importance in this respect are nanocrystalline materials of the FINEMET type, which were first prepared by a Japanese group [1] in 1988. These alloys feature such magnetic properties as a low coercive force (0.5–1.0 A/m) and a high saturation magnetization in excess of 1.4 T. Nanocrystalline alloys usually form during controlled crystallization of the amorphous phase, but because the initial amorphous alloys are prepared by melt ejection on a spinning substrate, both the amorphous and the nanocrystalline materials forming in subsequent crystallization are fabricated in the form of ribbons 30- to 50-μm thick. This complicates their application considerably. The 1990s were witness to the development of new bulk Fe-based ferromagnetic metallic glasses of a variety of compositions, such as Fe–(Al,Ga)–(P,C,B,Si), Fe–(Cr,Mo)–Ga–(P,C,B), and Fe–(Nb,Mo,Zr,W)–B [2–5]. These alloys were prepared by quenching a melt into a copper mould and had the form of rods 2 to 6 mm in diameter. They are soft magnetic, with a maximum saturation magnetization of 1.3 T and a coercive force of less than 5 A/m. It is known that the formation of the nanocrystalline state in amorphous, rapidly quenched alloys (e.g., Finemet, Nanoperm) increases the magnetic softness of the samples [6]. It appeared of interest to check whether such improvements could also be effected in the crystallization of bulk metallic glasses. It was therefore essential to explore the possible formation of a nanocrystalline structure in the crystallization of bulk amorphous alloys and the conditions favorable for this to occur. Bulk amorphous alloys usually have a complex chemical composition (with more than four components), which results in the simultaneous formation of several phases under heating and greatly complicates their phase analysis. The structure and chemical composition of the phases formed in crystallization and their influence on the magnetic properties of the samples have likewise been studied very poorly. The goal of the present work was to explore the possible formation of a nanocrystalline structure under controlled crystallization of a bulk amorphous $Fe_{72}Al_5P_{10}Ga_2C_6B_4Si_1$ alloy, determine the chemical composition of the phases produced in the crystallization, and investigate the correlation between the structure and magnetic properties.

2. EXPERIMENTAL TECHNIQUE

Bulk samples and thick ribbons of an amorphous $Fe_{72}Al_5P_{10}Ga_2C_6B_4Si_1$ alloy were prepared by melt quenching. The as-prepared materials had a purity of more than 99.8%. Most of the studies were conducted on ribbon-shaped samples ~0.2×2 mm^2 in cross section. The glass transition temperature T_g, the temperature of the onset of crystallization T_x, and the crystallization enthalpy ΔH of the alloy were determined by DSC using a SETARAM differential scanning calorimeter at a heating rate of 10 K/min. The samples were

annealed in a resistance furnace in vacuum at a pressure of 10^{-2} Pa. The in-plane saturation magnetization of the as-prepared and annealed samples and their coercive force were measured with a vibrating-sample magnetometer at room temperature.

The structure and phase composition of the as-prepared and annealed samples were studied by x-ray diffraction and transmission electron microscopy. X-ray diffraction measurements were conducted on a SIEMENS D-500 diffractometer with FeK_α radiation. Electron microscopic studies were performed on JEOL-100 CXII and JEOL-2010FX transmission electron microscopes with attachments for local energy-dispersive x-ray analysis. The latter technique was employed to probe the structure and chemical composition of individual crystals directly in the column of the transmission electron microscope.

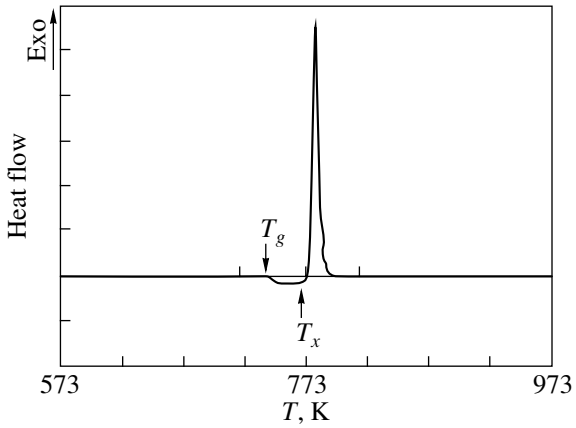

Fig. 1. DSC curve of a bulk amorphous $Fe_{72}Al_5P_{10}Ga_2C_6B_4Si_1$ alloy.

3. RESULTS

The as-prepared samples were amorphous. The DSC curve of the as-prepared alloy presented in Fig. 1 was used to derive the glass transition temperature (T_g = 748 K), the nucleation temperature (T_x = 771 K), and the enthalpy of crystallization (ΔH = 1033 J/g). The value of ΔH and the pattern of the DSC curves of the alloy are typical of crystallization of metallic glasses. The diffractogram of the as-prepared alloy contains only broad diffuse maxima characteristic of an amorphous structure.

Annealing at 723 K (i.e., below the glass transition temperature) for a long time (1000 h or longer) did not bring about crystallization of the amorphous phase.

Annealing at 783 K for 10 h, as well as longer thermal treatments, causes a nanocrystalline structure to form in the alloy. This temperature is higher than the glass transition point and lies in the region corresponding to the initial part of the maximum in the thermogram. Figure 2 displays the microstructure and an electron diffraction pattern (inset) of a sample annealed at a temperature of 783 K for 10 h. The diffraction pattern exhibits many individual reflections. The dark-field image (Fig. 2b) obtained in the reflection (specified by an arrow; see inset to Fig. 2a) reveals a multitude of crystalline precipitates with unequal axes, 30–40 nm in size.

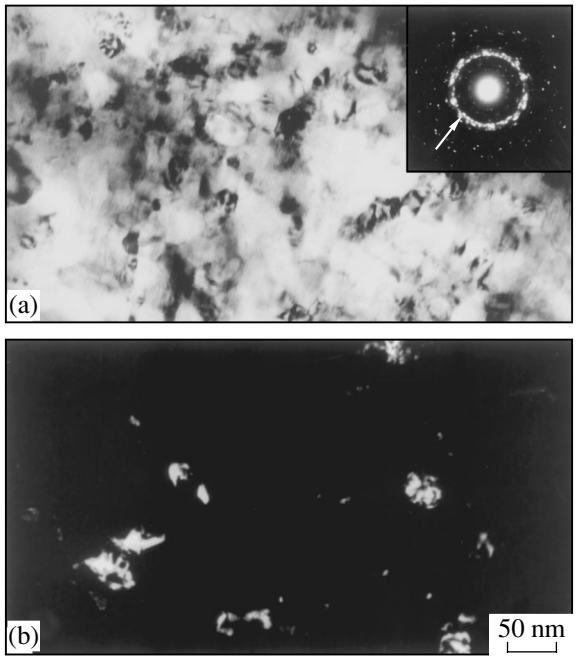

Fig. 2. Microstructure of the $Fe_{72}Al_5P_{10}Ga_2C_6B_4Si_1$ alloy annealed at 783 K for 10 h. (a) Bright-field image and (b) dark-field image.

Figure 3 presents diffraction patterns of samples of the alloy under study annealed at a temperature of 783 K for 10 and 140 h (curves *a* and *b*, respectively). The samples subjected to such anneals are completely crystallized. X-ray diffraction analysis showed them to contain three crystalline phases, two cubic and one tetragonal. The first of the cubic phases has a bcc lattice (space group *Im*3*m*) with lattice parameter a = 0.2872 nm, which corresponds to α-Fe. The second cubic phase has space group *Pm*3*m* and lattice parameter a = 0.3794 nm, which is close to the literature data for the Fe_3AlC phase [7]. The third phase can be characterized by a tetragonal lattice with space group $I\bar{4}$, which is similar to the lattice of the well-known Fe_3P phase [7] but with slightly modified parameters (a = 0.8987 nm, c = 0.4434 nm).

Local x-ray spectral analysis of the chemical composition of individual nanocrystals was performed directly in the column of the transmission electron microscope. The analysis covered a large number of nanocrystals. Figure 4 displays a transmission SEM photomicrograph of a sample annealed isothermally at 783 K for 10 h and the elemental spectrum of the sample (the analysis was carried out in transmission). The

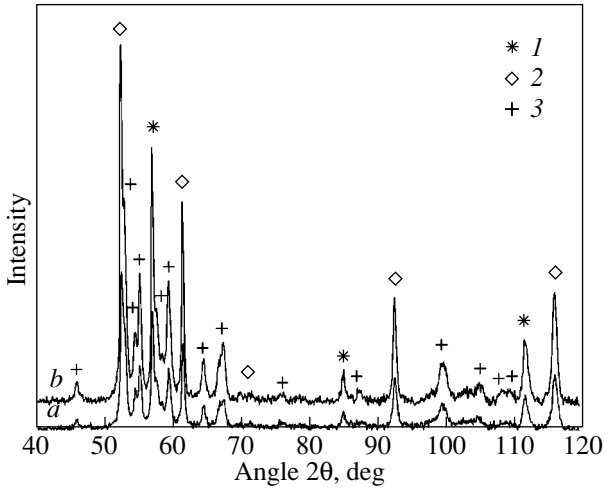

Fig. 3. Diffraction patterns of the $Fe_{72}Al_5P_{10}Ga_2C_6B_4Si_1$ alloy taken after annealing at 783 K for (*a*) 10 and (*b*) 140 h. (*1*) Lines of the bcc phase, (*2*) lines of a Fe_3P-type phase, and (*3*) lines of the Fe_3AlC phase.

structure is essentially a mixture of crystalline particles of different phases no greater than 40 nm in size. The characteristic chemical composition of different phases (without inclusion of light elements B and C), averaged over many measurements and normalized to 100%, is given in the table.

Figure 5 plots a hysteresis curve of the as-prepared (amorphous) sample obtained under application of an in-plane magnetic field. The coercive force and the saturation magnetization of the sample as derived from this curve are 1 Oe and 130 emu/g, respectively. The deviation of this curve from zero (see inset) is caused by the demagnetizing factor related to the sample shape. The values of the coercive force and saturation magnetization and the shape of the hysteresis curve are characteristic of bulk amorphous soft magnetic iron-based materials [8]. Figures 6a and 6b display the saturation magnetization and coercive force of the samples, respectively, plotted versus the time of annealing at 783 K. We readily see that, as the time of annealing is increased, H_c first grows to ~300 Oe after annealing for 20 h then subsequently decrease slowly to 225 Oe after 500 h of annealing. A further increase in the annealing time does not noticeably affect the magnitude of H_c. The saturation magnetization first decreases to 102 emu/g (t = 20 h) and then grows slowly to 113 emu/g as the annealing time is increased further.

Typical chemical composition of different phases

Grain sample	Element composition, at. %				
	Fe	Si	Al	Ga	P
1	84.5	8	6	0.5	1
2	79.5	2.5	1.5	0.5	16

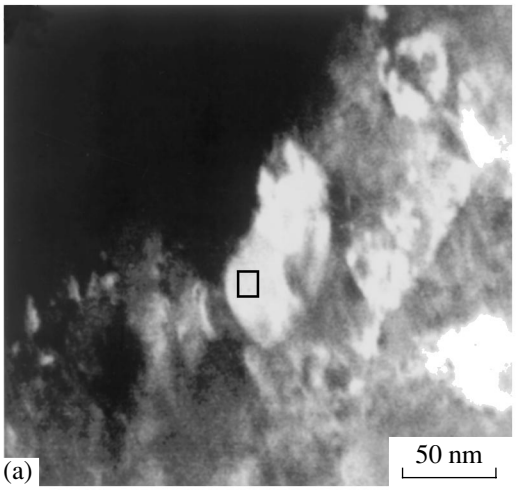

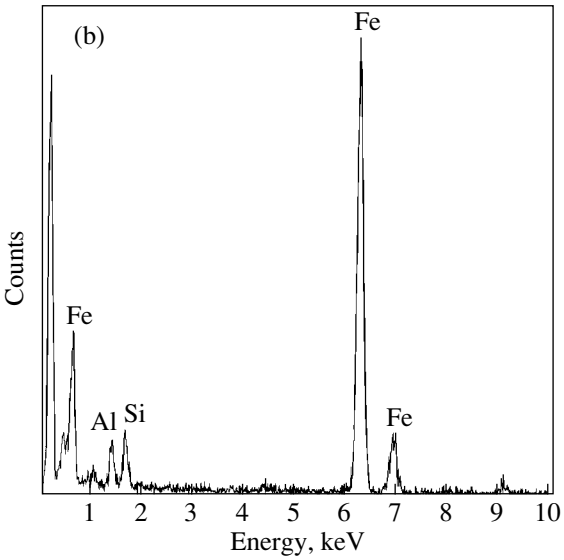

Fig. 4. (a) Photomicrograph of a sample of the $Fe_{72}Al_5P_{10}Ga_2C_6B_4Si_1$ alloy taken after thermal treatment at 783 K for 10 h and (b) the corresponding elemental spectrum (the square in the field of panel (a) identifies the point in the sample at which the analysis was made).

4. DISCUSSION OF THE RESULTS

We now consider issues concerning the formation of the nanocrystalline structure in the decomposition of the amorphous phase in the $Fe_{72}Al_5P_{10}Ga_2C_6B_4Si_1$ alloy. As already mentioned, one of the phases that precipitated in the sample crystallization is of the Fe_3P type. Diffraction analysis suggests that this phase has a tetragonal lattice, as do the phases $Fe_3B_{0.63}P_{0.37}$ with lattice parameters a = 0.8812 nm and c = 0.4375 nm [9] and $Fe_3B_{0.49}P_{0.51}$ (a = 0.888 nm, c = 0.4406 nm) [10] and the well-known tetragonal phase Fe_3P with unit cell parameters a = 0.91 nm and c = 0.4459 nm [7]. Using these data on the tetragonal phases, one can readily construct a concentration dependence of the lattice parameters for the $Fe_3B_xP_{1-x}$ crystalline phase (Fig. 7). This dependence reveals that the precipitated phase can

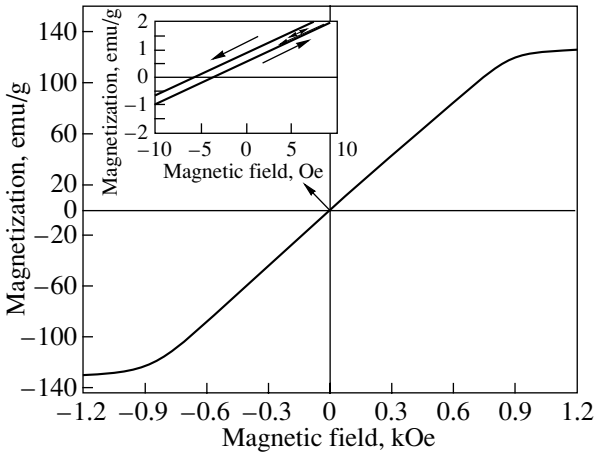

Fig. 5. Hysteresis curve of a sample of the amorphous $Fe_{72}Al_5P_{10}Ga_2C_6B_4Si_1$ alloy.

have a composition close to $Fe_3B_{0.24}P_{0.76}$, i.e., contain about 19 at. % P.

As seen from the table, grains of composition 2 have a high phosphorus content. Grains of this type also contain atoms of Al, Ga, and Si, which are larger in size than those of P. Dissolution of these components in the lattice likewise brings about an increase in the lattice parameters of the tetragonal phase, so that the content of phosphorus in the lattice should be less than 19 at. % and, thus, may correspond to composition 2. In addition to the above-mentioned elements, the lattice is obviously capable of dissolving the smaller atoms of boron and carbon, whose concentration could not be ascertained by the technique employed. It appears natural to assume, however, that composition 2 corresponds to the tetragonal phase.

Particles of composition 1 are practically free of phosphorus, but they contain a large amount of aluminum, which gives us grounds to assign this composition to the Fe_3AlC cubic phase; this phase apparently contains most of the aluminum and carbon present in the alloy. Note that the assumption this phase is present in the crystallized samples is corroborated by magnetic measurements. As seen from Fig. 6, the saturation magnetization reaches a minimum in an annealing time of 20 h. As the time of annealing is increased further, the saturation magnetization grows, whereas the phase composition does not change. It is known [11] that such a relation may be characteristic of the Fe_3AlC phase, whose thermal treatment may give rise to ordering of aluminum and carbon and to the formation of various substructures that differ in chemical composition and degree of atomic order [12]. We discuss the magnetic properties of the samples in more detail below.

The situation with the bcc phase remains unclear thus far, because its lattice parameter practically coincides with that of pure α-Fe, while an analysis of the chemical composition did not reveal nanocrystalline grains of this type. To eliminate this apparent contradiction, we carried out numerical modeling of the structure and calculated the x-ray scattering intensities from crystal phases of the assumed composition, with subsequent comparison of the calculated and experimental curves. Our analysis showed that the diffraction patterns can be identified, with a high degree of accuracy, with the above three phases, with their fractional contents after 10 h of annealing being 57% Fe_3P-type, 30% Fe_3AlC, and 13% bcc phase. Using these data and assuming most of the carbon to be bound in the Fe_3AlC phase, we come to the conclusion that the third (bcc)

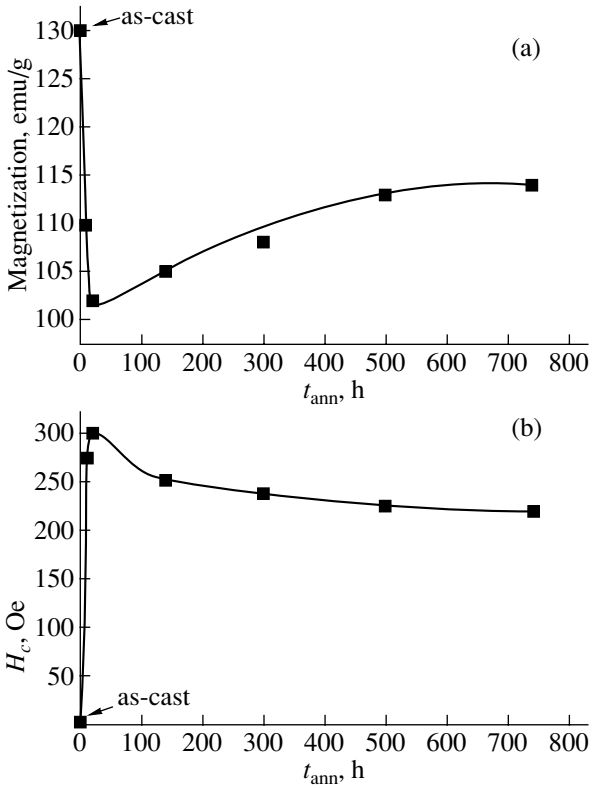

Fig. 6. (a) Saturation magnetization and (b) coercive force of samples of the $Fe_{72}Al_5P_{10}Ga_2C_6B_4Si_1$ alloy plotted vs. thermal treatment time at 783 K.

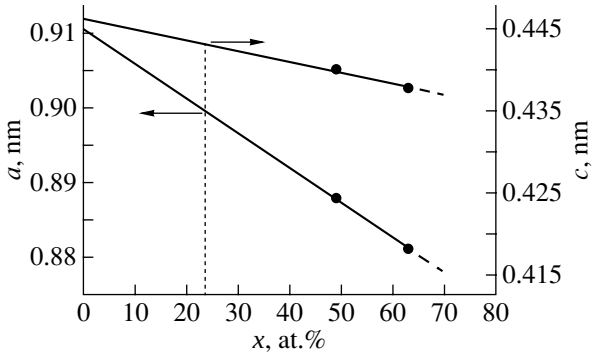

Fig. 7. Variation of the lattice parameters a and c of the $Fe_3B_xP_{1-x}$ ternary phase with B content.

phase in the $Fe_{72}Al_5P_{10}Ga_2C_6B_4Si_1$ alloy should have a composition very close to composition 1 of particles. Our estimates of the lattice parameter are consistent with the calculation; indeed, dissolution of the larger Al atoms (the atomic radius of Al is $R_{Al} = 0.143$ nm) in the phase of this composition is counterbalanced by that of smaller atoms (of the remaining alloy components), with the result that, in the final count, the lattice parameter Note that such a calculation of changes in the unit cell parameter should be considered a rough estimate only and can be used for low concentrations of the dissolved components. These estimates assumed very low dissolution of carbon in the bcc phase (or none at all), which is consistent with the Fe–C phase diagram. The concentration of the other components, in particular, of Al, Si, and Ga, falls in the limits of solubility of these elements in α-Fe (~20, 10, and 18 at. % at 500°C, respectively) [13].

No change is observed in the structure and phase composition of the samples when the duration of annealing is increased to 140 h. Annealing for 140 h brings about only a slight increase in nanocrystal size, which results in a decrease in the reflection halfwidth in the diffraction patterns.

As seen from Fig. 6a, the saturation magnetization as a function of annealing time reaches a minimum at time $t = 20$ h, after which a smooth growth is observed to set in. The saturation magnetization is known to be sensitive to variations in chemical composition, as well as to changes in the distribution of various atoms over lattice sites (in ordering alloys). Thus, the observed change in saturation magnetization could be associated with phase transformations occurring in the sample during the isothermal treatment. As already mentioned, crystallization of amorphous samples brings about the formation of three phases, namely, a solid solution of the alloy components in α-Fe, an Fe_3AlC phase, and an Fe_3P-type phase, and increasing the anneal time does not entail any change in the sample phase composition. One may therefore suggest that this behavior of the saturation magnetization is caused by variations in the magnetic characteristics of one of the crystalline phases during prolonged annealing. At room temperature (at which all magnetic measurements were carried out), the α-Fe and Fe_3P phases are ferromagnetic and there are no indications of any changes in their magnetic characteristics with the duration of high-temperature annealing. However, it is known that, by properly varying the conditions of thermal treatment and/or the concentration of an alloying addition in Fe–Al–C alloys, one can obtain an ordered carbide phase (or a *K* phase, with an Fe_3AlC stoichiometric composition) in three different states whose substructures differ in chemical composition and degree of atomic order. These compositions are identified with three Curie temperatures: $\theta_1 = 173$ K, $\theta_2 = 273$ K, and $\theta_3 = 513$ K [11, 12]. The existence of three Curie temperatures is explained as being due to the Fe atoms in the *K* phase residing in three states with different nearest neighbor atomic environments. The highest Curie temperature corresponds to the *K*-phase volume fraction most ordered in aluminum and carbon; it was revealed that such ordering sets in gradually during high-temperature treatment. Thus, it may be conjectured that in our case the growth of the saturation magnetization with increasing annealing time brings about a gradual transformation of the Fe_3AlC carbide phase from the paramagnetic to ferromagnetic state.

In any ferromagnet, one can discriminate several independent factors acting on the coercive force. If a material contains domains, there are factors that interfere with the irreversible displacement of domain boundaries (particles, dislocations, grain boundaries, platelet inclusions, and surface tension, which appears at the boundary of growing domains). It has been established, however, that magnetization switching occurring in the formation of a nanocrystalline structure in $Fe_{72}Al_5P_{10}Ga_2C_6B_4Si_1$ samples proceeds through incoherent rotation of the magnetization vectors [14]. The magnetization-switching regions are ~1–4 μm in size, which means that a domain contains numerous grains no greater than 50 nm in size. Thus, the coercive force in this case is the magnetic field that has to be applied to the sample to switch the magnetic moments of the magnetization-switching regions and can be written as [15]

$$H_c \sim aK_1/I_s, \tag{1}$$

where K_1 is the magnetocrystalline anisotropy constant, I_s is the saturation magnetization, and a is a numerical factor depending on the natural crystallographic magnetic anisotropy ($a \approx 1$). Hence, an increase in I_s should cause a decrease in the coercive force, and vice versa.

As pointed out earlier, the dependence of I_s on annealing time may be attributed to the phase transformations occurring in the sample during prolonged exposure to elevated temperatures. Earlier, we established that magnetization switching in a sample occurs through incoherent rotation of the magnetic field vectors; therefore, the quantities $H_c(t)$ and $I_s(t)$ should follow inverse courses, exactly what is seen in our case. The saturation magnetization reaches a minimum and the coercive force passes through a maximum at an annealing time $t = 20$ h. As the annealing time is increased even further, the value of I_s grows steadily and H_s decreases (Fig. 6).

5. CONCLUSIONS

We have studied the magnetic properties of a bulk amorphous $Fe_{72}Al_5P_{10}Ga_2C_6B_4Si_1$ alloy, their variation under heating, and the correlation between the magnetic properties and the structure formed. It was found that, when the alloy is heated, a nanocrystalline structure forms that consists of three phases, namely, a Fe_3P-type phase (space group $I\bar{4}$) with lattice parameters $a = 0.8987$ nm and $c = 0.4434$ nm, whose composition is close to $Fe_3B_{0.24}P_{0.76}$; a bcc phase (space group

*Im*3*m*) with unit cell parameter $a = 0.2872$ nm; and a Fe_3AlC-type phase (space group *Pm*3*m*) with lattice parameter $a = 0.3794$ nm. It was found that the saturation magnetization first decreases to 102 emu/g (at $t = 20$ h) and then grows smoothly as the time of annealing is increased to 113 emu/g. This variation in the magnetic properties of the samples apparently results from the Fe_3AlC-type phase undergoing ordering in aluminum and carbon in prolonged isothermal annealings. It was revealed that, as the annealing time increases, H_c first increases to ~300 Oe after 20 h of annealing, then falls off gradually to 225 Oe after annealing for 500 h, after which a further increase in the annealing time does not affect the magnitude of H_c noticeably. It was established that the magnetization-switching mechanism involving incoherent rotation of the magnetization vectors (which was revealed earlier in [14]) correlates well with the behavior of the coercive force and saturation magnetization with time.

ACKNOWLEDGMENTS

This study was supported by the Russian Foundation for Basic Research (project no. 03-02-17227), the program of the Presidium of the RAS "Fundamental Problems in the Physics and Chemistry of Nanosized Systems and Nanomaterials," and the program of the Department of Physical Sciences of the RAS "New Materials and Structures."

REFERENCES

1. Y. Yoshizawa, S. Ogurna, and K. Yamauchi, J. Appl. Phys. **64**, 6044 (1988).
2. A. Inoue, Y. Shinohara, and G. S. Gook, Mater. Trans., JIM **36**, 1420 (1995).
3. A. Inoue, A. Murakami, T. Zhang, and A. Takeuchi, Mater. Trans., JIM **38**, 189 (1997).
4. A. Inoue, T. Zhang, and A. Takeuchi, Appl. Phys. Lett. **71**, 464 (1997).
5. T. D. Shen and R. B. Schwarz, Appl. Phys. Lett. **75**, 49 (1999).
6. Y. Yoshizawa, K. Yamauchi, T. Yamane, and H. Sugihara, J. Appl. Phys. **64**, 6047 (1988).
7. *Pearson's Handbook of Crystallographic Data for Intermetallic Phases*, Ed. by P. Villars and L. D. Calvert (American Society for Metals, Metals Park, 1986), Vol. 3, p. 3528.
8. A. Inoue, A. Takeuchi, and B. Shen, Mater. Trans., JIM **42**, 970 (2001).
9. J. L. Walter, S. F. Bartram, and R. Russell, Metall. Trans. A **9** (6), 803 (1978).
10. G. E. Abrosimova, A. S. Aronin, and L. P. Varopaeva, Metallofizika (Kiev) **11** (3), 102 (1989).
11. V. A. Andryushchenko, A. G. Drachinskaya, T. V. Efimova, E. I. Nikolaĭchuk, and V. V. Polotnyuk, Metallofiz. Noveĭshie Tekhnol. **17** (5), 26 (1995).
12. V. A. Andryushchenko, A. G. Drachinskaya, T. V. Efimova, S. V. Levantovich, E. I. Nikolaĭchuk, and V. V. Polotnyuk, Ukr. Fiz. Zh. **37** (7), 1057 (1992).
13. O. Kubaschewski, *Iron-Binary Phase Diagrams* (Springer, Berlin, 1982; Metallurgiya, Moscow, 1985).
14. G. E. Abrosimova, A. S. Aronin, Yu. P. Kabanov, D. V. Matveev, and V. V. Molokanov, Fiz. Tverd. Tela (St. Petersburg) **46** (5), 858 (2004) [Phys. Solid State **46**, 885 (2004)].
15. S. V. Vonsovskiĭ and Ya. S. Shur, *Ferromagnetism* (GITTL, Moscow, 1948) [in Russian].

Translated by G. Skrebtsov

Physics of the Solid State, Vol. 46, No. 12, 2004, pp. 2238–2248. Translated from Fizika Tverdogo Tela, Vol. 46, No. 12, 2004, pp. 2164–2174.

MAGNETISM AND FERROELECTRICITY

Microwave EPR Spectroscopy of Cobalt-Doped Germanium Cuprate

S. V. Demishev[1, 4], A. V. Semeno[1], N. E. Sluchanko[1], N. A. Samarin[1], A. A. Pronin[1], Y. Inagaki[2], S. Okubo[2], H. Ohta[2], Y. Oshima[2], and L. I. Leonyuk[3†]

[1]Prokhorov General Physics Institute, Russian Academy of Sciences, ul. Vavilova 38, Moscow, 119991 Russia
e-mail: demis@lt.gpi.ru
[2]Molecular Photoscience Research Center, Kobe University, Kobe, 657-8501 Japan
[3]Moscow State University, Vorob'evy gory, Moscow, 119899 Russia
[4]Moscow Physicotechnical Institute, Dolgoprudnyĭ, Moscow oblast, Russia

Received April 26, 2004

Abstract—Resonance magnetoabsorption spectra of $CuGeO_3$ single crystals containing 2% Co impurity have been studied in the frequency range 60–360 GHz in magnetic fields of up to 16 T and in the temperature interval 2–60 K with the magnetic field **B** aligned parallel to the **a** crystallographic axis. In addition to the Cu^{2+} chain resonance, a new absorption line (unobserved previously in doped $CuGeO_3$ and deriving apparently from the Co^{2+} ions) was detected in EPR spectra. Quantitative analysis of the spectra suggests that the spin-Peierls transition occurs in about 10% Cu^{2+} chains, while the spin-Peierls state in the remaining 90% chains is completely destroyed by cobalt doping. The results obtained reveal considerable deviations from the universally accepted scenario of $CuGeO_3$ doping and are discussed within alternative theoretical models, namely, the quantum critical behavior (based on the EPR theory for quasi-one-dimensional systems) and a three-dimensional antiferromagnet with the Néel temperature lowered by disorder. © *2004 MAIK "Nauka/Interperiodica".*

1. INTRODUCTION

Since the discovery of the $CuGeO_3$ inorganic spin-Peierls compound [1], a large number of studies of the effect exerted by various impurities on the ground state of this low-dimensional magnet have been carried out. It has been found that variation of the properties of $CuGeO_3$ induced by doping with impurities, such as silicon [2, 3], zinc [4–7], magnesium [8, 9], and nickel [10–12], can be interpreted in terms of the universal T versus concentration x phase diagram, which is in qualitative agreement with the calculations performed in [13]. Among the specific features of the universal doping scenario are the coexistence of quasi-one-dimensional (1D) spin-Peierls and three-dimensional (3D) Néel state at low dopant concentrations, $x < x_c \sim 2$–4%, and a fast decrease in the temperature of transition to the spin-Peierls state, $T_{SP}(x)$, with increasing x. For $x > x_c$, the spin-Peierls state is completely suppressed, with only the transition to the antiferromagnetic phase being observed.

This result was obtained experimentally by studying both static and dynamic magnetic properties of doped $CuGeO_3$. In the coexistence region, $x < x_c$, both the electron paramagnetic resonance mode associated with the $S = 1/2$ antiferromagnetic chains and the antiferromagnetic resonance (AFMR) modes corresponding to the 3D Néel state are observed [2, 7, 9, 11]. Interestingly, the EPR spectra of doped samples did not reveal lines from the dopants in the $CuGeO_3$ matrix. Thus, the universal mechanism exhibits an important feature of, as it were, a loss of individual characteristics of a dopant, as a result of which doping brings about only a modification of the properties of the Cu^{2+} chains. Note that this behavior was observed both for the impurities substituting for germanium, for example, Si, and for the elements replacing copper (Zn, Mg, Ni). Furthermore, the doping mechanism was considered to be common for both the magnetic (Ni) [10–12] and nonmagnetic (Si, Zn, Mg) impurities [2–9].

At the same time, even the very first publications on the problem of $CuGeO_3$ doping pointed out the specific behavior of various impurities; in particular, manganese exhibited considerable deviations from the universal pattern [14]. Later studies revealed new cases of anomalous behavior that did not fit the standard scenario. For instance, Mg-doped samples demonstrated reentrance to the spin-Peierls state in the vicinity of x_c [15], an observation that apparently cannot be explained in terms of the theoretical approach proposed in [13]. It was shown in [16, 17] that doping $CuGeO_3$ with a magnetic iron impurity at a level of $x = 1\%$ suppresses both the spin-Peierls and antiferromagnetic transitions and gives rise to a quantum critical behavior. In this case, the ground state of the system for $T \leq 30$ K turns out to be Griffith's phase, which is characterized by a power-law divergence of the magnetic susceptibil-

† Deceased.

1063-7834/04/4612-2238$26.00 © 2004 MAIK "Nauka/Interperiodica"

ity of the sort $\chi(T) \propto 1/T^{0.35}$ [18, 19]. This apparently implies that, depending on the chemical nature, the same dopant concentration can be associated both with weak disorder, for which the universal scenario is valid [13], and with the strong-disorder case, in which long-range magnetic order turns out to be completely destroyed [16, 17, 20].

Because the deviations from universal behavior were found to be the strongest for Mn [14] and Fe [16, 17, 20], it appeared of interest to study the effect of various magnetic impurities on the physical properties and ground state of $CuGeO_3$. Our goal was to study cobalt-doped $CuGeO_3$ using microwave EPR ($\omega/2\pi > 60$ GHz). The choice of Co-doped samples for the study was motivated by several considerations. First, available data [21] on the influence of cobalt doping on the properties of $CuGeO_3$ show that this magnetic impurity provides a strong paramagnetic contribution to the magnetic susceptibility, against which one observes features believed [21] to be associated with the spin-Peierls transition. In these conditions, one should expect that additional lines deriving from absorption by Co atoms in the $CuGeO_3$ matrix will appear in the EPR spectra. (Recall that no signal from a dopant in $CuGeO_3$ has been observed earlier.) Second, it was of interest to compare the effect of various impurities of the iron subgroup substituting for copper in Cu^{2+} chains and having different spins: $S = 1$ (Ni^{2+}), $S = 3/2$ (Co^{2+}), and $S = 2$ (Fe^{2+}). Third, as far as we know, there is no information on EPR spectra of Co-doped $CuGeO_3$ samples in the literature.

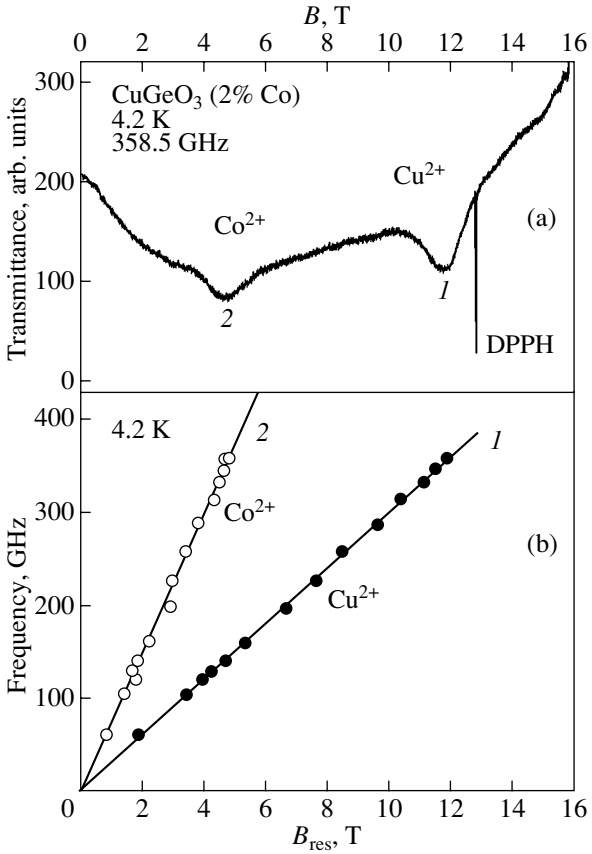

Fig. 1. (a) Transmittance spectrum and (b) dispersion curves of Co-doped $CuGeO_3$ taken at liquid-helium temperatures.

2. EXPERIMENTAL TECHNIQUES

$CuGeO_3$: Co single crystals with the desired concentration $x_{Co} = 2\%$ were prepared using a technique similar to the one employed in [21, 22]. Sample quality was checked by x-ray diffraction and Raman spectroscopy. The impurity content in a sample, as determined by chemical analysis, coincided, within experimental error, with the preset (batch) value. This fact is consistent with the data from [21], according to which the solubility limit of the Co impurity in $CuGeO_3$ at such doping levels is not reached. In addition, according to [21], the spin-Peierls transition is almost completely suppressed at $x_{Co} = 2\%$ and a strong paramagnetic contribution appears. This conclusion accounts for the choice of this composition for comprehensive study.

Resonance magnetoabsorption spectra of $CuGeO_3$: Co were studied with a cavity EPR spectrometer at a frequency $\omega/2\pi = 60$ GHz, and a quasioptical technique was employed in the range $\omega/2\pi = 100$–360 GHz. In the latter case, the transmission signal of a $CuGeO_3$: Co sample was measured as a function of magnetic field. Both in the cavity and quasi-optical experiments, measurement of the sample spectrum was paralleled by taking a reference absorption spectrum of the DPPH organic compound. EPR spectra of $CuGeO_3$: Co were obtained with a magnetic field **B** aligned with the **a** crystallographic axis.

3. EXPERIMENTAL RESULTS

3.1. EPR Spectra, g Factors, and Linewidths

An experimental resonance magnetoabsorption spectrum of $CuGeO_3$: Co consists of two broad lines which allow complete resolution at frequencies $\omega/2\pi > 100$ GHz (see the typical spectrum obtained at $T = 4.2$ K in Fig. 1a). In a first approximation, the frequencies $\omega_{1,2}$ of modes *1* and *2* were found to scale linearly with the resonance magnetic field: $\omega_{1,2} \sim B_{res}$ (Fig. 1b). This behavior indicates that both features *1* and *2* cannot be assigned to the antiferromagnetic resonance expected to appear in the standard mechanism of coexistence [13], because the $\omega(B_{res})$ dispersion curves for the AFMR modes in $CuGeO_3$ are essentially nonlinear, with $\omega(B_{res} = 0) \neq 0$ [2, 7, 11].

In addition to the spectra at various frequencies in the liquid-helium temperature region, we studied the effect of temperature on the parameters of lines *1* and *2* at a frequency of 315 GHz. As seen from Fig. 2, in the case of resonance *1*, a decrease in temperature brings

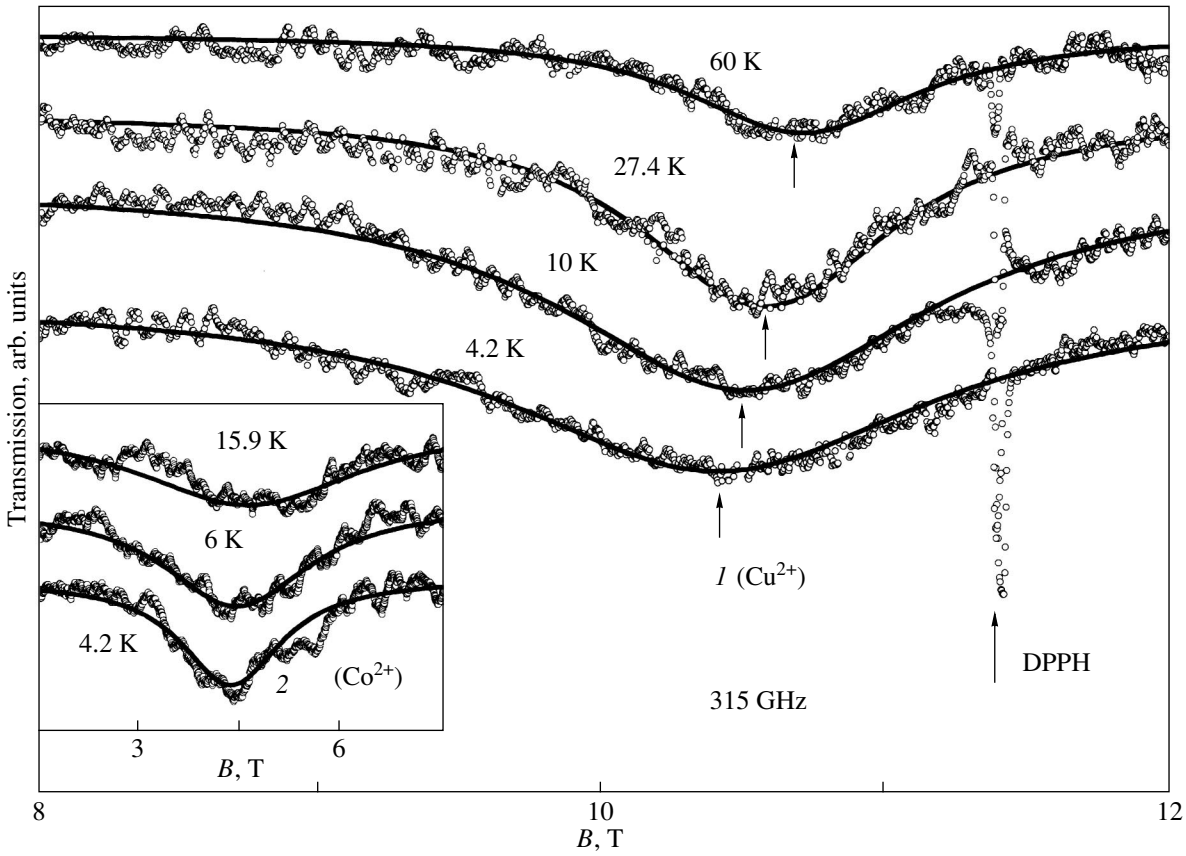

Fig. 2. Effect of temperature on resonances *1* (Cu^{2+}) and *2* (Co^{2+}). Arrows identify the position of resonance *1* for various temperatures, as well as the DPPH line. Solid lines correspond to fitting by Lorentzians (see text).

about a decrease in the resonance field and, simultaneously, a strong broadening of the absorption line. Resonance *1* retains Lorentzian shape throughout the temperature range covered. Fitting the experimental transmittance curves with a Lorentzian (solid lines in Fig. 2) permitted us to calculate the temperature dependences of the linewidth $w(T)$, resonance field $B_{res}(T)$, and integrated intensity $I(T)$ for the temperature range $2 \le T \le 60$ K.

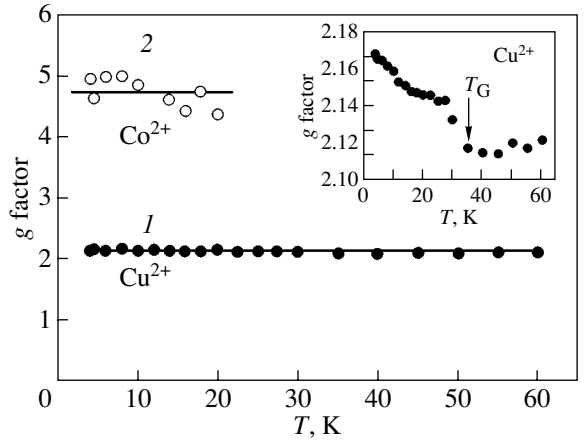

Fig. 3. *g* factors for $CuGeO_3$: Co. Inset shows, in expanded scale, the temperature dependence of the *g* factor for the Cu^{2+} chain resonance.

Resonance *2* at a frequency of 315 GHz is characterized by a smaller amplitude and, accordingly, a poorer signal-to-noise ratio (inset to Fig. 2), as a result of which the accuracy with which a line parameter can be extracted from fits with a Lorentzian model function is noticeably lower. Therefore, the $I(T)$ data for resonance *2* were derived by direct integration and $w(T)$ was subsequently estimated assuming this absorption line to be a Lorentzian. Note that, in view of the fairly large width of line *2*, the resonance field was determined in this case with too low an accuracy to allow discussion of the temperature dependence of this parameter (see inset to Fig. 2). Furthermore, line *2* was observed in the temperature range $2 \le T \le 20$ K, which is substantially smaller than that for resonance *1*.

In view of the EPR-like behavior of $\omega_{1,2} \sim B_{res}$, it appears reasonable, for proper assignment of the resonances, to consider the corresponding *g* factors (Fig. 3). We readily see that the *g* factor for resonance *1* is close to the value $g \approx 2.15$ characteristic of the EPR signal of Cu^{2+} chains in the **B** || **a** geometry [2]. Another argu-

ment in support of this assignment is the Lorentzian shape of the line, which is typical of the Cu^{2+} chain EPR in $CuGeO_3$ [16, 17, 23, 24].

The observed value of the *g* factor for resonance *2* turns out to be $g \approx 4.7 \pm 0.2$, which is approximately twice that of resonance *1* (Fig. 3). It is known that the cobalt impurity substitutes for copper in $CuGeO_3$ [21] and that, for certain crystal field symmetries, the Co^{2+} ion may possess a large *g* factor, up to $g \approx 4.3$ [25]. Thus, the resonance magnetoabsorption feature under study may be assumed to be due to EPR of Co^{2+} dopant ions in the $CuGeO_3$ matrix. In this case, the increase in the *g* factor from $g \approx 4.3$ to 4.7 may be attributed to either the crystal field splitting or the presence of strong effective coupling in spin clusters in doped germanium cuprate [11]. In Section 4, we discuss other possible assignments for resonance *2*.

Thus, the frequency and temperature dependences of the parameters characterizing the absorption lines of $CuGeO_3$: Co allow us to propose that the experimental spectra (Figs. 1, 2) originate from the Cu^{2+} chain EPR (mode *1*) and EPR of Co^{2+} impurity ions in the $CuGeO_3$ crystal structure (mode *2*).

Interestingly, the temperature dependence of the *g* factor for Cu^{2+} chains indicates the existence of a temperature region, $T \sim T_G$, where their magnetic properties undergo noticeable changes (inset to Fig. 3). For $T \geq T_G = 35$ K, the *g* factor depends only weakly on temperature, $g(T) \approx$ const, whereas in the range 30–35 K the *g* factor changes sharply. As the temperature is lowered still further in the $T < T_G$ region, the *g* factor continues to grow (see inset to Fig. 3).

The different physical natures of resonances *1* and *2* manifest themselves clearly in the temperature dependences of the linewidth $w(T)$ (Fig. 4). While the linewidth for resonance *2* (Co^{2+}) increases with temperature, in full agreement with the classical theory of spin relaxation [26], resonance *1* (Cu^{2+}) exhibits an anomalous growth of $w(T)$ with decreasing temperature in the interval $T \leq 60$ K. In the case of quasi-one-dimensional antiferromagnetic ($S = 1/2$) Cu^{2+} chains, the low-temperature broadening of the EPR line may reflect either the effect of a staggered field [24] or that the antiferromagnetic transition point is being approached [27] (the nature of this effect will be discussed in more detail in Section 4).

Thus, the experimental data presented graphically in Figs. 1–4 indicate that 2% Co doping of $CuGeO_3$ gives rise to the appearance of an absorption line, which is possibly associated with EPR of Co^{2+} ions in the $CuGeO_3$ matrix. The Co impurity also modifies the properties of the Cu^{2+} chains, which becomes manifest in an anomalous temperature dependence of the linewidth (in pure $CuGeO_3$, the EPR linewidth decreases with decreasing temperature [2, 7, 23]).

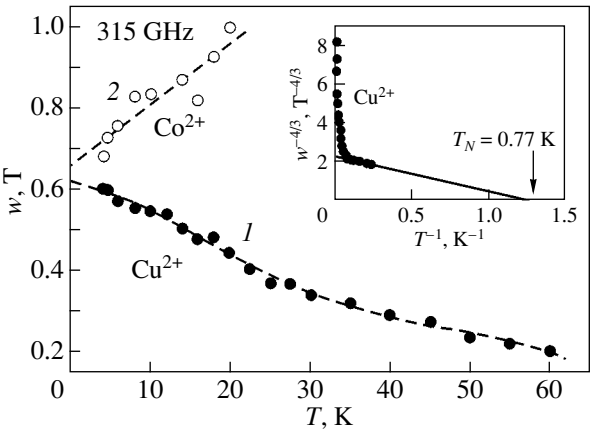

Fig. 4. Temperature dependence of the resonance linewidth for $CuGeO_3$: Co. Inset shows an analysis of the linewidth in terms of the three-dimensional antiferromagnet model (see text).

3.2. Temperature and Field Dependences of Integrated Intensity and Magnetization

Because resonance microwave absorption spectra of $CuGeO_3$: Co derive apparently from two EPR modes, it appeared of interest to analyze the temperature and frequency (field) dependences of integrated intensity. However, since the experiments were performed at frequencies high enough to separate the various spectral components, the fact that the integrated intensity may cease to be proportional to the magnetic susceptibility, $I(T) \sim \chi(T)$, had to be taken into account [25, 26]. For arbitrary values of the frequency and resonance magnetic field B_{res}, the integrated intensity can be cast in the form [17]

$$I(T) \sim \omega \frac{M(T, B_{res})}{B_{res}}, \quad (1)$$

where $M(T, B_{res})$ is the magnetization associated with the EPR mode $\omega(B_{res})$. In quasi-optical experiments performed in the millimeter- and submillimeter-wavelength ranges, one may conveniently use normalization to the DPPH line parameters:

$$\frac{I_{1,2}}{I_0} = \frac{M_{1,2}(T, B_{res}^{1,2})}{M_0(T, B_{res}^0)} \frac{B_{res}^0(\omega)}{B_{res}^{1,2}(\omega)}, \quad (2)$$

where indices *1*, *2*, and 0 label the integrated EPR line intensities for the Cu^{2+} chains, Co^{2+} ions, and DPPH, respectively. Because the DPPH magnetization can be derived with a high accuracy from independent measurements, Eq. (2) enables us to calculate the temperature and field dependences $M_1(T, B_{res})$ and $M_2(T, B_{res})$ for Cu^{2+} and Co^{2+} from the values of $I_{1,2}/I_0$, which are determined directly from experimental resonance magnetoabsorption spectra. Note that the ratio $I_{1,2}/I_0$ depends only weakly on the essentially nonmonotonic frequency response of transmission of the microwave

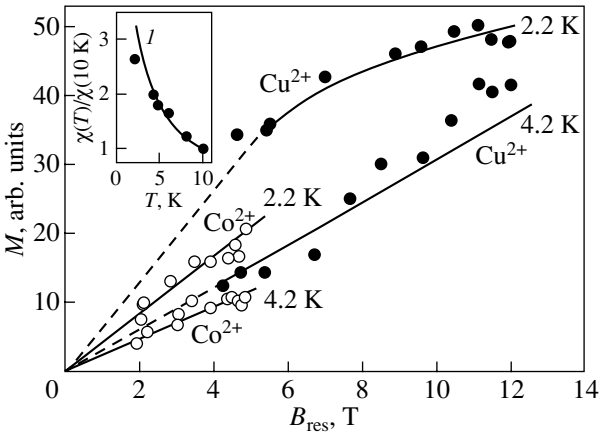

Fig. 5. Field dependences of various contributions to the $CuGeO_3$: Co magnetization derived from EPR data obtained at 4.2 and 2.2 K. Inset compares χ_{EPR} (points) with static-susceptibility data (curve *1*).

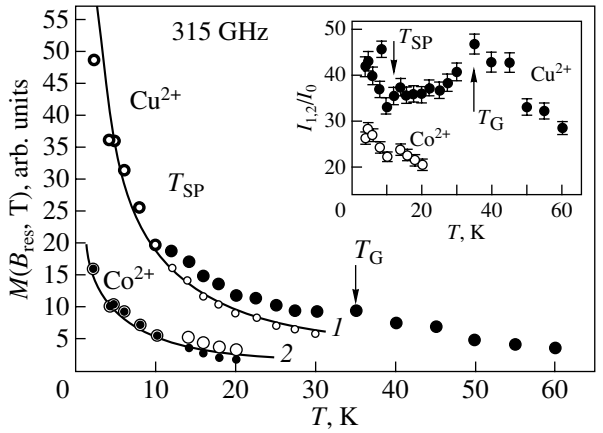

Fig. 6. Temperature dependences of various contributions to the magnetization of $CuGeO_3$: Co. Large circles relate to $M(T)$ data, and small circles are the results of subtracting the spin-Peierls contribution, $M(T)$–$M_{SP}(T)$. Inset presents the temperature dependence of integrated intensities of Cu^{2+} chain and Co^{2+} resonances normalized against the integrated DPPH resonance intensity. Curves represent theoretical relations: (*1*) Curie–Weiss law (Eq. (3)) or a power-law relation in the quantum critical behavior model (Eq. (4)) and (*2*) Curie–Weiss law (Eq. (3)).

line connecting the generator with the receiver; therefore, data treatment using Eq. (2) allows one to improve the accuracy of determination of the temperature and field dependences of magnetization from microwave EPR spectra. See [17] for a more detailed discussion of this technique.

The field dependences of different magnetization components derived from spectroscopic data are displayed in Fig. 5. For the Cu^{2+} chains, the range $T \geq 4.2$ K is seen to correspond to the linear response region, $M(B_{res}, T) \sim B_{res}$, up to $B_{res} \sim 12$ T ($\omega/2\pi \sim 360$ GHz), whereas at $T = 2.2$ K the magnetic moment is clearly seen to tend to saturate already at $B_{res} \sim 6$ T ($\omega/2\pi \sim 150$ GHz). Also, the magnetization of the Co^{2+} subsystem turns out to be a linear function of magnetic field for all the temperatures and frequencies covered (Fig. 5).

The correctness of the above procedure of separating the contributions to the total sample magnetization is illustrated in the inset to Fig. 5, where the points refer to the total spectroscopic susceptibility $\chi_{EPR} = M_1(T, B_{res1})/B_{res1} + M_2(T, B_{res2})/B_{res2}$ calculated for the frequency $\omega/2\pi = 315$ GHz and curve *1* plots the magnetic susceptibility $\chi(T)$ measured on the same sample with a vibrating-sample magnetometer. The data obtained by different methods above the liquid-helium temperature are seen to be in good agreement. For $T < 4.2$ K (for instance, $T = 2$ K in Fig. 5), the downturn of the $\chi_{EPR}(T)$ curve from $\chi(T)$ apparently reflects saturation of the Cu^{2+} chain magnetization (Fig. 5).

Thus, the sum of contributions from the EPR modes of the Cu^{2+} chains and Co^{2+} ions adequately describes the total magnetic susceptibility of the $CuGeO_3$: Co sample. The magnetic subsystem of the Co^{2+} ions determines the paramagnetic contribution to the $\chi_{Co^{2+}}(T)$ susceptibility, against which, according to [21], spin-Peierls features with $T_{SP}(x = 2\%) = 12.5$ K should be seen. If we adhere to the universal doping scenario [13], one should expect, for $T < T_{SP}(x = 2\%) = 12.5$ K, a drop in the Cu^{2+} chain magnetic susceptibility $\chi_{Cu^{2+}}$ to zero as a result of the spin gap opening. It is this behavior of $\chi_{Cu^{2+}}$ that was obtained by the procedure of subtracting the paramagnetic contribution from the total susceptibility $\chi(T) = \chi_{Cu^{2+}}(T) + \chi_{Co^{2+}}(T)$ used in [21] and permitted visualization of the spin-Peierls transition against a strong background of the paramagnetic contribution. It should be stressed that this interpretation of the magnetic data requires that the condition $\chi_{Co^{2+}}(T) \gg \chi_{Cu^{2+}}(T)$ be met.

The temperature dependences of integrated intensities and of the corresponding magnetizations associated with the Cu^{2+} chains and Co^{2+} ions are, however, at odds with the assumptions made in [21] (Fig. 6). We see immediately that the integrated intensities obtained for Cu^{2+} and Co^{2+} are comparable in magnitude, with $I_1 > I_2$ (see inset to Fig. 6). As a result, it turns out that the contribution of Cu^{2+} chains to the total sample magnetization is more than three times the impurity contribution due to the Co^{2+} ions.

Note also that the feature that was observed in the temperature dependences of the I_1/I_0 ratio and the magnetization $M_1(B_{res}, T)$ and could be assigned to the spin-Peierls transition is extremely weak. For comparison, the arrows in Fig. 6 indicate the temperature $T_{SP} = 12$ K corresponding to the peak in heat capacity recorded in

[21] for a $CuGeO_3$: Co sample with $x = 2\%$ and is probably associated with the spin-Peierls transition [21]. In the vicinity of $T_{SP} = 12$ K, the data in Fig. 6 show only a slight decrease in I_1 and M_1, which is comparable in magnitude to the measurement error, with no vanishing of the magnetic contribution due to Cu^{2+} chains for $T < T_{SP}$. Moreover, within the interval $2 < T < 30$ K, $M_1(B_{res}, T)$ grows practically monotonically (Fig. 6). As a result, the temperature dependence of magnetization of the Cu^{2+} subsystem reveals considerable deviations from the standard scenario.

Interestingly, the feature at $T = T_G = 35$ K observed on both the integrated-intensity and magnetization curves and corresponding to the onset of anomalous low-temperature growth of the g factor (Fig. 3) is much more pronounced. In the vicinity of $T_G = 35$ K, one clearly sees a maximum in the I_1/I_0 ratio (inset to Fig. 6), which can be associated with a break in the $M_1(T)$ curve for the Cu^{2+} chains (Fig. 6).

Thus, the totality of the experimental data obtained in this work suggests that there is a new characteristic temperature $T_G = 35$ K for $CuGeO_3$ containing 2% Co, at which the magnetic properties of Cu^{2+} spin chains undergo substantial changes. In the region $T < T_G$, strong suppression of the spin-Peierls features is observed, which is accompanied by a quasi-paramagnetic low-temperature growth of the magnetic moment (Fig. 6).

We should stress that, in contrast to [21], the use of microwave EPR spectroscopy permitted us not only to isolate the impurity paramagnetic component but also to accomplish model-free separation of the various contributions to the magnetic properties of $CuGeO_3$: Co without invoking any assumptions.

4. DISCUSSION OF THE RESULTS

4.1. Magnetic Properties of Cu^{2+} Chains and the Possible Quantum Critical Behavior

Consider first the temperature dependence of $M_1(T)$ for Cu^{2+} chains (Fig. 6). Obviously enough, if all Cu^{2+} chains in $CuGeO_3$: Co were to undergo the spin-Peierls transition, be it even with a strongly reduced gap in the magnetic excitation spectrum, the sample magnetization for $T < T_{SP}$ would only decrease with decreasing temperature. We believe therefore that the weak spin-Peierls anomaly at $T \sim 12$ K observed against the background of the paramagnetic contribution implies an inhomogeneous distribution of the cobalt impurity over the sample, as a result of which the spin-Peierls transition becomes completely suppressed in most of the chains, while in the smaller part a transition to a dimerized state is retained with a reduced transition temperature $T_{SP} = 12$ K. The fractional volume of chains in which the spin-Peierls transition still exists can be estimated from the amplitude of the jump in the temperature dependences of $I_1(T)$ and $M_1(T)$ and, using the data from Fig. 6, is found to be ~10%. This number of dimerized chains could prove enough to account for the heat capacity features at T_{SP} [21].

The region near the spin-Peierls transition is usually characterized, first, by a decrease in the Cu^{2+} chain EPR linewidth both for $T > T_{SP}$ and for $T < T_{SP}$ and, second, by the condition $g(T) \approx$ const [23]. Therefore, the low-temperature growth of the g factor (Fig. 3) and of the linewidth (Fig. 4) primarily reflect the characteristics of the main fraction of Cu^{2+} chains in which the spin-Peierls state is fully destroyed. Obviously enough, in these conditions, dimerization of a fraction of the chains should above all affect the temperature dependence of integrated intensity, exactly what is observed experimentally (Figs. 3, 4, 6).

To quantitatively analyze the temperature dependence of magnetization of those Cu^{2+} chains for which the spin-Peierls transition is completely suppressed, we corrected the $M_1(T)$ data in the region $T < T_G = 35$ K (Fig. 6) by subtracting the spin-Peierls part $M_{SP}(T)$[1].

The $M_1(T) - M_{SP}(T)$ dependence thus obtained was analyzed with the use of both the Curie–Weiss law

$$M(T) \sim \frac{1}{T - \Theta}, \tag{3}$$

and (taking into account the results from [16, 17]) the power-law relation corresponding to the quantum critical behavior [18, 19, 29],

$$M(T) \sim \frac{1}{T^{\alpha}}, \tag{4}$$

with the exponent $\alpha < 1$. In calculations for the Cu^{2+} chains, we considered only the linear response region, $T \geq 4.2$ K.

It was found that both Eqs. (3) and (4) permit a good fit to experimental data for the Cu^{2+} chains, with the curves corresponding to the best fits practically coinciding (curve *1* in Fig. 6). In the case of the Curie–Weiss law given by Eq. (3), the parameter Θ was estimated as $\Theta = -0.8 \pm 0.3$ K, and the best power-law fit was obtained with the exponent $\alpha = 0.93 \pm 0.3$. Thus, the temperature dependence of magnetization for the majority of Cu^{2+} chains with a completely suppressed spin-Peierls transition turns out to be fairly close to the Curie law.

[1] In subtracting the spin-Peierls contribution, we used the experimental temperature dependence of susceptibility $\chi_{SP}(T)$ found for pure $CuGeO_3$ in [23]. The $\chi_{SP}(T)$ function was redrawn in the $\chi_{SP}(T/T_{SP}^0)$ coordinates, where $T_{SP}^0 = 14$ K is the temperature of the spin-Peierls transition in pure $CuGeO_3$. The quantity $M_{SP}(T)$ was defined as $M_{SP}(T) = A\chi_{SP}(T \cdot T_{SP}/T_{SP}^0)$, and the value of the constant A was found by fitting the observed jump amplitude in the integrated intensity to magnetization at $T = T_{SP} = 12$ K (Fig. 6). Thus, we neglected the small deviation of the contribution to the $\chi_{SP}(T)$ curve from the Bonner–Fisher law [23, 28]; within the interval $2 < T < 60$ K, this deviation was less than the experimental error in determining $M(T)$.

This result seems fairly strange, because in the absence of dimerization the magnetization of a quasi-one-dimensional chain of $S = 1/2$ spins should be described by the Bonner–Fisher relation [28], according to which, in contrast to the Curie law, the magnetic susceptibility at low temperatures $T < J/k_B$ (J is the absolute value of the exchange integral in antiferromagnetic Cu^{2+} chains) decreases with decreasing temperature. Using the available values for J/k_B [30], we find that, for $CuGeO_3$, the magnetization should grow with temperature for $T < 100$ K, which is at odds with experiment (Fig. 6). Thus, observation of a $M(T)$ relation close to the Curie law may mean that doping of $CuGeO_3$ with magnetic impurities induces a transition from the quasi-one-dimensional to three-dimensional behavior of the spin chains. In this case, doped $CuGeO_3$ may be considered an anisotropic antiferromagnet obeying the Curie–Weiss law (3) with a negative constant Θ. Indeed, as shown above, the best fit to the experimental data on $M_1(T) - M_{SP}(T)$ (Fig. 6) is reached for $\Theta < 0$.

It is of interest to estimate the possible Néel temperature T_N for $CuGeO_3$: Co in terms of this assumption. From theoretical calculations [27], it follows that, as one approaches T_N in the paramagnetic region $T > T_N$, the EPR linewidth of an antiferromagnet scales as

$$w \sim \left(1 - \frac{T_N}{T}\right)^{-3/4}. \quad (5)$$

As seen from Eq. (5), the Néel temperature can be found by representing the experimental temperature dependence of $w(T)$ in the form $w^{-4/3} = f(T^{-1})$ and extrapolating the linear section to $w^{-4/3} = 0$. It can be seen from the inset to Fig. 4 that, for $T \leq 12$ K, the $w^{-4/3} = f(T^{-1})$ curve does indeed have a linear section corresponding to $T_N \approx 0.77$ K. This value is substantially smaller than the Néel temperatures characteristic of the universal T–x phase diagram of $CuGeO_3$. Indeed, according to [2–12], the Néel temperature should be $T_N \sim 2$–4 K at a concentration of 2%.

Interestingly, the above explanation of the "Curie-like" $M(T)$ behavior of the Cu^{2+} chains is not the only one possible. Let us assume that, despite the doping, $CuGeO_3$: Co retains the quasi-one-dimensional character of its magnetic subsystem. Viewed from the theoretical standpoint [31], the susceptibility of a one-dimensional spin chain with nonmagnetic defects should follow, in the absence of dimerization, the Curie law provided the condition $T \ll 4cJ/k_B$ is met, where c is the relative defect concentration in a chain. Assuming that $c \sim x \sim 0.02$ and $J/k_B \sim 100$ K [30] for an estimate, we come to the condition $T \ll 8$ K for the case under consideration, whereas the relation close to the Curie law is experimentally observed starting from $T \sim 30$ K (Fig. 6). Therefore, for $CuGeO_3$, it is the magnetic dopants that account for the totality of the features in its physical properties, including the anomalous temperature dependence of the Cu^{2+} chain magnetization.

In the quasi-one-dimensional case, the data obtained for $CuGeO_3$: Co (Figs. 1–6) also allow interpretation in terms of the disorder-induced quantum critical behavior [16–20, 29]. Let us consider the case where disorder in the magnetic subsystem (associated, for instance, with doping) is strong enough to bring about a substantial decrease in the temperature of transition to a magnetically ordered state, $T^*(x)$, or even completely suppress the magnetic order ($T^* = 0$). Then, within a certain temperature region $T^* < T < T_G$, the magnetic subsystem will reside in Griffith's phase [18, 19], characterized by a power-law divergence of magnetization (see Eq. (4)). As already mentioned, Eq. (4), just as the Curie–Weiss law, adequately describes the growth in $M_1(T) - M_{SP}(T)$ of the Cu^{2+} chains in the low-temperature region (Fig. 6).

The observation of quantum critical behavior in $CuGeO_3$ was reported earlier in [16, 17, 20]. It was shown that doping $CuGeO_3$ with an iron magnetic impurity to a concentration $x \sim 0.01$ completely suppresses the spin-Peierls state, which is accompanied by the onset of a low-temperature power-law asymptotic behavior of magnetization, Eq. (4), with an exponent $\alpha \approx 0.35$. The transition of $CuGeO_3$: Fe to Griffith's phase was observed to occur at $T_G \sim 20$–70 K [16, 17, 20]. Interestingly, unlike $CuGeO_3$: Co, the EPR spectra of $CuGeO_3$: Fe were observed to consist of only the Cu^{2+} chain line.

Comparison of the results reported in [16, 17, 20] with our present data shows, first, that the parameter α in the quantum critical behavior model, rather than being universal, depends on the random-field characteristics of a sample [16–20, 29]; therefore, the values of α for $CuGeO_3$ doped by different magnetic impurities may differ substantially. Hence, the exponent $\alpha = 0.93$ observed for $CuGeO_3$: Co is not in contradistinction with the model of quantum critical behavior. Second, the characteristic temperature $T_G = 35$ K found to exist for $CuGeO_3$: Co is consistent with the estimate of Griffith's temperature for $CuGeO_3$: Fe [16, 17, 20]. Thus, the quantum critical behavior model is capable not only of explaining the low-temperature features in the magnetization of Cu^{2+} chains in $CuGeO_3$ (Fig. 6) but also apparently of accounting for the features in the magnetic properties in the vicinity of T_G by relating them to a transition to Griffith's phase.

Note that the quantum critical behavior and the power-law dependence of magnetization, Eq. (4), can arise in spin systems of various dimensions characterized by various types of magnetic coupling (see [16] and references therein). Therefore, strictly speaking, the above arguments for the possible observation of the quantum critical regime in cobalt-doped $CuGeO_3$ do not provide any grounds to conclude that Cu^{2+} chains retain quasi-one-dimensional behavior in this material. Moreover, the appearance of a quantum critical region and the transition to Griffith's phase do not exclude the possibility of transition to a magnetically ordered (for

instance, antiferromagnetic) phase at still lower temperatures, a decrease in the magnetic transition temperature caused by disordering of the magnetic subsystem would be sufficient for the quantum critical behavior to set in [29].

4.2. Determination of the Effective Dimensionality of the Cu^{2+} Chains Magnetic Subsystem

As follows from the above discussion, in order to advance a consistent interpretation of the experimental data obtained in this study, one has first to determine the effective dimensionality of the magnetic subsystem of Cu^{2+} chains. The data presented in Figs. 5 and 6 are obviously insufficient for this purpose. Therefore, it appears of interest to consider the possibilities offered by the current theoretical ideas concerning the temperature dependences of the linewidth and of the g factor (Figs. 3, 4).

Oshikawa and Affleck recently proposed a new theory of EPR for one-dimensional uniform antiferromagnetic chains with spin $S = 1/2$ [24]. According to their theory, the presence of a staggered field in such a spin system induces simultaneous low-temperature growth of the EPR linewidth and of the g factor. In this case, as shown in [32], the linewidth $w(T)$ and the temperature-dependent correction to the g factor, $\Delta g(T)$, turn out to be connected through a universal relation,

$$\frac{w(T)}{\Delta g(T)} = 1.99\frac{k_B T}{\mu_B}, \qquad (6)$$

which does not depend on the amplitude of the staggered field and the exchange integral. This consequence of the theory of Oshikawa–Affleck is unique in EPR theory and is inherent precisely to the one-dimensional case [24, 32]. Therefore, comparison of experimental data and theoretical relation (6) may serve as an independent argument in determining the dimensionality of a magnetic subsystem [32].

The specific feature of the behavior predicted in [24, 32] manifests itself in a revealing way in estimating the ratio $w(T)/\Delta g(T)$ in the model of a three-dimensional antiferromagnet. In this case, the linewidth $w(T)$ in the paramagnetic region is given by Eq. (5) (see also [27]) and the variation of the g factor can be related to the difference between the local magnetic field (which acts directly on the spins) and an externally applied field, i.e., $\Delta g(T) \sim \chi(T)$ (the latter assumption is frequently invoked in interpreting EPR data on spin glasses [33]). Thus, for a three-dimensional antiferromagnet, we can write

$$\frac{w(T)}{\Delta g(T)} = A\frac{T^{3/4}(T+\Theta)}{(T-T_N)^{3/4}}, \quad T > T_N, \qquad (7)$$

where coefficient A depends on the constant of proportionality between the susceptibility and the correction to the g factor. It is seen from Eq. (7) that, in the three-dimensional case, we have $w(T)/\Delta g(T) \longrightarrow \infty$ as $T \longrightarrow T_N$, whereas for the one-dimensional case the Oshikawa–Affleck theory yields $w(T)/\Delta g(T) \longrightarrow 0$ as $T \longrightarrow 0$ (Eq. (6)).

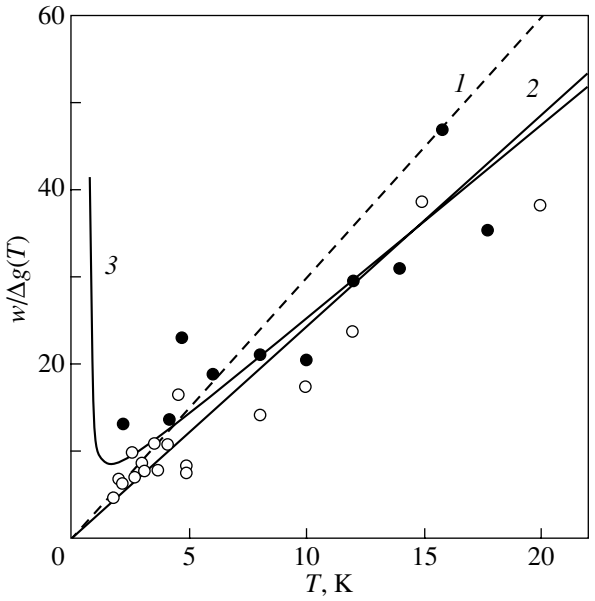

Fig. 7. $w(T)/\Delta g(T)$ function. Filled circles are experimental data for $CuGeO_3$: Co, and open circles are experimental data for $CuGeO_3$: Fe [32]. Curve *1* represents universal relation (6) from the Oshikawa–Affleck theory (one-dimensional case), curve *2* is a fit of experimental data for doped $CuGeO_3$ to a linear relation, and curve *3* is calculated in the model of a three-dimensional antiferromagnet (Eq. (7)).

As follows from the data obtained in the present study, $CuGeO_3$: Co reveals an anomalous low-temperature growth of the resonance linewidth and of the g factor for those Cu^{2+} chains for which the dimerization (disregarded by the Oshikawa–Affleck theory) is completely suppressed (see Figs. 3, 4 and discussion in Subsection 4.1). At the same time, the experimental data on $M(T)$ obtained for the Cu^{2+} chains (Fig. 6) for temperatures $T > 2$ K do not contain features characteristic of antiferromagnetic ordering [see also estimates of T_N based on the temperature dependence of the linewidth (inset to Fig. 4)]. Thus, Eqs. (6) and (7) can be used to analyze the experimental data presented in Figs. 3 and 4.

The ratio $w(T)/\Delta g(T)$ was calculated assuming that $\Delta g(T) = g(T) - g(30\ \text{K})$ (inset to Fig. 3) and taking the values of $w(T)$ for the Cu^{2+} chains from Fig. 4. The results obtained for $T < 20$ K are represented in Fig. 7 by filled circles. Because $CuGeO_3$: Fe exhibits analogous low-temperature anomalies in the temperature dependences of the linewidth and the g factor [16], one can find in the same figure the values of $w(T)/\Delta g(T)$ calculated for this material (open circles) in [32]. Note that, despite the substantial difference in the Cu^{2+} chain EPR line parameters between $CuGeO_3$: Co and

$CuGeO_3$: Fe [32], the values of $w(T)/\Delta g(T)$ for these materials practically coincide within experimental error. Moreover, the Oshikawa–Affleck theory (Eq. (6)) correctly predicts the amplitude and character of variation of the $w(T)/\Delta g(T)$ ratio with temperature for $CuGeO_3$ doped by magnetic impurities (curve *1* in Fig. 7). However, the graphs in Fig. 7 suggest that the calculation performed in [24] slightly overestimates the coefficient in Eq. (6). Fitting the experimental data with a linear relation yields $w(T)/\Delta g(T) = (1.63 \pm 0.07)k_BT/\mu_B$ (curve *2* in Fig. 7); i.e., the empirical value of the numerical factor turns out to be 20% smaller than the theoretical figure. However, taking into account, first, the accuracy and character of the approximations made in the Oshikawa–Affleck theory [24, 32] and, second, the existence of noticeable interchain exchange in $CuGeO_3$ [30], this agreement between the EPR theory for quasi-one-dimensional spin chains and experiment in the case of $CuGeO_3$ should be considered more than just satisfactory.

Because the $w(T)/\Delta g(T)$ criterion in the Oshikawa–Affleck theory does not contain any fitting parameters (Eq. (6)), the above analysis provides a convincing argument for the possibility of the Cu^{2+} spin chains in $CuGeO_3$: Co retaining their quasi-one-dimensional character under suppression of the spin-Peierls transition. At the same time, by using the values of Θ and T_N found in Subsection 4.1, as well as by considering coefficient A in Eq. (7) to be a fitting parameter, one can achieve reasonable agreement between the $w(T)/\Delta g(T)$ ratio calculated in the three-dimensional antiferromagnet model and experiment for $CuGeO_3$: Co (curve *3* in Fig. 7). We readily see from Fig. 7 that the difference between curves *1* and *2* on the one hand and curve *3* on the other will be most pronounced in the temperature region $T < 1$ K. Therefore, ultralow-temperature EPR study of $CuGeO_3$ doped by magnetic impurities is an important problem and will be considered in subsequent investigations.

4.3. EPR of Co^{2+} Ions in the $CuGeO_3$ Matrix

In the preceding subsection, we related resonance *2* observed in $CuGeO_3$: Co (Fig. 1a) to EPR absorption of the Co^{2+} impurity ions and excluded its possible assignment as an antiferromagnetic resonance mode (Subsection 3.1). Obviously enough, this feature in the resonance magnetoabsorption spectra cannot be related to a harmonic of the main Cu^{2+} chain resonance. Against this assumption argue both the frequency dependence of resonance *2* (Fig. 1b) and the fact that, in contrast to resonance *1*, the width of this line increases rather than decreasing with temperature (Fig. 4). The more exotic explanations involving, for instance, the possible appearance of a new, soliton-type excitation (the breathing mode) in the transmission spectra [24], predicted by the Oshikawa–Affleck theory, seem to be still less probable. Indeed, in this case, one should expect, first, suppression of the main Cu^{2+} chain resonance and, second, an essentially nonlinear $\omega_2(B)$ curve [24]. Neither of these predictions finds support in the experiment performed in the temperature region under study (Figs. 1, 2, 6).

However, the proposed explanation of resonance *2* as being due to a Co^{2+} EPR mode in the $CuGeO_3$ matrix appears nevertheless highly nontrivial, because no individual modes capable of modifying the properties of the Cu^{2+} chains in $CuGeO_3$ were known. It seems most likely that the formation of such features in magnetooptical spectra results from a nonuniform impurity distribution over the sample, which is apparently a characteristic feature of the $CuGeO_3$: Co system. This possibility is argued for by the analysis of $M(T)$ data performed for the Cu^{2+} chains (Fig. 6). These data suggest the existence of two types of Cu^{2+} chains, the first of which (volume fraction ~10%) exhibits the spin-Peierls transition, while the second (fractional volume ~90%) is characterized by a complete suppression of the spin-Peierls feature (see Subsection 4.1). This difference can obviously be accounted for by nonuniform doping of the spin chains in $CuGeO_3$: Co.

Because these anomalies are observed in the region of concentrations below the chemical solubility limit of the Co impurity in the $CuGeO_3$ matrix [21], it appears reasonable to relate them to the strong tendency to clusterization revealed by Co atoms. It may be conjectured that, in the regions where Co ion clusters form, the content of the cobalt impurity in Cu^{2+} chains should be lower and that the spin-Peierls transition should be retained in such chains. There are also grounds to expect that the ions located in clusters provide an independent contribution to the magnetic properties of a sample, which would manifest itself, in particular, in the form of an additional EPR line (Fig. 1). Therefore, the g-factor renormalization for Co^{2+} (Fig. 3) can be assigned either to interactions in a cluster (Subsection 3.1) or to the properties of Co clusters being affected by the surrounding Cu^{2+} chains. The validity of this interpretation is argued for, in particular, by the presence of a feature in the $I_2(T)$ and $M_2(T)$ curves near T_{SP} (Fig. 6). As a result, the nature of the Co^{2+} ion resonance in the $CuGeO_3$ matrix may prove very complex, such that deep enough insight into the various features of the characteristics of this absorption line and into the conditions of its formation could require additional theoretical studies.

As in the case of the Cu^{2+} chain resonance, we carried out a quantitative analysis of the temperature dependence of magnetization for this feature (Fig. 6). The analysis was done by subtracting the feature at $T_{SP} = 12$ K, a procedure similar to the one described above, after which the $M(T)$ data for resonance *2* were analyzed using the Curie–Weiss law, Eq. (3), and the power-law relation, Eq. (4). It was found that fitting experimental data (Fig. 6) with Eq. (4) increases the rms error of approximation by more than a factor of 1.5 as compared to the use of Eq. (3). The best fit was achieved for the Curie–Weiss law with a characteristic

temperature $\Theta = -1.8 \pm 0.5$ K (curve *2* in Fig. 6). Interestingly, the absolute value of Θ in this case noticeably exceeds the corresponding value for the Cu^{2+} chains, where Θ is approximately –0.8 K. It thus appears most likely that three-dimensional antiferromagnetic correlations in the Co^{2+} subsystem in $CuGeO_3$: Co are much more pronounced than in the Cu^{2+} chain subsystem. This finding stresses once more the difference between the physical natures of the two contributions determining the $CuGeO_3$: Co magnetism and of the related EPR features.

5. CONCLUSIONS

The results of the present studies of the resonance magnetoabsorption spectra of germanium cuprate suggest that doping of this compound with 2% cobalt gives rise to the appearance of unusual and thus far unknown features in the physical properties of doped $CuGeO_3$.

First of all, we note the formation of an EPR absorption line (resonance *2* in Figs. 1, 2) that differs markedly in terms of its characteristics from the resonance of the antiferromagnetic copper ion chains. The new feature reveals a linear dependence of frequency on magnetic field and has a g factor of ≈4.7, which is more than twice that for the Cu^{2+} chains, $g \approx 2.15$. Our analysis of the resonance shape shows a quantitative difference in the temperature dependence between the widths of the lines making up the EPR spectrum of $CuGeO_3$: Co. It is certainly nontrivial that, whereas the linewidth for resonance *2* decreases with decreasing temperature, in accordance with standard theories of spin relaxation, the Cu^{2+} chain EPR linewidth increases by three times as the temperature decreases from 60 to 4.2 K. Thus, doping with cobalt not only gives rise to the formation of a new line in the spectra but also noticeably modifies the properties of Cu^{2+} spin chains, thereby inducing anomalous low-temperature growth of the linewidth (recall that the linewidth of this resonance in $CuGeO_3$, as a rule, decreases with decreasing temperature [2, 7, 23]).

Considering the experimental results obtained in this study in terms of the universal T–x phase diagram [1–15], we have to point out that the temperature dependence of magnetization of the Cu^{2+} chains, $M_1(T)$, as calculated from the integrated intensity for the corresponding resonance (resonance *1* in Figs. 1, 2), reveals two characteristic features, namely, the already known spin-Peierls transition [21] occurring at $T_{SP} = 12$ K and a break in the $M_1(T)$ curve at $T_G = 35$ K. Note that, simultaneously with the magnetization feature, a low-temperature region of g-factor growth for the Cu^{2+} chain resonance appears in the temperature range $T < T_G$, thus providing an additional argument for the appearance of a new characteristic temperature T_G in $CuGeO_3$: Co that substantially exceeds all transition temperatures known to exist in the universal T–x phase diagram.

The analysis carried out in this work shows that, in order to explain the data obtained, one has to assume that the spin-Peierls transition occurs in about 10% of the Cu^{2+} chains, while in the remaining part of the volume (90% chains) the spin-Peierls state is completely destroyed by the cobalt doping. Such an unusual behavior can apparently be related to a spatially nonuniform dopant distribution in the sample, which gives rise to the formation of cobalt ion clusters in the germanium cuprate matrix. Consideration of the presently available theoretical approaches suggests that the formation of clusters of magnetic Co^{2+} ions is the most likely reason for the appearance of the new absorption line in the EPR spectra (Figs. 1, 2).

Analysis of magnetization data obtained on low-dimensional magnets should be performed by correctly subtracting the paramagnetic contribution of impurities, because this contribution masks the $M(T)$ dependence that is expected in theory for the quasi-one-dimensional case and is described by the Bonner–Fisher law. In this work, we have solved this problem experimentally without invoking any models or additional assumptions concerning the character of the paramagnetic background. We have shown that, under conditions of a destroyed spin-Peierls state in most of the Cu^{2+} chains, the temperature dependence of magnetization turns out to be close to the Curie law. Thus, the paramagnetic character of the susceptibility of $CuGeO_3$: Co is related not to the presence of paramagnetic impurities in a sample, as assumed earlier [21], but rather, to a considerable extent, to the intrinsic properties of doped Cu^{2+} chains.

The observed deviations from the universal doping scenario, which also include the absence of antiferromagnetic transitions in the magnetic subsystems of Cu^{2+} chains and Co^{2+} ions in the region $T > 2$ K, require that alternative theoretical approaches be sought. With this purpose in mind, we have carried out a comparative analysis of the experimental data in terms of (i) the model of the quantum critical behavior based on the EPR theory of Oshikawa–Affleck for quasi-one-dimensional systems and (ii) the model of three-dimensional antiferromagnets with the Néel temperature lowered by disorder. It has been established that both the models allow quantitative description of the experimental data for temperatures $T > 2$ K. The model of quantum critical behavior is, in our opinion, preferable to the methods proposed thus far for interpreting the experimental data, because this model convincingly explains the existence of the characteristic temperature $T_G = 35$ K by relating it to a transition to Griffith's phase. The final choice of the most adequate approach requires that EPR experiments be carried out on $CuGeO_3$: Co at ultralow temperatures, because it is in this region that the differences between the theoretical models under consideration should become manifest.

ACKNOWLEDGMENTS

This study was supported by the Russian Foundation for Basic Research (project no. 04-02-16574), INTAS (grant no. 03-51-3036), the Ministry of Education of the Russian Federation (project no. PD02-1.2-335 and the program "Integration"), and the programs of the Russian Academy of Sciences "Low-Dimensional Quantum Structures" and "Strongly Correlated Electrons in Semiconductors, Metals, Superconductors, and Magnetic Materials."

One of the authors (S.V.D.) is grateful to the Russian Science Support Foundation for the financial support and to the Venture Business Laboratory (Kobe University).

REFERENCES

1. M. Hase, I. Terasaki, and K. Uchinokura, Phys. Rev. Lett. **70** (23), 3651 (1993).
2. H. Nojiri, T. Hamamoto, Z. J. Wang, S. Mitsudo, M. Motokawa, S. Kimura, H. Ohta, A. Ogiwara, O. Fujita, and J. Akimitsu, J. Phys.: Condens. Matter **9** (6), 1331 (1997).
3. B. Grenier, J.-P. Renard, P. Veillet, C. Paulsen, R. Calemczuk, G. Dhalenne, and A. Revcolevschi, Phys. Rev. B **57** (6), 3444 (1998).
4. M. Hase, I. Terasaki, Y. Sasago, K. Uchinikura, and H. Obara, Phys. Rev. Lett. **71** (24), 4059 (1993).
5. Y. Sasago, N. Koide, K. Uchinokura, M. C. Martin, M. Hase, K. Hirota, and G. Shirane, Phys. Rev. B **54** (10), R6835 (1996).
6. K. Manabe, H. Ishimoto, N. Koide, Y. Sasago, and K. Uchinokura, Phys. Rev. B **58** (2), R575 (1998).
7. A. I. Smirnov, V. N. Glazkov, A. N. Vasil'ev, L. I. Leonyuk, S. Coad, D. McK Paol, G. Dhalenne, and A. Revcolevschi, Pis'ma Zh. Éksp. Teor. Fiz. **64** (4), 277 (1996) [JETP Lett. **64**, 305 (1996)].
8. T. Masuda, A. Fujioka, Y. Uchiyama, I. Tsukada, and K. Uchinokura, Phys. Rev. Lett. **80** (20), 4566 (1998).
9. V. N. Glazkov, A. I. Smirnov, K. Uchinokura, and T. Masuda, Phys. Rev. B **65** (6), 144427 (2002).
10. S. Coad, J.-G. Lussier, D. F. McMorrow, and D. McK Paul, J. Phys.: Condens. Matter **8** (3), 6251 (1996).
11. V. N. Glazkov, A. I. Smirnov, O. A. Petrenko, D. McK Paul, A. G. Vetkin, and R. M. Eremina, J. Phys.: Condens. Matter **10** (4), 7879 (1998).
12. P. E. Anderson, J. Z. Liu, and R. N. Shelton, Phys. Rev. B **57** (18), 11492 (1998).
13. M. Mostovoy, D. Khomskii, and J. Knoester, Phys. Rev. B **58** (13), 8190 (1998).
14. S. B. Oseroff, S.-W. Cheong, B. Aktas, M. F. Hundley, Z. Fisk, and L. W. Rupp, Phys. Rev. Lett. **74** (8), 1450 (1995).
15. V. Kiryukhin, Y. J. Wang, S. C. LaMarra, R. J. Birgeneau, T. Masuda, I. Tsukada, and K. Uchinokura, Phys. Rev. B **61** (14), 9527 (2000).
16. S. V. Demishev, R. V. Bunting, L. I. Leonyuk, E. D. Obraztsova, A. A. Pronin, N. E. Sluchanko, N. A. Samarin, and S. V. Terekhov, Pis'ma Zh. Éksp. Teor. Fiz. **73** (1), 36 (2001) [JETP Lett. **73**, 31 (2001)].
17. S. V. Demishev, R. V. Bunting, H. Ohta, S. Okubo, Y. Oshima, and N. E. Sluchanko, in *EPR in 21st Century*, Ed. by A. Kawarmori, J. Yamauchi, and H. Ohta (Elsevier, Amsterdam, 2002), Vol. 5, p. 741.
18. R. B. Griffiths, Phys. Rev. Lett. **23** (1), 17 (1969).
19. D. S. Fisher, Phys. Rev. Lett. **69** (3), 534 (1992); Phys. Rev. B **50** (6), 3799 (1994); Phys. Rev. B **51** (10), 6411 (1995).
20. S. V. Demishev, R. V. Bunting, A. A. Pronin, N. E. Sluchanko, N. A. Samarin, H. Ohta, S. Okubo, Y. Oshima, L. I. Leonyuk, and M. M. Markina, cond-mat/0110177.
21. P. E. Anderson, J. Z. Liu, and R. N. Shelton, Phys. Rev. B **56** (17), 11014 (1997).
22. S. V. Demishev, L. Weckhuysen, J. Vanacken, L. Trappeniers, F. Herlach, Y. Bruynseraede, V. V. Moshchalkov, A. A. Pronin, N. E. Sluchanko, N. A. Samarin, J. Meersschaut, and L. I. Leonyuk, Phys. Rev. B **58** (10), 6321 (1998).
23. S. V. Demishev, A. V. Semeno, N. E. Sluchanko, N. A. Samarin, A. N. Vasil'ev, and L. I. Leonyuk, Zh. Éksp. Teor. Fiz. **112** (5), 1727 (1997) [JETP **85**, 943 (1997)].
24. M. Oshikawa and I. Affleck, Phys. Rev. Lett. **82** (25), 5136 (1999); cond-mat/0108424.
25. W. Low, in *Solid State Physics* (Academic, New York, 1960), Suppl. 2 [*Paramagnetic Resonance in Solids* (Inostrannaya Literatura, Moscow, 1962), p. 115].
26. A. Abragam and B. Bleaney, *Electron Paramagnetic Resonance of Transition Ions* (Clarendon, Oxford, 1970; Mir, Moscow, 1972), Vol. 1.
27. H. Mori and K. Kawasaki, Prog. Theor. Phys. **28** (6), 971 (1962).
28. J. C. Bonner and M. E. Fisher, Phys. Rev. A **135** (3), A640 (1964).
29. A. J. Bray, Phys. Rev. Lett. **59** (5), 586 (1987).
30. L. P. Regnault, M. Ain, B. Hennion, G. Dhalenne, and A. Revcolevschi, Phys. Rev. B **53** (9), 5579 (1996).
31. L. N. Bulaevskiĭ, Fiz. Tverd. Tela (Leningrad) **11** (5), 1132 (1969) [Sov. Phys. Solid State **11**, 921 (1969)].
32. S. V. Demishev, Y. Inagaki, H. Ohta, S. Okubo, Y. Oshima, A. A. Pronin, N. A. Samarin, A. V. Semeno, and N. E. Sluchanko, Europhys. Lett. **63** (3), 446 (2003).
33. M. Zomack, K. Baberschke, and S. E. Barnes, Phys. Rev. B **27** (7), 4135 (1983).

Translated by G. Skrebtsov

Physics of the Solid State, Vol. 46, No. 12, 2004, pp. 2249–2257. Translated from Fizika Tverdogo Tela, Vol. 46, No. 12, 2004, pp. 2175–2183.

MAGNETISM AND FERROELECTRICITY

Jahn–Teller Transitions in YbXO$_4$ (X = V, P) Stimulated by a Strong Magnetic Field

Z. A. Kazei

Moscow State University, Vorob'evy gory, Moscow, 119899 Russia

e-mail: kazei@plms.phys.msu.su

Received January 27, 2004; in final form, April 27, 2004

Abstract—The effect of an external magnetic field directed along various symmetry axes of a crystal on Jahn–Teller-type structural phase transitions (quadrupole ordering) is studied in $YbPO_4$ and $YbVO_4$ crystals with zircon structure. In the absence of a magnetic field, the crystals are in a precritical state and do not exhibit a spontaneous quadrupole ordering. It is shown that, in a field $\mathbf{H} \parallel [110]$, the strain susceptibility χ_γ increases with the field and, at a sufficiently high field strength, an orthorhombic lattice deformation along the [100] axis arises in the crystals under study; i.e., a stimulated Jahn–Teller phase transition of γ symmetry occurs. Using interaction constants determined from independent experiments, we calculated phase diagrams and anomalies in the magnetic and magnetoelastic properties of the $YbPO_4$ and $YbVO_4$ crystals near the stimulated phase transitions, investigated the effect of various pairwise interactions on them, and analyzed possible experimental observations of the predicted effects. © *2004 MAIK "Nauka/Interperiodica".*

1. INTRODUCTION

The occurrence (or the absence) of the cooperative Jahn–Teller (JT) effect (quadrupole ordering) in various compounds is well known to be determined by the electronic structure of the rare-earth (RE) ion and the values of the quadrupole coupling constants. The splitting in the crystal field determines the presence of degenerate or quasi-degenerate levels with high quadrupole moments in the electronic spectrum, which are necessary for quadrupole ordering to occur. The total quadrupole constants G^μ are characteristics of the structure and vary in proportion to the Stevens parameter α_J^2 throughout the RE series if the main contribution to these constants comes from the single-ion magnetoelastic interaction (as is the case for the RE-zircon family) [1].

Systems with significant magnetoelastic interactions that do not exhibit spontaneous quadrupole phase transitions are of great interest. The systems in question are in a precritical state; i.e., the energy gap between the ground state without quadrupole moments and excited quadrupole-active levels is larger than the effect of quadrupole interactions. In such a system, quadrupole ordering can be induced by external stresses that drive the system close to the critical state [2, 3]. The conditions necessary for the phase transition to occur can be achieved only via significant changes in the electronic structure of the RE ion (e.g., a decrease in the energy gap), because the quadrupole interactions cannot be enhanced significantly.

In this connection, it is of interest to consider the quadrupole ordering near a gapless crossover that is accompanied by the formation of a degenerate ground state in a critical field H_{cr}. In this case, even weak pairwise interactions can produce a quadrupole or magnetic ordering near the crossover and lift the degeneracy. RE zircons exhibit numerous level-crossing effects [4–6] in the accessible field range and are a promising object for studying such induced transitions.

For the Yb ion, the parameter α_J is fairly large; therefore, we may expect that Yb zircons will exhibit quadrupole effects and even undergo phase transition if the electronic spectrum of the ion satisfies the necessary conditions. Investigations of the elastic, magnetic, and magnetoelastic properties of Yb zircons performed earlier made it possible to reliably determine the set of microscopic interaction constants [7–9]. The magnetic and magnetoelastic properties in weak fields exhibit quadrupole effects for $\mathbf{H} \parallel [100]$, namely, large contributions from quadrupole interactions to the third-order susceptibility $\chi_M^{(3)}$, magnetostriction, and the γ-symmetry elastic constant $C^\gamma = (c_{11} - c_{22})/2$. However, these interactions are insufficient to cause quadrupole ordering, which occurs when the corresponding strain susceptibility reaches a critical value of $\chi_\gamma^{-1} \le G^\gamma$. The absence of spontaneous γ-symmetry quadrupole ordering in Yb zircons was discussed in [9]. Experiments on ytterbium phosphate in ultrahigh magnetic fields directed along the tetragonal axis have revealed a maximum of the differential susceptibility associated with level crossing [10]. Numerical calculations also predict level crossing in ytterbium phosphate and vanadate in fields directed in the basal plane.

In this paper, possible Jahn–Teller transitions in $YbPO_4$ and $YbVO_4$ in strong magnetic fields are studied

1063-7834/04/4612-2249$26.00 © 2004 MAIK "Nauka/Interperiodica"

theoretically on the basis of experimentally determined microscopic interaction constants. It is shown that γ-symmetry quadrupole ordering (i.e., orthorhombic deformation of the tetragonal unit cell along the [100] direction) is stimulated by a magnetic field applied along the [110] axis. Using a general formalism, phase diagrams of $YbPO_4$ and $YbVO_4$ are calculated, which reveal reentrant transitions between the tetragonal and orthorhombic phases, and anomalies in the thermodynamic properties associated with these transitions are considered.

2. THEORETICAL CONSIDERATION

The total Hamiltonian of a 4*f* ion includes the crystal-field Hamiltonian H_{CF}, the Zeeman term H_Z (which describes the interaction between the angular momentum **J** and an external field **H**), and the quadrupole-interaction Hamiltonian H_{QT} and can be written as

$$H = H_{CF} + H_Z + H_{QT} + E_Q. \quad (1)$$

Using the equivalent-operator method and the molecular-field approximation for pairwise quadrupole interactions, these terms can be written in the form (see, e.g., [11] for more details)

$$H_{CF} = \alpha_J B_2^0 O_2^0 + \beta_J (B_4^0 O_4^0 + B_4^4 O_4^4) + \gamma_J (B_6^0 O_6^0 + B_6^4 O_6^4), \quad (2)$$

$$H_Z = -g_J \mu_B \mathbf{HJ}, \quad (3)$$

$$H_{QT} = -G^\alpha \langle O_2^0 \rangle O_2^0 - G^\gamma \langle O_2^2 \rangle O_2^2 - G^\delta \langle P_{xy} \rangle P_{xy}, \quad P_{xy} = \frac{1}{2}(J_x J_y + J_x J_y). \quad (4)$$

In these expressions, O_n^m and B_n^m ($n = 2, 4, 6$; $m = 0, 4$; $m \le n$) are operators and parameters of the crystal field, respectively; α_J, β_J, and γ_J are the Stevens parameters; g_J is the Landé factor; and μ_B is the Bohr magneton. The Zeeman term H_Z represents the interaction solely with an externally applied field, because bilinear interactions in $YbXO_4$ are negligibly weak and cause magnetic ordering at only ultralow temperatures [12].

The generalized quadrupole-interaction Hamiltonian is determined by the quadrupole constants $G^\mu = G_{ME}^\mu + K^\mu = (B^\mu)^2/C_0^\mu + K^\mu$ ($\mu = \alpha, \gamma, \delta$), contributed by both single-ion magnetoelastic (B^μ) and pairwise quadrupole (K^μ) interactions (C_0^μ is the background elastic constant in the absence of interactions). To describe quadrupole and magnetoelastic interactions (or distortions), we use symmetrized notation. The magnetoelastic γ- and δ-symmetry modes in the quadrupole Hamiltonian describe orthorhombic distortions of a tetragonal crystal along the [100] and [110] axes, respectively, which arise in the presence of an external magnetic field or in the quadrupole-ordered phase, whereas the α mode corresponds to crystal distortions preserving the tetragonal symmetry, i.e., to bulk (α1) and tetragonal (α2) deformations. The ε-symmetry terms, corresponding to monoclinic distortions in the *a*–*c* plane, are discarded in the Hamiltonian H_{QT}, because such terms do not contribute in the case of a magnetic field applied in the basal plane or along the tetragonal axis. For γ-symmetry pairwise quadrupole interactions, the term E_Q in the mean-field approximation has the form $E_Q = (1/2)K^\gamma \langle O_2^2 \rangle^2$.

The quadrupole moments $\langle O_2^\mu \rangle$, which are the expectation values of the operators O_2^μ, are determined by the eigenfunctions $|i\rangle$ and energy levels E_i of the RE ion and are linear functions of the symmetrized spontaneous or induced magnetoelastic strains ε^μ ($\mu = \alpha 1/\alpha 2, \gamma, \delta$):

$$Q^\mu = \langle O_2^\mu \rangle = \sum_i \langle i | O_2^\mu | i \rangle \exp(-E_i/k_B T)/Z, \quad Z = \sum_i \exp(-E_i/k_B T), \quad (5)$$

$$\varepsilon^\mu = A^\mu \langle O_2^\mu \rangle = \frac{B^\mu}{C_0^\mu} \langle O_2^\mu \rangle, \quad (6)$$

where O_2^μ is equal to O_2^0, O_2^2, and P_{xy} for $\mu = \alpha 1/\alpha 2$, γ and δ, respectively. The coefficients A^μ can be determined experimentally in relatively weak fields.

To consider quadrupole phase transitions, the strain susceptibility $\chi_\mu = \partial \langle O_2^\mu \rangle / \partial \varepsilon^\mu$ ($\mu = \alpha, \gamma, \delta$) is used; this susceptibility characterizes the response of the quadrupole component $\langle O_2^\mu \rangle$ to strain ε^μ and also describes the softening of the corresponding elastic constant C^μ. Given the eigenfunctions and energy levels of the RE ion (which are determined by the crystal field and the external magnetic field), the anisotropic susceptibility χ_μ can be calculated from the formula

$$\chi_\mu(T, H) = \sum_i f_i \left(-2 \sum_{j \ne i} \frac{|O_{2ij}^\mu|^2}{E_i - E_j} + \frac{1}{k_B T} |O_{2ii}^\mu|^2 \right), \quad (7)$$

where $O_{2ij}^\mu = \langle j | O_2^\mu | i \rangle$ are matrix elements and f_i is the Boltzmann factor of the *i*th level. The eigenvalues and eigenfunctions that are needed to calculate the strain susceptibility, magnetization, and magnetostriction are found by numerically diagonalizing the total Hamiltonian, in which the α-, γ-, and δ-symmetry quadrupole interactions (also depending on the electronic structure) are included self-consistently.

The properties in strong magnetic fields are calculated using the interaction constants determined from magnetic measurements in relatively weak fields for all symmetry modes [9]. The magnetoelastic constants for the orthorhombic modes in Yb zircons are comparable in magnitude; for the γ-orthorhombic mode in the vanadate and phosphate, we have $B^\gamma/\alpha_J = 14.2 \times 10^3$ K ($G^\gamma \approx 100$ mK) and $B^\gamma/\alpha_J = 13.9 \times 10^3$ K ($G^\gamma \approx 150$ mK), respectively, and for the δ mode, $B^\delta/\alpha_J = -19.2 \times 10^3$ K ($G^\delta \sim 1$ K) and $B^\delta/\alpha_J = -16.2 \times 10^3$ K ($G^\delta \sim 1$ K), respectively. The effect of the magnetoelastic α and δ modes on the γ-symmetry quadrupole ordering is also taken into account in the calculations. It should be stressed that, for the Hamiltonian written in the normalized form (2)–(4), the single-ion and pairwise interaction constants depend on the crystalline structure and on the type of RE ions involved (in particular, their Stevens parameters) but are independent of the energy spectrum and wave functions of RE ions. The electronic structure influences the response of the RE ion to external fields (in our case, the strain susceptibility $\chi_\mu(T, H)$). The validity of this approach is supported by numerous studies on various RE compounds, in particular, RE zircons, for which adequate quantitative description of level-crossing effects and induced transitions in strong magnetic fields has been attained.

3. RESULTS AND DISCUSSION

3.1. Strain Susceptibility and Phase Diagram

The strain susceptibility determines the conditions under which quadrupole ordering occurs; more specifically, the second-order phase transition arises at a temperature T_Q satisfying the condition $\chi_\gamma^{-1}(T_Q) = G^\gamma$. The temperature dependence of χ_γ^{-1} for YbVO$_4$ and YbPO$_4$ in zero magnetic field exhibits Van Vleck behavior characterized by a low-temperature plateau at ~0.6 K, whose height determines the critical value of the quadrupole interaction constant G^γ (Fig. 1, curves *1*). Since the constant G^γ for the ytterbium vanadate and phosphate is only ~100 and 150 mK, respectively, both compounds are in a precritical state and remain in the tetragonal phase in the absence of a magnetic field.

The occurrence of γ-symmetry quadrupole ordering in the presence of a magnetic field of different symmetry can be easily understood by analyzing the dependence of the deformation susceptibility χ_γ on magnetic field. The case of magnetic fields applied along the [110] and [001] axes is the simplest according to symmetry arguments. Indeed, a magnetic field applied along the [001] axis decreases χ_γ, i.e., drives the system away from the quadrupole ordering (Fig. 1, curves *4*). The application of a magnetic field along the [110] axis, on the contrary, causes χ_γ to increase at low temperatures. In fields higher than 50 and 175 T for ytterbium vanadate and phosphate, respectively, the electronic system undergoes a transition to the critical state and the quadrupole component $\langle O_2^2 \rangle$ becomes ordered at a temperature T_Q, which is determined as shown in Fig. 1. The increase in the strain susceptibility χ_γ caused by the application of an external magnetic field **H** ∥ [110] at low temperatures is explained by both a decrease in the energy spacing E_2–E_1 between the lower levels and a modification of the matrix elements O_{2ij}^2. As the external field is increased further, the susceptibility χ_γ at low temperatures starts to decrease (curves *3*) and χ_γ^{-1} again becomes higher than G^γ for the com-

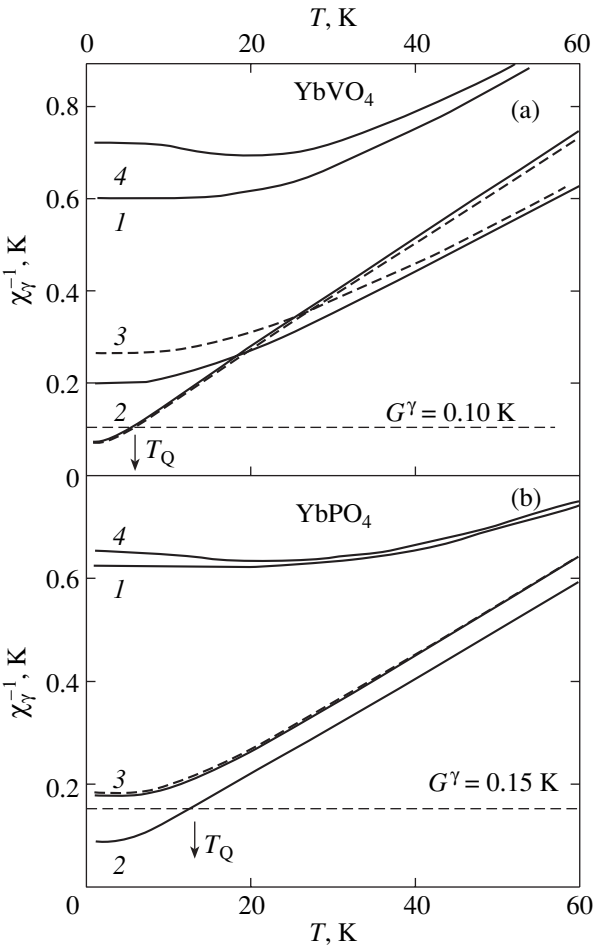

Fig. 1. Temperature dependence of the inverse strain susceptibility χ_γ^{-1} in magnetic fields **H** ∥ [110] for (a) YbVO$_4$ and field strength H equal to (*1*) 0, (*2*) 60, and (*3*) 280 T; (b) YbPO$_4$ and H equal to (*1*) 0, (*2*) 200, and (*3*) 280 T; and in magnetic fields **H** ∥ [001] (curves *4* for H equal to (a) 10 and (b) 20 T). Calculations are performed without (solid curves) and with inclusion (dashed curves) of quadrupole interactions with $G^\alpha = 50$ mK. Arrows indicate the quadrupole transition temperature T_Q at which χ_γ^{-1} becomes equal to the quadrupole interaction constant G^γ at the given magnetic field.

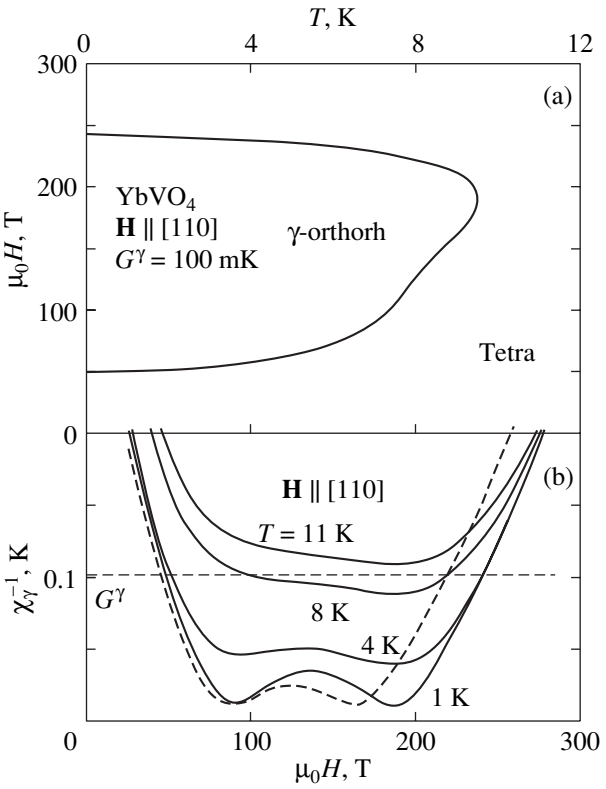

Fig. 2. (a) Structural phase diagram of $YbVO_4$ calculated with inclusion of γ-symmetry quadrupole interactions for transitions from the tetragonal to γ-orthorhombic phase stimulated by a magnetic field **H** || [110] and (b) isothermal $\chi_\gamma^{-1}(H)$ dependences at various temperatures calculated without (solid curves) and with inclusion (dashed curve) of quadrupole interactions with G^α = 50 mK, from which it follows that two phase transitions occur.

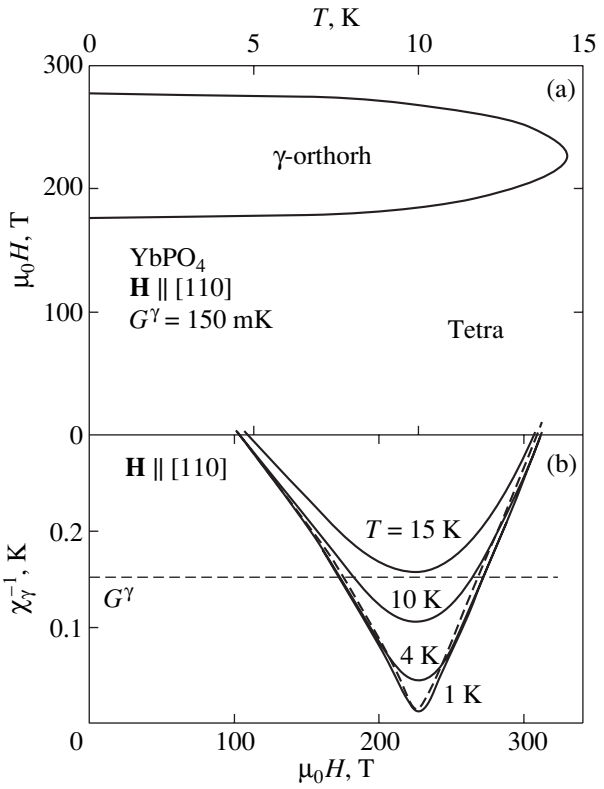

Fig. 3. (a) Structural phase diagram of $YbPO_4$ calculated with inclusion of γ-symmetry quadrupole interactions for transitions from the tetragonal to γ-orthorhombic phase stimulated by a magnetic field **H** || [110] and (b) isothermal $\chi_\gamma^{-1}(H)$ dependences at various temperatures calculated without (solid curves) and with inclusion (dashed curve) of quadrupole interactions with G^α = 50 mK, from which it follows that two phase transitions occur.

pounds under study; therefore, the electronic system turns back to the tetragonal phase.

The *H–T* diagram for stimulated transitions from the tetragonal to the γ-orthorhombic phase can be found by equating the inverse strain susceptibility χ_γ^{-1} to the quadrupole constant G^γ at different magnetic fields and temperatures (Figs. 2, 3). The critical fields for a given crystal field depend only on the values of G^γ determined earlier [9]. From the field dependence of $\chi_\gamma^{-1}(H)$, it follows that the quadrupole-ordered phase is stable over a limited field range. In ytterbium vanadate, the γ-orthorhombic phase exists over a wider field range, from H_{c1} = 50 T to H_{c2} = 240 T; however, the critical temperature is lower, $T_c \sim 10$ K. In $YbPO_4$, the quadrupole phase is stable in the range from H_{c1} = 175 T to H_{c2} = 275 T and the critical temperature is somewhat higher, $T_c \sim 15$ K. In principle, the lower critical field H_{c1} can be measured experimentally; however, as shown below, this transition is very sensitive to deviations of the field from the [110] axis, which makes its observation difficult.

The field dependences of χ_γ^{-1} for $YbPO_4$ have a clearly defined minimum near $H_{cr} \sim 230$ T; this value coincides with the crossover field for this field orientation. Calculations of the Zeeman effect show that, at $H_{cr} \sim 230$ T, gapless crossing of lower levels occurs; i.e., quadrupole ordering arises near the degenerate state of the Yb^{3+} ion in a magnetic field. For $YbVO_4$, the field dependences of χ_γ^{-1} have two closely spaced minima at ~90 and ~190 T corresponding two crossovers, which agrees with the calculations of the Zeeman effect. This unusual situation is caused by occasional combinations of the crystal field parameters and explains the wider region of existence of the quadrupole-ordered phase in $YbVO_4$ as representing two overlapping regions. We note that, for a smaller value of the quadrupole constant, $G^\gamma < 50$ mK (e.g., in a dilute RE subsystem), the two regions of existence of the quadrupole-ordered phase will not overlap and the system will

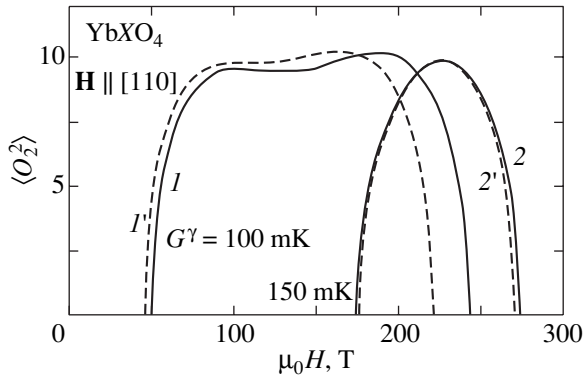

Fig. 4. Field dependence of the order parameter $\langle O_2^2 \rangle$ in $YbVO_4$ (curves *1*, *1*') and $YbPO_4$ (curves *2*, *2*') at 2 K for magnetic fields applied along the [110] axis; curves *1*' and *2*' represent calculated dependences with inclusion of fully symmetric quadrupole interactions with $G^\alpha = 50$ mK.

undergo four phase transitions stimulated by a magnetic field.

The field dependence of the order parameter $\langle O_2^2 \rangle$ for Yb zircons at 2 K is shown in Fig. 4. Both phase transitions are seen to be second-order. The large value of the quadrupole component $\langle O_2^2 \rangle$ arising in the ordered phase is indicative of a significant γ-symmetry orthorhombic strain, $\varepsilon^\gamma = A^\gamma \langle O_2^2 \rangle \sim 3 \times 10^{-3}$, which is comparable to that observed in spontaneous Jahn–Teller transitions in RE zircons. The α-symmetry quadrupole interactions with $G^\alpha = 50$ mK slightly decrease the critical fields for both transitions except for the lower critical field H_{c1} for $YbPO_4$. The largest change takes place for the higher critical field H_{c2}, as can be seen by comparing the solid and dashed curves in Figs. 1–3, which are calculated with and without allowance, respectively, for the quadrupole interaction constant G^α.

3.2. Magnetization in a Strong Magnetic Field

3.2.1. The case of H || [100]. An external magnetic field affects the spectrum and wave functions of the Yb^{3+} ion and can drive the system close to the critical state depending on the field orientation. A magnetic field **H** || [100] induces strains of the same symmetry as the quadrupole component responsible for the phase transition and brings about the appearance of γ-symmetry quadrupole terms in the Hamiltonian H_{QT}. These terms make additional contributions to the magnetic and magnetoelastic properties. Calculated isotherms of the magnetization in fields **H** || [100] at $T = 2$ K are shown in Figs. 5 and 6 for $YbVO_4$ and $YbPO_4$, respectively. From comparing the curves calculated with (solid curves) and without (dashed curves) allowance

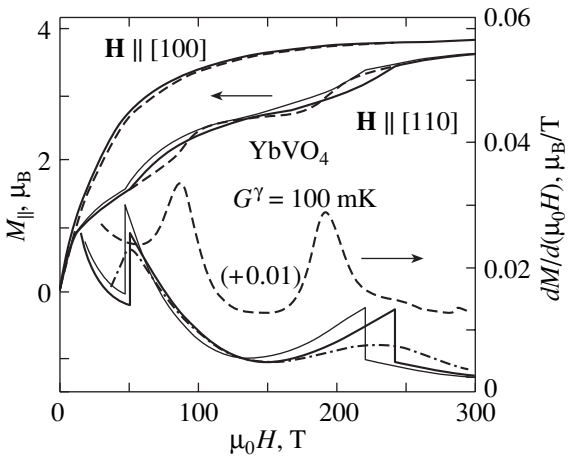

Fig. 5. Field dependences of the magnetic moment $M_\parallel$ along the applied magnetic field for $YbVO_4$ at $T = 2$ K in the case of **H** || [100] and **H** || [110]. The dependences are calculated without (dashed curves) and with inclusion (solid curves) of quadrupole interactions with $G^\gamma = 100$ mK (left-hand ordinate axis). The derivative $dM_\parallel/dH$ for **H** || [110] (solid curves) and for fields deviated through an angle of $\Delta\varphi = 1°$ in the basal plane (dash-dotted curve) clearly shows transitions to the quadrupole-ordered phase (right-hand ordinate axis); the dashed curve for $G^\gamma = 0$ is shifted along the vertical axis by +0.01. Thin curves represent field dependences calculated with inclusion of fully symmetric quadrupole interactions with $G^\alpha = 50$ mK.

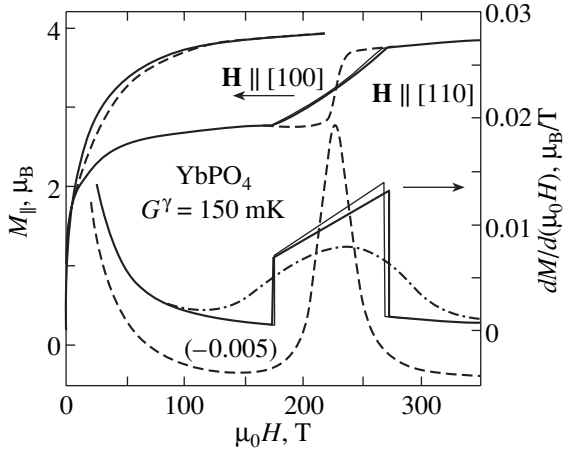

Fig. 6. Field dependences of the magnetic moment $M_\parallel$ along the applied magnetic field for $YbPO_4$ at $T = 2$ K in the case of **H** || [100] and **H** || [110]. The dependences are calculated without (dashed curves) and with inclusion (solid curves) of quadrupole interactions with $G^\gamma = 150$ mK (left-hand ordinate axis). The derivative $dM_\parallel/dH$ for **H** || [110] (solid curves) and for fields deviated through an angle of $\Delta\varphi = 1°$ in the basal plane (dash-dotted curve) clearly shows transitions to the quadrupole-ordered phase (right-hand ordinate axis); the dashed curve for $G^\gamma = 0$ is shifted along the vertical axis by –0.005. Thin curves represent field dependences calculated with inclusion of fully symmetric quadrupole interactions with $G^\alpha = 50$ mK.

for the quadrupole interactions, it follows that the contribution from these interactions for $G^{\gamma} = 100$ and 150 mK is as high as 10–15% at low temperatures in fields ~30–50 T. At higher fields, the quadrupole contribution becomes smaller.

3.2.2. The case of H || [110]. In fields **H** || [110], the situation is more interesting, because the strain induced by a field and the strain associated with the phase transition differ in symmetry. After a magnetic field applied along the [110] axis transfers the system to the critical state (i.e., the quadrupole component $\langle O_2^2 \rangle$ becomes ordered), the [110] axis in the γ-orthorhombic phase is no longer a symmetry axis and the paramagnetic moment deviates from this direction toward the tetragonal [100] axis. As a result, the component of the magnetic moment parallel to the field is changed and a nonzero transverse component arises; therefore, the onset of the induced JT effect is signaled by the appearance of this transverse component. The degeneracy of the energy levels of the Yb^{3+} ion is lifted near H_{cr}, and a finite gap appears. Figures 5 and 6 show field dependences of the longitudinal magnetization component $M_{\|}(H)$ for **H** || [110] at 2 K calculated with and without inclusion, respectively, of the quadrupole interactions characterized by the constant G^{γ}.

In the $YbPO_4$ crystal, the situation is simpler. In the absence of G^{γ} interactions or at temperatures above T_{cr}, there is no contribution from the quadrupole component $\langle O_2^2 \rangle$. In this case, the $M_{\|}(H)$ and $dM_{\|}/dH$ curves exhibit smooth anomalies characteristic of the degenerate ground state of the RE ion that occurs in gapless crossover (see dashed curves for **H** || [110] in Figs. 5, 6). At temperatures below T_{cr}, the magnetization curve changes near the critical crossover field H_{cr}; more specifically, the curve exhibits kinks at $H_{c1} < H_{cr}$ and $H_{c2} > H_{cr}$, which correspond to jumps in the derivative $dM_{\|}/dH$ (solid curves in Figs. 5, 6). These jumps are similar to those predicted and observed earlier in $TmPO_4$ for **H** || [100] near the critical field $H_c = 9.5$ T [13]. In the quadrupole-ordered phase, the susceptibility $dM_{\|}/dH$ varies linearly with field and is temperature-independent. In the disordered phase, on the contrary, the susceptibility near H_{c1} and H_{c2} increases as the temperature is increased, so that the jumps in the $dM_{\|}(H)/dH$ curves become less pronounced.

A similar situation is observed for the $YbVO_4$ crystal, with the only difference that two closely spaced crossovers occur in the disordered phase (Fig. 5). Therefore, the $M_{\|}(H)$ and $dM_{\|}/dH$ curves for the disordered phase exhibit two anomalies, which are smoother than those observed in $YbPO_4$. The quadrupole-ordered phase arises near the critical field for each of the crossovers, which causes the anomalies in the curves to change in character. Furthermore, the $dM_{\|}(H)/dH$ curves become nonmonotonic in the quadrupole-ordered phase. Taking into account the α-symmetry quadrupole interactions with $G^{\alpha} = 50$ mK slightly increases the jump in susceptibility at H_{c2} in Yb phosphate and at H_{c1} in Yb vanadate (thin lines in Figs. 5, 6). The effect of the δ-symmetry quadrupole interactions with $G^{\delta} \sim 1$ K (not shown in Figs. 5, 6) manifests itself most clearly in the noticeably increased anomaly in the $dM_{\|}(H)/dH$ curve at H_{c2} for $YbPO_4$.

Note that the anomalies in the longitudinal magnetization $M_{\|}$ and its derivative $dM_{\|}(H)/dH$ do not depend on the domain state of the crystals in the quadrupole-ordered phase, because both types of domains differing in the sign of the quadrupole component $\langle O_2^2 \rangle$ make equal contributions to $M_{\|}(H)$ if the field is strictly directed along the [110] axis. The anomalies in the $M_{\|}(H)$ and $dM_{\|}(H)/dH$ curves become highly smoothed even for small deviations of the applied field from the [110] axis in the basal plane (see dash-dotted curves constructed for $\Delta\varphi = 1°$ in Figs. 5, 6), and the critical fields H_{c1} and H_{c2} shift noticeably in such a way that the region of existence of the quadrupole-ordered phase is widened. The strong dependence of the stimulated JT effect on field deviations from the [110] axis in Yb zircons is the main problem complicating experimental observations of this effect.

The most distinctive feature of the stimulated JT transition is the appearance of the transverse magnetic-moment component $M_{\perp}$ due to the crystal symmetry lowering for which the [110] axis is no longer a twofold axis. The $M_{\perp}(H)$ dependence at 2 K is shown in Fig. 7 for different orientations of the field in the basal plane near the [110] axis. The calculated component $M_{\perp}(H)$ for $\Delta\varphi = 0$ is zero in fields up to the lower critical field H_{c1}; then, this component increases sharply and remains nonzero up to the field H_{c2} (curves *1* in Fig. 7). In the range $H_{c1} < H < H_{c2}$, the maximum value of $M_{\perp}$ is $\sim 2.2\mu_B$ for both zircons and the angle between the magnetic moment and the field in this case reaches values of ~32° and 35° for $YbVO_4$ and $YbPO_4$, respectively. Note that, experimentally, the transverse component $M_{\perp}$ in fields above H_{c1} was close to zero if γ-orthorhombic domains were distributed with approximately equal probability. By comparing Figs. 4 and 7, we see that the $M_{\perp}(H)$ dependence is similar to the field dependence of the order parameter $\langle O_2^2 \rangle = \langle J_x^2 - J_y^2 \rangle$, which is, in fact, directly related to the transverse component. When the field is directed exactly along the [110] axis, we have $\langle J_x \rangle = \langle J_y \rangle$ and $\langle O_2^2 \rangle = M_{\perp} = 0$. In the case of a small deviation from this axis, we have $\langle J'_x \rangle = \langle J_x + \Delta J \rangle$, $\langle J'_y \rangle = \langle J_y - \Delta J \rangle$, $\langle O_2^2 \rangle \sim \langle J_x \Delta J \rangle$, and $M_{\perp} \sim \langle \Delta J \rangle$.

For the Yb zircons under study, however, the transverse component $M_{\perp}$ is also significant in the case of small deviations of the magnetic field from the [110]

axis in the basal plane. From symmetry considerations, it follows that, for nonzero values of $\Delta\varphi$, a nonzero component $M_\perp$ is induced by a weak field even in the absence of quadrupole interactions (curves *2* in Fig. 7), because the small component of the magnetic field along the [100] axis strongly influences the electronic structure and induces a quadrupole moment $\langle O_2^2 \rangle$, which is the order parameter for the phase transition in question. Interestingly, the $M_\perp(H)$ dependence for small misorientation of the field in the absence of quadrupole interactions is similar in shape to the field dependence of the order parameter $\langle O_2^2 \rangle$ (in particular, the maximum is reached in the same field region). The quadrupole interactions increase the transverse component $M_\perp$ in this case, as can be seen by comparing curves *3* and *2* for $\Delta\varphi = 0.5°$ in Fig. 7. Curves *2* and *3* are qualitatively similar, and their quantitative difference decreases rapidly as the deviation of the field from the [110] axis in the basal plane increases. A quantitative difference occurs only in the case of fields directed exactly along the [110] axis, where the component $M_\perp$ is zero in the absence of G^γ quadrupole interactions.

3.3. Magnetostriction along the [110] and [001] Axes

Our calculations show that the stimulated JT effect is accompanied by noticeable anomalies in magnetostriction. To study the stimulated JT effect in YbXO$_4$ for **H** ∥ [110], one should measure strains along the [110] and [001] axes in the $(1\bar{1}0)$ plane, for which the contributions from both types of JT domains are equal. The strains along the [110] and [001] axes in this case are

$$\varepsilon_c = \lambda_{110}^{001} = \frac{1}{\sqrt{3}}\varepsilon^{\alpha 1} + \frac{2}{\sqrt{6}}\varepsilon^{\alpha 2},$$
$$\varepsilon_b = \lambda_{110}^{110,\bar{1}10} = \left(\frac{1}{\sqrt{3}}\varepsilon^{\alpha 1} - \frac{1}{\sqrt{6}}\varepsilon^{\alpha 2}\right) \pm \frac{1}{\sqrt{2}}\varepsilon^{\delta}. \quad (8)$$

The strain along the *c* axis is seen to be determined only by the change in one quadrupole component, $\varepsilon_c^\alpha(H) = (A^{\alpha 1}/\sqrt{3} + 2A^{\alpha 2}/\sqrt{6})[\langle O_2^0(H)\rangle - \langle O_2^0(0)\rangle]$ (i.e., $\varepsilon^{\alpha 1} \sim \varepsilon^{\alpha 2} \sim \Delta\langle O_2^0\rangle$), where the coefficients $A^{\alpha 1}$ and $A^{\alpha 2}$ are combinations of the magnetoelastic constants $B^{\alpha 1}$ and $B^{\alpha 2}$ and of the elastic constants $C_0^{\alpha 1}$, $C_0^{\alpha 2}$, and $C_0^{\alpha 12}$. The field dependence of ε_b is determined by two different contributions, namely, $\varepsilon^\delta(H) = (B^\delta/C_0^\delta)\langle P_{xy}(H)\rangle$ and $\varepsilon_b^\alpha(H) = (A^{\alpha 1}/\sqrt{3} - A^{\alpha 2}/\sqrt{6})[\langle O_2^0(H)\rangle - \langle O_2^0(0)\rangle]$. For YbPO$_4$, the coefficients $A^{\alpha 1} = -1.1 \times 10^{-4}$, $A^{\alpha 2} = 1.6 \times 10^{-4}$, and $(1/\sqrt{2})(B^\delta/C_0^\delta) = -1.7 \times 10^{-3}$ were determined in [9].

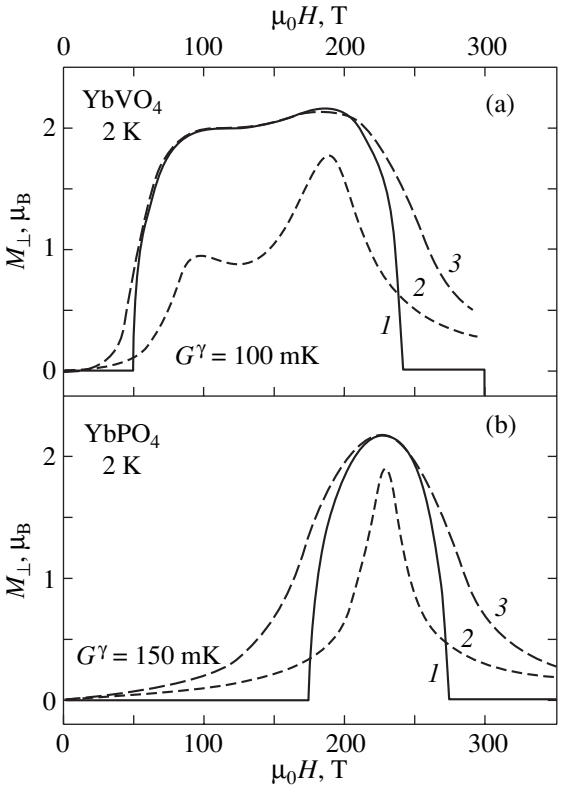

Fig. 7. Field dependences of the paramagnetic-moment component perpendicular to the applied field for YbVO$_4$ and YbPO$_4$ calculated (*2*) without and (*1*, *3*) with inclusion of quadrupole interactions characterized by the constant G^γ for various deviations of the field $\Delta\varphi$ from the [110] axis: (*1*) 0° and (*2*, *3*) 0.5°.

Thus, the magnetostriction is determined by different quadrupole moments. In both the crossover and the stimulated JT transition, anomalies are exhibited not only by the active quadrupole component $\langle O_2^2 \rangle$ responsible for ordering but also by the quadrupole components $\langle O_2^0 \rangle$ and $\langle P_{xy} \rangle$. Let us consider the magnetostriction associated with the JT transition in Yb phosphate, where anomalies are more pronounced. The field dependences of $\varepsilon_c(H)$ and $\varepsilon_b(H)$ calculated for $G^\gamma = 150$ mK exhibit characteristic kinks at temperatures below 15 K (Fig. 8a) and anomalies associated with a crossover at $T > 15$ K. The $\varepsilon_c(H)$ dependence is determined by the quadrupole moment $\langle O_2^0 \rangle$ alone and exhibits a characteristic jump, similar to those observed in magnetization curves. The shape and width of the jump under the conditions of the stimulated JT effect vary noticeably (cf. curves *1*, *1*" in Fig. 8), and the jump remains noticeable as the field deviates slightly from the [110] axis (curve *1*'). The contributions from the quadrupole moments $\langle O_2^0 \rangle$ and $\langle P_{xy} \rangle$ to the strain $\varepsilon_b(H)$ in Yb phosphate differ in sign, but the field dependence

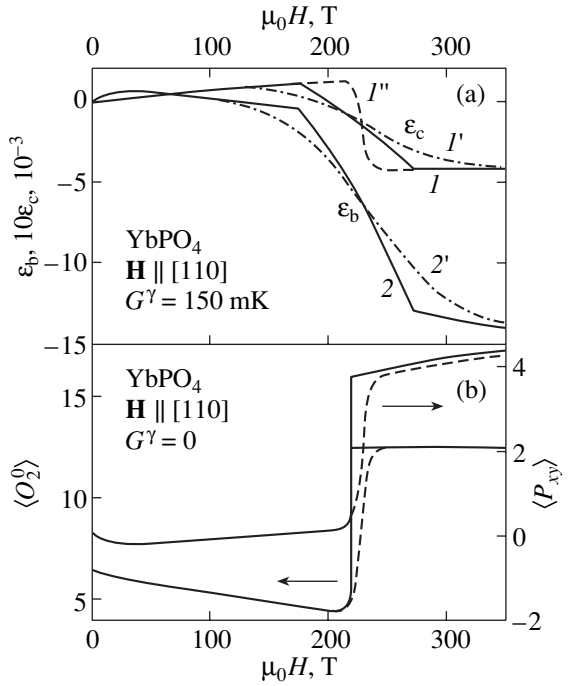

Fig. 8. Calculated field dependences (a) of strains ε_c and ε_b along the [110] and [001] axes in $YbPO_4$ at $T = 2$ K (*1*, *1*", *2*) in fields $\mathbf{H} \parallel [110]$ for $G^\gamma = 0$ and (*1*', *2*') in fields deviated through an angle of $\Delta\varphi = 1°$ in the basal plane for G^γ = 150 mK and (b) of the quadrupole components $\langle O_2^0 \rangle$ and $\langle P_{xy} \rangle$ in the absence of the JT transition for $G^\gamma = G^\alpha = G^\delta$ = 0 (dashed curves) and for $G^\gamma = 0$, G^α = 50 mK, and G^δ= 0.5 K (solid curves).

of the strain is mainly determined by $\varepsilon^\delta(H)$ (curve *2*), which is larger in magnitude and whose anomaly continues to exist with a small misorientation of the magnetic field (curve *2*').

Using the calculated field dependences of the nonzero quadrupole components for $\mathbf{H} \parallel [110]$ in the absence of the stimulated JT effect (Fig. 8b), we can analyze the role played by weak quadrupole interactions in the stimulated JT effect and their influence on the phase diagram. The quadrupole component $\langle O_2^0 \rangle$ is nonzero even in a zero magnetic field and changes jumpwise at a crossover (in Yb phosphate, this jump is $\Delta\langle O_2^0 \rangle \sim 10$), thereby causing discontinuous jumps in the corresponding terms in the Hamiltonian H_{QT} and shifting the critical fields for the stimulated transition. The strongest effect is produced by the fully symmetric interactions on the upper critical field H_{c2} in Yb vanadate (Fig. 4). The change in the quadrupole component $\langle P_{xy} \rangle$ is approximately two times smaller, but this change causes the critical field for the crossover to shift noticeably because of the larger quadrupole constant G^δ, which has a maximum value in RE zircons. In Yb phosphate, in particular, these interactions with $G^\delta \sim$ 1 K would give rise to a very sharp change in the component $\langle P_{xy} \rangle$ (first-order phase transition) near the crossover in the absence of the stimulated JT effect and to more pronounced anomalies in the magnetization and magnetostriction curves in the presence of the JT effect.

4. CONCLUSIONS

The idea that, in an electronic system close to a critical state, the JT effect can be stimulated by external stresses with symmetry different from that of the quadrupole order parameter was first suggested theoretically in [2, 13]. In Yb zircons, a magnetic field applied along the [110] axis acts as external stress and drives the γ-symmetry quadrupole component close to the critical state by rearranging both the energy levels and wave functions of the system. Because of the extremely high sensitivity of the effect (and, in particular, the critical parameters of the phase diagram) to the energy spectrum and wave functions of the RE ion, analysis should be performed by taking into account the actual crystal field and the specific features of the magnetoelastic interactions. For this reason, we have carried out a consistent analysis of this effect in $YbVO_4$ and $YbPO_4$ in the framework of a fairly general formalism.

Note that the stimulated JT effect under study differs essentially from the JT effect induced by stresses with symmetry identical to that of the quadrupole order parameter. Indeed, in the latter case, the stresses applied to a crystal in the disordered state immediately induce the corresponding quadrupole component, which is enhanced significantly by the quadrupole interactions. This induced effect is observed in RE zircons with spontaneous quadrupole ordering at temperatures above the critical temperature, e.g., in $DyVO_4$ for the γ-symmetry quadrupole component in a magnetic field $\mathbf{H} \parallel [100]$ and in a number of intermetallic compounds (e.g., $TmAg_2$ [14]).

In the calculations described above, we used the theoretical model of the stimulated JT effect that was proposed in [2, 3] for $TmPO_4$ and improved significantly in [13] with inclusion of all specific features of the ground multiplet in the crystal field and all symmetry-allowed magnetoelastic interactions. This model has been shown to be adequate for describing the effect under study in $TmPO_4$ on the basis of magnetoelastic constants determined from independent experiments, i.e., without any fitting parameters. The mechanism of the stimulated JT effect is the field-induced significant change in the wave functions and energy spacings between the ground and quadrupole-active excited levels, which enhances the strain susceptibility χ_γ; the JT effect arises when χ_γ reaches the critical value defined by the condition $G^\gamma = \chi_\gamma^{-1}(T_Q)$. The essential difference in the stimulated JT effect between $TmPO_4$ and $YbXO_4$

is that Tm phosphate is very close to the critical state and the induced JT transition in this compound is not associated with a crossover. However, the anomalies in magnetization and susceptibility associated with the stimulated JT effect are qualitatively similar in these RE zircons.

At the quadrupole transition temperature T_Q, the parallel component of the magnetic moment varies only slightly and exhibits only a small increase in its derivative. The change in the magnetic moment caused by the stimulated JT effect is primarily its deviation from the direction of **H** ∥ [110] toward the [100] axis due to the appearance of the nonzero quadrupole component $\langle O_2^2 \rangle$. Experiments performed on $TmPO_4$ in [13] showed that an experimental technique in which the parallel and transverse components of the magnetic moment are measured simultaneously as a function of the field direction is an efficient method for studying stimulated quadrupole phase transitions.

Interestingly, the anomalies in the magnetization and differential susceptibility that are associated with quadrupole ordering in $YbPO_4$ are qualitatively similar to those predicted to occur in the case of magnetic ordering near a gapless crossover, e.g., in $HoBa_2Cu_3O_{7-\delta}$ [15]. Specifically, at these phase transitions, the jump in the magnetization $M_\parallel(H)$ is broadened and the susceptibility $dM_\parallel(H)/dH$ undergoes jumps and then varies linearly in both quadrupole- and magnetically ordered phases. Both of these two transitions are associated with instability of the degenerate state at a crossover; this instability is removed by weak quadrupole or bilinear interactions, with the consequence that the magnetic moment deviates from the field direction and a nonzero transverse component appears.

Experimental observation of the stimulated JT transitions in YbXO$_4$ is possible, in principle, but poses severe problems. In addition to the strong dependence of the magnetic anomalies on deviation of the field from the [110] axis, one should take into account the magnetocaloric effect that accompanies magnetization of a crystal in pulsed magnetic fields. Simple calculations ignoring pair interactions and phase transitions show that, in the process of adiabatic magnetization in a field **H** ∥ [110], YbXO$_4$ crystals are first heated (by $\Delta T \sim 20$ K) and then cooled sharply near the crossover field. However, only exact calculations with inclusion of all existing interactions can reveal whether or not a crystal is cooled below T_c in the adiabatic regime with an initial temperature $T_{st} \sim 2$ K.

ACKNOWLEDGMENTS

This study was supported in part by the Russian Foundation for Basic Research (project no. 03-02-16809) and the International Science and Technology Center (project no. 2029).

REFERENCES

1. P. Morin and Z. Kazei, J. Phys.: Condens. Matter **11**, 1289 (1999).
2. B. G. Vekhter, V. N. Golubev, and M. D. Kaplan, Pis'ma Zh. Éksp. Teor. Fiz. **45** (3), 136 (1987) [JETP Lett. **45**, 168 (1987)].
3. M. D. Kaplan and G. O. Zimmerman, Phys. Rev. B **52** (1), 1 (1995).
4. P. Morin, J. Rouchy, and Z. Kazei, Phys. Rev. B **51** (21), 15 103 (1995).
5. A. Kirste, M. von Ortenberg, A. A. Demidov, Z. A. Kazei, N. P. Kolmakova, V. V. Platonov, A. A. Sidorenko, and O. M. Tatsenko, Physica B (Amsterdam) **336**, 335 (2003).
6. J.-M. Broto, H. Rakoto, and Z. A. Kazei, J. Phys.: Condens. Matter **15**, 8767 (2003).
7. J. Nipko, M. Grimsditch, C.-K. Loong, S. Kern, M. M. Abraham, and L. A. Boatner, Phys. Rev. B **53** (5), 2286 (1996).
8. P. C. Becker, N. Edelstein, G. M. Williams, J. A. Koningstein, L. A. Boatner, and M. M. Abraham, Phys. Rev. B **45**, 5027 (1992).
9. Z. A. Kazei, N. P. Kolmakova, and O. A. Shishkina, Zh. Éksp. Teor. Fiz. **120** (6), 1445 (2001) [JETP **93**, 1250 (2001)].
10. Z. A. Kazei, N. P. Kolmakova, R. Z. Levitin, V. V. Platonov, A. A. Sidorenko, and O. M. Tatsenko, Physica B (Amsterdam) **246–247**, 483 (1998).
11. P. Morin, J. Rouchy, and D. Schmitt, Phys. Rev. B **37** (10), 5401 (1988).
12. J. A. Hodges, J. Phys. (Paris) **44** (7), 833 (1983).
13. P. Morin and Z. Kazei, Phys. Rev. B **55** (14), 8887 (1997).
14. P. Morin and J. Rouchy, Phys. Rev. B **48** (1), 256 (1993).
15. Z. A. Kazei, A. A. Demidov, and N. P. Kolmakova, J. Magn. Magn. Mater. **258–259**, 590 (2003).

Translated by Yu. Epifanov

Physics of the Solid State, Vol. 46, No. 12, 2004, pp. 2258–2262. Translated from Fizika Tverdogo Tela, Vol. 46, No. 12, 2004, pp. 2184–2188.

MAGNETISM AND FERROELECTRICITY

Magnetization Behavior and Metamagnetic Transitions in Electron-Doped Manganites Induced by a Strong Magnetic Field

S. M. Dunaevsky and V. V. Deriglazov

Konstantinov St. Petersburg Nuclear Physics Institute, Russian Academy of Sciences, Gatchina, Leningrad oblast, 188300 Russia

e-mail: dunaevsk@mail.pnpi.spb.ru

Received May 18, 2004

Abstract—The behavior of magnetization M of the $R_xA_{1-x}MnO_3$ manganites (R = La, Pr, Nd, Sm, etc., A = Ca, Sr, Ba) in the electron doping region ($x < 0.4$) is studied as a function of external magnetic field H. The $M(H)$ relations for homogeneous magnetic structures are obtained by performing band calculations in the double-exchange model. Three different types of magnetization behavior corresponding to three electron concentration ranges ($x < 0.14$, $0.14 < x < 0.27$, $x > 0.27$) are revealed. The $M(H)$ relations are interpreted in terms of the phase diagram for the homogeneous ground state of the manganites calculated for $H = 0$, and the results agree qualitatively with experimental data on the magnetization of $Sm_xCa_{1-x}MnO_3$. © *2004 MAIK "Nauka/Interperiodica".*

1. One of the still unsolved problems in the physics of doped manganites $R_xA_{1-x}MnO_3$ (R = La, Pr, Nd, Sm, etc.; A = Ca, Sr, Ba, etc.) is description of their magnetic properties for $x < 0.5$. At such high concentrations of divalent elements, the free carriers are e_g electrons from manganese, which, as a result of double exchange (DE), would seem to favor the onset of ferromagnetic (FM) ordering in the system. Experiment revealed, however, alternation of only antiferromagnetic (AFM) structures, *G–C–A*, with increasing electron concentration x, while the ferromagnetic F structure appeared solely in the hole doping region, $x > 0.5$. It was shown in [1–3] that the *G–C–A* alternation of the AFM phases, observed to occur in the electron doping region at low temperatures, is a characteristic property of the degenerate double-exchange model of manganites with two and four inequivalent manganese ions in a unit cell. As the electron concentration increases, the magnetization first grows monotonically and then drops to zero for $x \cong 0.1$–0.2. This type of behavior was experimentally observed in [4–6], where the magnetization M first increased with doping and then vanished near $x = 0.2$. In [5, 6], the behavior of the magnetic properties of the $Sm_xCa_{1-x}MnO_3$ manganite ($0 < x < 0.33$) was studied in strong dc and pulsed magnetic fields of up to 50 T. The dependence of the sample magnetization $M(H)$ on the external magnetic field thus obtained was treated in [5, 6] in terms of phase separation and metamagnetic transitions.

We report on a numerical calculation of the dependence of the magnetization of electron-doped manganites on external magnetic fields for $T = 0$. We made use of the same model of the manganite crystal structure with four inequivalent Mn atoms in a *Pnma* unit cell as that employed in constructing the ground-state phase diagram [1]. The magnetization was determined for a homogeneous magnetic structure found by minimizing the total energy of the system in an external magnetic field.

2. The effective Hamiltonian is taken to be the model Hamiltonian of the degenerate DE model [2], which in a local atomic basis can be written as

$$H = H_{\mathrm{DE}} + H_\Delta + H_M,$$

$$H_{\mathrm{DE}} = \sum_{i\alpha\sigma} \varepsilon_{i\alpha} d^\dagger_{i\alpha\sigma} d_{i\alpha\sigma}$$

$$- J_H S \sum_{i\alpha\sigma} \sigma d^\dagger_{i\alpha\sigma} d_{i\alpha\sigma} + \sum_{\langle ij\rangle \alpha\beta\sigma'\sigma} t^{\sigma\sigma'}_{ij\alpha\beta} d^\dagger_{i\alpha\beta} d_{j\beta\sigma'}, \qquad (1)$$

$$H_\Delta = -\Delta \sum_{i\alpha\beta\sigma} (d^\dagger_{i\alpha\sigma} d^\dagger_{i\beta\sigma}) \begin{pmatrix} \cos\theta_i^o & \sin\theta_i^o \\ \sin\theta_i^o & -\cos\theta_i^o \end{pmatrix} \begin{pmatrix} d_{i\alpha\sigma} \\ d_{i\beta\sigma} \end{pmatrix},$$

$$H_M = J_{AF} \sum_{\langle ij\rangle} \mathbf{S}_i \mathbf{S}_j - g\mu_{\mathrm{B}} H \sum_{i\alpha\sigma} \left(S_i^z + \frac{1}{2} d^\dagger_{i\alpha\sigma} d_{i\alpha\sigma} \right).$$

Here, indices α and β label degenerate e_g atomic orbitals and indices i and j enumerate the atoms; $d^\dagger_{i\alpha\sigma}$ and $d_{j\beta\sigma'}$ are operators of creation and annihilation of electrons at site i with spins directed along or counter to the spin $\mathbf{S}_i$ of localized t_{2g} electrons ($S = 3/2$, $\sigma = \uparrow, \downarrow$);

$\varepsilon_{i\alpha}$ is the energy of an atomic orbital of type α; J_H is the intra-atomic Hund integral; J_{AF} is the interatomic exchange integral of the Heisenberg model for neighboring local spins; Δ is the Jahn–Teller-type splitting of the e_g level; θ_i^o are the angles of intra-atomic orbital mixing of e_g electrons; and $t_{ij\alpha\beta}$ are effective hopping integrals between local components of spinor states of the nearest neighbor manganese ions. In the double-exchange model, e_g-electron hopping occurs without spin flip; therefore, the hopping integral $t_{ij\alpha\beta}$ depends on the mutual orientation (the angle θ_{ij}^s) of neighboring spins $\mathbf{S}_i$ and $\mathbf{S}_j$, which we assume to be classical. Since the oxygen ions in the perovskite structure are located between the manganese ions, the effective hopping integral $t_{ij\alpha\beta}$ can be expressed through the hopping integral connecting the e_g orbital of the manganese with the p orbital of the nearest oxygen ion (the Koster–Slater parameter $V_{pd\sigma}$) in second-order perturbation theory. The hopping integral $t_{ij\alpha\beta}$ also depends on the orbital states of e_g electrons on the Mn ions and is anisotropic in real space (its explicit form can be found in [2]). Due to this dependence, a e_g-level splitting lifts the orbital degeneracy (similar to how Hund interaction lifts spin degeneracy in the double-exchange mechanism) and long-range order specific for each magnetic structure sets in in the system [13].

The formalism of the calculation is described in [7], together with the explicit form of the Hamiltonian matrix.

Hamiltonian (1) contains a new term, as compared to the Hamiltonian used in [1]; this term accounts for the interaction of local spins and e_g electrons with a magnetic field. We assume, as before, that the magnetic properties of the manganites are determined by the manganese subsystem only. Thus, the model is capable of revealing only general features of the behavior of the system in a magnetic field. The minimum of the total energy was found in the space of variables including the spherical coordinates of local spins and the orbital angles for the four Mn atoms (similar to how this was done in [1]). Hamiltonian (1) is axially symmetric in spin space, with the symmetry axis being aligned with the magnetic field, irrespective of the orientation of the crystallographic axes. It is this situation that is characteristic of strong magnetic fields (higher than the magnetic anisotropy field). It was shown in [8] that the magnetization of a manganite single crystal ceases to be dependent on the direction of an applied field with respect to the crystallographic axes for $\mu_0 H > 1$ T. The total energy is minimal when the total FM moment of the spin subsystem is directed along the magnetic field. By choosing the polar axis to be along the FM moment of the structure (parallel to the magnetic field) and the azimuthal axis to be in the plane defined by any two spins, we reduce the number of variables and, thus, take into account the degeneracy associated with the symmetry of the spin part of the Hamiltonian. Since all magnetic structures of the ground state are collinear or coplanar [1], one can eventually reduce the number of variables to seven. As follows from calculations, the orbital angles within the same phase do not change as the applied field is increased. Thus, the action of a magnetic field within a phase reduces actually only to a variation of the three angles between the spin sublattices, θ_{ij}^s, i.e., to a coplanar canting of the spin structure toward the direction of the field.

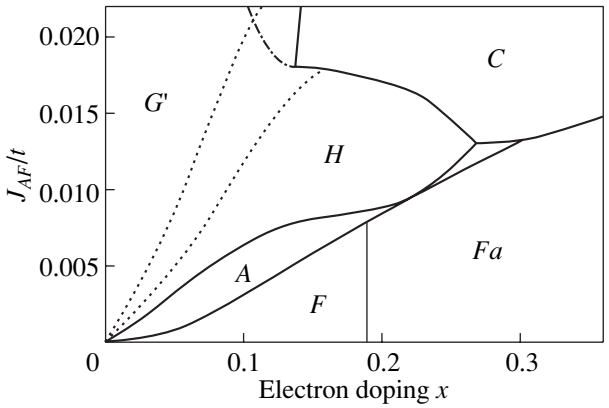

Fig. 1. Phase diagram of the ground state of a manganite with four manganese atoms per unit cell calculated for the parameters $J_H = 2.5t$ and $\Delta = 1.5tx$. Phase notation is given in the text.

The parameters of the model are the dimensionless quantities J_{AF}/t, J_H/t, and Δ/t.

3. To consider the dependence of magnetization on external magnetic field, we use the manganite ground-state phase diagram obtained by us earlier for $\mathbf{H} = 0$ in [1]. Figure 1 displayspart of this diagram in J_{AF}/t versus x coordinates calculated for the manganite model with four manganese atoms in the unit cell of a *Pnma* structure for the model parameters $J_H = 2.5t$ and $\Delta = 1.5tx$. In this diagram, *G*' stands for the canted coplanar, *C* and *A* stand for the collinear AFM structures, and *F* and *Fa* denote FM structures with different types of orbital ordering. Phase *H* is a collinear ferrimagnetic structure in which one of the four local spins is antiparallel to the other three. Its cell-averaged local moment is $\langle m_z \rangle/m = 1.5\mu_B$, which is half the saturated FM moment. The existence of this phase is a unique feature of the four-sublattice model; this phase does not exist in the simpler and universally accepted model with two manganese atoms in a unit cell. Phase *H* can be conceived of as the following collinear superposition of basis vectors **F**, **A**, **C**, and **G** of irreducible representations of the *Pnma* symmetry group:

$$\mathbf{H} = \frac{1}{2}(\mathbf{F}-\mathbf{A}-\mathbf{C}-\mathbf{G}). \qquad (2)$$

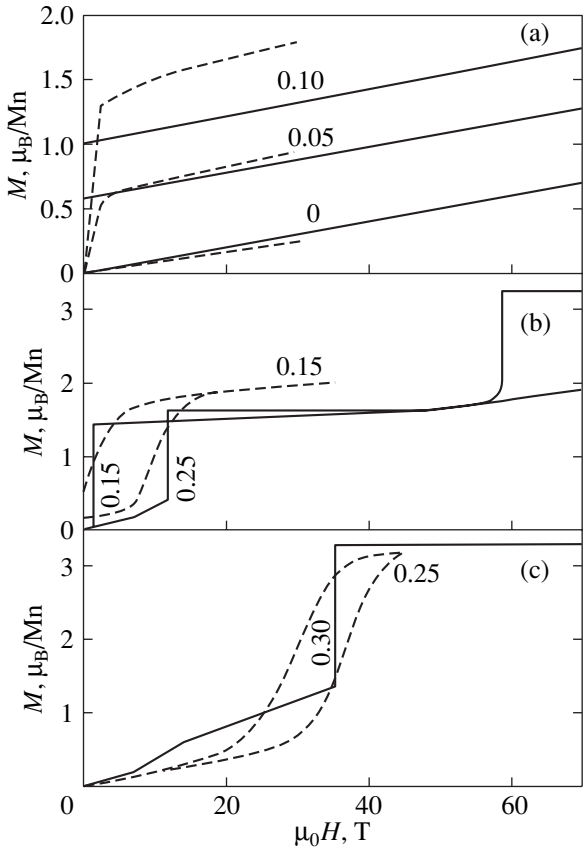

Fig. 2. Theoretical relations connecting magnetization with magnetic field and calculated for $J_{AF} = 0.019t$, $J_H = 2.5t$, and $\Delta = 1.5tx$ for three electron concentration ranges (solid lines): (a) $x < 0.14$, (b) $0.14 < x < 0.27$, and (c) $x > 0.27$. Dashed lines represent experimental relations for $Sm_xCa_{1-x}MnO_3$ [6].

The boundary between *G*' and *H* is not sharp; in fact, they are separated by a transition region in which the *G*' structure is continuously canted to become phase *H* as *x* is increased. A more detailed description of all the magnetic and orbital structures can be found in [1].

We calculated the dependence of magnetization *M* on magnetic field for different electron concentrations *x* by using the cross section of the phase diagram that corresponds to the interatomic exchange parameter $J_{AF} = 0.019t$ lying in the region of realistic values where, as *x* increases, the phase diagram predicts alternation of the *G*' and *C* phases and then (for $x > 0.4$) phase *A*; this alternation is usually observed in manganites in the electron doping region [2].

The action of an external magnetic field favoring FM ordering of local spins corresponds effectively to a shift on the phase diagram toward lower values of the J_{AF}/t parameter at fixed *x*. Therefore, the phase diagram has three electron concentration regions within which the magnetization behaves differently as the external magnetic field is increased. In the first region ($x < 0.14$), the starting phase *G*' persists up to very strong fields. In the second region ($0.14 < x < 0.27$), the system transfers, with increasing field, from phase *C* first to phase *H* and subsequently to the strongest magnetized phase *F*. In the third case (for $x > 0.27$), the system converts from phase *C* directly to the saturated FM phase.

Numerical calculations based on Hamiltonian (1) corroborate the qualitative pattern of the behavior of *M* with increasing *H*. Figure 2 illustrates the behavior of magnetization (measured in Bohr magnetons per manganese atom) for all three cases. The dashed lines indicate experimental data obtained for the $Sm_xCa_{1-x}MnO_3$ system. Throughout the field range covered, up to 70 T (for this field, $\mu_B H/t = 0.04$, where $t = 0.1$ eV), the magnetization follows a nearly linear course, $M = M_0 + \chi H$, for $x = 0$, 0.05, and 0.10 in the first region (Fig. 2a). Note that the magnetic susceptibility remains almost the same with increasing *x*, while the initial magnetization M_0 grows monotonically. A metamagnetic transition can only take place at still higher magnetic fields.

Within the region $0.14 < x < 0.27$ (Fig. 2b) in fields below 20 T, phase *C* makes a transition to phase *H* with a magnetization slightly in excess of 1.5 μ_B due to the e_g electrons. The actual value of the critical transition field depends on the distance from the starting point ($J_{AF} = 0.019t$) to the interphase boundary on the diagram; more specifically, the larger this distance, the higher the critical field. Simultaneously with a change in the type of magnetic structure, the phase transition brings about a sharp change in the character of orbital ordering. The behavior of magnetization above the transition point depends on whether the transition occurred directly to the *H* phase (subregion $0.16 < x < 0.27$) or to the strongly canted phase *G*', which is close to *H* (subregion $0.14 < x < 0.16$). For example, for $x = 0.25$ and a field $\mu_0 H = 12$ T, the $C \longrightarrow H$ transition occurs, after which the magnetization remains constant as the external magnetic field increases to $\mu_0 H = 50$ T; then, another metamagnetic transition occurs at $\mu_0 H = 60$ T, now to the saturated FM phase. For $x = 0.15$, after the $C \longrightarrow G'$ transition at $\mu_0 H = 2$ T, one observes a weak increase in magnetization throughout the field range covered. In the third region ($0.27 < x < 0.36$; Fig. 2c), only one transition is possible, from the AFM phase *C* directly to the FM orbitally ordered phase *Fa*. Thus, for $x = 0.3$, the applied field first cants the spin structure of the starting phase *C*, after which, at $\mu_0 H \approx 35$ T, a transition to the saturated FM phase occurs.

The dashed lines in Fig. 2 show the results of low-temperature magnetization measurements carried out in pulsed magnetic fields on the $Sm_xCa_{1-x}MnO_3$ system ($x \le 0.33$) [6], which also suggest the existence of three types of *M*(*H*) behavior. The boundaries of the regions are, however, somewhat different: $x \le 0.1$, $0.1 < x < 0.2$, and $x \ge 0.2$.

In the first region (Fig. 2a), our calculations agree qualitatively with the experimental data obtained in fields in excess of 7–10 T. The pronounced discrepancy

in magnetization seen at $x = 0.1$ should apparently be assigned to the model being too rough. The fact that the magnetic susceptibility for all x in this region is approximately the same as in pure $CaMnO_3$ suggests that the magnetic sublattice canting determines the $M(H)$ dependence in strong magnetic fields. The experimental results obtained in this doping region are treated in [6] in terms of phase separation, more specifically, the appearance of embedded FM regions in a G-type AFM matrix, and it is these regions that are responsible for the increase in magnetization with increasing x. This hypothesis is also supported by neutron diffraction studies and electrical resistivity measurements performed on the samples. However, the large remanent magnetization cannot be explained in terms of phase separation. Assuming complete macroscopic phase separation, where all free carriers are concentrated within the FM regions, the maximum possible magnetization (per Mn atom) can be estimated using the relation $M_0 = g\mu_B x(S + x_c/2)/x_c$ with $g = 2$, where x_c is the lowest electron concentration at which FM ordering can occur in the manganites. In manganites, we generally have $x_c \geq 0.5$, because the FM ground state has been observed only in the hole doping region [2]. For $x = x_c$, the cluster magnetization M_0 is $(3 + x_c)\mu_B$, while for $x = 0.1$, we have $M_0 = 0.7\mu_B$, which is half the remanent magnetization of $Sm_{0.1}Ca_{0.9}MnO_3$ obtained by linear extrapolation to $H = 0$ from the field region $10 < \mu_0 H < 35$ T (Fig. 2a). Now, if we assume $M_0 = 1.4\ \mu_B$, then x_c will be 0.23. At this electron concentration, however, the AFM phase C is the ground state for all manganites. If phase separation reduces to the formation of one-electron FM polarons (microscopic phase separation), then $M_0 = g(7/2)\mu_B x$ [9], which yields the same estimate, $M_0 = 0.7\mu_B$, for $x = 0.1$.

Figure 3 plots a theoretical dependence of magnetization on electron concentration (solid line), calculated for $J_{AF} = 0.019t$ using Hamiltonian (1). The various symbols in Fig. 3 specify the available experimental data on magnetization M_0, which were obtained in weak magnetic fields or found by extrapolation to $H = 0$, for the calcium-based manganites $R_xCa_{1-x}MnO_3$ (R = La [4], Sm [5, 6], Y [9], Pr [10], Ho [11], Bi [12]) in the region of their electron doping, $0 < x < 0.2$. Figure 3 also shows a region where, according to the above estimates, the values of magnetization are not at odds with the concept of complete phase separation (shaded region). The points Sm(I) and Sm(II) correspond to data on M_0 derived by linear extrapolation to $H = 0$ from regions $\mu_0 H < 7$ T for dc fields [5] and regions $\mu_0 H < 35$ T [6] for pulsed magnetic fields. Unfortunately, the data for Pr and Ho are somewhat fragmentary. Nevertheless, neutron diffraction data suggest that the manganites doped with holmium and bismuth have a homogeneous canted G structure (for $x < 0.09$ in the case of bismuth). The manganites doped by La [4] and Y [9] have a magnetization that, judging from the above estimates, can be identified with total phase separation. The behavior of the magnetization of $Sm_xCa_{1-x}MnO_3$ in the field region $\mu_0 H < 10$ T (Fig. 2a) apparently exhibits incomplete phase separation, with part of the e_g electrons remaining in the canted AFM phase G'. Such a pattern was proposed in [12] for bismuth–calcium manganites with $x > 0.09$. The crossover of magnetization to a linear dependence above $\mu_0 H > 10$ T, where the magnetic susceptibility is close to that calculated for the G' canted phase, implies transition of the system to a homogeneous phase state. The field-induced increase in FM canting improves the conditions for conduction in the AFM matrix and possibly fosters transition of free electrons from the FM clusters to this matrix, thus reducing the cluster volume. As a result, the system becomes more conducting and the spin canting increases still more due to the double exchange, to eventually become the only source of the FM moment.

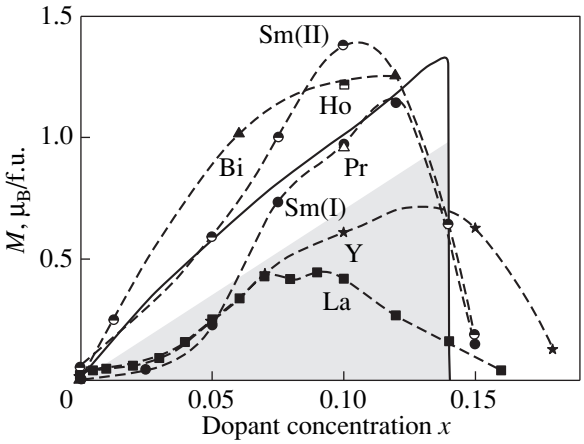

Fig. 3. Experimental low-temperature values of the magnetization of $R_xCa_{1-x}MnO_3$ (R = La, Sm, Y, Pr, Ho, Bi) measured at different values of x [4–6, 9–12]. The shaded region corresponds to complete phase separation. Solid line plots the theoretical $M(x)$ relation for $J_{AF}/t = 0.019$, $J_H/t = 2.5$, and $\Delta/t = 1.5x$.

In the second region (Fig. 2b), $Sm_{0.15}Ca_{0.85}MnO_3$ is driven by the field from phase C to an unsaturated state whose magnetization $M \cong 2\mu_B$ is slightly higher than the above value calculated for the H structure. This is apparently associated with the original phase separation $C + G'$ near the interphase boundary with a remanent magnetization of $\sim 0.3\mu_B$ due to an admixture of the G' phase. In a field of ~5 T, only the AFM matrix C undergoes a metamagnetic transition to the H phase, whereas the component G' remains practically unchanged. The further weak growth of the magnetization should most likely be assigned to field-induced canting of the impurity structure G'. The transition of the fairly stable matrix phase H to the saturated FM state should be expected to occur in much stronger fields. Thus, in this phase, the magnetic field–driven phase transition can also be interpreted as a metamag-

netic transition between homogeneous phases, which does not involve an increase in the degree of phase separation.

A magnetic field transfers the $Sm_{0.25}Ca_{0.75}MnO_3$ manganite from phase *C* directly to the saturated FM state (Fig. 2c), which, as shown by calculations, is characteristic of the third concentration region.

4. Thus, the response of manganites to a strong magnetic field in the electron doping region can be qualitatively interpreted in terms of a phase diagram of homogeneous states obtained for zero-field conditions. An external magnetic field may serve as a probe for the part of the phase diagram that is beyond realistic values of the exchange parameters (J_{AF}/t, J_H/t) and thus can be used as an experimental tool to better understand the ground state of the manganites. The existence of a doping region with unsaturated ferromagnetism in strong fields can be accounted for within a more general model assuming four manganese atoms per unit cell. Any analysis of a magnetic structure in this region (for instance, based on neutron diffraction measurements) should take into account the possible presence of the ferrimagnetic phase *H*, which is a collinear superposition of elementary spin structures described by Eq. (2). The selection rules valid for diffraction maxima in this case allow any combination of the Miller indices, which makes identification of this phase a far from easy problem.

REFERENCES

1. S. M. Dunaevsky and V. V. Deriglazov, Fiz. Tverd. Tela (St. Petersburg) **46** (3), 495 (2004) [Phys. Solid State **46**, 510 (2004)].
2. S. M. Dunaevsky, Fiz. Tverd. Tela (St. Petersburg) **46** (2), 193 (2004) [Phys. Solid State **46**, 193 (2004)].
3. S. M. Dunaevsky and V. V. Deriglazov, Fiz. Tverd. Tela (St. Petersburg) **45** (4), 681 (2003) [Phys. Solid State **45**, 714 (2003)].
4. J. J. Neumeier and J. L. Cohn, Phys. Rev. B **61** (21), 14319 (2000).
5. R. Mahendiran, A. Maignan, C. Martin, M. Hervieu, and B. Raveau, Phys. Rev. B **62** (17), 11644 (2000).
6. M. Respaud, J. M. Broto, H. Rakoto, J. Vanacken, P. Wagner, C. Martin, A. Maignan, and B. Raveau, Phys. Rev. B **63** (14), 144426 (2001).
7. S. M. Dunaevsky and V. V. Deriglazov, Preprint No. 2522, PNPI (Petersburg Nuclear Physics Inst., St. Petersburg, 2003).
8. J. Hemberger, A. Krimmel, T. Kurz, H.-A. Krug von Nidda, V. Yu. Ivanov, A. A. Mukhin, A. M. Balbashov, and A. Loidl, Phys. Rev. B **66** (9), 094410 (2002).
9. H. Aliaga, M. T. Causa, B. Alascio, H. Salva, M. Tovar, D. Vega, G. Polla, G. Leyva, and P. Konig, J. Magn. Magn. Mater. **226–230**, 791 (2001).
10. C. Martin, A. Maignan, M. Hervieu, B. Raveau, Z. Jirak, M. M. Savosta, A. Kurbakov, V. Trounov, G. Andre, and F. Bouree, Phys. Rev. B **62** (10), 6442 (2000).
11. K. Hagdorn, D. Hohlwein, J. Ihringer, K. Knorr, W. Prandl, H. Ritter, H. Schmid, and Th. Zeiske, Eur. Phys. J. B **11**, 243 (1999).
12. P. N. Santhosh, J. Goldberger, P. W. Woodward, T. Vogt, V. P. Lee, and A. J. Epstein, Phys. Rev. B **62** (22), 14928 (2000).

Translated by G. Skrebtsov

Physics of the Solid State, Vol. 46, No. 12, 2004, pp. 2263–2267. Translated from Fizika Tverdogo Tela, Vol. 46, No. 12, 2004, pp. 2189–2192.

MAGNETISM AND FERROELECTRICITY

Phase Transition in $CdHfO_3$

N. V. Shpilevaya, M. F. Kupriyanov, B. S. Kul'buzhev, and Yu. V. Kabirov

Research Institute of Physics, Rostov State University, pr. Stachki 194, Rostov-on-Don, 344090 Russia

e-mail: shpilevay@mail.ru

Received April 16, 2004

Abstract—The phase transition from an orthorhombic phase (space group *Pnma*) to a rhombohedral phase (space group *R*3*m*) of the $CdHfO_3$ hafnate is investigated using methods of structural analysis. It is shown that crystal lattices of both phases contain polar structural units (octahedra, cubooctahedra). On this basis, it is assumed that the orthorhombic and rhombohedral phases of the $CdHfO_3$ compound are the antiferroelectric and ferroelectric phases, respectively. © *2004 MAIK "Nauka/Interperiodica".*

1. INTRODUCTION

Earlier investigations into the structure and properties of single crystals and ceramic samples of cadmium hafnate $CdHfO_3$ have revealed a phase transition with a maximum of the permittivity at T = 605°C [1, 2]. Aver'yanova *et al.* [1] interpreted this transition as an antiferroelectric phase transition, because the phase observed at room temperature was identified as an orthorhombic phase and was characterized by a superstructure (with respect to perovskite) unit cell. As follows from the data obtained by Dernier and Remeika [3], this phase of the $CdHfO_3$ compound has an orthorhombic unit cell with space group *Pbnm* and the unit cell parameters A_O = 5.5014(8) Å, B_O = 5.6607(8) Å, and C_O = 7.969(1) Å. According to the temperature investigations performed by Spinko *et al.* [2], the $CdHfO_3$ compound undergoes the following sequence of phase transitions with an increase in temperature: orthorhombic phase *I* (0–605°C) ⟶ orthorhombic phase *II* (605–700°C) ⟶ rhombohedral phase (above 700°C). However, Dernier and Remeika [3] did not reveal orthorhombic phase *II*. These authors established that the high-temperature rhombohedral phase has a hexagonal unit cell with space group $R\bar{3}c$ and the unit cell parameters A_H = 5.747(4) Å and C_H = 13.49(1) Å.

Unfortunately, the data available in the literature on the crystal structure and properties of the $CdHfO_3$ compound and its transformations with temperature are very scarce. Moreover, it remains unclear whether cadmium hafnate is a ferroelectric or an antiferroelectric. In this respect, the purpose of the present work was to refine the structural parameters of the $CdHfO_3$ compound at room temperature and in the temperature ranges of the aforementioned phase transitions.

2. EXPERIMENTAL TECHNIQUE

The structure of polycrystalline $CdHfO_3$ was investigated using x-ray diffraction on a DRON-3M diffractometer (CuK_α radiation) equipped with a UVR-1200 high-temperature chamber. The temperature of the sample at each point was maintained constant to within ±0.5 K with the use of a VRT-2 heat controller. The x-ray diffraction patterns of the $CdHfO_3$ compound were measured in the Bragg–Brentano geometry ($20° < 2\theta < 100°$; scan step, 0.08 deg; exposure time per frame, 1 s) with computer data recording. The x-ray diffraction measurements were performed at different temperatures in steps of ΔT = 50 (away from the phase transition) and 20 K (in the vicinity of the phase transition). The structure refinement of the $CdHfO_3$ compound was carried out with the PowderCell 2.3 program package [4]. The unit cell parameters and atomic (thermal, positional) parameters were refined for possible variants of space groups.

3. RESULTS AND DISCUSSION

Proper processing of the experimental data made it possible to refine the space group of symmetry and to determine the atomic parameters of the crystal structure of the $CdHfO_3$ hafnate over the entire range of temperatures under investigation.

As in [3], it was established that, in the temperature range $20 \le T \le 500$°C, the crystal structure of the $CdHfO_3$ hafnate has orthorhombic symmetry with space group *Pnma*. The temperature investigations into the structural transformations of the $CdHfO_3$ compound demonstrated that, in the range $550 \le T \le 730$°C, the orthorhombic (*O*) phase coexists with the rhombohedral (*R*) phase characterized by space group *R*3*m*. Figure 1 depicts fragments of the x-ray diffraction patterns of the $CdHfO_3$ compound with different contents of the orthorhombic and rhombohedral phases at temperatures of 690 and 710°C. The structural parameters

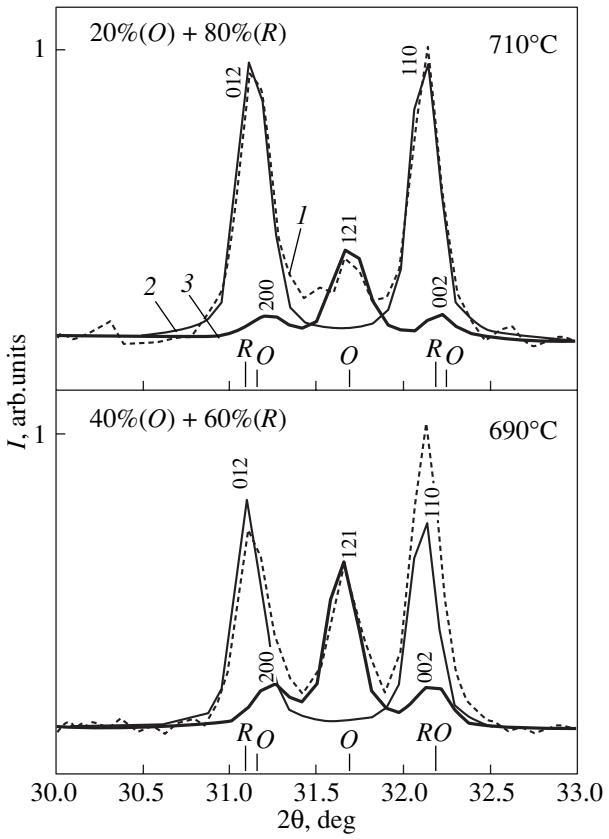

Fig. 1. Fragments of (*1*) the experimental x-ray diffraction patterns of the $CdHfO_3$ compound with different contents of the orthorhombic and rhombohedral phases, (*2*) the calculated x-ray diffraction patterns of the $CdHfO_3$ compound in the orthorhombic phase, and (*3*) the calculated x-ray diffraction pattern of the $CdHfO_3$ compound in the rhombohedral phase.

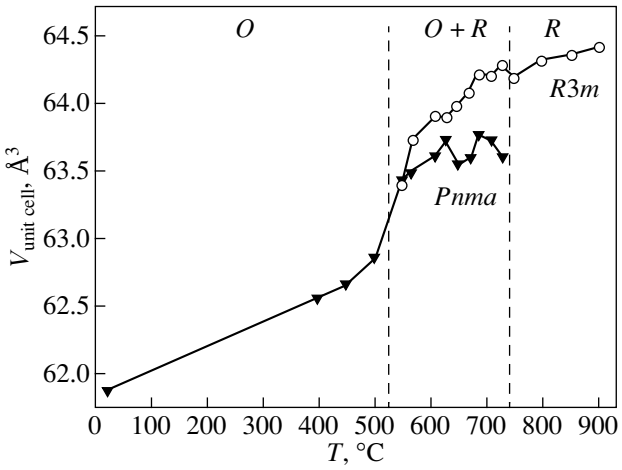

Fig. 2. Temperature dependences of the volumes of the unit subcells in the crystal structure of the $CdHfO_3$ compound in the orthorhombic and rhombohedral phases.

of the orthorhombic and rhombohedral phases and their contents in the $CdHfO_3$ compound were determined by processing the x-ray diffraction patterns. It was found that, at temperatures above 730°C, the $CdHfO_3$ compound has a rhombohedral structure.

The table presents the structural parameters of the orthorhombic phase at a temperature of 20°C and the rhombohedral phase at 900°C. Here, we used the following designations: A_O, B_O, and C_O are the parameters of the orthorhombic unit cell, which is a superstructure (fourfold) unit cell with respect to the monoclinic (*M*) perovskite subcell with the lattice parameters $a_M = c_M$, b_M, and β_M; A_H and C_H are the unit cell parameters of the rhombohedral phase in the hexagonal (*H*) setting; and a_R and α_R are the parameters of the rhombohedral perovskite subcell. The atomic coordinates *x*, *y*, and *z* are given in terms of cell fractions. The table also lists the metal–oxygen bond lengths $l_{(Me\text{–}O)}$ calculated from the structural parameters. In the orthorhombic phase, the metal–oxygen bonds have different lengths: the Cd atoms form two short and two long bonds with O atoms of the *II* type (O*II*), which are located in the same layer (perpendicular to the B_O edge), and four long and four short bonds with O atoms of the *I* type (O*I*), which are arranged in the layer occupied by the Hf atoms. The Hf atoms form two short and two long bonds with the O*I* atoms and two relatively long bonds with the O*II* atoms. In the rhombohedral phase, the Cd atoms form six lengthened bonds with the O atoms located in the same layer of the closest cubic packing (perpendicular to the C_H edge) and six shortened bonds with the O atoms positioned in the nearest layers of the packing. The Hf atoms are arranged between the layers of the closest cubic packing and form three short and three long bonds with the O atoms of the adjacent layers.

It can be seen from the table that the Debye–Waller factors *B* for individual atoms involved in the crystal structure of the $CdHfO_3$ compound are characterized by the following feature: the Debye–Waller factor *B* for cadmium atoms is approximately equal to the factor *B* for hafnium atoms and substantially exceeds the value of *B* for oxygen atoms in both the orthorhombic and rhombohedral phases. This relationship between the thermal parameters implies that the root-mean-square displacements of the metal atoms are considerably greater than those of the oxygen atoms. A similar feature was revealed earlier for many lead-containing perovskites studied in [5–8] and was explained by a superposition of thermal atomic displacements and statistically disordered local displacements of the atoms involved.

The temperature dependences of the volumes of the unit subcells in the crystal structure of the $CdHfO_3$ compound in the orthorhombic and rhombohedral phases (Fig. 2) were constructed from data on the temperature dependences of the lattice parameters for the perovskite subcells of both phases. On this basis, we

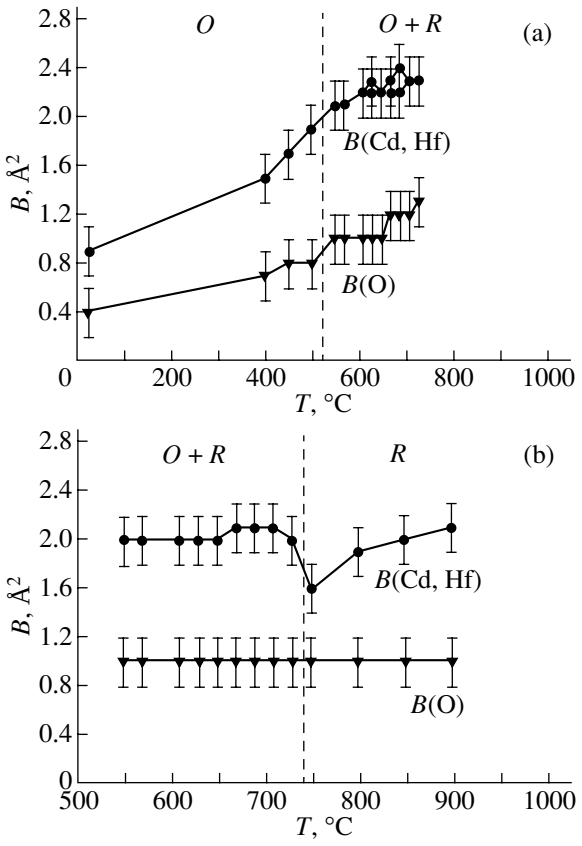

Fig. 3. Temperature dependences of the Debye–Waller factors for individual atoms in the crystal structure of the $CdHfO_3$ compound in the (a) orthorhombic and (b) rhombohedral phases.

determined the coefficients of volume expansion β. The coefficients of volume expansion for the monoclinic and rhombohedral subcells are designated as β_M and β_R, respectively. It can be seen that the coefficients of volume expansion β for the pure orthorhombic and rhombohedral phases are considerably smaller than those obtained in the temperature range of coexistence of these phases: the coefficient β_M in the range $20 \le T \le 525$°C is approximately equal to the coefficient β_R in the range $740 \le T \le 900$°C and amounts to 2.86×10^{-5} K^{-1}, whereas the values of β_M and β_R in the range $525 \le T \le 740$°C are approximately equal to 12.7×10^{-5} K^{-1}. It should be noted that, with a decrease in the temperature, the volume of the perovskite subcell drastically decreases (by 0.687 Å^3) upon formation of the orthorhombic phase at 730°C (this behavior is characteristic of phase transitions to an antiferroelectric phase).

From analyzing the temperature dependences of the metal–oxygen bond lengths in the crystal structure of the $CdHfO_3$ compound, we can make the following inferences. As the temperature increases, the maximum changes are observed in the Cd–O bond lengths for both the orthorhombic and rhombohedral phases. For example, upon heating of the orthorhombic phase in the range $650 \le T \le 710$°C, the long Cd–O*II* bond is significantly shortened and the short Cd–O*I* bond is lengthened; as a result, the lengths of these bonds become nearly equal to each other. The long Cd–O*I* bond is also substantially shortened. Upon heating of the rhombo-

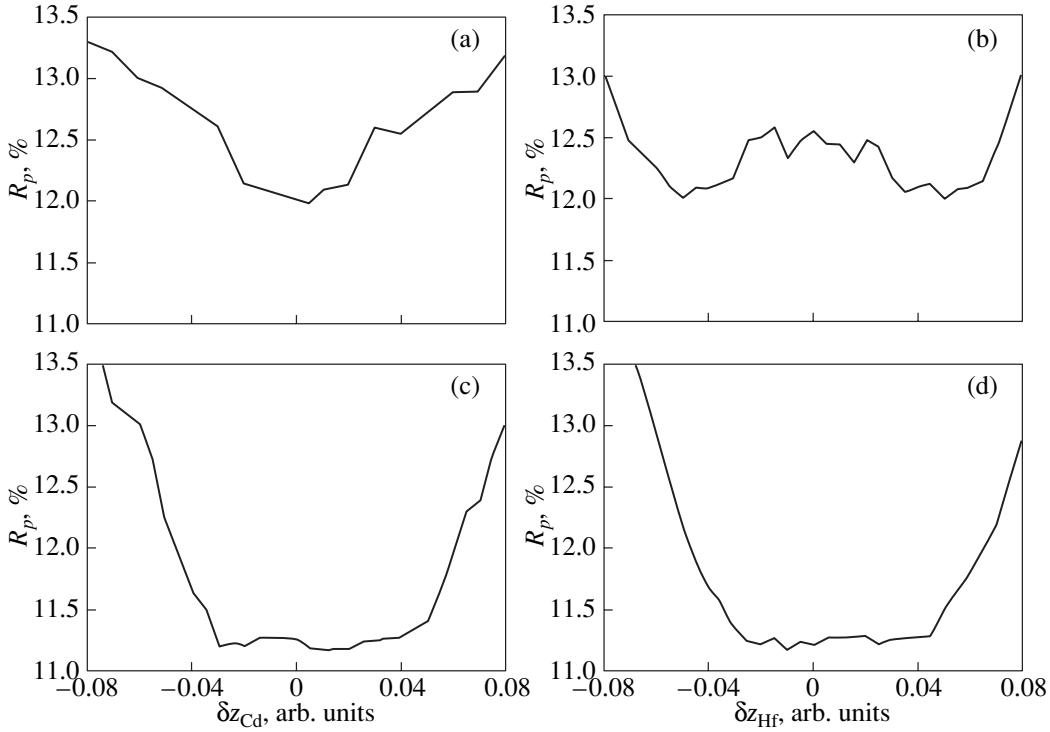

Fig. 4. Dependences of the discrepancy factor R_p on the atomic displacements for the $CdHfO_3$ compound in the (a, b) orthorhombic and (c, d) rhombohedral phases.

Structural parameters and metal–oxygen bond lengths $l_{(Me–O)}$ for the orthorhombic (*O*) and rhombohedral (*R*) phases of the $CdHfO_3$ compound

$CdHfO_3$(*O*) *T* = 20°C					$CdHfO_3$(*R*) *T* = 900°C				
Space group *Pnma* = D_{2h}^{16}					Space group *R*3*m* = C_{3v}^{5}				
N = 51					*N* = 28				
P = 12					*P* = 8				
A_O = 5.6559 Å		$a_M = c_M$ = 3.9423 Å			A_H = 5.5838(5) Å		a_R = 4.0109 Å		
B_O = 7.9654 Å		b_M = 3.9827 Å			C_H = 7.1592 Å		α_R = 91°47′		
C_O = 5.4934 Å		β_M = 91°47′							
Atom	*x*	*y*	*z*	*B*, Å^2	Atom	*x*	*y*	*z*	*B*, Å^2
Cd	0.550	0.250	0.505	0.9(2)	Cd	0.000	0.000	0.010	2.1
Hf	0.500	0.000	0.000	0.9	Hf	0.000	0.000	0.510	2.1
O*I*	0.260	0.020	0.235	0.4	O	0.550	0.550	0.000	1
O*II*	0.530	0.250	0.030	0.4					
Atom		Bond length			Atom		Bond length		
Me	O	$l_{(Me–O)}$, Å			*Me*	O	$l_{(Me–O)}$, Å		
Cd	O*I* (1)	2.79(2)			Cd	O(1)	2.79		
Cd	O*I* (2)	2.54			Cd	O(2)	2.73		
Cd	O*II* (1)	2.77			Hf	O(1)	2.05		
Cd	O*II* (2)	2.53			Hf	O(2)	1.96		
Hf	O*I* (1)	1.88							
Hf	O*I* (2)	2.08							
Hf	O*II*	2.01							

Note: *N* is the number of reflections, and *P* is the number of parameters refined.

hedral phase, the length of the short Cd–O bond increases and approaches the length of the long Cd–O bond. The Hf–O bond lengths change only slightly with a variation in the temperature for both the orthorhombic and rhombohedral phases.

Figure 3 shows the temperature dependences of the Debye–Waller factors for individual atoms involved in the crystal structure of the $CdHfO_3$ compound in the orthorhombic and rhombohedral phases. It can be seen from this figure that the Debye–Waller factors *B* for cadmium and hafnium atoms in the crystal structure of the orthorhombic and rhombohedral phases are substantially larger than the Debye–Waller factors *B* for oxygen atoms. It is worth noting that the Debye–Waller factors *B* for cadmium, hafnium, and oxygen atoms in the crystal structure of the orthorhombic phase monotonically increase with an increase in the temperature, whereas the Debye–Waller factor *B* for oxygen atoms in the crystal structure of the rhombohedral phase does not depend on the temperature. The sharp minimum observed in the temperature dependences of the Debye–Waller factors *B* for cadmium and hafnium atoms at temperatures $T \approx 730$–750°C (Fig. 3b) is most likely associated with the first-order phase transition from the orthorhombic phase to the rhombohedral phase [9].

For both phases, the distances *d* between the metal atoms and the centers of gravity O_Σ of the oxygen atoms involved in their nearest environment were calculated from the data presented in the table. (Note that the cadmium atoms are located in the cubooctahedral oxygen environment, whereas the hafnium atoms are arranged in the octahedral environment.) As a result, we obtained the distances $d_{(Cd–O_\Sigma)} = 0.21$ Å and $d_{(Hf–O_\Sigma)} = 0$ for the orthorhombic phase at $T = 20$°C. For the rhombohedral phase, we determined the distances $d_{(Cd–O_\Sigma)} = d_{(Hf–O_\Sigma)} = 0.072$ Å at $T = 900$°C. It was found that, in both phases, there are atomic groups in which the centers of gravity of the oxygen and metal atoms are displaced with respect to each other. Therefore, we can assume that these phases possess antiferroelectric and ferroelectric properties.

In order to verify the validity of the structural model obtained for the $CdHfO_3$ compound in the orthorhombic and rhombohedral phases, we analyzed the discrepancy factor R_p as a function of the atomic coordinates (Fig. 4). It can be seen from Figs. 4a and 4b that, for the

orthorhombic phase, the minimum discrepancy factor R_p is achieved at $\delta z_{Cd} = 0.005$ and $\delta x_{Cd} = \pm 0.05$. Thus, the refinement of the $CdHfO_3$ structure in this phase leads to the most probable structural model, according to which the cadmium atoms are characterized by antiparallel displacements along the x axis. For the rhombohedral phase, the discrepancy factor R_p reaches a minimum at $\delta z_{Cd} = \delta z_{Hf} = 0.01$ (Figs. 4c, 4d).

ACKNOWLEDGMENTS

We would like to thank R.I. Spinko for supplying the cadmium hafnate samples used in our experiments.

This work was supported by the Russian Foundation for Basic Research, project no. 04-03-32039.

REFERENCES

1. L. I. Aver'yanova, I. N. Belyaev, Yu. I. Gol'tsov, L. A. Solov'ev, R. I. Spinko, and O. I. Prokopalo, Fiz. Tverd. Tela (Leningrad) **10** (11), 3416 (1968) [Sov. Phys. Solid State **10**, 2698 (1969)].
2. R. I. Spinko, V. N. Lebedev, R. V. Kolesova, and E. G. Fesenko, Kristallografiya **18** (4), 849 (1973) [Sov. Phys. Crystallogr. **18**, 536 (1973)].
3. P. D. Dernier and J. P. Remeika, Mater. Res. Bull. **10**, 187 (1975).
4. W. Krause and G. Nolze, J. Appl. Crystallogr. **29**, 301 (1996).
5. P. Bonneau, H. Garnier, E. Husson, and A. Morell, Mater. Res. Bull. **24**, 201 (1989).
6. V. Chernyshov, S. Zhukov, S. Vakhrushev, and H. Shenk, Ferroelectr. Lett. Sect. **23** (1), 43 (1997).
7. A. R. Lebedinskaya and M. F. Kupriyanov, Phase Transit. **75** (3), 289 (2002).
8. R. Kolesova, V. Kolesov, M. Kupriyanov, and R. Skulski, Phase Transit. **68**, 621 (1999).
9. K. Itoh and K. Fujihara, Ferroelectrics **120**, 175 (1991).

Translated by O. Borovik-Romanova

Physics of the Solid State, Vol. 46, No. 12, 2004, pp. 2268–2274. Translated from Fizika Tverdogo Tela, Vol. 46, No. 12, 2004, pp. 2193–2199.

MAGNETISM AND FERROELECTRICITY

Memory Effect in $Ba_{0.85}Sr_{0.15}TiO_3$ Ferroelectric Films on Silicon Substrates

É. N. Myasnikov*, S. V. Tolstousov*, and K. Yu. Frolenkov**

**Rostov State Pedagogical University, Rostov-on-Don, 344082 Russia*

***Orel State Technical University, Orel, 302020 Russia*

e-mail: mastrozin@mail.ru, Lara@ostu.ru

Received February 24, 2004; in final form, May 13, 2004

Abstract—$Ba_{0.85}Sr_{0.15}TiO_3$ ferroelectric films on single-crystal silicon wafers were grown and studied. X-ray diffraction and electron microscopy studies showed that the films are characterized by a limited texture with a perovskite structure. It was shown that the grown films can be used as recording media for nonvolatile rerecorded data carriers in kinematic-type external memory devices. A possible mechanism of data recording and storage in the structures was considered. *© 2004 MAIK "Nauka/Interperiodica".*

1. INTRODUCTION

Perovskite-type ferroelectric materials characterized by residual polarization, which can be switched by an external field, and high permittivity were discovered in the late 1950s and early 1960s [1, 2]. Unfortunately, the deposition of such materials on semiconductor substrates for producing nonvolatile memory was complicated because of the absence of thin-film growth technology [3]. However, after the advent of methods for growing high-temperature superconducting films in the mid-1980s, it turned out that these technologies could be applied to grow thin ferroelectric films. For this reason, significant interest again arose in the application of ferroelectric materials for nonvolatile memory devices [3–11].

The operating principle of such devices is as follows [1–8]. A ferroelectric film contains a significant number of domains characterized by a certain electric polarization vector. The total polarization of individual domains characterizes the spontaneous polarization of the film, i.e., the nonzero total dipole moment per unit volume. The magnitude and spatial orientation of spontaneous polarization can be changed under an external electric field. The film becomes single-domain in strong fields. Exposing a strong opposite electric field to a certain surface area can repolarize domains of the ferroelectric film within this area, which can be detected. Thus, the polarization of ferroelectric films can be used to develop nonvolatile memory devices in which repolarized domains are information carriers. Such devices have a number of advantages over conventional magnetic and optical ones.

The objective of this work is to study the possible application of ferroelectric films of complex oxides, deposited onto silicon substrates using a novel technology, as recording media of information carriers for kinematic-type external memory devices, as well as to study the mechanisms of data recording and storage and the technical characteristics of these structures.

2. EXPERIMENTAL

It is known that the physical properties of ferroelectric films depend heavily on the state of their surface and of the silicon substrate surface, stoichiometry, crystallinity, density, microstructure, crystallographic orientation, the presence of structural defects, and, hence, on the methods of film growth [3, 7]. This dependence causes significant differences in the parameters of bulky and film ferroelectrics and, on the other hand, results in a wide scatter in the characteristics of films themselves [1, 7].

The initial composition of a ferroelectric film was selected by us such that (i) the film and substrate would be characterized by approximately identical temperature expansion coefficients, (ii) the film material would demonstrate good adhesion to silicon, and (iii) the memory effect would be significant. These requirements are satisfied by compositions whose main components are BaO, TiO_2, ZrO_2, SrO, and PbO [8]. The best results were obtained for films of a $Ba_{0.85}Sr_{0.15}TiO_3$ solid solution, the data on which are considered below. As a substrate for film deposition, we used single-crystal KDB-12 and KÉF-4.5 silicon wafers doped with boron (*p*-type conductivity) and phosphorus (*n*-type conductivity), respectively.

The best method for growing thin ferroelectric films of the chosen composition is high-frequency cathode sputtering in an oxygen atmosphere [12].

Stoichiometric-composition targets for cathode sputtering were made by pressing various mixtures of the above-mentioned oxides. Transport of molecules of the target material during cathode sputtering is controlled by the sputtering coefficient selectivity [12].

1063-7834/04/4612-2268$26.00 © 2004 MAIK "Nauka/Interperiodica"

This coefficient depends on the atomic number of the target elements and the evaporation temperature. Therefore, in general, certain components are sputtered preferentially. The reaction of neutral excited atoms knocked out of the target with oxygen atoms becomes possible as they recede from the target and lose energy. The distance at which the reaction takes place depends on the oxygen pressure. If the target–substrate distance exceeds the oxide formation distance, condensation takes place on the molecular level. In addition to what was said above, one should take into account the controlling influence of the silicon substrate temperature on the ordering of the vacuum condensate structure when thin films of complex oxides are grown, especially in the presence of chemically active and volatile components (e.g., lead) [3]. For this reason, optimum growth conditions for ferroelectric films of complex oxides were selected by varying the silicon substrate temperature, oxygen pressure in the vacuum chamber, and the target–substrate distance. Deposition was carried out using a URM-014 setup.

The best properties were exhibited by films grown at substrate temperatures of 450–500°C, oxygen pressures of several tens of pascals in the chamber, and substrate–target distances of several centimeters. Sputtering was carried out at a frequency of 13–14 MHz; the condensation rate (which depends on the magnetic field strength and the HF generator power) reached ~0.01 μm/min. The thickness of grown films, measured using an MII-4 microinterferometer, was 0.50 ± 0.05 μm.

The relative permittivity ε of ferroelectric films was determined by a commonly accepted technique [1, 2] using an E8-2 capacitor bridge, an external low-frequency G3-33 generator, and an F582 null indicator. The measuring field was selected to be the minimum allowed for sensitivity and noise stability reasons.

Measurements were carried out at a measuring field frequency of 1000 Hz. The relative permittivity of the films under study was calculated taking into account the formation of a SiO_2 layer at the silicon substrate surface during HF sputtering in an oxygen atmosphere [7].

X-ray diffraction studies of the deposited films were carried out using a DRON-2.0 diffractometer and the Bragg–Brentano focusing technique in the 2θ mode (θ is the angle between the beam and the reflecting atomic plane) [13, 14]. X-ray diffraction patterns of the films were used to determine the unit cell parameter (splittings of the peak corresponding to spontaneous deformation were not observed), texture type, microstrain $\Delta d/d$ (d is the interplane distance), and size D of coherent-scattering regions. The accuracy of determination of the unit cell parameter, limited by the width of reflections, was ±0.0003 nm. The texture type (preferential orientation of crystals) was estimated from the deviation of the relative reflection intensities from the reference intensities (for a polycrystal). The structural and deformation characteristics $\Delta d/d$ and D, typical of x-ray diffraction [15], were used to describe the film crystallization quality. The quantities $\Delta d/d$ and D were determined from the x-ray reflection widths using the conventional approximation method [16]. The $\Delta d/d$ and D determination errors did not exceed 15 and 30%, respectively. The method did not allow us to determine the size of coherent-scattering regions smaller than 100 nm.

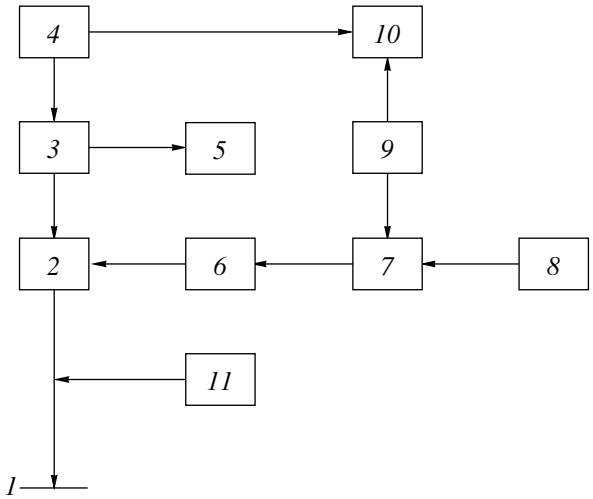

Fig. 1. Block diagram of the measuring testbed: (*1*) wafer with a recording–reproduction probe, (*2*) key of recording–reproduction mode switching, (*3*) reproduction generator ($20 \le \nu \le 50$ MHz), (*4*) B5-47 power supply (0–15 V) of the generator, (*5*) ChZ-34A frequency meter, (*6*) pulse polarity reversal key, (*7*) pulsed amplifier, (*8*) G5-72 master oscillator, (*9*) B5-50 dc voltage supply, (*10*) Shch4313 digital multimeter, and (*11*) precision positioning unit (step is 0.1 μm).

The structure of ferroelectric films of complex oxides deposited onto silicon substrates was studied by the conventional technique [17] using an RÉM-200 electron microscope. Images of the surface of freshly deposited films of complex oxides on silicon substrates and films after plasmachemical etching were obtained with a magnification of 10 000. Plasmachemical etching was carried out in a two-chamber Plasma-600 setup with electrodeless induction excitation of a 600-W charge in a medium containing freon-14 (CF_4) and oxygen [18]. The end of film etching was indicated by an increase in the temperature in the setup chamber, since etching of oxides is not accompanied by heat release [19].

Capacitance–voltage (C–V) characteristics of the structures were measured according to the technique described in [5] by using an electrostatic probe and a testbed, shown schematically in Fig. 1. A probe with a tip rounding radius of 0.5 ± 0.03 μm was specially made by sharpening tungsten wire electrochemically. This probe parameter was measured using an MII-4 microinterferometer.

Capacitance–voltage characteristics were determined as follows [5]. After applying a voltage of any

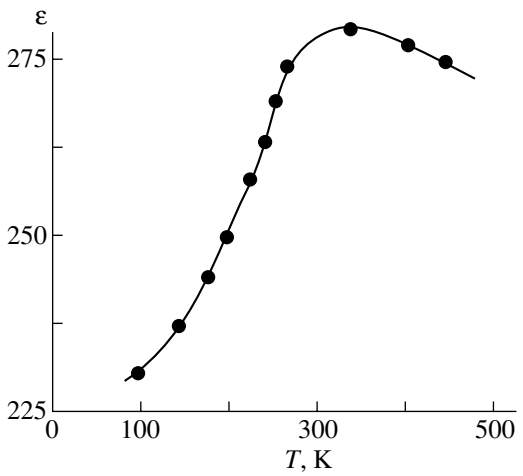

Fig. 2. Temperature dependence of the relative permittivity ε(*T*) of the films under study.

polarity (exceeding the threshold for film polarization switching $U = \pm 80$ V) to the probe, the voltage was decreased in steps to zero with simultaneous measurement of the frequency using a ChZ-34A frequency meter. On reaching zero, the voltage polarity was reversed and the measurement was continued with increasing the voltage up to values exceeding the film switching threshold and then back again. The memory effect mechanism in the structures under study was determined, depending on the direction of tracing the obtained *C–V* hysteresis loops, according to the recommendations given in [20, 21].

To check the reproducibility of the ferroelectric properties of complex-oxide films on silicon substrates, *C–V* characteristics were measured at three randomly chosen points arranged at various distances from the silicon wafer center.

The resolution of the structures was determined using the following technique [5]. A sample fixed in the measuring testbed (Fig. 1) was moved in steps of 0.4 μm with respect to the tungsten probe. The sample displacement was monitored using a readout-measuring system with a mechanotronic transducer. Recording was carried out by applying voltage pulses with an amplitude $U = \pm 80$ V to the probe. The recorded information was determined by measuring the deviation of the reproduction generator frequency with a ChZ-34A frequency meter as a sample was moved in steps of 0.1 μm to the initial position. The measurement results were used to construct the dependence of the deviation of the reproduction generator frequency on the sample displacement with respect to the tungsten probe.

The rate of repolarization of ferroelectric films was determined using the technique proposed by Merz [22], which consists in the following. Rectangular voltage pulses of alternating polarity were applied to the samples under study, and the current pulses arising as the polarization direction was reversed were measured. The current pulse duration characterizes the domain switching time τ_s.

The number of information-rerecording cycles in the structures was monitored using the measuring testbed (Fig. 1). Experimental samples were exposed to voltage pulses of alternating polarity of identical amplitude (±80 V) and duration (50 μs). After 10^2, 10^4, 10^6, 10^7, and 10^8 cycles, the *C–V* characteristics were constructed.

The storage time of signals thus recorded was also determined using the testbed (Fig. 1) by measuring the signal reproduction amplitude after each 12 days (~10^6 s) over 4 months (~10^7 s) and extrapolating the time dependence to longer times. The voltage across flat regions of the sample was preliminarily measured 10 min after its polarization.

3. RESULTS AND DISCUSSION

When studying the temperature dependence of the relative permittivity of complex-oxide films grown on silicon substrates by HF sputtering in an oxygen atmosphere, a maximum in the ε(*T*) curve was detected in the range of the expected ferroelectric phase transition temperature of bulk materials [1] (see Fig. 2). However, this maximum is extremely small and diffuse over a wide temperature range. A smoothing of anomalies in the ε(*T*) dependence follows immediately from the existence of a transition layer [7]. Moreover, the ε(*T*) dependence of the films under study contains distinct features of a diffuse ferroelectric phase transition; this behavior is characteristic of vacuum condensates and is caused by imperfections in their structure [12]. In general, the properties of ferroelectrics undergoing diffuse phase transitions are described (at least approximately) by treating such materials as an assembly of small regions (microvolumes) that exhibit typical ferroelectric behavior but differ in terms of their ferroelectric parameters (this parameter is generally taken to be the Curie temperature T_C [1]).

X-ray diffraction patterns of the structures under study are shown in Fig. 3.

Figure 3a depicts a diffraction pattern of a silicon single crystal ((100) cut), which shows a reflection from the (200) plane at an angle $2\theta = 41.9°$, as well as a set of lines in the angular range of 30°–31° belonging to unidentified silicon compounds (presumably, α quartz SiO_2 and SiO).

Figure 3b shows an x-ray diffraction pattern of an insulator–silicon oxides–silicon composition. The insulator film is significantly textured (there is only one reflection at $2\theta = 57.2°$). The diffraction peak in the range corresponding to the silicon oxides is much stronger, which indicates an increase in the oxide layer thickness. The crystallographic orientation of the film face does not coincide with that of the silicon (100) plane; therefore, there is no reflection from the (200) silicon plane. The film is rather thin, ~0.5-μm thick.

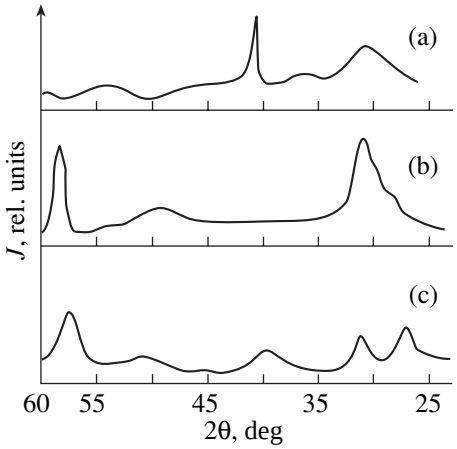

Fig. 3. X-ray diffraction patterns of (a) a (100)-cut silicon single crystal and (b, c) insulator–silicon oxide–silicon compositions with an insulator, thickness of 0.5 and 5.3 μm, respectively.

The increased background can be explained by the fact that the film is in the coalescence stage.

Figure 3c corresponds to a structure similar to that shown in Fig. 3b, but the ferroelectric film thickness is 5.3 μm. Reflections from the (100), (110), and (200) planes indicate strengthening of texture unlocking. Broadening of the peak at 57° indicates that there is a weak texture and significant stresses in the film. A sharper peak at 31.5° in comparison to that shown in Fig. 3b points to the fact that the silicon oxide film continues to grow and to be textured. The small peak height results from screening by the thicker insulator film.

The results obtained suggest that the film has a perovskite structure at least up to a thickness of 0.5 μm and that the film material is highly textured.

The data shown in Fig. 3 relate to ordered crystalline films with the highest degree of crystallization characterized by the following structure deformation parameters: the size of coherent-scattering regions is $D >$ 100 nm, and the microstrain is $\Delta d/d \sim 0.01$. The degree of order of the film structure could be varied by varying the silicon substrate temperature. In particular, a decrease in this temperature resulted in structure disordering, which manifested itself in the broadening and disappearance of x-ray reflections. Further studies of the properties of complex oxide films grown from silicon substrates at various temperatures showed that film structure disordering is accompanied by a degradation of their ferroelectric properties.

The results of electron microscopy studies of the surface of a freshly deposited film of complex oxides are shown in Fig. 4.

These data suggest that there exists a certain spatial order in the grain (crystallite) orientation in the films at hand.

To confirm the existence of the crystalline phase, the samples were subject to plasmachemical etching. It was assumed that the crystalline phase would be retained during etching since it is more stable thermodynamically than the amorphous one, while the latter would be etched. After plasmachemical etching, the samples were studied using an electron microscope (Fig. 5).

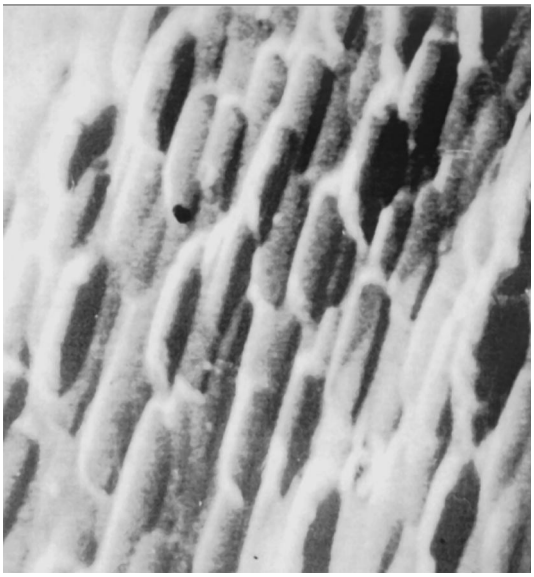

Fig. 4. Microstructure of the surface of a freshly deposited complex oxide film (10000×).

The data obtained confirmed the presence of the crystalline phase in the films, with the preferred crystallite orientation being normal to the sample surface. X-ray diffraction and electron microscopy studies showed that the film of complex oxides is characterized by a so-called limited (or complete) texture, i.e., that

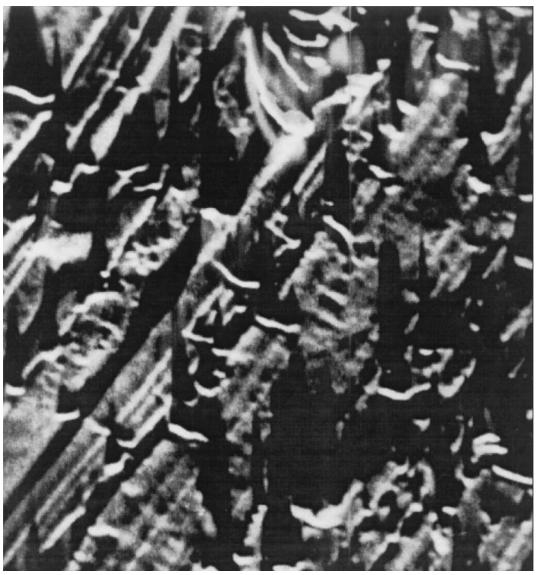

Fig. 5. Microstructure of the surface of a complex-oxide film after plasmachemical etching (10000×).

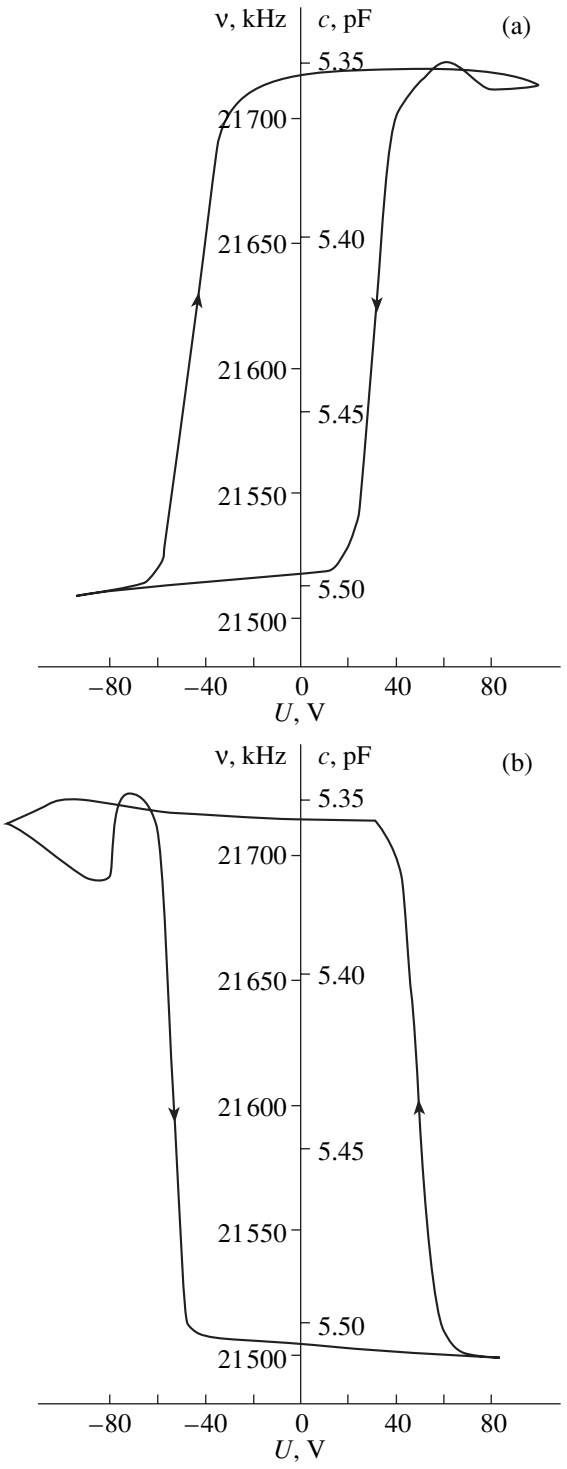

Fig. 6. Capacitance–voltage characteristics of ferroelectric films deposited onto (a) KDB-12 and (b) KÉF-4.5 silicon wafers.

crystallographic planes and directions of the same type in the grain lattices of the coating are parallel [14, 23].

The *C–V* characteristics of the ferroelectric film deposited onto KDB-12 and KÉF-4.5 silicon substrates

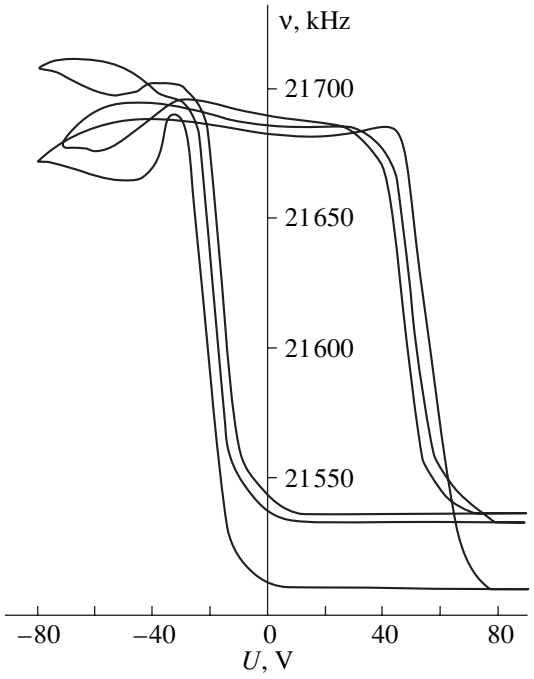

Fig. 7. Capacitance–voltage characteristics measured at three randomly chosen points of the sample under study.

are shown in Fig. 6. We can see that, as the voltage decreases from +80 to –80 V, the frequency changes by ~200 kHz, which corresponds to a capacitance change of within 0.12 pF. The *C–V* characteristics of ferroelectric films deposited onto *p*- and *n*-type silicon wafers are different but are mirror-symmetric with respect to each other. Since the direction of tracing of *C–V* hysteresis loops is opposite to the direction of tracing of hysteresis loops due to polarization processes in ferroelectrics, we deal with an injection-type hysteresis [20]. Thus, the mechanism of information recording and storage in the structures under study is controlled by the injection of carriers from the semiconductor and their trapping by traps in the ferroelectric or transition layer. The mirror symmetry of *C–V* hysteresis loops in *p*- and *n*-type silicon films presumably suggests (despite the fact that electron and hole injection processes should differ significantly) that the mechanism of carrier accumulation and conservation in the ferroelectric or transition layer is associated with polarization processes in the ferroelectric film, which is in agreement with the data from [4].

Figure 7 shows *C–V* characteristics measured at three randomly chosen points in the sample.

The data obtained show that the change in the capacitance of a deposited layer can be as great as 0.01–0.02 pF (or 25–35 kHz in frequency units). Changes in the amplitude of a recorded signal over the sample area are caused by (i) nonuniformities of the thickness and, hence, the capacitance of the deposited insulating layer; (ii) the inhomogeneous distribution of structural

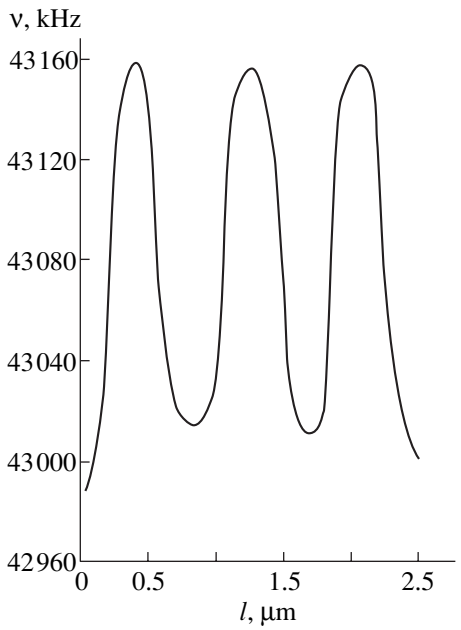

Fig. 8. Resolution measured in the structures under study.

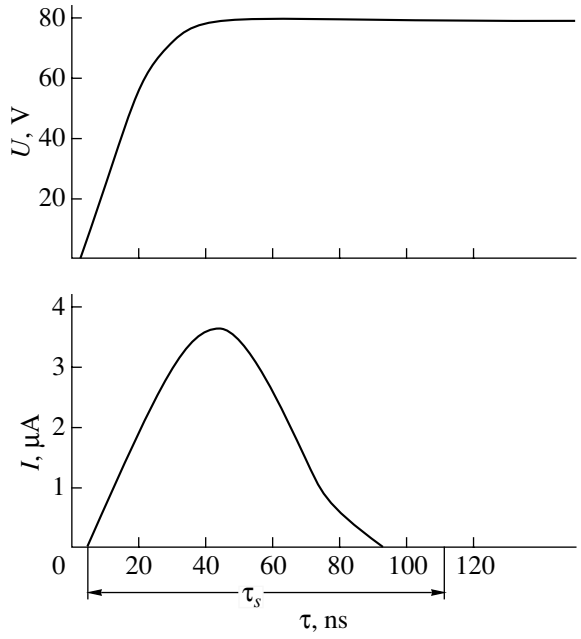

Fig. 9. Time dependences of the applied electric voltage U and switching current I in the structure under study.

defects decreasing the degree of film structure order; and (iii) nonuniform fields of elastic stresses over the film thickness, which are induced due to nonuniform heating of the silicon substrate during the formation of complex-oxide films. These causes are associated with technological difficulties, which can be eliminated by making appropriate improvements to the industrial equipment and growth conditions of complex-oxide films. The change in the capacitance of the depletion silicon layer was very small in comparison with the change in the capacitance of the deposited film (did not exceed 0.003 pF) and had almost no influence on the memory effect.

The dependence of the frequency of the reproduction generator on the sample displacement with respect to the tungsten probe is shown in Fig. 8. It was experimentally established that, in the case where structures interact with a tungsten probe having a tip rounding radius of 0.5 μm, the resolution is no worse than 0.8 μm, which suggests that it is actually possible to attain an information recording density of 10^{12}–10^{13} bit/m^2. The repolarization rate in complex oxide films can be judged from Fig. 9. These data indicate that the domain switching time in the ferroelectric films under study is shorter than 100 ns. This can provide a data transmission rate of no lower than 10 Mbit/s for an appropriately chosen information recording–reproduction circuit.

The structures under study exhibited high reproducibility of their C–V characteristics from cycle to cycle even after 10^8 rerecording cycles of an electric signal (Fig. 10). The time dependence of the reproduced signal amplitude is logarithmic (Fig. 11). Extrapolating this dependence to longer times shows that the amplitude of a reproduced signal exceeds 50% of the initial value in 10 years ($t \sim 3 \times 10^8$ s) of information storage. This is a quite satisfactory result for the recording of media of nonvolatile data carriers.

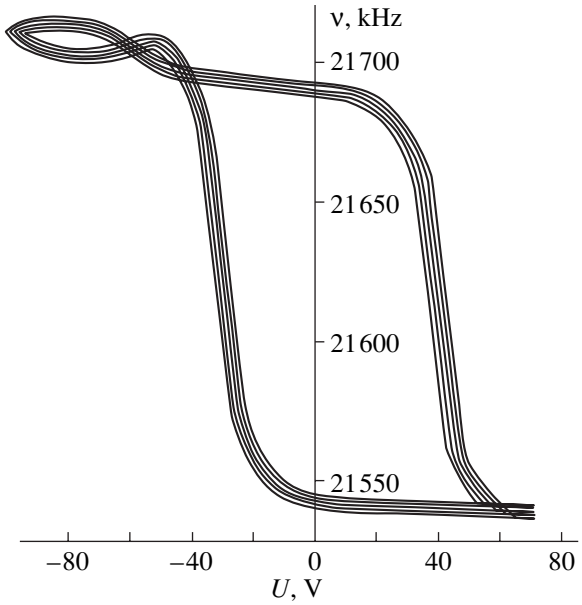

Fig. 10. Reproducibility of capacitance–voltage characteristics of films after 10^2, 10^4, 10^6, 10^7, and 10^8 switching cycles.

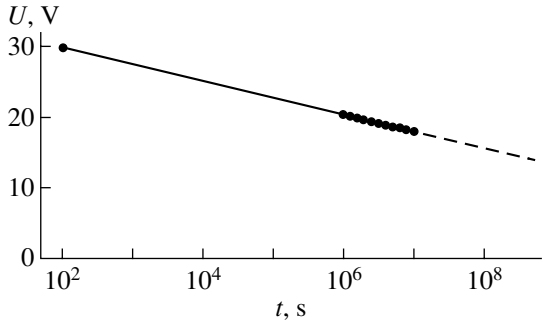

Fig. 11. Time dependence of the electric signal amplitude.

4. CONCLUSIONS

A growth technology for complex-oxide films of large area (tens of centimeters squared) on single-crystal silicon has been developed. The films are characterized by a broad peak in the temperature dependence of their permittivity in the range of an expected ferroelectric phase transition temperature for bulk materials. X-ray diffraction and electron microscopy studies have shown that a deposited film of complex oxides is characterized by a limited texture with perovskite structure at least up to a thickness of 0.5 μm.

A possible mechanism of information recording and storage in the structures under study has been considered.

Electrophysical studies of the structures demonstrated the possibility of applying them as recording media of information carriers for kinematic-type external memory devices with the following parameters: a recording surface density of larger than 10^{12} bit/m^2, a data transmission rate during information recording and reproduction of no lower than 10 Mbit/s, a number of rerecording cycles that can be greater than 10^8, and a storage time of recorded data of no shorter than 10 years.

ACKNOWLEDGMENTS

This study was supported by the Orel Branch of the Institute of Information Problems of the Russian Academy of Sciences.

REFERENCES

1. M. E. Lines and A. M. Glass, *Principles and Applications of Ferroelectrics and Related Materials* (Clarendon, Oxford, 1977; Mir, Moscow, 1981).
2. J. C. Burfoot and I. G. W. Taylor, *Polar Dielectrics and Their Applications* (Univ. of California Press, Berkeley, Calif., 1979; Mir, Moscow, 1981).
3. A. S. Sigov, Soros. Obraz. Zh., No. 10, 83 (1996).
4. I. L. Baginskiĭ and É. G. Kostsov, Avtometriya, No. 4, 88 (1988).
5. K. Yu. Frolenkov and S. G. Kim, Avtometriya, No. 4, 22 (1994).
6. N. V. Presnetsov and K. Yu. Frolenkov, Élektron. Promst, No. 4, 29 (2000).
7. Yu. Ya. Tomashpol'skiĭ, *Film Ferroelectrics* (Radio i Svyaz', Moscow, 1984) [in Russian].
8. S. V. Tolstousov, Ferroelectrics **100**, 151 (1989).
9. Ho Hyung Lee, D. Hesse, and N. Zakharov, Science **296** (5575), 2006 (2002).
10. R. Ramesh and D. G. Schlom, Science **296** (5575), 1975 (2002).
11. R. Krause, Electron. News **40** (2013), 4 (1994).
12. V. P. Dudkevich and E. G. Fesenko, *Physics of Ferroelectric Films* (Rostov. Gos. Univ., Rostov-on-Don, 1979) [in Russian].
13. G. B. Bokiĭ and M. A. Poraĭ-Koshits, *X-ray Analysis* (Mosk. Gos. Univ., Moscow, 1964) [in Russian].
14. *Handbook of Thin-Film Technology*, Ed. by L. I. Maissel and R. Glang (McCraw-Hill, New York, 1970; Sovetskoe Radio, Moscow, 1977), Vol. 2.
15. Yu. A. Bagryatskiĭ, *X-ray Diffraction Analysis in Physical Metallurgy* (Metallurgizdat, Moscow, 1961) [in Russian].
16. G. V. Kurdyumov and L. I. Lysak, Zh. Tekh. Fiz. **17** (9), 993 (1947).
17. B. N, Vasichev, *Electron Microscopy* (Znanie, Moscow, 1980) [in Russian].
18. Yu. G. Poltavtsev and A. S. Knyazev, *Technology of Surface Treatment in Microelectronics* (Tekhnika, Kiev, 1990) [in Russian].
19. O. S. Moryakov, *Technology of Semiconductor Devices and Products of Microelectronics: Ion-Beam Treatment* (Vysshaya Shkola, Moscow, 1990), Book 7 [in Russian].
20. *Properties of Metal–Dielectric–Semiconductor Structures*, Ed. by A. V. Rzhanov (Nauka, Moscow, 1976) [in Russian].
21. K. Sugibuchi, J. Kurogi, and H. Endo, J. Appl. Phys. **46** (7), 2877 (1975).
22. W. J. Merz, Phys. Rev. **95** (3), 690 (1954).
23. A. A. Babad-Zakhryapin, *Coating Defects* (Énergoatomizdat, Moscow, 1987) [in Russian].

Translated by A. Kazantsev

Physics of the Solid State, Vol. 46, No. 12, 2004, pp. 2275–2280. Translated from Fizika Tverdogo Tela, Vol. 46, No. 12, 2004, pp. 2200–2205.

LATTICE DYNAMICS AND PHASE TRANSITIONS

Features of a Shear Elastic Wave Propagating in an Acoustic Superlattice of the Magnet–Ideal Diamagnet Type: The Reflectance

O. S. Tarasenko, S. V. Tarasenko, and V. M. Yurchenko

Donetsk Physicotechnical Institute, National Academy of Sciences of Ukraine, Donetsk, 83114 Ukraine

e-mail: tarasen@host.dipt.donetsk.ua

Received August 14, 2003; in final form, February 4, 2004

Abstract—The influence of the inhomogeneous exchange interaction on the conditions of a shear elastic wave reflection from the surface of a bounded magnetic superlattice consisting of ferromagnetic and superconducting layers is studied. © *2004 MAIK "Nauka/Interperiodica".*

1. INTRODUCTION

Magnetic–nonmagnetic composite structures characterized by additional translation symmetry are conventionally considered from the viewpoint of their electrodynamic properties (magnetic photonic crystals), since these properties are spatially modulated in such structures [1]. However, if the nonmagnetic medium (medium 2) in a magnetic photonic crystal is an ideal superconductor ($\lambda/d \longrightarrow 0$, where λ is the London penetration depth and d is the superconducting layer thickness), electromagnetic wave propagation along the normal to the interfaces in such a structure becomes impossible. In the presence of an acoustic contact, the spectrum of collective excitations of such a composite magnetic medium will be determined mainly by the elastic interlayer interaction. In this case, not only the electrodynamic but also the elastic properties of the composite medium are spatially modulated [1]; therefore, the magnet–ideal diamagnet superlattice is a simple example of a one-dimensional magnetic phononic crystal. Consistent study of its high-frequency properties requires correct consideration of the magnetoelastic interaction. However, such structures, as a rule, have been studied only from the viewpoint of the coexistence of magnetic and superconducting states [2, 3].

In general, this problem should be solved using the *T*-matrix method [4]. For a gyrotropic magnetic medium, this method requires application of at least fourth-order square matrices, even in the case of a one-dimensional acoustic magnetic superlattice. This problem is complicated further by the fact that the dynamic properties of a magnetic medium are characterized by rather strong spatial dispersion, which is caused by an inhomogeneous exchange interaction [5]. However, analytical study of the resonant properties of a composite structure is significantly simplified if the analysis is restricted to the long-wavelength limit of the spectrum of normal vibrations [6, 7]. For example, in the case of a two-component superlattice with period $D = d_1 + d_2$ (d_1 and d_2 are the layer thicknesses), the wave vector components normal to the layer interface ($k_{\parallel,1}$ in medium 1 and $k_{\parallel,2}$ in medium 2) should satisfy the conditions

$$|k_{\parallel 1}|d_1 \ll 1, \quad |k_{\parallel 2}|d_2 \ll 1 \tag{1}$$

(thin-layer superlattice [6, 7]) and the frequency ω should satisfy the inequality

$$\omega \ll \min(s_1\pi/d_2, s_2\pi/d_2), \tag{2}$$

where s_1 and s_2 are the velocities of a shear elastic wave in unbounded media 1 and 2, respectively.

In this limit, the dynamics of a one-dimensional photonic–phononic crystal can be studied using the effective-medium approximation. Indeed, in the range of frequencies ω and wavenumbers $k_\perp$ satisfying inequalities (1) and (2), the superlattice can be considered a hypothetical spatially homogeneous medium characterized by the quantities

$$\langle A\rangle \equiv (A_1d_1 + A_2d_2)/D \tag{3}$$

averaged over the superlattice period (with allowance for the interlayer electrodynamic and elastic boundary conditions). In Eq. (3), A_1 and A_2 are any physical quantities related to media 1 and 2 and $\langle A\rangle$ is their value averaged over one superlattice period D [4, 6, 7].

From the viewpoint of possible applications of phononic crystals, of particular interest is the problem of reflection of a bulk elastic wave incident on the outer superstructure surface. However, this problem for a magnetic phononic crystal of the magnet–ideal diamagnet type still remains unsolved.

In this paper, by consistently including the magnetoelastic and inhomogeneous exchange interactions, we study the reflection of a bulk elastic SH wave incident

from the depth of a magnetic superlattice of the ferromagnet–ideal superconductor type on its surface.

2. BASIC RELATIONS

Let us consider an acoustic magnetic two-component superlattice that consists of a system of equidistant identical ferromagnetic (FM) layers of thickness d_1 (medium 1) coupled acoustically with superconducting layers of medium 2 of thickness d_2 each. If the layers strictly alternate with each other, such a structure will feature additional translation symmetry with period $D = d_1 + d_2$ along the normal **n** to the interlayer interface.

The FM medium is assumed to be an easy-axis ferromagnet (whose easy axis is taken to be the *z* axis). To simplify the consideration, we further assume that magnetic and nonmagnetic media are isotropic in terms of their elastic and magnetoelastic properties. In this case, the energy density *W* of the uniaxial FM crystal can be written as [8]

$$W = 0.5\alpha(\nabla m)^2 - 0.5bm_z^2 - mH_m + \gamma m_i m_k u_{ik} + \lambda_1 u_{ii}^2 + \mu_1 u_{ik}^2, \quad (4)$$

where α, b, and γ are the inhomogeneous-exchange, easy-axis anisotropy, and magnetoelastic-interaction constants, respectively; H_m is the magnetic dipole field; λ_1 and μ_1 are the Lame coefficients of the magnetic medium; and u_{ik} is the elastic strain tensor. It is obvious that the corresponding thermodynamic potential of nonmagnetic medium 2 in the two-component magnetic superlattice under study includes only the elastic energy with Lame coefficients λ_2 and μ_2. Thus, the elastic dynamics of medium 2 can be described using only the basic equation of continuum mechanics for the lattice displacement vector **u**. For FM medium 1, a closed set of dynamic equations should include not only elastodynamics equations but also magnetostatic equations and the Landau–Lifshitz equation for the ferromagnetism vector.

Taking into account acoustic continuity of the superlattice under study, the ideal diamagnetic properties of medium 2 ($\lambda = 0$) [9], and the fact that the spins at the boundaries of each magnetic layer are completely free, we obtain the following relations at the interfaces of magnetic and nonmagnetic layers [5]:

$$u_1 = u_2, \quad \xi = d_1 + DN, DN, \quad (5)$$

$$\sigma_{ik}^{(1)} n_k^{(1)} = \sigma_{ik}^{(2)} n_k^{(2)}, \quad \xi = d_1 + DN, DN, \quad (6)$$

$$B_1 n = 0, \quad \xi = d_1 + DN, DN, \quad (7)$$

$$\partial m/\partial\xi = 0, \quad \xi = d_1 + DN, DN, \quad (8)$$

where $N = 0, 1, 2, \ldots$, and ξ is the coordinate along the normal **n** to the layer interfaces. Under conditions (1) and (2), a consistent inclusion of boundary conditions (5)–(7) results in the possibility of considering the superlattice to be a hypothetical spatially homogeneous medium, whose elastic dynamics is described by effective elastic moduli. In the case of a shear elastic wave propagating with frequency ω and wavenumber $k_\perp$, it can be shown that this wave can propagate through an infinite FM medium and, hence, through the acoustic magnetic superlattice described by Eqs. (4)–(8) in the following configuration: $\mathbf{n} \parallel x$, $\mathbf{k}_\perp \parallel y$, and $\mathbf{u} \parallel \mathbf{M} \parallel z$ (**M** is the equilibrium magnetization vector). We assume that, in addition to conditions (1)–(8), the following inequality is satisfied:

$$\omega \ll \omega_0 + c(\pi/d_1)^2, \quad (9)$$

where $c \equiv \alpha g M_0$, with g being the magnetomechanical ratio and M_0 being the saturation magnetization. In this case, for the above configuration of vectors **n**, $\mathbf{k}_\perp$, **m**, and **u**, the effective elastic moduli that define the dispersion relation for a normal magnetoelastic SH wave propagating in the superlattice described by Eqs. (5)–(8) (with inclusion of the dynamic magnetoelastic and magnetic dipole interactions) can be written in the following form:

$$\begin{gathered}
\mathbf{n} \parallel x, \quad \mathbf{k}_\perp \parallel y, \quad \mathbf{u} \parallel \mathbf{M} \parallel z, \\
\bar{c}_{55} = c_{55}^{(1)} c_{55}^{(2)} (\Delta f_2)^{-1}, \quad \Delta \equiv c_{55}^{(1)} + c_{55}^{(2)} f_1 f_2^{-1}, \\
\bar{c}_{44} = f_1 c_{44}^{(1)} + f_2 c_{44}^{(2)} - f_1 f_2 (c_{45}^{(1)})^2 \Delta^{-1}, \\
\bar{c}_{45} = -\bar{c}_{54} = f_1 c_{45}^{(1)} c_{55}^{(2)} \Delta^{-1}, \quad c_{45}^{(1)} = -c_{54}^{(1)} = \nu_* \mu_1, \\
c_{44}^{(1)} = c_{55}^{(1)} = \nu\mu_1, \\
c_{44}^{(2)} = c_{55}^{(2)} = \mu_2,
\end{gathered} \quad (10)$$

where

$$\begin{gathered}
\nu \equiv \frac{(\mu_0 + ck_\perp^2 - \omega_{\text{me}})(\omega_0 + ck_\perp^2) - \omega^2}{(\omega_0 + ck_\perp^2)^2 - \omega^2}, \\
\nu_* \equiv \frac{\omega\omega_{\text{me}}}{(\omega_0 + ck_\perp^2)^2 - \omega^2}.
\end{gathered} \quad (11)$$

Here, $\omega_0 = g(H_A + H_{\text{me}})$ is the homogeneous ferromagnetic resonance frequency in the unbounded ferromagnet [5], $\omega_{\text{me}} = gH_{\text{me}}$ is the magnetoelastic gap, H_A is the uniaxial magnetic anisotropy field, and H_{me} is the magnetoelastic field.

We note that relations (10) and (11) do not include effects associated with the magnetic dipole interaction. Indeed, Eqs. (10) and (11) are derived in the effective medium approximation under the condition that Eqs. (7) are satisfied everywhere over each of the magnetic layers of the superlattice. As a result, the inclusion of the magnetic dipole interaction does not give rise to additional contributions (apart from the magnetoelastic one) to the spatial or temporal dispersion of elastic

moduli (10) and (11) for the magnet–ideal diamagnet superlattice.

In what follows, we assume that $\rho_1 = \rho_2 = \rho$ and $\mu_1 = \mu_2 = \mu$. Therefore, for the infinite acoustic superlattice under study, the spectrum of the shear normal SH wave ($u_z = A\exp(ik_\parallel x + ik_\perp y - i\omega t)$, A is the amplitude), taking into account the magnetoelastic and inhomogeneous exchange interactions, can be written as

$$\omega^2/s_t^2 = c_\parallel k_\parallel^2 + c_\perp k_\perp^2, \tag{12}$$

where $s_t^2 \equiv \mu/\rho$ and

$$c_\parallel = c_{55}/\mu = \frac{(\omega_0 + ck_\perp^2)(\omega_0 + ck_\perp^2 - \omega_{me}) - \omega^2}{(\omega_0 + ck_\perp^2)^2 - f_2(\omega_0 + ck_\perp^2)\omega_{me} - \omega^2},$$

$$c_\perp = \bar{c}_{44}/\mu$$

$$= \frac{(\omega_0 + ck_\perp^2)(\omega_0 + ck_\perp^2 - \omega_{me}) - \omega^2 + \omega_{me}^2 f_1 f_2}{(\omega_0 + ck_\perp^2)^2 - f_2(\omega_0 + ck_\perp^2)\omega_{me} - \omega^2}, \tag{13}$$

$$c_* = \bar{c}_{54}/\mu = \frac{f_1\omega\omega_{me}}{(\omega_0 + ck_\perp^2)^2 - f_2(\omega_0 + ck_\perp^2)\omega_{me} - \omega^2}.$$

From Eqs. (12) and (13), it follows that the dependence of the wave vector component normal to the surface on the wave frequency ω and wavenumber $k_\perp$ for the shear elastic wave under study is given by the equation $k_\parallel^2 = -\alpha^2 k_\perp^2$, where

$$\alpha^2 = \frac{c_\perp - \omega^2/s_t^2 k_\perp^2}{c_\parallel} > 0. \tag{14}$$

Thus, within the effective-medium approximation, under conditions (1)–(3) and (9), and in the presence of inhomogeneous exchange and magnetoelastic interactions, the SH wave is a single-component excitation. Therefore, in the case where the superlattice under study is semi-infinite and occupies the upper half-space $x > 0$, the spatial structure of the field of elastic lattice displacements (**u** ⊥ **n**) in the normal SH wave incident on the superlattice surface from its depth (**u** ∥ z, **k** ∈ xy, **n** ∥ x) is defined from Eqs. (10)–(14) by

$$u_z = [A_-\exp(-ik_\parallel x) + A_+\exp(ik_\parallel x)] \times \exp(i\omega t - ik_\perp y). \tag{15}$$

The incident wave will be a bulk wave if $k_\parallel^2 > 0$. Calculations show that this case is possible if the frequency ω and wavenumber $k_\perp$ of the shear elastic wave in the superlattice (in the geometry under discussion) satisfy one of the following relations:

$$\begin{aligned} &k_\perp > k_*, \quad \omega_2(k_\perp) < \omega < \omega_-(k_\perp), \\ &k_\perp < k_*, \quad \omega_-(k_\perp) < \omega < \omega_2(k_\perp), \\ &\omega > \omega_+(k_\perp) \end{aligned} \tag{16}$$

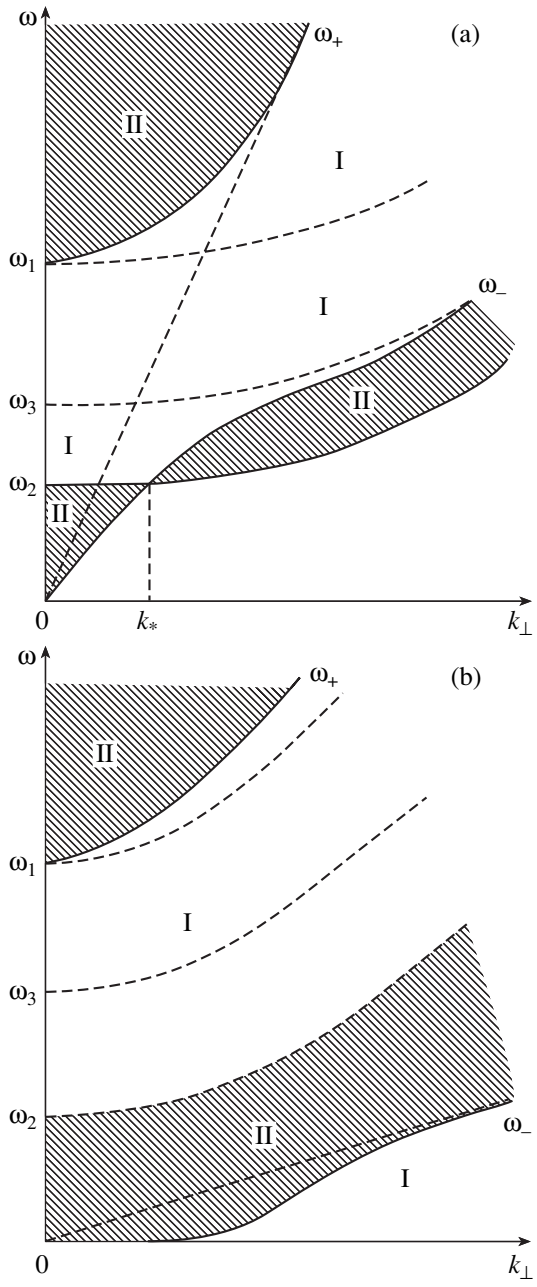

Fig. 1. Area II is the region of possible existence of bulk elastic waves of the SH type ($k_\parallel^2 > 0$) in a thin-layer superlattice consisting of an easy-axis ferromagnet and an ideal superconductor at **k** ⊥ y, **u** ∥ yz, and **n** ∥ x; (a) $s^2 > 4c\omega_0$ and (b) $s^2 < 4c\omega_0$.

at $s^2 > 4c\omega_0$ (Fig. 1a) and

$$\begin{aligned} &\omega > \omega_+(k_\perp), \\ &\omega_- < \omega < \omega_2(k_\perp) \end{aligned} \tag{17}$$

at $s^2 < 4c\omega_0$ (Fig. 1b).

Here, $\omega_1^2 \equiv (\omega_0 + ck_\perp^2)^2 - f_2(\omega_0 + ck_\perp^2)\omega_{me}$, $\omega_2^2 \equiv (\omega_0 + ck_\perp^2)^2 - (\omega_0 + ck_\perp^2)\omega_{me}$, $\omega_\pm^2(k_\perp) \equiv 0.5P +$

$\sqrt{0.25P^2 - Q}$, $P \equiv \omega_1^2 + s_t^2 k_\perp^2$, $Q \equiv \omega_3^2 s_t^2 k_\perp^2$, and $\omega_3^2 \equiv (\omega_0 + ck_\perp^2)(\omega_0 + ck_\perp^2 - \omega_{me}) + \omega_{me}^2 f_1 f_2$. It is easy to verify that $\omega_1 > \omega_3 > \omega_2$. The wavenumber k_* is determined from the condition $\omega_2(k_*) = \omega_-(k_*)$.

Let us consider the reflection of this bulk elastic SH wave from the boundary between the magnetic superlattice and a nonmagnetic medium.

3. REFLECTION OF THE BULK SHEAR WAVE FROM THE SURFACE OF THE SEMI-INFINITE MAGNETIC SUPERLATTICE

We consider a bulk transverse SH wave polarized perpendicular to the plane of incidence (the *xy* plane; $\mathbf{u} \parallel \mathbf{M} \parallel z$) and incident from the magnetic-superlattice depth onto the acoustically continuous interface ($x = 0$) of two half-spaces occupied by the FM superlattice ($x > 0$) and an elastically isotropic superconductor ($x < 0$). Within the effective-medium approximation, using the conventional calculation scheme [10] and Eqs. (12), (13), and (15), the reflectance R can be written in the form

$$R = \frac{c_\parallel k_\parallel - (a\tilde{k}_\parallel - ic_*\sigma k_\perp)}{c_\parallel k_\parallel + (a\tilde{k}_\parallel - ic_*\sigma k_\perp)} \quad \text{(F–S configuration)}, \tag{18}$$

where $k_\parallel^2 \equiv \omega^2/s_*^2 - k_\perp^2$, $a \equiv \mu_*/\mu$, μ_* is the shear modulus, and s_* is the elastic wave velocity. Hereafter, the notation F–S is used to indicate the interface of the semi-infinite superconductor (*S*) and the semi-infinite magnetic superlattice. Relation (18) remains valid in the case where the interface $x = 0$ between the half-spaces occupied by the magnetic superlattice and superconductor is a glide-type interface (in this case, the limit $a \longrightarrow 0$ should be taken in Eq. (18)). If $a \neq 0$ in Eq. (18), the reflected bulk SH wave will undergo a gyrotropy-induced additional phase shift with respect to the incident wave, $R = \exp(i\phi)$. This effect also takes place in the case of $a = 0$:

$$\tan(\phi/2) = \frac{\sigma\omega\omega_{me} f_1}{\omega_2^2 - \omega^2}\left[\frac{k_\perp}{k_\parallel}\right]. \tag{19}$$

In the presence of gyrotropy ($c_* \neq 0$), the bulk SH wave with $\mathbf{u} \parallel z$ also cannot pass completely through the acoustically continuous interface ($a \neq 0$) between the semi-infinite magnetic superlattice and superconductor for those ω and $k_\perp$ at which $k_\parallel^2 > 0$; i.e., in Eq. (18), $0 < |R| < 1$. In this case, both transmitted and reflected bulk shear waves will have a phase shift with respect to the bulk elastic SH wave incident on the superlattice surface.

In both cases $a = 0$ and $a \neq 0$, the phase shift of the reflected wave will be nonreciprocal with respect to the substitution $k_\perp \longrightarrow -k_\perp$ for given values of the frequency ω and the wavenumber $k_\perp$. At $a \neq 0$, according to Eqs. (18) and (13), the phase shift is determined not only by the gyrotropic properties of the superlattice but also by the relative value of the acoustic parameters of adjacent media and is given by

$$\tan(\phi/2) = aq\frac{(\omega + \sigma\omega_-)(\omega - \sigma\omega_+)}{\omega_2^2 - \omega^2}\left[\frac{k_\perp}{k_\parallel}\right] \tag{20}$$

($q^2 > 0$, $q^2 \equiv -k_\parallel^2/k_\perp^2$). As a result, $R = 1$ in relation (18) at $\omega = \omega_-$ and $\sigma = -1$ or at $\omega = \omega_+$ and $\sigma = 1$.

As follows from Eq. (18), $R = -1$ at $k_\parallel = 0$; i.e., the homogeneous bulk shear SH wave cannot propagate along the acoustically continuous ($a \neq 0$) or mechanically free ($a = 0$) superlattice–superconductor interface ($x = 0$). In the case of a mechanically free surface of the magnetic superlattice ($a = 0$), this effect is caused by gyrotropy. In accordance with the general theory of wave processes [10], the reflectance R given by Eqs. (18) and (13) (after the substitution $k_\parallel \longrightarrow i\alpha k_\perp$) can have a pole in the ω–$k_\perp$ plane, which corresponds to a surface acoustic SH wave characterized by the dispersion relation $\Omega_s(k_\perp)$ and propagating (in the geometry in question) along the acoustically continuous ($a \neq 0$) or mechanically free ($a = 0$) superlattice–superconductor interface with $\mathbf{n} \parallel x$, $\mathbf{u} \parallel z$, and $\mathbf{k}_\perp \parallel y$.

Under the conditions of total internal reflection ($k_\parallel^2 < 0$ in Eq. (18)), a beam of shear elastic waves incident from the depth of the ferromagnet–superconductor superlattice onto its surface undergoes not only a phase shift ϕ upon reflection but also a longitudinal displacement $\Delta \equiv -\partial\phi/\partial k_\perp$ along the interface (the Schoch effect) [10]. Calculations show that, due to gyrotropy, the Schoch effect is also possible for the glide interface.

Taking into account Eq. (19) for $a = 0$, we obtain

$$\Delta = \frac{-2k_\parallel}{k_\parallel^2 + \kappa^2 k_\perp^2}\left[\kappa + \frac{\kappa k_\perp^2 c_\perp}{c_\parallel k_\parallel^2}\right], \tag{21}$$

where

$$\kappa \equiv \frac{c_*\sigma}{c_\parallel}, \quad k_\parallel^2 > 0.$$

In the case of a continuous acoustic contact ($a \neq 0$), Eq. (21) is generalized as

$$\Delta = \frac{-2k_\parallel^2}{k_\parallel^2 + \kappa^2 k_\perp^2}\left[\frac{\kappa}{k_\parallel} + \frac{\kappa k_\perp^2 c_\perp}{c_\parallel k_\parallel^3} + \frac{a\omega^2}{k_\parallel c_\parallel s_*^2 q k_\perp^2}\right], \tag{22}$$

where

$$\kappa \equiv \frac{-aq + c_*\sigma}{c_\parallel}, \quad k_\parallel^2 > 0, \quad q^2 \equiv 1 - \omega^2/(s_*^2 k_\perp^2).$$

It follows from Eqs. (18)–(22) that, at the short-wavelength extreme point of the spectrum of the second-type

shear surface acoustic wave, $R \longrightarrow 1$ and, hence, $\Delta = 0$, whereas at the long-wavelength extreme point of the spectrum, we have $R \longrightarrow -1$ and, formally, $\Delta \longrightarrow \infty$.

Because of gyrotropy, the value and sign of the longitudinal displacement Δ of the reflected acoustic beam at the given ω and $|k_\perp|$ are nonreciprocal with respect to sign reversal of the wave vector projection onto the propagation direction of the incident SH wave; i.e., $\Delta(k_\perp) \neq \Delta(-k_\perp)$. In the case where the gyrotropy effect is macroscopic (i.e., for a magnetic superlattice with collinear ordering of the equilibrium magnetic moments of adjacent FM layers), a negative displacement of the reflected beam of bulk shear waves is possible for a medium of the type under consideration at both $a = 0$ and $a \neq 0$.

Gyrotropy-induced additional features in the reflection of the bulk elastic SH wave from the magnetic superlattice–superconductor interface also arise for a magnetic superlattice–superconductor–magnetic superlattice (F–S–F) sandwich structure.

4. REFLECTION OF THE BULK SHEAR WAVE FROM THE SURFACE OF A NONMAGNETIC LAYER INSERTED INTO AN INFINITE MAGNETIC SUPERLATTICE

Let us consider an infinite superlattice consisting of an easy-axis ferromagnet (medium 1) and an ideal superconductor (medium 2) into which an elastically isotropic ideal superconducting layer of thickness $2d$ ($-d < x < d$) is inserted, i.e., an F–S–F structure. If conditions (5)–(8) are satisfied at all interlayer interfaces, this three-layer structure is acoustically continuous. In this case, within the effective-medium approximation under conditions (1)–(3) and (9), the reflectance V for the shear bulk elastic wave ($\mathbf{u} \parallel z$, $\mathbf{k} \in xy$) incident from the upper half-space onto the interface $x = d$ between the magnetic superlattice and the superconducting layer can be written, using Eqs. (13), in the form

$$V = \frac{V_{32} + V_{21}(1 + V_{23} + V_{32})\exp(i4\tilde{k}_\parallel d)}{1 - V_{23}V_{21}\exp(i4\tilde{k}_\parallel d)}, \qquad (23)$$

where

$$V_{23} = \frac{-(c_\parallel k_\parallel - c_*\sigma k_\perp) + a\tilde{k}_\parallel}{c_\parallel k_\parallel - c_*\sigma k_\perp + a\tilde{k}_\parallel},$$
$$V_{21} = \frac{-(c_\parallel k_\parallel + c_*\sigma k_\perp) + a\tilde{k}_\parallel}{c_\parallel k_\parallel + c_*\sigma k_\perp + a\tilde{k}_\parallel}, \qquad (24)$$
$$V_{32} = \frac{(c_\parallel k_\parallel + c_*\sigma k_\perp) - a\tilde{k}_\parallel}{c_\parallel k_\parallel - c_*\sigma k_\perp + a\tilde{k}_\parallel}.$$

Here, according to the notation used in [10], V_{ij} is the reflectance for the bulk single-component SH wave incident from medium i onto the interface ij; subscripts 1–3 label the medium at $x < -d$, the layer in the region $-d < x < d$, and the medium at $x > d$, respectively.

We see that, for the elastic bulk SH wave incident on the surface of the superconducting layer ($-d < x < d$) bound rigidly to the adjacent media, the reflectance V tends to zero as $d \longrightarrow 0$.

As $d \longrightarrow \infty$, Eqs. (23), (24), and (13) for V reduce to Eqs. (18) and (13) for the reflectance of the shear elastic SH wave ($V \longrightarrow R$) in the case of an acoustically continuous interface between the magnetic superlattice and semi-infinite superconductor. The poles of the reflectance given by Eqs. (23), (24), and (13) in the ω–$k_\perp$ plane, after the substitution $ik_\parallel \longrightarrow \pm\alpha k_\perp$ ($ik_\parallel \longrightarrow -\alpha k_\perp$ for $x > d$ and $ik_\parallel \longrightarrow \alpha k_\perp$ for $x < -d$), coincide with the spectrum of the gap SH wave localized near the superconducting layer incorporated into the infinite magnetic superlattice. By calculating the magnitude of the reflectance V given by Eqs. (23), (24), and (13), one can verify that, due to gyrotropy, the elastic SH wave can completely pass through the structure under study ($|V| = 0$) only if the defect superconducting layer is half-wave [10], i.e., $2\tilde{k}_\parallel d = p\pi$, with $p = 1, 2, \ldots$ ($\tilde{k}_\parallel^2 > 0$). If $\tilde{k}_\parallel^2 < 0$, complete transmission, as well as total reflection, of the shear elastic wave incident on the superconducting layer ($-d < x < d$) is impossible for the structure under consideration, i.e., $0 < |V| < 1$. Furthermore, it follows from Eqs. (23), (24), and (13) that the elastic bulk SH wave reflected from the superconducting layer undergoes a phase shift ψ ($\tan\psi = \mathrm{Im}\,V/\mathrm{Re}\,V$) with respect to the incident wave.

The reflectance behavior is qualitatively different in the case where an incorporated superconducting layer of thickness $2d$ is in acoustic contact with the semi-infinite magnetic superlattices of the configuration under study, arranged both at $x < -d$ and $x > d$ (collinear ordering of the magnetic moments of the adjacent layers) but with antiparallel directions of the magnetic moments at $x > d$ and $x < -d$ (according to the notation introduced above, such a structure can be referred to as F_+–S–F_-). Calculations show that Eq. (23) for the SH wave reflected from the surface $x = d$ of the defect superconductor layer also remains valid for the F_+–S–F_- configuration (for this case, we designate the reflectance as V_{+-}) for the same geometry of the SH wave ($\mathbf{u} \parallel z$, $\mathbf{k} \in xy$, $\mathbf{n} \parallel x$). However, in this case, in the notation introduced in Eq. (13), we have in Eq. (23)

$$V_{23} = V_{21} = \frac{-(c_\parallel k_\parallel - ic_*\sigma k_\perp) + a\tilde{k}_\parallel}{c_\parallel k_\parallel - ic_*\sigma k_\perp + a\tilde{k}_\parallel},$$
$$V_{32} = \frac{c_\parallel k_\parallel + ic_*\sigma k_\perp - a\tilde{k}_\parallel}{c_\parallel k_\parallel - ic_*\sigma k_\perp + a\tilde{k}_\parallel}. \qquad (25)$$

Therefore, for an ultrathin superconducting layer, $2k_\parallel d \longrightarrow 0$, the reflectance for the elastic SH wave $\tilde{V}_{+-}$

is nonzero. Calculations show that this case corresponds to an acoustically continuous interface of two semi-infinite magnetic superlattices of the ferromagnet–superconductor type if the equilibrium orientations of their magnetic moments, being coincident with the z axis, differ by 180° for $x > 0$ and $x < 0$. An analysis shows that, after the substitution $ik_\parallel \longrightarrow \pm\alpha k_\perp$ ($ik_\parallel \longrightarrow -\alpha k_\perp$ for $x > 0$ and $ik_\parallel \longrightarrow \alpha k_\perp$ for $x < 0$), the pole of the reflectance given by Eqs. (23), (25), and (13) determines the spectrum of the gap SH wave with $\mathbf{u} \parallel z$ and $\mathbf{k}_\perp \parallel y$, localized near the superconducting layer ($-d < x < d$) that acoustically couples the two semi-infinite magnetic superlattices. In contrast to the case of the gap SH wave formed in the F–S–F structure, the dispersion relation for the gap SH wave in the F_+–S–F_- structure is factored and is nonreciprocal with respect to the reversal of the propagation direction:

$$[\alpha c_\parallel + c_*\sigma + aq\tanh(qk_\perp d)] \times [\alpha c_\parallel + c_*\sigma + aq\coth(qk_\perp d)] = 0, \quad (26)$$

where $q^2k_\perp^2 \equiv -\tilde{k}_\parallel^2$ and the notation is the same as that in Eq. (13).

An analysis of Eq. (26) shows that such a gap wave exists provided that

$$\alpha c_\parallel + c_*\sigma < 0. \quad (27)$$

The spectrum of this localized excitation has two branches if

$$|\alpha c_\parallel + c_*\sigma| > a/(k_\perp d), \quad (28)$$

and a single branch otherwise.

5. CONCLUSIONS

Thus, by including both the magnetoelastic and inhomogeneous exchange interactions within the effective-medium approximation, we have considered the reflection features of a shear bulk elastic wave incident on the surface of a semi-infinite acoustic thin-layer superlattice consisting of an easy-axis ferromagnet and an ideal superconductor from its depth. An analysis has been carried out for the case of parallel orientation of the equilibrium magnetic moments of adjacent in-plane-magnetized FM layers of the superlattice.

Even in the case of a mechanically free surface, gyrotropy has been shown to cause (i) a phase shift for the reflected SH wave, (ii) the Schoch effect for a beam of shear bulk SH waves incident from the magnetic superlattice depth onto its surface under conditions of total internal reflection, and (iii) the impossibility of glide of the homogeneous bulk SH wave even along the mechanically free surface of the magnetic superlattice.

For the interface between the semi-infinite magnetic superlattice and superconductor, gyrotropy causes all the above-mentioned effects to be nonreciprocal with respect to sign reversal of the projection of the wave vector of the elastic SH wave onto the superlattice surface.

In the case of a superconducting layer incorporated into the magnetic superlattice under study, a propagating gap elastic SH wave can be formed that is localized near this layer. The spectrum of this wave is reciprocal with respect to reversal of the direction of propagation.

ACKNOWLEDGMENTS

One of the authors (S.V.T.) is grateful to I.E. Dikshtein for his support of this study and helpful discussions.

REFERENCES

1. I. L. Lyubchanskii, N. N. Dadoenkova, M. I. Lyubchanski, E. A. Shapovalov, and Th. Rasing, J. Phys. D **36** (1), R277 (2003).
2. Yu. A. Izyumov, Yu. N. Proshin, and M. G. Khusainov, Usp. Fiz. Nauk **172** (2), 113 (2002) [Phys. Usp. **45**, 109 (2002)].
3. D. Budelmann, J. Holmlund, J. Andreasson, H. Rodriguez, H. Adrian, V. Merkt, and M. Rübhausen, Phys. Rev. B **67**, R140507 (2003).
4. M. G. Cottam and D. R. Tilley, *Introduction to Surface and Superlattice Excitations* (Cambridge Univ. Press, Cambridge, 1989).
5. A. G. Gurevich, *Magnetic Resonance in Ferrites and Antiferromagnets* (Nauka, Moscow, 1973) [in Russian].
6. S. M. Rytov, Akust. Zh. **2** (1), 72 (1956) [Sov. Phys. Acoust. **2**, 68 (1956)].
7. S. M. Rytov, Zh. Éksp. Teor. Fiz. **29**, 605 (1955) [Sov. Phys. JETP **2**, 466 (1955)].
8. E. A. Turov and V. G. Shavrov, Usp. Fiz. Nauk **140** (3), 429 (1983) [Sov. Phys. Usp. **26**, 593 (1983)].
9. V. I. Al'shits, A. S. Gorkunova, and A. L. Shuvalov, Zh. Éksp. Teor. Fiz. **110** (9), 924 (1996) [JETP **83**, 509 (1996)].
10. L. M. Brekhovskikh, *Waves in Layered Media*, 2nd ed. (Nauka, Moscow, 1973; Academic, New York, 1980).

Translated by A. Kazantsev

Physics of the Solid State, Vol. 46, No. 12, 2004, pp. 2281–2285. Translated from Fizika Tverdogo Tela, Vol. 46, No. 12, 2004, pp. 2206–2209.

LATTICE DYNAMICS AND PHASE TRANSITIONS

The Influence of Phase Transitions in the Rb_2CdI_4 Ferroelastic on the Exciton Absorption Spectrum

V. K. Miloslavskiĭ*, O. N. Yunakova*, and E. N. Kovalenko**

** Kharkov National University, pl. Svobody 4, Kharkov, 61077 Ukraine*

e-mail: Vladimir.K.Miloslavsky@univer.kharkov.ua

*** Scientific Center of Physics and Technology, Ministry of Education and National Academy of Sciences of Ukraine, ul. Novgorodskaya 1, Kharkov, 61145 Ukraine*

Received April 23, 2004

Abstract—The parameters of the long-wavelength exciton band for Rb_2CdI_4 films are investigated in the temperature range 90–410 K. It is found that the Rb_2CdI_4 films undergo a sequence of phase transitions at temperatures T_{c1} = 380 K (paraphase ⟶ incommensurate phase), T_{c2} = 290 K (incommensurate phase ⟶ ferroelastic phase *I*), and T_{c3} = 210 K (ferroelastic phase *I* ⟶ ferroelastic phase *II*). The parameters of the exciton band (such as the spectral position and the half-width) measured during heating and cooling of the Rb_2CdI_4 film differ significantly. This is especially true for the incommensurate phase. Upon heating of the incommensurate phase, the domain boundaries become frozen, whereas the cooling of this phase is accompanied by the generation of solitons and their pinning, which, in turn, results in a first-order phase transition at the temperature T_{c2}. It is revealed that the oscillator strength of the exciton band anomalously increases in the range of existence of commensurate phase *I* ($T_{c3} \le T \le T_{c2}$) due to ordering of the Rb_2CdI_4 crystal lattice. © *2004 MAIK "Nauka/Interperiodica".*

1. INTRODUCTION

Thermographic investigations have revealed that a complex compound, namely, Rb_2CdI_4, with a melting temperature of 216°C is formed in the RbI–CdI_2 system [1]. The Rb_2CdI_4 compound is similar in the type and symmetry of the crystal lattice to compounds with a β-K_2SO_4-type structure (Cs_2CdI_4 [2, 3], Rb_2ZnCl_4 [4, 5], K_2ZnCl_4 [6, 7], etc.), which exhibit ferroelastic properties. As a rule, the phase transitions in Rb_2CdI_4 crystals have been determined by analyzing the temperature dependences of the permittivity [8] and the intensity of the impurity luminescence bands of Mn^{2+} ions [9]. The results obtained in the cited works are somewhat contradictory. In particular, Shimizu and Takashige [8] revealed phase transitions at temperatures of 150 and 210 K and interpreted the phase transition observed at 210 K as a first-order transition. On the other hand, Bolesta and Furgala [9] revealed phase transitions at temperatures of 216, 291, 325, and 384 K and proposed the following sequence of phases for the Rb_2CdI_4 compound (by analogy with a more thoroughly studied isostructural compound, Cs_2CdI_4 [2, 3]): the paraphase is observed at $T > 384$ K, the incommensurate phase exists in the temperature range 384–325 K, and the commensurate ferroelastic phases are observed at temperatures below 325 K. The aforementioned phase transitions at 150 and 325 K contradict the phase transitions found in the isomorphic compound Cs_2CdI_4, in which, according to detailed investigations, there occur only three phase transitions in the temperature range 77–400 K.

To the best of our knowledge, exciton absorption spectra have not been investigated for the aforementioned compounds, except for the Cs_2CdI_4 compound, which was studied in [10]. However, it is of interest to elucidate the influence of phase transitions on the optical electronic spectra. In our earlier work [10], we devised a method for preparing thin films from the Rb_2CdI_4 compound, which has a structure of the β-K_2SO_4 type and is isostructural to Cs_2CdI_4. For the Rb_2CdI_4 compound, we observed intense exciton bands in the range of the fundamental absorption edge. Analysis of the exciton band in the temperature range 90–400 K makes it possible to determine the effect of both the exciton–phonon interaction and phase transitions on the spectral position, the half-width, and the oscillator strength of the band [10, 11]. The absorption spectra in the energy range 2–6 eV were discussed in detail in [10]. In the present work, we investigated how the phase transitions affect the parameters of the longest-wavelength and most intense band A_0.

2. SAMPLE PREPARATION AND EXPERIMENTAL TECHNIQUE

Thin films of the Rb_2CdI_4 compound were grown through vacuum evaporation of a mixture prepared from pure powders of RbI and CdI_2 (stoichiometric compositions) onto quartz substrates heated to 100°C

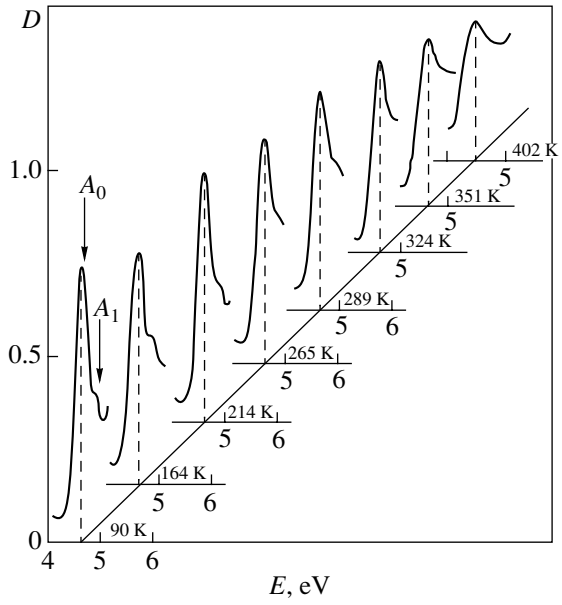

Fig. 1. Long-wavelength exciton absorption bands for the Rb_2CdI_4 film at different temperatures in the range 90–402 K. The spectra are measured during heating of the sample. The film thickness is equal to 130 nm.

according to the procedure described in [10]. The mixture of powders was preliminarily melted under a screen, the liquid fraction of the melt was evaporated, and the remaining crystalline precipitate was deposited on the substrate at a higher temperature. Then, the films were annealed at a temperature of 100°C for 1 h. The Rb_2CdI_4 films prepared according to this procedure had a structure of the β-K_2SO_4 type [10]. This structure was confirmed using electron diffraction analysis. The lattice parameters of the crystals were determined to be $a = 10.6 \pm 0.1$ Å, $b = 8.4 \pm 0.1$ Å, and $c = 14.9 \pm 0.1$ Å.

The film thickness was determined by the Tolansky method [12]. For the recording of the absorption spectra, we used 100- to 130-nm-thick films. The absorption spectra were measured on an SF-46 spectrophotometer.

The absorption spectra in the range 3.6–5.1 eV were recorded in the temperature range 90–410 K, including the temperatures of possible phase transitions. The spectral measurements were performed in a vacuum cryostat in the temperature range 90–293 K and in a standard thermostat at higher temperatures. Since the high-temperature phases could be frozen upon rapid cooling of the samples, the shape of the exciton band was examined at 90 K. It was found that the intensity of the *A* band increases with time and that the spectrum ceases to vary within two or three hours after cooling. The absorption spectrum in the range of the exciton band was recorded at a specified temperature (±5 K) for 20 min upon heating of the sample and for 30 min upon cooling.

The parameters of the long-wavelength band A_0 (position E_m, half-width Γ, oscillator strength f) were determined according to the technique proposed in our previous work [13]. The A_0 band was approximated by a single-oscillator symmetric profile, which is a linear combination of Lorentzian and Gaussian lines. The parameters of the exciton band (E_m, Γ, f) were chosen such that the calculated and experimental profiles at the long-wavelength wing were best fitted.

3. TEMPERATURE DEPENDENCE OF THE PARAMETERS OF THE LONG-WAVELENGTH EXCITON BAND FOR THE Rb_2CdI_4 COMPOUND

Figure 1 shows the absorption spectrum of the Rb_2CdI_4 thin film. It can be seen from this figure that, in the measured energy range, the spectrum consists of two bands, namely, the strong long-wavelength band A_0 and the adjacent weaker band A_1. The intensity of the A_0 band slightly decreases in the temperature range 90–200 K, which corresponds to ferroelastic phase *II*. However, upon transition to ferroelastic phase *I* ($T_{c3} \cong 210$ K), the intensity of the A_0 band increases. Further heating of the sample and transitions to the incommensurate phase ($T_{c2} \cong 290$ K) and the paraphase ($T_{c1} \cong 380$ K) lead to a broadening of the A_0 band and a decrease in the intensity at the maximum.

The parameters of the A_0 band were determined for 22 temperatures upon heating and cooling of the sample. The parameters thus obtained are as follows: the position E_m and the half-width Γ of the band; the imaginary part of the permittivity at the maximum of the band $\varepsilon_{2m} = (2nk)_m$; and the parameter α, which determines the fraction of the Gaussian component in the mixed profile. As can be seen from Fig. 2, the temperature dependences $E_m(T)$ and $\Gamma(T)$ differ significantly upon heating and cooling of the sample. The differences in the parameters E_m and Γ are largest in the range of existence of the incommensurate phase ($T_{c2} \le T \le T_{c1}$) and are smallest in the range of the paraphase. Moreover, an increase in the temperature T brings about a shift in the maximum of the A_0 band toward the low-frequency range and an increase in the half-width Γ. The specific features observed in the temperature dependences $E_m(T)$ and $\Gamma(T)$ are associated primarily with the electron–phonon interaction. In order to exclude the temperature memory effects, we averaged the parameters E_m and Γ obtained upon heating and cooling: $\bar{E}_m = 0.5(E_{m\uparrow} + E_{m\downarrow})$ and $\bar{\Gamma} = 0.5(\Gamma_\uparrow + \Gamma_\downarrow)$. From analyzing the dependences $\bar{E}_m(T)$, it follows that the parameter $\bar{E}_m$ decreases almost linearly with an increase in the temperature in the ranges far from the phase transition temperature T_{ci}: $d\bar{E}_m/dT = -0.6 \times 10^{-4}$ eV/K at $T < T_{c3}$ and $d\bar{E}_m/dT = -6.7 \times 10^{-4}$ eV/K at $T_{c1} > T > T_{c3}$. These values are equal in order of magnitude to those obtained for similar ionic crystals for which the temperature shift

of the A_0 band is governed by the electron–phonon interaction. In the range of existence of the paraphase ($T > T_{c1}$), the quantity $d\bar{E}_m/dT = -2.0 \times 10^{-4}$ eV/K is considerably less than that determined for the low-temperature phases. This can be associated with the fact that the temperatures of existence of the paraphase are close to the melting temperature. Deviations from the above dependences are observed in the range of the phase transitions. For example, the A_0 band in the temperature range 180–210 K is shifted by 0.02 eV toward high energies. Most likely, this shift is caused by the phase transition of the crystal from the triclinic phase at $T < T_{c3}$ to the monoclinic phase at $T > T_{c3}$ [2, 3].

The dependence $\bar{\Gamma}(T)$ exhibits an intricate behavior over the entire range of temperatures. At temperatures away from the phase transition point T_{ci}, the dependence $\bar{\Gamma}(T)$ exhibits a linear behavior and is described by the expression

$$\bar{\Gamma}(T) = \bar{\Gamma}(0) + aT,$$

where the parameter $a = d\bar{\Gamma}/dT$ is constant to within experimental error and equal to $(9 \pm 1) \times 10^{-4}$ eV/K. The linear behavior of the dependence $\bar{\Gamma}(T)$ indicates the occurrence of low-dimensional excitons in all three crystalline phases of the Rb_2CdI_4 compound. According to the theoretical analysis, the linear dependence $\Gamma(T)$ is characteristic of two-dimensional excitons [14]. This result is consistent both with the crystal lattice of the Rb_2CdI_4 compound, which is isomorphic to the crystal lattice of Cs_2CdI_4 [2, 3], and with the possible localization of excitons in CdI_4^{2-} tetrahedra, which form layers in the *ab* plane of the orthorhombic crystal. These layers are widely spaced (c = 14.9 Å), and Rb^+ ions are located between them. Moreover, the residual broadening $\bar{\Gamma}(0)$, which is determined by the defect structure of the crystal lattice, increases upon transitions to the low-temperature phases: $\bar{\Gamma}(0)$ = 0.1 eV in the orthorhombic phase ($T < T_{c2}$), 0.13 eV in the monoclinic phase ($T_{c3} < T < T_{c2}$), and 0.18 eV in the triclinic phase ($T < T_{c3}$).

The averaged dependences $\bar{E}_m(T)$ and $\bar{\Gamma}(T)$ reflect the interaction of excitons with phonons. However, the temperature dependences of the real parameters upon heating and cooling exhibit a considerably more complex behavior (Figs. 2a, 2b). The differences in the dependences $E_m(T)$ and $\Gamma(T)$ are especially significant in the temperature ranges corresponding to ferroelastic phase *I* and the incommensurate phase. The phase transition to the monoclinic phase upon heating is considerably smeared in the range of 200 K, and the curve $E_m(T)$ in the range from T_{c3} to T_{c2} is shifted toward high energies by 0.03 eV as compared to the curve $E_m(T)$ obtained upon cooling. This suggests that the sample

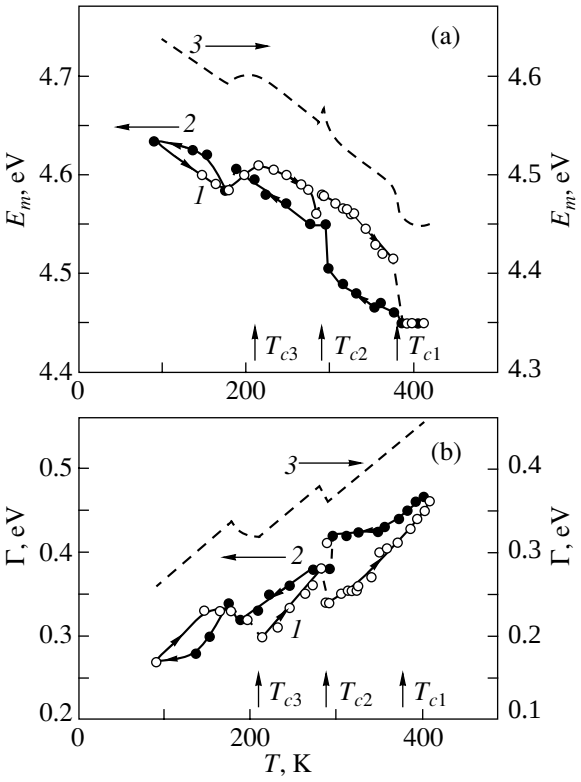

Fig. 2. Temperature dependences of (a) the position $E_m(T)$ and (b) the half-width $\Gamma(T)$ of the A_0 band for the Rb_2CdI_4 film upon (*1*) heating and (*2*) cooling of the sample and (*3*) the averaged dependences $\bar{E}_m(T)$ and $\bar{\Gamma}(T)$.

possesses thermal inertia and contains a portion of the low-temperature triclinic phase at $T > T_{c3}$. Furthermore, the phase transition at a temperature $T_{c2} \cong 290$ K upon heating is not accompanied by a noticeable shift of the curve $E_m(T)$ at $T > T_{c2}$ and manifests itself only as a jump in the half-width Γ by 0.04 eV. It seems likely that the commensurate phase upon heating is partially retained at the temperatures of existence of the incommensurate phase due to the pinning of domain boundaries at lattice defects. Only at a temperature $T_{c1} \cong$ 380 K is the transition to the paraphase attended by a sharp jump in the parameter E_m by 0.06 eV. It should be noted that, at temperatures intermediate between T_{c1} and T_{c2}, even slight cooling of the sample by 20 K does not lead to hysteresis phenomena and the curves $E_m(T)$ and $\Gamma(T)$ obtained upon heating are reproduced upon cooling. For the paraphase, the curves $E_m(T)$ coincide upon heating and cooling. However, the dependence $E_m(T)$ measured upon cooling of the sample at $T < T_{c1}$ differs substantially from that obtained upon heating: the jump at $T = T_{c1}$ is absent and $E_m(T)$ increases nonlinearly with a decrease in the temperature *T*. Such a behavior of the dependence $E_m(T)$ indicates the generation of solitons at temperatures close to the phase transition point T_{c2}. A sharp increase in the parameter $E_m(T)$

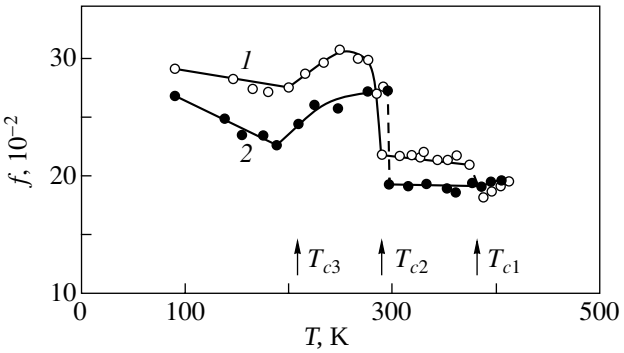

Fig. 3. Temperature dependences of the oscillator strength $f(T)$ of the A_0 band for the Rb_2CdI_4 film upon (*1*) heating and (*2*) cooling of the sample.

by ~0.05 eV at $T = T_{c2}$ suggests that this transition is a first-order phase transition. At these temperatures, we observed a characteristic hysteresis loop.

As the phase transition point T_{c2} is approached from high temperatures, the dependence $\Gamma(T)$ exhibits a less steep behavior (Fig. 2b). This is probably associated with the partial pinning of solitons at film defects. The pinning most likely is eliminated upon transition to the commensurate phase, because the half-width Γ at the temperature T_{c2} decreases by 0.04 eV. However, the larger values of $\Gamma(T)$ at $T < T_{c2}$ as compared to those upon heating indicate that the pinning of solitons is partly retained in the commensurate phase.

Defects of the crystal lattice play an important role in thermal memory [15, 16]. Distortions of the incommensurate phase due to the pinning of solitons more clearly manifest themselves in thin films, in which the lattice defects are grain boundaries and misfit dislocations at the film–substrate interface. To put it differently, thin films are characterized by longer relaxation times of metastable states and a more pronounced anomalous thermal hysteresis. This can explain the considerable differences in the dependences $E_m(T)$ and $\Gamma(T)$ at temperatures of the incommensurate phase of the Rb_2CdI_4 compound upon heating and cooling.

The oscillator strength of the A_0 band was determined according to the expression

$$f = \frac{mv}{4\pi e^2\hbar^2}\varepsilon_{2m}E_m\Gamma[1 - 0.322\alpha],$$

where v is the volume per molecule (the unit cell contains four molecules) and α is the fraction of the Gaussian component in the mixed profile of the A_0 band. As can be seen from Fig. 3, the general tendency observed in the dependence $f(T)$ suggests that the oscillator strength decreases with an increase in the temperature; more precisely, the oscillator strength $\bar{f}(T)$ decreases from 0.28 at 90 K to 0.20 at 420 K.

The observed decrease in the oscillator strength $f(T)$ of the A_0 band indicates that this band has a zero-phonon nature, because the oscillator strength of zero-phonon bands decreases with a variation in the Debye–Waller factor [17]. However, in the temperature range of existence of the commensurate monoclinic phase (200–290 K), the oscillator strength $\bar{f}(T)$ increases to 0.285 in an unusual manner. This increase is confirmed by the measured optical density spectra (Fig. 1). Furthermore, the fraction of the Gaussian component in the mixed profile at temperatures corresponding to commensurate phase *I* (200–290 K) decreases as compared to that for low-temperature commensurate phase *II* ($T <$ 200 K). The appearance of the Gaussian component in the initial Lorentzian profile of the exciton band is caused both by the disordering of the crystal lattice due to the formation of defects [11] and by the dynamical inhomogeneous broadening with an increase in the concentration of phonons upon heating of the sample and phonon–phonon interaction [18, 19]. Therefore, we can make the inference that the crystal lattice of the Rb_2CdI_4 film in the commensurate monoclinic phase has the most ordered structure. This inference is consistent with the considerable decrease in the half-width of the band $\bar{\Gamma}(0)$ upon transition from the triclinic phase to the monoclinic phase (Fig. 2). A similar jump in the temperature dependence of the oscillator strength $f(T)$ for the Cs_2CdI_4 compound in the range $T_{c3} \le T \le T_{c2}$ was also observed in our earlier work [10].

The difference between the thermal memories of the Rb_2CdI_4 film upon heating and cooling also manifests itself in the difference between the dependences $f(T)$ measured during heating and cooling. In particular, the oscillator strength $f(T)$ obtained upon cooling is smaller for the incommensurate phase and considerably smaller for commensurate phase *I*, even though the half-widths $\Gamma(T)$ for these two phases are larger. The possible reason for the decrease in the oscillator strength $f(T)$ is the pinning of solitons at lattice defects. The pinning is retained at temperatures $T < T_{c2}$ and hinders ordering of the domain boundaries in the commensurate phase. Moreover, the temperature dependence of the oscillator strength $f(T)$ is also affected by the first-order transition from the incommensurate phase to the paraphase upon heating of the sample and by the first-order transition from the incommensurate phase to the commensurate phase upon cooling.

4. CONCLUSIONS

Thus, the investigation into the temperature dependences of the spectral parameters of narrow exciton bands makes it possible to reveal phase transitions and thermal memory effects in ferroelastics. The method proposed in this work can be used to examine phase transitions in other classes of materials whose absorption spectra exhibit narrow exciton bands.

REFERENCES

1. I. N. Belyaev, E. A. Shurginov, and N. S. Kudryashov, Zh. Neorg. Khim. **17** (10), 2812 (1972).
2. K. S. Aleksandrov, S. V. Melnikova, I. N. Flerov, A. D. Vasilev, A. I. Kruglik, and I. T. Kokov, Phys. Status Solidi A **105** (2), 441 (1988).
3. V. Touchard, M. Louer, J. P. Auffredic, and D. Louer, Rev. Chim. Miner. **24** (4), 414 (1987).
4. V. V. Gladkiĭ, V. A. Kirikov, I. S. Zheludev, and I. V. Gavrilova, Fiz. Tverd. Tela (Leningrad) **29** (6), 1690 (1987) [Sov. Phys. Solid State **29**, 973 (1987)].
5. O. G. Vlokh, A. V. Kityk, and I. I. Polovinko, Kristallografiya **32** (1), 140 (1987) [Sov. Phys. Crystallogr. **32**, 78 (1987)].
6. O. G. Vlokh, B. V. Kaminskiĭ, I. I. Polovinko, and S. A. Sveleva, Fiz. Tverd. Tela (Leningrad) **28** (9), 2911 (1986) [Sov. Phys. Solid State **28**, 1637 (1986)].
7. T. Nattermann, Phys. Status Solidi B **133** (1), 65 (1986).
8. F. Shimizu and M. Takashige, J. Phys. Soc. Jpn. **67** (7), 2555 (1998).
9. I. M. Bolesta and Yu. M. Furgala, Ukr. Fiz. Zh. **36** (11), 1654 (1991).
10. O. N. Yunakova, V. K. Miloslavskiĭ, and E. N. Kovalenko, Fiz. Tverd. Tela (St. Petersburg) **45** (5), 888 (2003) [Phys. Solid State **45**, 932 (2003)].
11. I. Kh. Akopyan, D. N. Gromov, A. V. Mishchenko, A. E. Monov, B. V. Novikov, and M. D. Yaufman, Fiz. Tverd. Tela (Leningrad) **26** (9), 2628 (1984) [Sov. Phys. Solid State **26**, 1593 (1984)].
12. *Physics of Thin Films: Advances in Research and Development*, Ed. by G. Haas and R. Toon (Academic, New York, 1975; Mir, Moscow, 1978), Vol. 4.
13. V. K. Miloslavskiĭ, O. N. Yunakova, and Sun Tsya-Lin, Opt. Spektrosk. **78** (3), 436 (1995) [Opt. Spectrosc. **78**, 391 (1995)].
14. M. Schreiber and Y. Toyozawa, J. Phys. Soc. Jpn. **51** (5), 1528 (1982).
15. B. A. Strukov, V. M. Arutyunova, and Y. Uesu, Fiz. Tverd. Tela (Leningrad) **24** (10), 3061 (1982) [Sov. Phys. Solid State **24**, 1732 (1982)].
16. K. Hamano, Y. Ikeda, T. Fujimoto, K. Ema, and S. Hirotsu, J. Phys. Soc. Jpn. **49** (6), 2278 (1980).
17. M. Matsuura and H. Buttner, Phys. Rev. B **21** (2), 679 (1980).
18. V. K. Miloslavskiĭ and O. N. Yunakova, Opt. Spektrosk. **57** (1), 85 (1984) [Opt. Spectrosc. **57**, 51 (1984)].
19. V. K. Miloslavskiĭ and O. N. Yunakova, Ukr. Fiz. Zh. **31** (1), 50 (1986).

Translated by O. Borovik-Romanova

Physics of the Solid State, Vol. 46, No. 12, 2004, pp. 2286–2291. From Fizika Tverdogo Tela, Vol. 46, No. 12, 2004, pp. 2210–2215.

LOW-DIMENSIONAL SYSTEMS AND SURFACE PHYSICS

Peculiarities of Gallium Crystallization in Confined Geometry¶

B. F. Borisov[1], E. V. Charnaya[1, 2], A. V. Gartvik[1], C. Tien[2], Yu. A. Kumzerov[3], and V. K. Lavrentev[4]

[1] *Institute of Physics, St. Petersburg State University, Petrodvorets, St. Petersburg, 198504 Russia*
**e-mail: charnaya@mail.ru*
[2] *Department of Physics, National Cheng Kung University, Tainan, 70101 Taiwan*
[3] *Ioffe Physicotechnical Institute, Russian Academy of Sciences, Politekhnicheskaya ul. 26, St. Petersburg, 194021 Russia*
[4] *Institute of High-Molecular Combinations, St. Petersburg, 199004 Russia*

Received March 16, 2004

Abstract—The freezing and melting phase transitions for gallium embedded into a porous glass with a pore size of about 8 nm were studied using acoustic, NMR, and x-ray techniques. It was shown that the broadened solidification and melting transitions upon deep cooling up to complete freezing at 165 K were due to the formation of β-Ga within pores. The offset of confined β-Ga melting was lowered by about 21 K compared to the bulk β-Ga melting point. Both melting and freezing in pores were irreversible. The fulfillment of some special thermal conditions led to gallium crystallization into other modifications. The role of heterogeneous crystallization in freezing of confined gallium is discussed. © *2004 MAIK "Nauka/Interperiodica".*

1. INTRODUCTION

Recently, a great deal of attention has been focused on studies of surface and size effects induced by confined geometry. Properties of materials embedded into nanoporous matrices have been shown to differ remarkably from those in bulk. In particular, metals confined within porous glasses and artificial opals manifest alterations in their superconducting behavior [1–3], atomic mobility in the melted state [4], melting and freezing processes [5–9], electronic features [10], and crystalline structure [11, 12]. Studies of melting and freezing of metals in confined geometry have revealed some common features, such as a noticeable reduction of the phase transition temperatures and a rather reproducible thermal hysteresis upon cooling and warming. These changes in the behavior of confined metals were similar to the anomalies observed to date upon melting and freezing for simple and organic liquids within nanoporous matrices (see [13, 14] and references therein). Some other properties were specific for melting and freezing in particular metals. For instance, acoustic and NMR measurements on mercury in porous glasses were treated within the model of liquid skin formed upon melting [7, 8] similarly to melting of isolated metallic particles [15, 16].

The melting and freezing processes of gallium in confined geometry were studied in [9, 11, 12] and in the references therein. The first NMR, acoustic, calorimetric and resistance measurements carried out for gallium embedded into artificial opals and porous glasses with pore sizes of 4 and 200 nm revealed noticeable depression of the melting and freezing temperatures compared to the melting point of bulk α-gallium accompanied by a pronounced hysteresis. The melting process was reported to be strongly broadened, while the freezing could be quite sharp. However, contrary to the case of confined mercury and other liquids, the hysteresis loops observed for gallium within most porous matrices were complicated by two or more steps upon cooling and warming. Later x-ray studies showed that gallium in nanometer-size pores can crystallize into different modifications [11, 12]. Note that bulk gallium also occurs in different crystalline phases [17, 18]. Under ambient pressure, bulk liquid gallium crystallizes into α-Ga with a melting point of 303 K and the supercooled melt can freeze into β-Ga (melting point, 256.5 K). Other bulk crystalline modifications occur only under high pressure. Solid modifications of gallium submicrometric droplets coincide with the bulk ones [19]. According to [11, 12, 20], confined gallium modifications depend on pore size and geometry. They included the bulk α- and β-gallium, as well as some modifications with symmetry different from known bulk gallium structures. In particular, a tetragonal modification [11] was observed in artificial opals and in porous glasses with a pore size of 4 nm. Polymorphism of confined gallium explained the complex character of its freezing and melting transitions. However, the processes of simultaneous or consecutive crystallization into various modifications and their interrelation with pore geometry and thermal history remained unclear. The reduction of the gallium phase transition temperatures and irreversible melting agreed, according to [9, 11], with the predictions of the Gibbs–Thompson equation developed for isolated small spherical particles. Nevertheless, the coexistence within pores of various crystalline

¶ This article was submitted by the authors in English.

species, along with their structure disordering and some other experimental facts discussed in [11, 12], prevented quantitative treatment. Another aspect of gallium solidification that was discussed in [9, 11, 12] concerned the nature of nucleation (homogeneous or heterogeneous) in confined geometry and the reasons for thermal hysteresis upon cooling and warming. While the experimental results obtained in [9] made it possible to suggest the significant role played by heterogeneous crystallization within pores, the matter remained unclear until now.

The aim of the present paper is to study, using acoustic, NMR, and x-ray methods, the melting and freezing processes for gallium in a porous glass with pores about 8 nm in size in connection with the problems stated above.

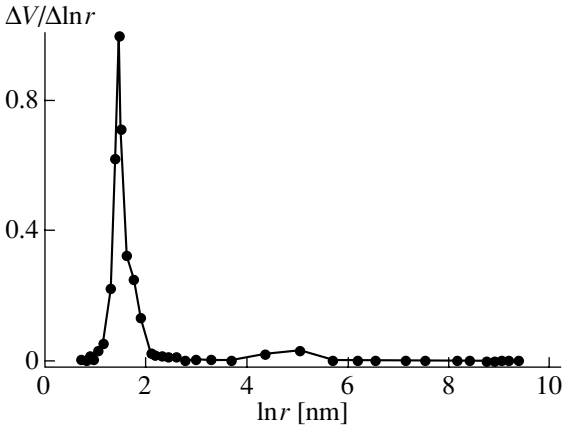

Fig. 1. Pore size distribution in the porous glass under study according to mercury intrusion porosimetry.

2. EXPERIMENTAL

Samples of porous glass used in the present work were prepared from phase-separated soda borosilicate glass with pore structure produced by acid leaching. The pore size was found to be equal to 8.4 nm by mercury intrusion porosimetry and small angle x-ray scattering. The pore volume distribution versus pore diameter according to mercury porosimetry is shown in Fig. 1. Liquid gallium was introduced into pores under a high pressure of up to 10 kbar. The filling factor of the pore volume was near 85%.

Numerous acoustic investigations of porous matrices filled with liquids showed that the velocity of the longitudinal as well as transverse ultrasonic waves changes noticeably upon melting or freezing of embedded materials following changes in the effective elastic moduli of the samples [7–9, 21, 22]. This allows the use of acoustic methods for detailed studies of the melting and freezing processes in confined geometry. We employed the conventional pulse ultrasound technique [23] at a frequency of 7 MHz, which gave the relative longitudinal sound velocity value

$$\Delta v/v = [v(T) - v(T = 295\ \mathrm{K})]/v(T = 295\ \mathrm{K})$$

with an accuracy better than 10^{-5}. All measurements were made during continuous slow cooling or warming of the sample within the range 295–160 K at various rates of temperature change. The temperature gradient in the sample did not exceed 0.05 K/cm.

NMR measurements were carried out using a pulse Broker Avance 400 NMR spectrometer. The ^{71}Ga NMR signal corresponding to liquid gallium was observed at various stabilized temperatures in the range from 295 to 160 K. Since the integral intensity of the signal is proportional to the total amount of melted gallium, NMR provides direct information on the fraction of liquid and solid gallium phases within pores. The operating frequency was 122 MHz. The temperature was controlled to within 0.5 K. Prior to each measurement, the sample was kept at a fixed temperature for about 5 min. To detect the NMR line, a single pulse sequence with phase cycling was applied with a pulse duration of 2.5 μs. The repetition time was 0.1 s.

The x-ray diffraction measurements were performed using a commercial powder DRON-2.0 diffractometer with CuK_α radiation at several temperatures between 180 and 295 K. During measurements, the temperature was stable within 2 K. The x-ray patterns were recorded within an angle range of 20° to 80° with a scan speed of 0.5 deg/min.

3. RESULTS AND DISCUSSION

The temperature dependence of the intensity of the ^{71}Ga NMR line corresponding to liquid gallium upon cooling from room temperature down to 160 K and consecutive warming on the rate of temperature change between measurements of about 50 K/h is presented in Fig. 2. It shows that confined gallium starts to freeze at about 215 K and the solidification process ends at about 165 K. Upon warming, the melting process becomes noticeable only above 195 K and the total amount of gallium melts near 235 K. Note that smooth alterations in the NMR signal intensity outside of the gallium phase transitions obviously arise due to the Curie law for nuclear susceptibility. The full hysteresis loops upon cooling and warming at a similar rate of temperature change were quite reproducible; the temperatures of the onset and offset of the phase transformations shifted by no more than several degrees. Measurements of the temperature dependences of ultrasound velocity for similar thermocycles also showed hysteresis loops associated with the melting and freezing processes (Fig. 2), which agree well with the NMR data.

As can be seen in Fig. 2, both the melting and freezing processes are noticeably lowered compared to those for bulk α-Ga and smeared over large temperature ranges. X-ray measurements showed that the freezing observed is related to the formation within pores of a single crystalline modification coinciding with β-Ga.

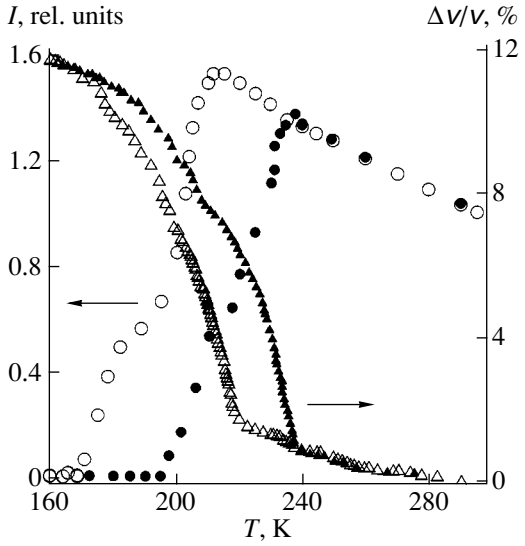

Fig. 2. Temperature dependences of the NMR signal intensity I (circles) and relative ultrasound velocity $\Delta v/v$ (triangles) for the full freezing–melting thermocycle upon cooling (open symbols) and warming (closed symbols).

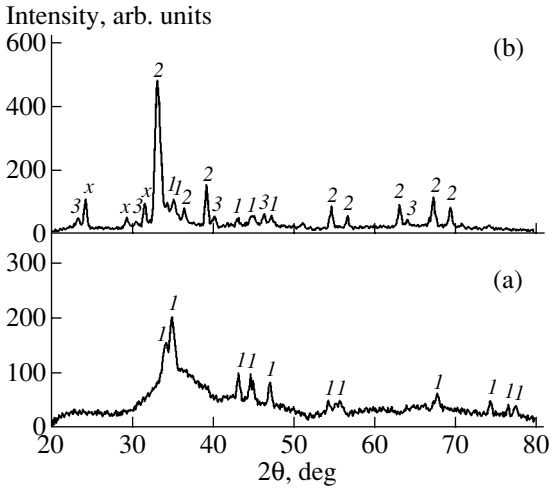

Fig. 3. X-ray powder diffraction patterns obtained (a) at 211 K upon cooling from room temperature and (b) at 220 K after consecutive cooling from room temperature to 205 K, warming to 240 K, cooling to 190 K, and warming to 220 K. Peaks corresponding to β-Ga, the tetragonal modification, α-Ga and to a unidentified structure are marked with *1*, *2*, *3*, and *x*, respectively.

The x-ray pattern obtained at 211 K after cooling from room temperature is shown in Fig. 3a.

The width of the peaks in Fig. 3a was greater than the instrumental broadening (0.3°). Hence, following [11, 12], one can evaluate the average size of confined metallic crystallites from the peak broadening using the Schemer equation [24]. The obtained size of about 25 nm is noticeably larger than the pore diameter. This means that the crystallization front passes through gallium within several neighbor pores. A similar difference in the pore diameters and crystallite sizes was also found for gallium in other nanoporous matrices [11, 12], for indium in Vycor glass [5], and for some wetting liquids, such as O_2, D_2, and CO_2 (see [25] and references therein), in contrast to confined mercury [6].

Using acoustic methods, we then performed detailed studies of the influence of the rate of temperature change and thermal history on the melting and freezing processes for confined gallium. The measurements showed that, when thermocycles started at room temperature and cooling continued down to below 204 K, the main hysteretic behavior was reproducible independent of the cooling or warming rate. Namely, freezing started near 215 K and the offset of melting was seen near 235 K. It was also found that both melting and freezing were completely irreversible; that is, when crystallization was interrupted at some intermediate temperature and the sample under study was warmed up, the velocity curve upon warming did not coincide with that upon cooling but merged with the warming branch of the full hysteresis loop at higher temperatures. An example is shown in Fig. 4a. Similarly, when the sample was cooled down after incomplete melting, the velocity curve tended to merge with the cooling branch of the full hysteresis loop. Note that the irreversible freezing in confined geometry was also seen in other liquids [7, 13, 22] and can be explained by the hysteresis between freezing and melting. However, a temperature range of reversible melting was found upon warming for some liquids in porous matrices, including mercury [7, 8, 13], contrary to the results obtained for gallium in the present and previous studies.

Normally, the treatment of the melting and freezing phase transitions for confined liquids is based on models developed for isolated spherical or cylindrical particles [8, 13, 21, 22]. Simple theories predict a reduction of the melting or freezing points for small particles because of a large surface-to-volume ratio. For spherical particles, the melting temperature depression ΔT_m is given by the Gibbs–Thompson equation [26]

$$\Delta T_m = 2\gamma v_0 T_b / Lr, \quad (1)$$

where r is the particle radius, γ is the surface tension of the solid, L is the latent heat of fusion, T_b is the bulk melting temperature, and v_0 is the molar volume of the solid. Freezing is mostly treated as a result of supercooling. This explains the hysteresis between solidification and melting and, therefore, the irreversible behavior upon freezing. However the geometric-freezing model was also discussed for porous media [22, 27]. According to this model, crystallization in confined particles is considered similarly to structural phase transformations in solids. Then it is controlled by pore geometry and the depression of the freezing temperature ΔT_f for spherical particles is given by

$$\Delta T_f = 3\alpha v_0 T_b / Lr, \quad (2)$$

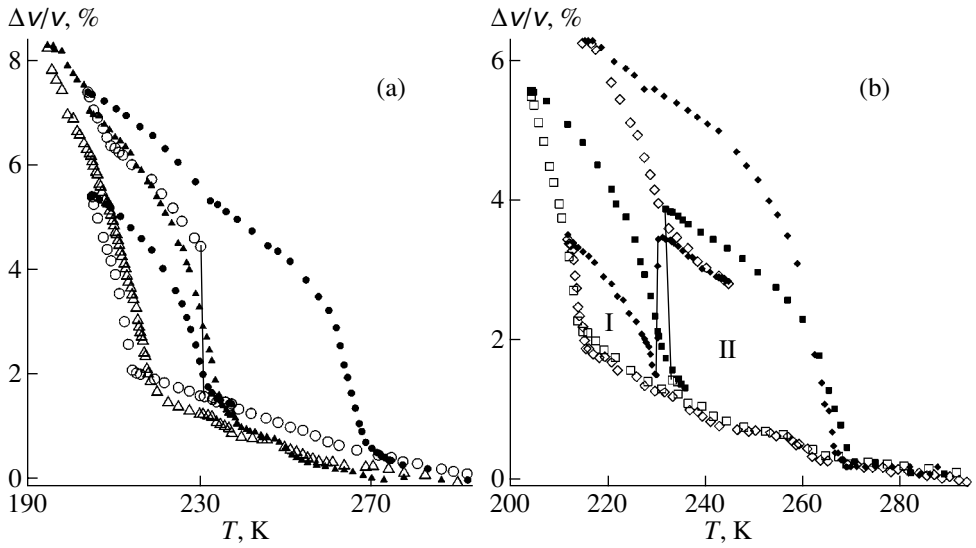

Fig. 4. Temperature dependences of the relative ultrasound velocity $\Delta v/v$ upon cooling (open symbols) and warming (closed symbols) for thermocycles started at room temperature. The straight lines are drawn to guide the eye. (a) Triangles: cooling to 194.4 K and warming to room temperature. Circles: cooling to 204.7 K, warming to 237.2 K, cooling to 203.7 K, and warming to room temperature. (b) Diamonds: cooling to 204.4 K, warming to 235.5, cooling to 232 K, and warming to room temperature. Squares: cooling to 211.8 K, warming to 245 K, cooling to 215 K, and warming to room temperature.

where α is the surface energy. However, the geometric-freezing model does not provide a proper explanation for the hysteresis. A more complicated analysis implies the formation of a liquid layer (liquid skin) surrounding the solid core of a small particle (see [16, 28] and references therein).

Relationships (1) and (2) predict that the phase transitions occur at a temperature determined by the particle radius. Thus the total processes in confined geometry should be irreversible and the distribution of particle sizes should result in broadening of the phase transition. This idea has been used in some studies to find the pore size distribution from the melting processes of cyclohexane [14]. On the other hand, the liquid skin model predicts that the melting process of a particular particle occurs within a temperature range where the liquid layer becomes thicker [28]. Within this range, melting should be reversible until the offset point where the solid core melts. Therefore, the absence of the reversible melting range upon warming for gallium allows us to suggest that the liquid skin model is not applicable to confined gallium, contrary to confined mercury and isolated metallic particles [7, 15, 16], or the melting broadening due to the pore size distribution is much more essential than the smearing due to liquid layer formation.

According to Fig. 1, both the onset of freezing and the offset of melting for confined β-gallium are shifted to low temperatures as compared to the melting point of bulk β-Ga. The lowering of the offset of melting is about 21 K, while for β-Ga within pores in the opal [11] it was near 10 K. Since the pore sizes for the opal can be estimated as 50 and 100 nm [11], this result qualitatively agrees with predictions of the Gibbs–Thompson equation. Taking into account the irregular shape of confined particles, affected by the pore geometry, and particle interconnection, one can hardly expect exact agreement. Note also that the temperatures of the onset of freezing are almost the same in the porous glass under study and in the opal (about 215 K).

Acoustic studies also showed that the fulfillment of special conditions of thermocycling could drastically change the total process of gallium crystallization. For instance, when the sample was cooled to a temperature lying below the onset of freezing and then consecutively warmed to 237.2 K and again cooled, the velocity underwent a jump just below the offset of melting in full thermocycles (Fig. 4). After the jump, the velocity branches corresponding to cooling and warming merged together only near 270 K (Fig. 4). The effect was quite reproducible. As has been found in previous acoustic studies of melting and freezing in confined liquids, including confined metallic melts, the increase in ultrasound velocity reveals the process of crystallization within pores [7–9, 21, 22]. Thus, the abrupt increase in ultrasound velocity observed near 230 K can be treated as crystallization into another gallium modification (or several modifications), with the offset of melting at about 270 K. It should be noted that gallium crystallizes near 230 K only partially. The other gallium remains liquid and freezes at lower temperatures, as can be seen in Fig. 4.

To confirm the suggestion regarding gallium crystallization into modifications different from β-Ga, we carried out additional x-ray studies. The x-ray pattern obtained at 220 K after a thermocycle corresponding to

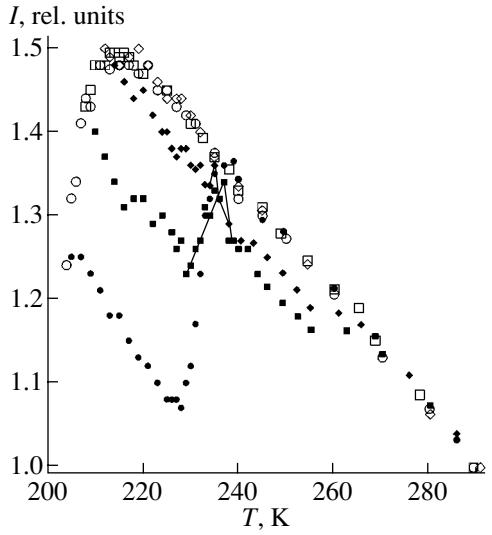

Fig. 5. Temperature dependences of the NMR signal intensity *I* for three thermocycles started at room temperature. Circles indicate cooling to 204 K; squares, to 208 K; and diamonds, to 212 K. Open and closed symbols correspond to cooling and warming, respectively. The straight lines are drawn to guide the eye.

the conditions described above revealed additional peaks (Fig. 3b). The most intense peaks (marked with *2*) coincided with those belonging to a tetragonal modification found recently in porous glass with pores of 4 nm and in artificial opals [11, 12]. According to [29], it has the lattice parameters $a = 3.25$ Å and $c = 4.95$ Å and differs from known bulk gallium structures [18]. Using the lattice parameters a and c, we can estimate the crystal density ρ assuming that the unit cell contains three atoms: $\rho = 6.65$ g/cm^3. The value obtained is larger than the density of liquid gallium ($\rho = 6.095$ g/cm^3), as for other known gallium modifications, except the solid α phase ($\rho = 5.91$ g/cm^3) [17, 18]. Weaker peaks (marked with *3* in Fig. 3b) can be attributed to the disordered α phase following x-ray data published in [11] for gallium embedded into artificial opals. Three other peaks (marked with *x*) were not identified. Thus, according to the x-ray data obtained, hysteresis loop I in Fig. 4b arises due to the formation of β-Ga, while hysteresis loop II is related chiefly to crystallization into the tetragonal modification and, to a lesser extent, into α-Ga and an unidentified phase.

According to acoustic studies, freezing at about 230 K into the tetragonal and α modifications could also occur when the sample is cooled to a temperature lying below the onset of freezing and 204 K (at a rate less than 15 K/h below about 235 K and less than 40 K/h at other temperatures) and consecutively warmed (Fig. 4b). It should be expected that the decrease in the total amount of liquid gallium caused by partial crystallization at about 230 K can be detected by NMR. While precise NMR measurements require a long time due to the large number of acquisitions and it is not easy to fulfill the necessary conditions, we obtained results that agreed with the results of acoustic studies (Fig. 5). The crystallization was seen via the decrease in the total amount of liquid gallium near 235–238 K, in contrast to the results observed after deeper cooling. Note that, according to Fig. 5, the amount of additional gallium modification is rather small as compared to the alterations in ultrasound velocity. This difference could arise due to some variations in the thermal conditions during NMR and acoustic measurements. It is also necessary to take into account that the relative sensitivity of velocity to gallium freezing within pores depends on the elastic properties of particular crystalline modifications.

The results obtained showed that, while gallium confined within the porous glass under study normally starts to freeze near 215 K, liquid gallium in pores is in a metastable state at higher temperatures and can crystallize under certain conditions. Such peculiar features of confined gallium are related to its ability to occur in several different crystalline modifications, which melt at particular temperatures, and with its tendency toward supercooling. Fairly similar behavior can be observed in bulk gallium. When gallium is supercooled at ambient pressure well below the α-Ga melting point, it can crystallize into β-Ga [17]. It is also known that supercooled bulk gallium crystallizes below 303 K into the α modification upon cooling, as well as upon warming, if heterogeneous nucleation is initiated. The fact that the process of additional crystallization in confined gallium at about 230 K was observed only after preparatory cooling below the onset of ordinal freezing near 215 K (Fig. 4) shows the importance of the presence of a small amount of frozen gallium in pores. One can suggest that such crystallites serve as nucleation centers, which provoke heterogeneous crystallization. One can also suggest that the thermal conditions used in the present studies influence the geometry and the number of crystallites to make crystallization near 230 K possible.

4. CONCLUSIONS

Studies of the freezing and melting for gallium confined within porous glass with a pore size of 8 nm showed that the solidification and melting transitions upon deeper cooling up to complete freezing starting at about 215 K are due to the formation of β-Ga within pores. The melting and freezing temperature ranges were shifted noticeably downwards as compared to the bulk β-Ga melting point. Both melting and freezing were irreversible. The irreversibility of melting contradicts the liquid skin model and allows us to suggest that the broadening of the melting process arises mainly due to the pore size distribution, contrary to the case of confined mercury. The results obtained also revealed that fulfilling some special thermal conditions leads to gallium crystallization at about 230 K into the tetragonal gallium modification, which until now had only been

found in confined geometry, and into the disordered α phase. The fact that the crystallization needs a certain amount of crystallites of another confined gallium modification to start demonstrates the important role of heterogeneous nucleation in freezing within pores.

ACKNOWLEDGMENTS

The present work was partially supported by the National Science Council of Taiwan under grant no. 91-2112-M-006-017.

REFERENCES

1. M. J. Graf, T. E. Huber, and C. A. Huber, Phys. Rev. B **45**, 3133 (1992).
2. E. V. Charnaya, C. Tien, K. J. Lin, Yu. A. Kumzerov, and C.-S. Wur, Phys. Rev. B **58**, 467 (1998).
3. C. Tien, C.-S. Wur, K. J. Lin, E. V. Charnaya, and Yu. A. Kumzerov, Phys. Rev. B **61**, 14833 (2000).
4. E. V. Charnaya, T. Loeser, D. Michel, C. Tien, D. Yaskov, and Yu. A. Kumzerov, Phys. Rev. Lett. **88**, 097602 (2002).
5. K. M. Unruh, T. E. Huber, and C. A. Huber, Phys. Rev. B **48**, 9021 (1993).
6. Yu. A. Kumzerov, A. A. Nabereznov, S. B. Vakhrushev, and B. N. Savenko, Phys. Rev. B **52**, 4772 (1995).
7. B. F. Borisov, E. V. Charnaya, P. G. Plotnikov, W.-D. Hoffmann, D. Michel, Yu. A. Kumzerov, C. Tien, and C. S. Wur, Phys. Rev. B **58**, 5329 (1998).
8. E. V. Charnaya, P. G. Plotnikov, D. Michel, C. Tien, B. F. Borisov, I. G. Sorina, and E. I. Martynova, Physica B (Amsterdam) **299**, 56 (2001).
9. B. F. Borisov, E. V. Charnaya, T. Loeser, D. Michel, C. Tien, C. S. Wur, and Yu. A. Kumzerov, J. Phys.: Condens. Matter **11**, 10259 (1999).
10. E. V. Charnaya, D. Michel, C. Tien, Yu. A. Kumzerov, and D. Yaskov, J. Phys.: Condens. Matter **15**, 5469 (2003).
11. E. V. Charnaya, C. Tien, K. J. Lin, and Yu. A. Kumzerov, J. Phys.: Condens. Matter **10**, 7273 (1998).
12. E. V. Charnaya, C. Tien, K. J. Lin, and Yu. A. Kumzerov, Phys. Rev. B **58**, 11089 (1998).
13. H. K. Christenson, J. Phys.: Condens. Matter **13**, R95 (2001).
14. J. H. Strange, M. Rahan, and E. G. Smith, Phys. Rev. Lett. **71**, 3589 (1993).
15. L. Gråbek, J. Bohr, H. H. Andersen, A. Johansen, E. Johnson, L. Sarholt-Kristensen, and I. K. Robinson, Phys. Rev. B **45**, 2628 (1992).
16. T. Ben David, Y. Lereah, G. Deutsher, R. Kofman, and P. Cheyssac, Philos. Mag. A **71**, 1135 (1995).
17. *Chemistry of Aluminum, Gallium, Indium and Thallium*, Ed. by A. J. Downs (Blackie, London, 1993).
18. *Powder Diffraction File, Inorganic Phases* (International Centre for Diffraction Data, Newtown Square, PA, 1992).
19. A. Di. Cicco, Phys. Rev. Lett. **81**, 2942 (1998).
20. C. Tien, C. S. Wur, K. J. Lin, J. S. Hwang, E. V. Charnaya, and Yu. A. Kumzerov, Phys. Rev. B **54**, 11880 (1996).
21. C. L. Jackson and G. B. McKenna, J. Chem. Phys. **93**, 9002 (1990).
22. E. Molz, A. P. Y. Wong, M. H. W. Chan, and J. R. Beamish, Phys. Rev. B **48**, 5741 (1993).
23. J. Williams and J. Lamb, J. Acoust. Soc. Am. **30**, 308 (1958).
24. B. E. Warren, *X-ray Diffraction* (Addison-Wesley, Reading, MA, 1989).
25. D. W. Brown, P. E. Sokol, A. P. Clarke, M. A. Alam, and W. J. Nuttall, J. Phys.: Condens. Matter **9**, 7317 (1997).
26. Ph. Buffat and J.-P. Borrel, Phys. Rev. A **13**, 2287 (1976).
27. J. Warnock, D. D. Awschalom, and M. W. Shafer, Phys. Rev. Lett. **57**, 1753 (1986).
28. R. R. Vanfleet and J. M. Mochel, Surf. Sci. **341**, 40 (1995).
29. I. G. Sorina, E. V. Charnaya, L. A. Smirnov, Yu. A. Kumzerov, and C. Tien, Phys. Solid State **40**, 1407 (1998).

Physics of the Solid State, Vol. 46, No. 12, 2004, pp. 2292–2300. Translated from Fizika Tverdogo Tela, Vol. 46, No. 12, 2004, pp. 2216–2223.

LOW-DIMENSIONAL SYSTEMS AND SURFACE PHYSICS

Waves in a Superlattice with Arbitrary Interlayer Boundary Thickness

V. A. Ignatchenko* and O. N. Laletin**

**Kirensky Institute of Physics, Siberian Division, Russian Academy of Sciences, Akademgorodok, Krasnoyarsk, 660036 Russia*

e-mail: vignatch@iph.krasn.ru

***Krasnoyarsk State University, Krasnoyarsk, 660041 Russia*

Received February 4, 2004; in final form, March 31, 2004

Abstract—The transmittance $D(\omega)$, reflectance $R(\omega)$, and dispersion $\omega(k)$ are investigated for waves of various nature propagating through a one-dimensional superlattice (multilayer structure) with arbitrary thickness of the interlayer boundary. The dependences of the band gap widths $\Delta\omega_m$ and their positions in the wave spectrum of the superlattice on the interlayer boundary thickness d and the band number m are calculated. Calculations are performed in terms of the modified coupled-mode theory (MCMT) using the frequency dependence of $R(\omega)$, as well as in the framework of perturbation theory using the function $\omega(k)$, which made it possible to estimate the accuracy of the MCMT method; the MCMT method is found to have a high accuracy in calculating the band gap widths and a much lower accuracy in determining the gap positions. It is shown that the m dependence of $\Delta\omega_m$ for electromagnetic (or elastic) waves is different from that for spin waves. Furthermore, the widths of the band gaps with $m = 1$ and 2 are practically independent of d, whereas the widths of all gaps for $m > 2$ depend strongly on d. Experimental measurements of these dependences allow one to determine the superlattice interface thicknesses by using spectral methods. © *2004 MAIK "Nauka/Interperiodica".*

1. INTRODUCTION

Propagation of waves of various nature (electromagnetic, elastic, spin, etc.) and their spectra in media with one-dimensional periodic modulation of the material parameters—multilayer structures or superlattices (SLs)—has been investigated theoretically in numerous studies. This problem is discussed in monographs [1–5] and reviews [6, 7]. The dispersion laws and wave propagation factors in SLs are determined to a large degree by the geometry of the modulation profile of the material parameters of the SLs. As a rule, rectangular and sinusoidal spatial modulations of parameters have been considered in the literature. Rectangular modulation corresponds to the case of maximally sharp boundaries between the SL layers (zero boundary thickness), and sinusoidal modulation corresponds to the limiting case of maximally smooth boundaries (the "boundary" thickness is equal to the "layer" thickness). A model with a rectangular modulation profile has been widely used when studying electromagnetic [8–11], elastic [12–16], and spin [17–22] waves. Waves of various physical nature for the model with a sinusoidal modulation profile of the material parameters were investigated in [23, 24]. In [25], spin waves were considered for both cases.

However, in real SLs, the modulation profile of the material parameters can be intermediate between these two limiting cases. For this reason, a model of an SL was proposed in [26] in which modulation is proportional to the Jacobian elliptic sine:

$$\rho(z) = \kappa\left(\frac{\mathbf{K}}{\mathbf{K}-\mathbf{E}}\right)^{1/2} \mathrm{sn}\left(\frac{\pi z}{2d}\right), \qquad (1)$$

where $d = \pi l/8\mathbf{K}$ is the SL interlayer boundary thickness; l is the SL period ($l/2 - d$ is the layer thickness); $\mathbf{K}$ and $\mathbf{E}$ are the complete elliptic integrals of the first and second kind, respectively; and κ is the modulus of these elliptic integrals. The factor before the elliptic sine corresponds to the normalization $\langle\rho^2(z)\rangle = 1$ (angle brackets mean averaging over the period l). The general form of function (1) is shown in Fig. 1. Depending on the modulus κ, this function describes the limiting

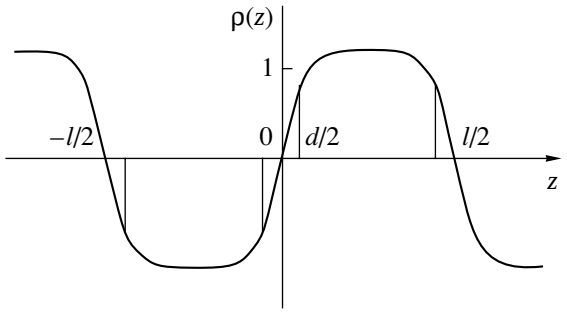

Fig. 1. Function given by Eq. (1) for $\kappa = 0.994$ ($d/l = 0.218$).

cases of a rectangular profile ($d/l = 0$, $\kappa = 1$, $\mathbf{K} = \infty$), a sinusoidal profile ($d/l = 1/4$, $\kappa = 0$, $\mathbf{K} = \pi/2$), and all intermediate values d/l. In Eq. (1), the boundary thickness d is determined such that the main variation in the material parameter occurs over the distance d for all values of d/l (Fig. 1). The basic feasibility of spectral methods of studying the boundary structure in SLs was demonstrated in [26]. In order to realize such methods, the theory needs to be extended in several directions. The present study deals with two of these directions. One of them is related to the fact that in [26] the spectrum of standing waves was calculated, while, in experiments with standing waves, only the wave dispersion law is studied directly. The other parameters (the reflectance and transmittance) are measured in experiments with traveling waves. Therefore, it is necessary to analyze the case of propagating waves for the model proposed in [26]. In the second direction of study, one should develop a more exact theory in order to find the dispersion law of waves for such a model. Both directions require the application and development of appropriate approximate methods of calculation, since the second-order equation with a coefficient whose coordinate dependence is described by an elliptic sine belongs to the general class of Hill equations and cannot be reduced to any well-known equations of this class. In particular, this equation cannot be reduced to the Lamé equation, which contains an elliptic sine squared.

2. WAVE PROPAGATION IN SUPERLATTICES

By way of example, we consider the propagation of electromagnetic waves in an SL with permittivity periodically modulated along the z axis:

$$\epsilon(z) = \epsilon'[1 - \gamma\rho(z)] - i\epsilon''. \quad (2)$$

Here, ϵ' and ϵ'' are the static components of the real and imaginary parts of the permittivity, respectively; γ is the relative root-mean-square modulation of the real part of the permittivity; and $\rho(z)$ is a periodic function with period l satisfying the conditions $\langle\rho(z)\rangle = 0$ and $\langle\rho^2(z)\rangle = 1$. We restrict ourselves to weakly perturbed media; i.e., we set $\gamma \ll 1$. We also assume that the order of magnitude of the ϵ''/ϵ' ratio does not exceed γ. We are interested in the solutions to the system of Maxwell equations near the frequencies of the Bragg resonances corresponding to the boundaries of the mth Brillouin zones. We consider waves propagating along the z axis. To find an approximate solution, we use the modified coupled-mode theory (MCMT) (see [27] and review [7]; the development of the application of the MCMT to optical waveguides is reviewed in [28]; originally, the coupled-mode theory was suggested in [29]). In this theory, a system of equations for the amplitudes of two waves propagating in opposite directions is written out. The coupling parameters $\kappa_m^{\pm}$ in this system can be written as

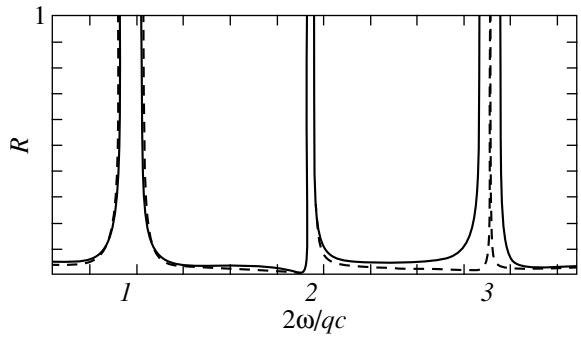

Fig. 2. $R(\omega)$ dependence for a semi-infinite SL near the first three Brillouin zones for rectangular (solid curve) and sinusoidal (dashed curve) modulations of the SL.

$$\kappa_m^{\pm} = \frac{1}{4l}\oint_0^l \frac{dz}{\epsilon(z)}\frac{d\epsilon(z)}{dz}\exp(\pm 2i\psi(z) \mp 2i\omega\tilde{n}z/c \pm imqz) + \frac{1}{4l}\sum_{j=1}^{N}\ln\frac{\epsilon(z_j+0)}{\epsilon(z_j-0)}\exp(\pm 2i\psi(z_j) \mp 2i\omega\tilde{n}z_j/c \pm imqz_j), \quad (3)$$

where $\psi(z) = \frac{\omega}{c}\int_0^l \sqrt{\epsilon(z')}dz'$, $\tilde{n} = c\psi(l)/\omega l$, $q = 2\pi/l$, the principal value of the integral is implied, and the sum takes into account the contribution of the permittivity jumps at discontinuity points z_j. Relation (3) is the main result of the MCMT, since all measured physical quantities, in particular, the reflectance $R(\omega)$ and transmittance $D(\omega)$, can be expressed in terms of the coupling parameters $\kappa_m^{\pm}$ (see, for example, [7]).

Figure 2 shows the frequency dependence of the reflectivity R calculated for a semi-infinite medium ($L \longrightarrow \infty$) in the absence of absorption ($\epsilon'' = 0$) for two well-known cases of limiting values of the boundary thickness: $d/l = 0$ (the case of a rectangular SL profile, represented by the solid curve in Fig. 2) and $d/l = 1/4$ (the case of a sinusoidal SL profile, represented by the dashed curve). The $R(\omega)$ dependence is plotted in the vicinity of three Brillouin zones, $m = 1$, 2, and 3. We see that the band gap widths are practically equal in the two limiting cases for both $m = 1$ and 2. However, for $m = 3$, these widths differ substantially. We intend to use this difference to construct the theoretical foundation for experimental determination of the boundary thickness d from spectral measurements. To this end, we must, first of all, obtain the dependence of the coupling parameters $\kappa_m^{\pm}$ on the SL parameters. Assuming that the function $\rho(z)$ in Eq. (2) has no discontinuities, we

retain in Eq. (3) only the integral, into which we substitute the Fourier expansion of this function. If the gap number m is such that $m\gamma/2 \ll 1$, then the integrand in Eq. (3) can be expanded in powers of the small parameter γ. Keeping terms of up to the order of γ^3 and integrating, we obtain

$$\begin{aligned}\kappa_m^{\pm} &= \pm\frac{imq}{8}e^{\pm i\Phi}\Bigg[2\gamma\left(1+i\frac{\epsilon''}{\epsilon'}-\frac{\epsilon''^2}{\epsilon'^2}\right)\rho_{\mp m}\\ &+\gamma^2\Bigg\{\frac{2\omega\sqrt{\epsilon'}}{mqc}\left(1+\frac{3i}{2}\frac{\epsilon''}{\epsilon'}\right)\sum_n\frac{\mp m-n}{n}\rho_n\rho_{\mp m-n}\\ &+\left(1+2i\frac{\epsilon''}{\epsilon'}\right)\sum_n\rho_n\rho_{\mp m-n}\Bigg\}\\ &+\gamma^3\Bigg\{\frac{\omega\sqrt{\epsilon'}}{2mqc}\sum_{n+p\neq 0}\frac{\mp m-n-p}{n+p}\rho_n\rho_p\rho_{\mp m-n-p}\\ &+\sum_{n,p}\left(\mp\frac{\omega^2\epsilon'}{m^2q^2c^2}\frac{\mp m-n-p}{np}+\frac{\omega\sqrt{\epsilon'}}{mqc}\frac{\mp m-p}{p}+\frac{2}{3}\right)\\ &\times\rho_n\rho_p\rho_{\mp m-n-p}\Bigg\}+\ldots\Bigg],\end{aligned} \tag{4}$$

where

$$\begin{aligned}\Phi &= \frac{\omega\sqrt{\epsilon'}}{iqc}\Bigg[\left(1+\frac{i}{2}\frac{\epsilon''}{\epsilon'}\right)\gamma\sum_n\frac{\rho_n}{n}\\ &+\frac{1}{4}\gamma^2\sum_{n+p\neq 0}\frac{\rho_n\rho_p}{n+p}+\ldots\Bigg].\end{aligned} \tag{5}$$

After substituting Eq. (4) into the corresponding expressions for the transmittance D and reflectance R, their ω dependences can generally be constructed for any modulation profile and any thickness L of the SL. Using the $D(\omega)$ or $R(\omega)$ dependences, we can find, in particular, the gap widths at the boundaries of the Brillouin zones as functions of the interface thickness.

Let us obtain the explicit dependences of the gap widths on d for a simpler model of a semi-infinite SL in a nonabsorbing medium. In this case, in the region of band gaps, the function $R(\omega)$ has flat tops with $R = 1$. Using this condition, we obtain equations for the frequencies $\omega_m^{\pm}$ bounding the mth band gap:

$$\omega_m^{\pm} = \frac{c}{\tilde{n}}\left(\frac{mq}{2}\pm\left|\kappa_m^+\kappa_m^-\right|^{1/2}\right). \tag{6}$$

In these equations, the coefficients $\kappa_m^{\pm}$ depend on $\omega_m^{\pm}$. By solving these equations, we can find the width of the mth band gap $\Delta\omega_m = \omega_m^+ - \omega_m^-$. We set $\epsilon'' = 0$ in Eq. (4) and substitute $\kappa_m^{\pm}$ defined by these expressions into Eqs. (6). By solving the obtained equations for $\omega_m^{\pm}$ to within the terms of the order of γ^3, we obtain

$$\begin{aligned}\omega_m^{\pm} &= \frac{mqc}{2\sqrt{\epsilon'}}\Bigg[1+\frac{1}{8}\gamma^2\\ &\pm\frac{1}{16}\gamma^3\left(|\rho_m|\mp\sum_{n+p\neq 0}\rho_n\rho_p\rho_{-n-p}\right)\\ &\pm\left|\frac{1}{2}\rho_m\gamma+\frac{m}{4}\gamma^2\sum_p\frac{\rho_p\rho_{m-p}}{p}\pm\frac{m}{8}|\rho_m|\gamma^3\right.\\ &\left.\times\sum_p\frac{\rho_p\rho_{m-p}}{p}+\frac{1}{16}\gamma^3S_m\right|\Bigg],\end{aligned} \tag{7}$$

where

$$\begin{aligned}S_m &= \sum_{n+p\neq 0}\frac{m-n-p}{n+p}\rho_n\rho_p\rho_{m-n-p}\\ &+\sum_{n,p}\left(\frac{m^2}{np}+\frac{2}{3}\right)\rho_n\rho_p\rho_{m-n-p}.\end{aligned} \tag{8}$$

From these expressions, the gap widths can be found to be (to within terms of the order of γ^2)

$$\Delta\omega_m = \frac{mqc}{2\sqrt{\epsilon'}}\left|\rho_m\gamma+\frac{m}{2}\gamma^2\sum_p\frac{\rho_p\rho_{m-p}}{p}\right|. \tag{9}$$

Expressions (7)–(9) are valid for any shape of the SL profile $\rho(z)$ represented by the Fourier harmonics ρ_n in them.

Let us consider the functions having the so-called symmetry of the third kind [30],

$$\rho(z+l/2) = -\rho(z). \tag{10}$$

For all functions of this class, the Fourier harmonics ρ_n vanish for even n. Using this property, we can simplify Eqs. (7):

$$\omega_m^{\pm} = \frac{mqc}{2\sqrt{\epsilon'}}$$

$$\times\begin{cases} 1+\frac{1}{8}\gamma^2 \pm \left|\frac{\rho_m}{2}\gamma + \frac{S_m}{16}\gamma^3\right| \pm \frac{|\rho_m|}{16}\gamma^3, & \text{for odd } m \\ 1+\frac{1}{8}\gamma^2 \pm \frac{m}{4}\gamma^2\left|\sum_p \frac{\rho_p\rho_{m-p}}{p}\right|, & \text{for even } m. \end{cases} \quad (11)$$

The gap widths at the boundaries of odd and even Brillouin zones are found to be

$$\Delta\omega_m = \frac{mqc}{2\sqrt{\epsilon'}}\begin{cases} \left|\rho_m\gamma + \frac{S_m}{8}\gamma^3\right| + \frac{|\rho_m|}{8}\gamma^3, & \text{for odd } m \\ \frac{m}{2}\gamma^2\left|\sum_p \frac{\rho_p\rho_{m-p}}{p}\right|, & \text{for even } m. \end{cases} \quad (12)$$

Using these expressions, the gaps $\Delta\omega_m$ for the model of an SL with arbitrary boundary thickness described by Eq. (1) are plotted as functions of d/l in Fig. 3a for odd gaps and in Fig. 3b for even gaps. In both figures, the gap widths are normalized to the width of the first band gap for an SL with a sinusoidal profile, $\Delta\omega_{1\,\text{sine}}$. The expressions for the widths of odd gaps obtained previously in [26] correspond to the term proportional to γ in Eq. (12) for odd m. In [26], expressions and plots are obtained for gap widths in the spectrum of spin waves; the corresponding dependences for electromagnetic waves can be obtained from them with the following substitution: $\nu = (\omega/c)^2\epsilon_e$ and $\epsilon = \gamma(\omega/c)^2\epsilon_e$ [in the notation of [26], ϵ_e is the permittivity and ϵ is the coefficient (having the dimension of the wave number) of the function $\rho(z)$ in the wave equation]. For the odd Brillouin zones, the dependences of $\Delta\omega_m$ on d/l obtained in [26] (see also [31]) and in this study are qualitatively similar; namely, $\Delta\omega_m$ is virtually independent of d/l for $m = 1$ and rapidly decreases with increasing d/l for $m > 1$. A quantitative difference, related to the inclusion of the terms of third order in γ for odd gaps, is manifested as d/l approaches 1/4; in this case, the term proportional to γ in Eq. (12) tends to zero and for $d/l = 1/4$ the terms that remain in Eq. (12) for odd m describe $\Delta\omega_m$ for odd gaps of a sinusoidal SL. Another difference is related to the appearance of a dip on the $\Delta\omega_m(d)$ plots for odd gaps (for $m = 3$, the dip is close to $d/l = 1/4$; for $m = 5$ and 7, the dip is not seen in the scale chosen).

The dependences of $\Delta\omega_m$ on d/l for even gaps (the lower line in Eq. (12)) are obtained in this study for the first time. In Fig. 3b, we see that the gap $\Delta\omega_m$ is virtually independent of d/l for $m = 2$ and decreases rapidly with increasing d/l for $m > 2$. For an SL with a rectangular profile, $\Delta\omega_m$ for even gaps increases linearly with m. We recall that the expressions obtained remain valid only for those m for which the condition $m\gamma/2 \ll 1$ is satisfied. Therefore, for SLs with $d/l = 0$, the theory developed here is valid only for the values of m for which the widths of even gaps remain smaller than the widths of odd gaps.

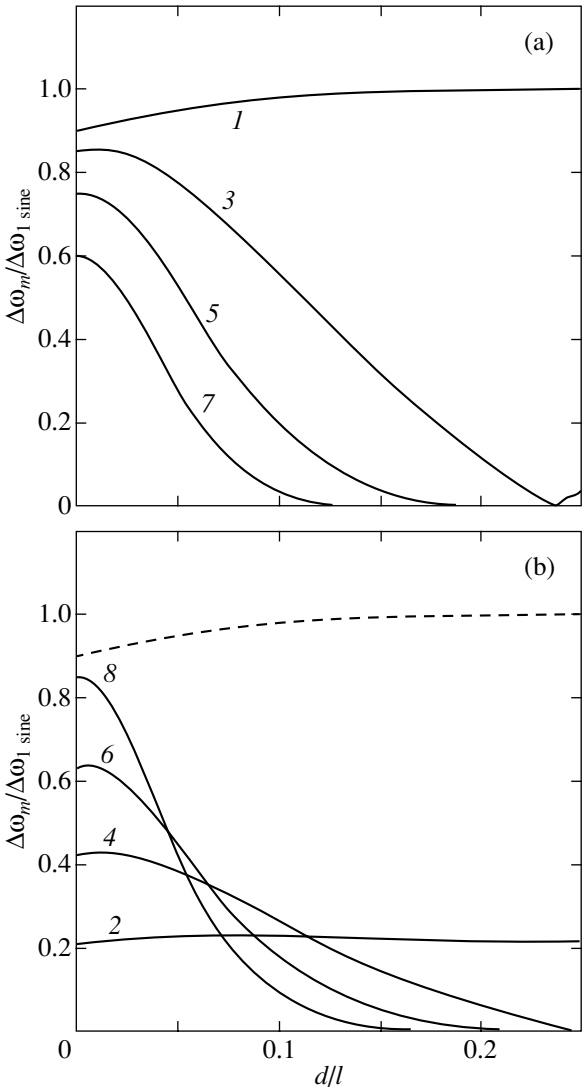

Fig. 3. Dependences of the gap widths $\Delta\omega_m$ at the edge of the mth Brillouin zone on d/l for (a) odd and (b) even gaps for $\gamma = 0.15$. The values of m are indicated on the corresponding curves. The dashed line in panel (b) shows the gap width for the first zone.

3. WAVE DISPERSION LAW

We study the wave dispersion laws in an SL with an arbitrary boundary thickness in the general form for electromagnetic, elastic, and spin waves simultaneously. Such an approach is possible, since the form of the dispersion laws is determined above all by the structure of the SL and its boundary. In this approach, the SL is characterized by a periodic z dependence of a material parameter $A(z)$, which is different for waves of different nature. For example, this parameter can be the

permittivity for electromagnetic waves, the density of the material or a force constant for elastic waves, or the magnetization, anisotropy, or exchange constant for spin waves. By analogy with Eq. (2), we write $A(z)$ as

$$A(z) = A[1 - \gamma\rho(z)], \tag{13}$$

where A and γ are the static component and the relative root-mean-square modulation of this parameter (the imaginary part of $A(z)$ is disregarded).

We write the wave equation in the form

$$\frac{d^2\mu}{dz^2} + [\nu - \eta\rho(z)]\mu = 0, \tag{14}$$

where the function μ and the parameters ν and η are expressed differently for electromagnetic, elastic, and spin waves. Thus, for spin waves, $\nu = (\omega - \omega_0)/\alpha gM$, where ω_0 is the ferromagnetic resonance frequency, α is the exchange parameter, g is the gyromagnetic ratio, and M is an external magnetic field; for electromagnetic and elastic waves, we have $\nu \propto \omega^2$, etc. (see [26]).

According to the Floquet theorem, the solution to Eq. (14) for waves propagating along the z axis can be represented in the form

$$\mu(z) = e^{-ikz}\sum_{n=-\infty}^{\infty}\mu_n e^{inqz}. \tag{15}$$

Substituting this expression and the Fourier expansion of the function $\rho(z)$ into Eq. (14), we obtain an infinite system of equations for the Fourier transforms μ_n and ρ_n:

$$(\nu - \nu_n)\mu_n = \eta\sum_{n_1}\mu_{n_1}\rho_{n-n_1}, \tag{16}$$

where $\nu = (k - nq)^2$. The dispersion law $\nu = \nu(k)$ can be obtained by equating to zero the determinant of system (16), which contains an infinite number of rows and columns. Numerical analysis of $N \times N$ determinants with finite numbers of rows and columns N allows us to study the wave dispersion law approximately.

However, in many cases, it is more convenient to derive an equation for $\nu(k)$ by expanding into a series in η. This series can be obtained in different ways. We suggest yet another way, where the presence of certain terms in the sums is explicitly forbidden. This approach will be used below when analyzing the effect of such exclusion on the form of the dispersion equation. For generality, we provisionally omit the restriction $\langle\rho(z)\rangle = 0$ used in this study. The quantity ρ_{n-n_1}, which appears on the right-hand side of Eq. (16), can be written in the form

$$\rho_{n-n_1} = \rho_{n-n_1}\delta_{nn_1} + \rho_{n-n_1}\big|_{n_1\neq n}. \tag{17}$$

After substituting Eq. (17) into Eq. (16), we obtain

$$(\nu - \tilde{\nu}_n)\mu_n = \eta\sum_{n_1\neq n}\mu_{n_1}\rho_{n-n_1}, \tag{18}$$

where $\tilde{\nu}_n = \nu_n + \eta\rho_0$. Increasing the index of n_i in Eq. (18) by 1, we express μ_{n_1} from the obtained equation and substitute the result into the right-hand side of Eq. (18). Thus, we obtain

$$(\nu - \tilde{\nu}_n)\mu_n = \eta^2\sum_{n_1\neq n}\sum_{n_2\neq n_1}\frac{\rho_{n-n_1}\rho_{n_1-n_2}\mu_{n_2}}{\nu - \tilde{\nu}_{n_1}}. \tag{19}$$

We represent the product $\rho_{n-n_1}\rho_{n_1-n_2}$ in a form similar to that of Eq. (17),

$$\rho_{n-n_1}\rho_{n_1-n_2} = \rho_{n-n_1}\rho_{n_1-n_2}\delta_{nn_2} + \rho_{n-n_1}\rho_{n_1-n_2}\big|_{n_2\neq n}, \tag{20}$$

and substitute it into Eq. (19), which assumes the form

$$\left(\nu - \tilde{\nu}_n - \eta^2\sum_{n_1\neq n}\frac{\rho_{n-n_1}\rho_{n_1-n}}{\nu - \tilde{\nu}_{n_1}}\right)\mu_n = \eta^2\sum_{n_1\neq n}\sum_{\substack{n_2\neq n\\ n_2\neq n_1}}\frac{\rho_{n-n_1}\rho_{n_1-n_2}\mu_{n_2}}{\nu - \tilde{\nu}_{n_1}}. \tag{21}$$

Next, we increase the index of n_i in Eq. (18) by 2, express μ_{n_2} from the obtained equation, substitute the result into the right-hand side of Eq. (21), and represent the product of the three functions ρ_i in a form analogous to Eq. (20). Continuing this process and using the condition $\mu_n \neq 0$, we obtain the equation

$$\nu - \tilde{\nu}_n - \eta^2\sum_{n_1\neq n}\frac{\rho_{n-n_1}\rho_{n_1-n}}{\nu - \tilde{\nu}_{n_1}} - \eta^3\sum_{n_1\neq n}\sum_{\substack{n_2\neq n\\ n_2\neq n_1}}\frac{\rho_{n-n_1}\rho_{n_1-n_2}\rho_{n_2-n}}{(\nu - \tilde{\nu}_{n_1})(\nu - \tilde{\nu}_{n_2})} - \ldots = 0. \tag{22}$$

In [32], this equation was derived using a different method. However, that derivation was somewhat inaccurate, since the exclusion of the terms $n_i \neq n_{i-1}$ in the sums was disregarded.

Next, we apply the original idea of the authors of [32], who represented a series similar to Eq. (22) in a form corresponding to the dispersion equation in the

weak-coupling approximation. In our notation, this representation for the main branch has the form

$$(\nu - \tilde{\nu}_0 - \tilde{T}^{(0)})(\nu - \tilde{\nu}_m - T^{(0)}) = T^{(-m)}T^{(m)}, \quad (23)$$

where $T^{(m)}$, $T^{(-m)}$, $T^{(0)}$, and $\tilde{T}^{(0)}$ are series containing no resonant factors. By taking into account all the exclusions $n_i \neq n_{i-1}$, these series can be written as

$$T^{(-m)} = \eta\rho_{-m} + \eta^2 \sum_{n_1 \neq 0, m} \frac{\rho_{-n_1}\rho_{n_1 - m}}{\nu - \tilde{\nu}_{n_1}}$$

$$+ \eta^3 \sum_{n_1 \neq 0, m} \sum_{\substack{n_2 \neq 0, m \\ n_2 \neq n_1}} \frac{\rho_{-n_1}\rho_{n_1 - n_2}\rho_{n_2 - m}}{(\nu - \tilde{\nu}_{n_1})(\nu - \tilde{\nu}_{n_2})} + \ldots,$$

$$T^{(m)} = \eta\rho_m + \eta^2 \sum_{n_1 \neq 0, m} \frac{\rho_{m - n_1}\rho_{n_1}}{\nu - \tilde{\nu}_{n_1}}$$

$$+ \eta^3 \sum_{n_1 \neq 0, m} \sum_{\substack{n_2 \neq 0, m \\ n_2 \neq n_1}} \frac{\rho_{m - n_1}\rho_{n_1 - n_2}\rho_{n_2}}{(\nu - \tilde{\nu}_{n_1})(\nu - \tilde{\nu}_{n_2})} + \ldots, \quad (24)$$

$$T^{(0)} = \eta^2 \sum_{n_1 \neq 0, m} \frac{\rho_{m - n_1}\rho_{n_1 - m}}{\nu - \tilde{\nu}_{n_1}}$$

$$+ \eta^3 \sum_{n_1 \neq 0, m} \sum_{\substack{n_2 \neq 0, m \\ n_2 \neq n_1}} \frac{\rho_{m - n_1}\rho_{n_1 - n_2}\rho_{n_2 - m}}{(\nu - \tilde{\nu}_{n_1})(\nu - \tilde{\nu}_{n_2})} + \ldots,$$

$$\tilde{T}^{(0)} = \eta^2 \sum_{n_1 \neq 0, m} \frac{\rho_{-n_1}\rho_{n_1}}{\nu - \tilde{\nu}_{n_1}}$$

$$+ \eta^3 \sum_{n_1 \neq 0, m} \sum_{\substack{n_2 \neq 0, m \\ n_2 \neq n_1}} \frac{\rho_{-n_1}\rho_{n_1 - n_2}\rho_{n_2}}{(\nu - \tilde{\nu}_{n_1})(\nu - \tilde{\nu}_{n_2})} + \ldots.$$

Equations for the boundaries of the band gaps are obtained by setting $k = mq/2$ in Eq. (23) and have the form

$$\nu = \tilde{\nu}_0 + \frac{\tilde{T}^{(0)} + T^{(0)}}{2} \pm \sqrt{\frac{(\tilde{T}^{(0)} - T^{(0)})^2}{4} + T^{(-m)}T^{(m)}}. \quad (25)$$

Expressions (23)–(25) differ from the corresponding expressions in [32] (in particular, in this study, we have $T^{(-m)} \neq T^{(m)*}$). However, for the case $\langle\rho(z)\rangle = 0$, where exclusions of the form $n_i \neq n_{i-1}$ become unnecessary, the expressions in [32] and our equations (22)–(25) assume the same form. In this case, Eq. (25) takes the form

$$\nu = \nu_0 + T^{(0)} \pm |T^{(-m)}|. \quad (26)$$

By solving Eq. (26) to within terms of the order of η^2, we obtain expressions for the gap boundaries,

$$\nu_m^{\pm} = \nu_0 + \eta^2 \sum_{n_1} \frac{|\rho_{n_1}|^2}{\nu_0 - \nu_{n_1}} \pm \left| \eta\rho_m + \eta^2 \sum_{n_1} \frac{\rho_{n_1}\rho_{m - n_1}}{\nu_0 - \nu_{n_1}} \right| \quad (27)$$

and for the gap widths,

$$\Delta\nu_m = 2\left| \eta\rho_m + \eta^2 \sum_{n_1} \frac{\rho_{n_1}\rho_{m - n_1}}{\nu_0 - \nu_{n_1}} \right|. \quad (28)$$

Just as in Section 2, we consider functions $\rho(z)$ with symmetry of the third kind. With such a function, we seek a solution to Eq. (26) to within terms of the order of η^3 and obtain expressions for $\nu_m^{\pm}$,

$$\nu_m^{\pm} = \nu_0 + \eta^2 \sum_{n_1} \frac{|\rho_{n_1}|^2}{\nu_0 - \nu_{n_1}} \pm \eta^3 |\rho_m| \sum_{n_1} \frac{|\rho_{n_1}|^2}{(\nu_0 - \nu_{n_1})^2}$$
$$\pm \left| \eta\rho_m + \eta^3 \sum_{n_1, n_2} \frac{\rho_{n_1}\rho_{n_2 - n_1}\rho_{m - n_2}}{(\nu_0 - \nu_{n_1})(\nu_0 - \nu_{n_2})} \right|, \quad \text{for odd } m,$$
$$\nu_m^{\pm} = \nu_0 + \eta^2 \left(\sum_{n_1} \frac{|\rho_{n_1}|^2}{\nu_0 - \nu_{n_1}} \pm \left| \sum_{n_1} \frac{\rho_{n_1}\rho_{m - n_1}}{\nu_0 - \nu_{n_1}} \right| \right), \quad \text{for even } m, \quad (29)$$

and for $\Delta\nu_m$,

$$\Delta\nu_m = \begin{cases} \left| 2\eta\rho_m + 2\eta^3 \sum_{n_1, n_2} \frac{\rho_{n_1}\rho_{n_2 - n_1}\rho_{m - n_2}}{(\nu_0 - \nu_{n_1})(\nu_0 - \nu_{n_2})} \right| \\ - 2\eta^3 |\rho_m| \sum_{n_1} \frac{|\rho_{n_1}|^2}{(\nu_0 - \nu_{n_1})^2}, \\ \text{for odd } m, \\ 2\eta^2 \left| \sum_{n_1} \frac{\rho_{n_1}\rho_{m - n_1}}{\nu_0 - \nu_{n_1}} \right|, \quad \text{for even } m. \end{cases} \quad (30)$$

These expressions describe the gaps in the spectrum of spin waves. For electromagnetic waves, using Eq. (2) for the permittivity ($\epsilon \equiv \epsilon'$, $\epsilon'' = 0$), from Eq. (29) we obtain an expression for $\omega_m^{\pm}$ to within terms of the order of γ^3:

$$\omega_m^{\pm} = \frac{mqc}{2\sqrt{\epsilon}}\begin{cases} 1 \pm \left|\frac{\rho_m}{2}\gamma \pm \frac{|\rho_m|\rho_m}{2}\gamma^2 + \left(\frac{m^2\rho_m}{8}S_1 + \frac{m^4}{32}S_3 + \frac{|\rho_m|^2\rho_m}{2}\right)\gamma^3\right| \\ + \left(\frac{m^2}{32}S_1 - \frac{|\rho_m|^2}{8}\right)\gamma^2 \pm \left(\frac{3m^2|\rho_m|}{16}S_1 - \frac{m^4|\rho_m|}{32}S_2 - \frac{3|\rho_m|^3}{16}\right)\gamma^3, \\ \text{for odd } m \\ 1 + \left(\frac{m^2}{8}\sum_{n_1}\frac{|\rho_{n_1}|^2}{n_1(m-n_1)} \pm \frac{m}{4}\left|\sum_{n_1}\frac{\rho_{n_1}\rho_{m-n_1}}{n_1}\right|\right)\gamma^2, \quad \text{for even } m, \end{cases} \tag{31}$$

where

$$S_1 = \sum_{n_1}\frac{|\rho_{n_1}|^2}{n_1(m-n_1)}, \quad S_2 = \sum_{n_1}\frac{|\rho_{n_1}|^2}{n_1^2(m-n_1)}, \quad S_3 = \sum_{n_1, n_2}\frac{\rho_{n_1}\rho_{n_2-n_1}\rho_{m-n_2}}{n_1(m-n_1)n_2(m-n_2)}. \tag{32}$$

Generally, it is not easy to determine the widths of odd gaps from Eq. (31), since in the uppermost line of this equation the modulus is taken from an expression that has a variable sign. Therefore, we write out expressions for the gap widths with an accuracy of γ^2;

$$\Delta\omega_m = \frac{mqc}{2\sqrt{\epsilon}}\begin{cases} |\rho_m|\gamma, & \text{for odd } m, \\ \frac{m}{2}\gamma^2\left|\sum_{n_1}\frac{\rho_{n_1}\rho_{m-n_1}}{n_1}\right|, & \text{for even } m. \end{cases} \tag{33}$$

Let us compare formula (11) for the boundaries of the band gaps $\omega_m^{\pm}$ obtained by the MCMT method with an analogous formula (31) obtained from the exact dispersion equation. We see that the coefficients of the corresponding powers of γ in these formulas are described by substantially different expressions (except for the coefficients of the first power of γ, which coincide). It should be emphasized that the expressions for these coefficients in Eq. (31) are exact, since they were obtained, using perturbation theory, from the exact dispersion equation (22) (or from Eq. (26), which is equivalent to it). Therefore, the difference in the corresponding coefficients between Eq. (31) and Eq. (11) characterizes the accuracy of the MCMT method. In order to get a clear idea about this accuracy, we consider Eqs. (31) and (11) for two limiting cases of boundary thickness: $d/l = 0$ (a rectangular profile) and $d/l = 1/4$ (a sinusoidal profile). For a rectangular profile, the expressions for $\omega_m^{\pm}$ obtained by the MCMT method coincide with the corresponding expressions from perturbation theory, at least up to terms of the order of γ^2, and have the form

$$\omega_m^{\pm} = qc/2\sqrt{\epsilon}\begin{cases} m \pm \frac{\gamma}{\pi} + \frac{\gamma^2}{8}m \pm \ldots, & \text{for odd } m \\ m + (1 \pm 2)\frac{\gamma^2}{8}m + \ldots, & \text{for even } m. \end{cases} \tag{34}$$

For a sinusoidal profile, the expressions for $\omega_m^{\pm}$ obtained by the MCMT method differ from the corresponding results of perturbation theory. It appears that the difference between the results obtained by the MCMT method and the results of perturbation theory are greater for the positions of the band gaps than for their widths. Thus, for the boundary frequencies of the first Brillouin zone, we have

$$\omega_1^{\pm} = qc/2\sqrt{\epsilon}\left\{1 \pm \frac{\sqrt{2}}{4}\gamma + \begin{cases} \frac{5}{32}\gamma^2 \pm \frac{19\sqrt{2}}{2^9}\gamma^3 + \ldots, \\ \frac{4}{32}\gamma^2 \pm \frac{20\sqrt{2}}{2^9}\gamma^3 + \ldots, \end{cases}\right. \tag{35}$$

where the lower line corresponds to the MCMT method and the upper line to perturbation theory.

To plot the band gap width as a function of the interface thickness d, we used Eqs. (30) and (31), into which we substituted ρ_m corresponding to the Fourier harmonics of the elliptic sine in Eq. (1). For $\gamma = 0.15$, the $\Delta\omega_m(d/l)$ curves for both odd and even gaps differ only slightly from the corresponding curves in Fig. 3, which were obtained by the MCMT method in the previous section (in the chosen scale, the corresponding curves coincide). The d dependences of $\Delta\nu_m$ for spin waves are plotted in Fig. 4a for odd gaps and in Fig. 4b for even gaps. In both figures, the gap widths are normalized to the width of the first band gap of the SL with a sinusoidal profile, $\Delta\nu_{1\,\text{sine}}$. The $\Delta\nu_m(d)$ and $\Delta\omega_m(d)$ dependences are qualitatively similar; namely, the gap widths are virtually independent of d for $m = 1$ and 2 and rapidly decrease with increasing d for $m > 2$. For odd gaps, both the $\Delta\nu_m(d)$ and $\Delta\omega_m(d)$ curves exhibit dips, which are not seen in the scale of Fig. 4a. By comparing Figs. 3 and 4, we see that, for electromagnetic and spin

waves, the dependences of the gap width on the gap number m are qualitatively different; the difference is most clearly seen for a rectangular modulation profile. For $d/l = 0$, the width of odd gaps for electromagnetic (and, accordingly, elastic) waves depends only weakly on m (Fig. 3a). The width of odd gaps for spin waves decreases rapidly with increasing m (in proportion to $1/m$ if we neglect the effects of the order of η^3; see Fig. 4a). The differences between the m dependences for even gaps are even more substantial. While $\Delta\nu_m$ for spin waves decreases as $1/m$ with increasing m (Fig. 4b), $\Delta\omega_m$ for electromagnetic waves grows in proportion to m (Fig. 3b).

4. CONCLUSIONS

Thus, we have considered wave propagation in one-dimensional superlattices (multilayer structures) with arbitrary thickness of the interlayer boundaries in the structures. To describe the superlattice (SL), we have used a model suggested earlier in [26], in which the modulation profile of a material parameter along the SL axis is described by a Jacobian elliptic sine. The MCMT method was used to study the frequency dependences of the transmittance $D(\omega)$ and reflectance $R(\omega)$ for electromagnetic waves in such an SL. Perturbation theory was used to study the $\omega(k)$ dispersion relations for electromagnetic, elastic, and spin waves in SLs with modulation of the corresponding material parameter (dielectric constant, density of the material, or magnetic anisotropy). The experimental situation where traveling waves are studied corresponds to measurement of the reflectance $R(\omega)$ (or the transmittance $D(\omega)$). With standing waves in any resonator (for example, in the case of spin-wave resonance in a thin magnetic film), the $\omega(k)$ dispersion relation is studied. In both cases, the measured $R(\omega)$ and $\omega(k)$ dependences reveal common features (namely, the frequencies of the gap boundary positions $\omega_m^{\pm}$). In the $\omega(k)$ dispersion law, these frequencies are observed directly, whereas the $R(\omega)$ dependence reveals them as the boundary frequencies of the Bragg mirrors. The analytical expressions obtained for $\omega_m^{\pm}$ by different methods from the $R(\omega)$ and $\omega(k)$ dependences turned out to be substantially different. Since the coefficients of the powers of η found from the $\omega(k)$ dispersion relation are exact, their comparison with the corresponding coefficients of the series in η obtained from the $R(\omega)$ dependence using the MCMT method allowed us to estimate the accuracy of the method. The gap widths were determined by this method with a substantially higher accuracy than the gap positions. The high accuracy of the MCMT method was also noted in [33], where the results obtained by using this method were compared with the results of numerical solution of the wave equation.

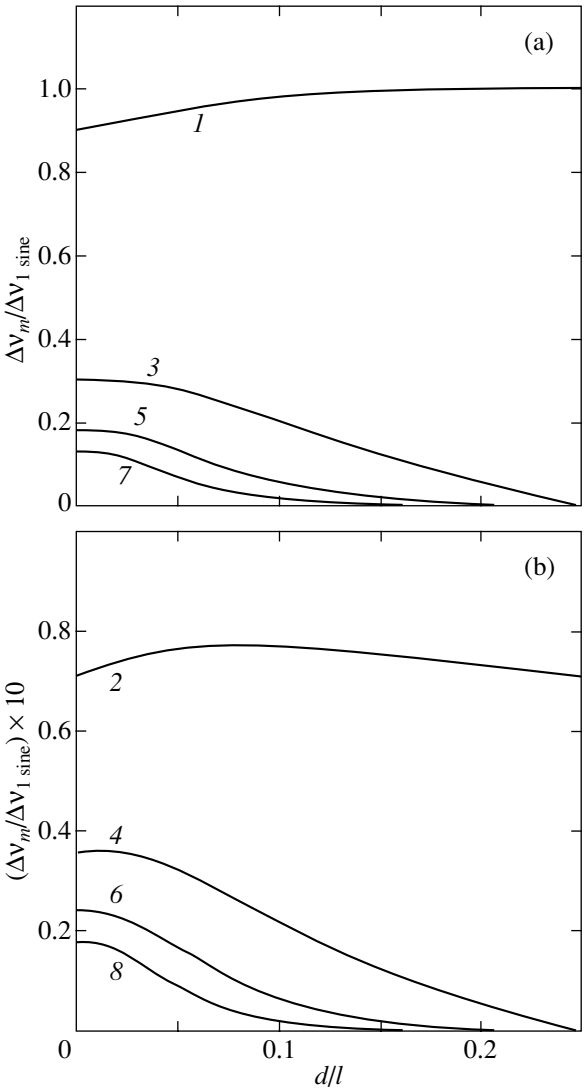

Fig. 4. Dependences of the gap widths $\Delta\nu_m$ at the edge of the mth Brillouin zone on d/l for (a) odd and (b) even gaps for $\eta/q^2 = 0.1$. The values of m are indicated on the corresponding curves. Note that the ordinate scales in panels (a) and (b) are different.

The dependences of the band gap widths $\Delta\omega_m$ and the gap positions in the spectrum on the boundary thickness d have been calculated using both the frequency dependence of the reflectance $R(\omega)$ and the dispersion law. The calculations were performed for both odd and even Brillouin zones of the SL (in a first approximation of perturbation theory, an analogous calculation for odd gaps was performed for the first time in [26]). The dependences of the band gap widths on the gap number for electromagnetic (or elastic) waves ($\Delta\omega_m$) and for spin waves ($\Delta\nu_m$) are different in character. In the case of $d = 0$, for odd gaps, $\Delta\omega_m$ depends only weakly on m, whereas $\Delta\nu_m \propto 1/m$; for even gaps, we have $\Delta\omega_m \propto m$, whereas $\Delta\nu_m \propto 1/m$. The d dependences of the band gap widths are similar in

character; namely, the band gap widths for the first and second Brillouin zones are virtually independent of d and the widths of all gaps with $m > 2$ have a strong d dependence. We found a dip in the dependences of $\Delta\omega_m$ and $\Delta\nu_m$ on d/l for $m = 3$, 5, and 7, when higher order terms of perturbation theory were taken into account. The obtained results theoretically substantiate possible experimental methods of measuring the boundary thickness in SLs by using spectral methods. In these methods, it is necessary to measure the widths of two band gaps: $\Delta\omega_1$ and, for example, $\Delta\omega_3$. Then, using the plots in Fig. 3 for electromagnetic or elastic waves and the plots in Fig. 4 for spin waves, one can find d/l from the ratio $\Delta\omega_3/\Delta\omega_1$.

ACKNOWLEDGMENTS

This study was supported by the Russian Foundation for Basic Research (grant no. 04-04-16174), the Krasnoyarsk Regional Scientific Foundation (grant no. 12F0013C), and, in part, by the "Dynasty" Foundation and the International Center for Fundamental Physics in Moscow.

REFERENCES

1. L. Brillouin, *Wave Propagation in Periodic Structures* (Dover, New York, 1953; L. Brillouin and M. Parodi, Inostrannaya Literatura, Moscow, 1959).
2. L. M. Brekhovskikh, *Waves in Layered Media*, 2nd ed. (Nauka, Moscow, 1973; Academic, New York, 1980).
3. V. A. Belyakov, *Diffraction Optics of Complex-Structured Periodic Media* (Nauka, Moscow, 1988; Springer, New York, 1992).
4. F. G. Bass, A. A. Bulgakov, and A. P. Tetervov, *High-Frequency Properties of Semiconductors with Superlattices* (Nauka, Moscow, 1989) [in Russian].
5. M. Born and E. Wolf, *Principles of Optics*, 4th ed. (Pergamon, Oxford, 1969; Nauka, Moscow, 1970).
6. Ch. Elachi, Proc. IEEE **64** (12), 1666 (1976).
7. S. Yu. Karpov and S. N. Stolyarov, Usp. Fiz. Nauk **163** (1), 63 (1993) [Phys. Usp. **36**, 1 (1993)].
8. P. Yeh, A. Yariv, and Chi-Shain Hohg, J. Opt. Soc. Am. **67** (4), 423 (1977).
9. N. G. Bebenin, Zh. Éksp. Teor. Fiz. **103** (6), 2154 (1993) [JETP **76**, 1077 (1993)].
10. P. Erdös, E. Liviotti, and R. C. Herndon, J. Phys. D: Appl. Phys. **30** (3), 338 (1997).
11. I. O. Bogul'skiĭ, S. Ya. Vetrov, and A. V. Shabanov, Opt. Spektrosk. **84** (5), 823 (1998) [Opt. Spectrosc. **84**, 742 (1998)].
12. V. G. Savin and N. A. Shul'ga, Akust. Zh. **21** (2), 260 (1975) [Sov. Phys. Acoust. **21**, 161 (1975)]; Akust. Zh. **21** (3), 448 (1975) [Sov. Phys. Acoust. **21**, 276 (1975)].
13. B. Djafari-Rouhani, L. Dobrzynski, O. H. Duparc, R. E. Camley, and A. A. Maradudin, Phys. Rev. B **28** (4), 1711 (1983).
14. B. Djafari-Rouhani, A. A. Maradudin, and R. F. Wallis, Phys. Rev. B **29** (12), 6454 (1984).
15. J. Mendialdua, T. Szwacka, A. Rodrigues, and L. Dobrzynski, Phys. Rev. B **39** (15), 10674 (1989).
16. S. Ya. Vetrov and V. F. Shabanov, Pis'ma Zh. Tekh. Fiz. **17** (5), 34 (1991) [Sov. Tech. Phys. Lett. **17**, 169 (1991)].
17. P. Grunberg and K. Mika, Phys. Rev. B **27** (5), 2955 (1983).
18. R. E. Camley, T. S. Rahman, and D. L. Mills, Phys. Rev. B **27** (1), 261 (1983).
19. Yu. V. Gribkova and M. I. Kaganov, Pis'ma Zh. Éksp. Teor. Fiz. **47** (11), 588 (1988) [JETP Lett. **47**, 682 (1988)].
20. B. Hillebrands, Phys. Rev. B **41** (1), 530 (1990).
21. R. E. Camley and R. L. Stamps, J. Phys.: Condens. Matter **5** (23), 3727 (1993).
22. V. V. Kruglyak and A. N. Kuchko, Fiz. Met. Metalloved. **92** (3), 3 (2001) [Phys. Met. Metallogr. **92**, 211 (2001)].
23. T. Tamir, H. C. Wang, and A. A. Oliner, IEEE Trans. Microwave Theory Tech. **12**, 323 (1964).
24. C. Yen, K. F. Casey, and Z. Kaprielian, IEEE Trans. Microwave Theory Tech. **13**, 297 (1965).
25. Yu. N. Gorobets, A. E. Zyubanov, A. N. Kuchko, and K. D. Shedzhuri, Fiz. Tverd. Tela (St. Petersburg) **34** (5), 1486 (1992) [Sov. Phys. Solid State **34**, 790 (1992)].
26. V. A. Ignatchenko, Yu. I. Mankov, and A. A. Maradudin, Phys. Rev. B **62** (3), 2181 (2000).
27. N. N. Martynov and S. N. Stolyarov, Kvantovaya Élektron. (Moscow) **5** (8), 1853 (1978).
28. W. P. Huang, J. Opt. Soc. Am. A **11** (3), 963 (1994).
29. H. Kogelnik, Bell Syst. Tech. J. **48** (9), 2909 (1969).
30. I. N. Bronshteĭn and K. A. Semendyaev, *Handbook on Mathematics* (GIFML, Moscow, 1962), p. 551 [in Russian].
31. V. A. Ignatchenko, Yu. I. Mankov, and A. A. Maradudin, Phys. Rev. B **65** (1), 024207 (2002).
32. S. Yu. Karpov, O. V. Konstantinov, and M. É. Raĭkh, Fiz. Tverd. Tela (Leningrad) **22** (11), 3402 (1980) [Sov. Phys. Solid State **22**, 1991 (1980)].
33. B. M. Bolotovskiĭ, V. E. Volovel'skiĭ, N. N. Martynov, and S. N. Stolyarov, Preprint FIAN (Physical Inst., USSR Academy of Sciences, Moscow, 1989).

Translated by I. Zvyagin

Physics of the Solid State, Vol. 46, No. 12, 2004, pp. 2301–2305. Translated from Fizika Tverdogo Tela, Vol. 46, No. 12, 2004, pp. 2224–2228.

LOW-DIMENSIONAL SYSTEMS AND SURFACE PHYSICS

Evolution of $NaNO_2$ in Porous Matrices

C. Tien[1], E. V. Charnaya[1, 2], S. V. Baryshnikov[3], M. K. Lee[1], S. Y. Sun[1], D. Michel[4], and W. Böhlmann[4]

[1]*Department of Physics, National Cheng Kung University, Tainan, 70101 Taiwan*
[2]*Fock Institute of Physics, St. Petersburg State University, St. Petersburg, 198504 Russia*
e-mail: charnaya@paloma.spbu.ru
[3]*Blagoveshchensk State Pedagogical University, Blagoveshchensk, 675002 Russia*
[4]*Faculty of Physics and Geosciences, University of Leipzig, Leipzig, D-04103 Germany*

Received May 13, 2004

Abstract—NMR and dielectric studies of $NaNO_2$ loaded into an SBA-15 mesoporous matrix are reported. The spin–lattice relaxation rate and the ^{23}Na NMR line shift, as well as the permittivity, were measured within a broad temperature interval including the ferroelectric phase transition in $NaNO_2$. The phase transition temperature of sodium nitrite in as-prepared samples was shown to differ substantially from that characteristic of a bulk crystal. The permittivity grows strongly in the vicinity of the phase transition. Heating a sample causes the properties of $NaNO_2$ embedded in pores to gradually approach those of bulk crystals. © *2004 MAIK "Nauka/Interperiodica".*

1. INTRODUCTION

Studies of small ferroelectric particles and thin films have shown that their properties differ strongly from those of bulk crystals [1, 2]. The observed effects were most strongly pronounced near ferroelectric phase transitions. It has been found that the phase transition temperatures usually shift from those of bulk samples, that the phase transitions become diffuse, and that the ferroelectric properties disappear at certain particle dimensions (see [3–5] and references therein). Particle dimensions were also observed to affect the spontaneous polarization, domain structure, and permittivity. Many of these size effects allow interpretation within theoretical models developed for polar dielectrics (see, e.g., [2, 6–10]) on the basis of the Landau theory and the Ising model. Other size phenomena specific of some ferroelectrics can also be expected to appear.

Small ferroelectric particles can be produced by loading ferroelectric materials into nanoporous matrices [11–13]. In this case, the particle size is governed by the pore dimensions, with ferroelectric particles forming a framework whose geometry obeys that of the pore structure. Ferroelectric nanoparticles embedded in pores are model systems convenient for studying the size effect in polar dielectrics.

The present communication reports on NMR and dielectric studies of sodium nitrite $NaNO_2$ embedded in the molecular framework of SBA-15.

2. EXPERIMENT

The porous matrices used were SBA-15 silicate molecular frameworks. These materials have a honeycomb-type hexagonal structure with a wall thickness of 0.6–0.8 nm and a calibrated size of pore channels. SBA-15 was synthesized by the technique described in [14]. The pore size as derived from nitrogen adsorption–desorption isotherms was found to be 52 Å. The specific channel surface area was 764 m^2/g.

$NaNO_2$ was loaded into nanopores in the following way. A mixture of dehydrated SBA-15 powder and $NaNO_2$ was prepared in the required ratio. Distilled water was added to the mixture to make the $NaNO_2$ solution penetrate into the pores. Next, the mixture was placed into a furnace and heated to 373 K to evaporate the water, after which the temperature was raised to the $NaNO_2$ melting point (544 K). The powder thus prepared was pelletized at a pressure of 8000–10000 kg/cm^2.

Measurements of NMR spectra and spin–lattice relaxation times of ^{23}Na nuclei for $NaNO_2$ in pores were performed on a Bruker Avance-400 pulsed spectrometer. The Larmor precession frequency was 105.8 MHz in a field of 9.4 T. The studies were carried out in the temperature range from 245 to 455 K, including the ferroelectric transition temperature, which is 437 K for a bulk $NaNO_2$ sample. A sample of polycrystalline $NaNO_2$ was used for reference. The static NMR spectrum of ^{23}Na (spin $I = 3/2$) of bulk polycrystalline sodium nitrite consists primarily of a central $1/2 \leftrightarrow -1/2$ transition broadened by second-order quadrupole interactions [15]. Our measurements showed the spectra of $NaNO_2$ in pores to have the same pattern. The spin–lattice relaxation rate was derived from the central-line recovery following magnetization reversal by a 180° pulse. We also performed measurements of the

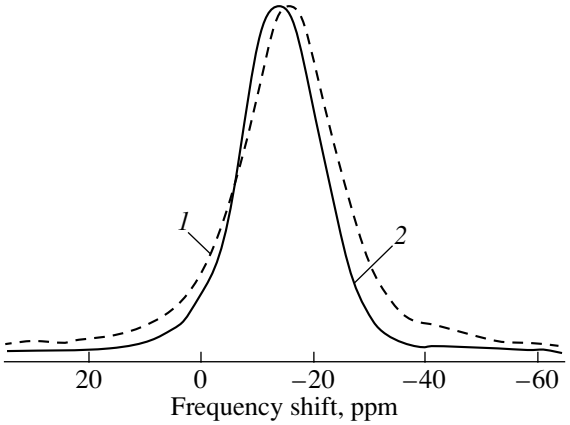

Fig. 1. ^{23}Na NMR line at 455 K (*1*) for $NaNO_2$ in pores and (*2*) for polycrystalline $NaNO_2$.

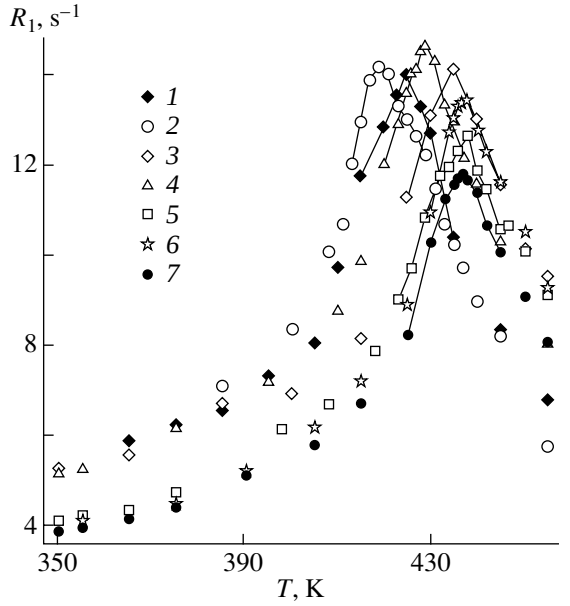

Fig. 2. (*1*–*6*) Temperature dependence of the spin–lattice relaxation rate R_1 of ^{23}Na in $NaNO_2$ embedded in SBA-15 pores, measured under cooling from 455 K in the course of (*1*) the first, (*2*) second, (*3*) third, (*4*) fourth, (*5*) fifth, and (*6*) sixth cycles, and (*7*) the corresponding dependence for bulk polycrystalline $NaNO_2$. Solid lines connect experimental points.

temperature dependence of the NMR line shift with respect to the position of the ^{23}Na line in a 1 M aqueous solution of NaCl at 295 K. All NMR measurements were carried out at fixed temperatures under cooling of the samples heated at 455 K for an hour. The temperature stabilization was no worse than 0.5 K.

The dielectric measurements were conducted at a frequency of 1 MHz with an E7-12 LCR meter. A Ga–In paste served as the electrode material. Prior to measurements, the samples were held in a furnace at 400 K for 2–3 h to remove the water adsorbed from air. The studies were performed in the same temperature interval as the NMR measurements.

3. RESULTS

Figure 1 shows a static ^{23}Na NMR spectrum of $NaNO_2$ in SBA-15 taken at 455 K in the first heating run, together with the line from polycrystalline $NaNO_2$. The spectrum is essentially a single line corresponding to the central transition, shifted and broadened as compared to that of the bulk sample.

The spin–lattice relaxation measurements revealed that the recovery of the central line of $NaNO_2$ in pores is fitted well by an exponential for all temperatures. This is consistent with the spin–lattice relaxation studies conducted on bulk polycrystalline $NaNO_2$ in [15] and the theoretical analysis of quadrupole relaxation in polycrystalline samples performed in [16]. Thus, the recovery curves can be described by the spin–lattice relaxation time T_1 or the spin–lattice relaxation rate $R_1 = 1/T_1$. The temperature dependence of R_1 for the $NaNO_2$ loaded in SBA-15 is given in the form of a graph in Fig. 2, together with the temperature dependence for bulk polycrystalline $NaNO_2$, for several successive heating–cooling thermocycles. We readily see that the maximum of R_1 for $NaNO_2$ in SBA-15 shifts along the temperature axis relative to its position for polycrystalline $NaNO_2$ and that its height varies somewhat from one cycle to another. The shift of the R_1 maximum is more clearly pronounced in the first cycles and can be both positive and negative, reaching a value of −18 K (Fig. 2).

However, when the cooling was stopped at 385 K and the sample was repeatedly heated (Fig. 3), the results of the R_1 measurements were found to coincide within experimental error with the data obtained under cooling.

After four heating–cooling cycles of $NaNO_2$ in SBA-15, the temperature of the maximum in R_1 stabilized and approached that of the ferroelectric phase transition in a bulk crystal (Fig. 2). The relaxation rate became practically equal to that of bulk sodium nitrite, except in a temperature interval near the phase transition.

The position of the NMR line also varied with time. Figure 4 displays temperature dependences of the ^{23}Na NMR line shift for $NaNO_2$ in SBA-15 (together with the corresponding dependence for the bulk sample), measured in two of the temperature cycles described above. One readily sees a marked difference in the line shifts between the embedded $NaNO_2$ and the polycrystalline $NaNO_2$ obtained during the first cooling, whereas in the subsequent cycles the NMR line shift for the sodium nitrite embedded in pores approaches that in the bulk sample.

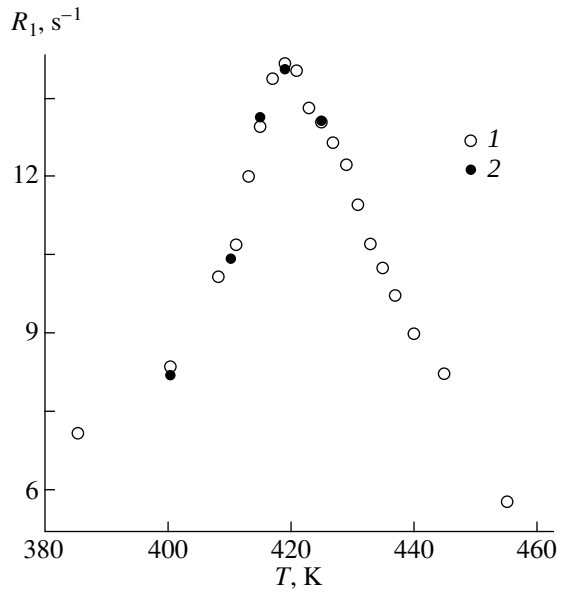

Fig. 3. Temperature dependence of the spin–lattice relaxation rate R_1 of ^{23}Na in $NaNO_2$ embedded in SBA-15 pores, measured under (*1*) cooling from 455 to 385 K and (*2*) subsequent heating.

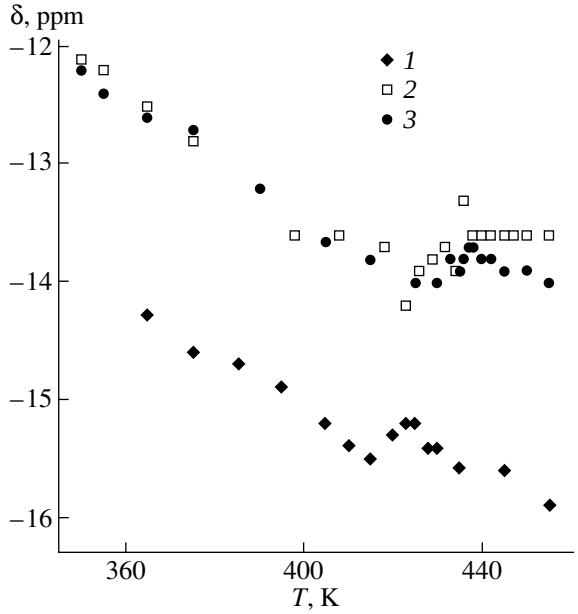

Fig. 4. (*1*, *2*) Temperature dependence of the ^{23}Na NMR line shift δ in $NaNO_2$ embedded in SBA-15 pores, measured under cooling from 455 K during (*1*) the first and (*2*) fifth cycles, and (*3*) the corresponding dependence for bulk polycrystalline $NaNO_2$.

The results of permittivity measurements displayed in Fig. 5 likewise attest to the evolution of properties occurring in successive heating–cooling cycles. During the first heating, the permittivity maximum is clearly pronounced and shifted relative to that for the bulk $NaNO_2$ sample. In the subsequent cycles, however, the maximum decreased in magnitude and broadened.

4. DISCUSSION OF THE RESULTS

Under heating, bulk $NaNO_2$ undergoes two consecutive structural phase transitions, from the ferroelectric to an incommensurate antiferroelectric phase at T_c = 437 K and, subsequently, to the paraelectric phase at 438 K. The ferroelectric properties are due to the specific atomic arrangement in the NO_2 group. At low temperatures, the NO_2 groups lie in the *bc* plane of the orthorhombic unit cell, with their dipole moments directed along the polar axis *b*. In the course of the transition from the ferroelectric state, the dipole moments tilt about the *c* axis [17], so that above the Curie temperature they are oriented with equal probability along both directions of the *b* axis. The reorientation of the NO_2 groups contributes to the spin–lattice relaxation of Na nuclei. Numerous comprehensive experimental studies of the spin relaxation of ^{23}Na nuclei in single-crystal and polycrystalline sodium nitrite have shown the maximum in the spin–lattice relaxation rate to lie at the ferroelectric phase transition point (see [15, 18] and references therein). A theoretical model was proposed to explain the acceleration of relaxation near the transition point, taking into account thermally activated random hopping of NO_2 groups and the temperature dependence of spontaneous polarization [18].

The spin–lattice relaxation rate for ^{23}Na in $NaNO_2$ passing through a maximum near the ferroelectric phase transition point offers a good opportunity to determine the critical temperature T_c for $NaNO_2$ embedded in nanoporous matrices. As seen from Fig. 2, the ferroelectric transition temperature for $NaNO_2$ loaded in SBA-15 is not constant; it depends on the thermal prehistory of a sample and eventually approaches the critical temperature for a bulk $NaNO_2$ sample. No such temporal evolution of phase transition temperatures in small ferroelectric particles has been observed thus far. It should be stressed that T_c variations for $NaNO_2$ in pores became observable only after heating above the ferroelectric transition point. The position of the maximum in the spin–lattice relaxation rate and, hence, the transition temperature did not vary noticeably during measurements similar to those exemplified in Fig. 3.

The results obtained in studies of the temperature dependence of the NMR line shift (Fig. 4) show that the variations in phase transition temperature were accompanied by structural changes of $NaNO_2$ inside pores. Indeed, the shift of the central NMR line of quadrupole nuclei in powder samples is the sum of the isotropic chemical and second-order quadrupole shifts, which depend on the character of the chemical bonds and electric crystal fields. As is evident from Fig. 4, the shift of

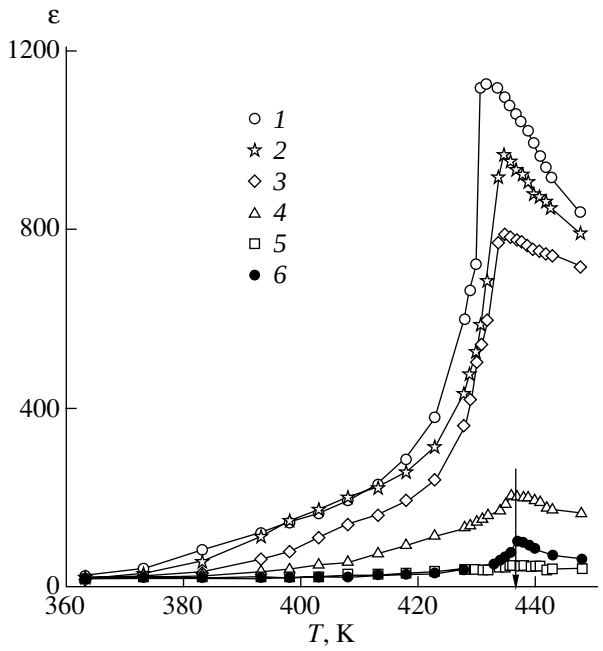

Fig. 5. (*1–5*) Temperature dependence of the permittivity ε of $NaNO_2$ embedded in SBA-15 pores, measured in the course of (*1*) the first, (*2*) second, (*3*) third, (*4*) fourth, and (*5*) fifth cycles, and (*6*) the corresponding dependence for bulk polycrystalline $NaNO_2$. Solid lines connect experimental points. The arrow identifies the phase transition temperature of bulk $NaNO_2$.

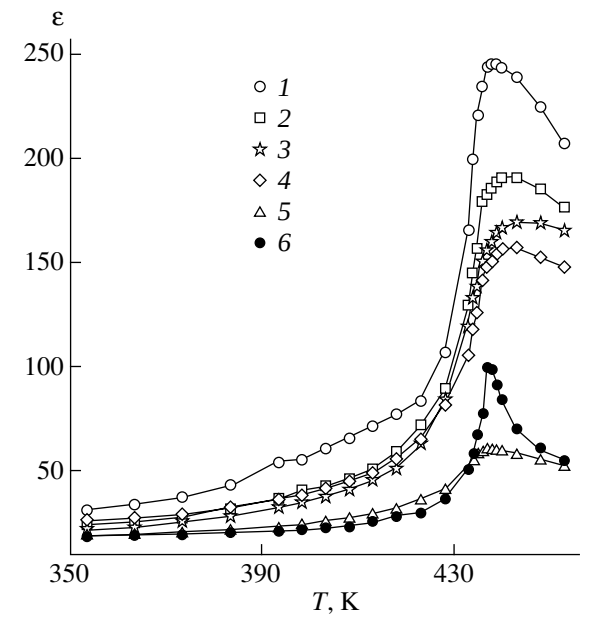

Fig. 6. (*1–5*) Temperature dependence of the permittivity ε of $NaNO_2$ embedded in silica gel pores, measured in the course of (*1*) the first, (*2*) second, (*3*) third, (*4*) fourth, and (*5*) fifth cycles, and (*6*) the corresponding dependence for bulk polycrystalline $NaNO_2$. Solid lines connect experimental points.

the central line for $NaNO_2$ in pores eventually coincides with that observed for a bulk sample of sodium nitrite. Note that the breaks in the $\delta(T)$ relations are obviously due to the variations in the quadrupole and chemical shifts at the phase transition.

As-prepared samples of sodium nitrite in SBA-15 have a very high permittivity ε near the ferroelectric phase transition, whereas in the course of aging the anomaly in permittivity decreases and the $\varepsilon(T)$ profile spreads out (Fig. 5). The permittivity of embedded $NaNO_2$ can be estimated from the Lichtenekker formula derived for mixtures, $\ln\varepsilon^* = x\ln\varepsilon_1^* + (1-x)\ln\varepsilon_2^*$, where ε^* is the complex permittivity of the mixture; ε_1^* and ε_2^* are the permittivities of the $NaNO_2$ particles and the porous matrix, respectively; and x is the volume concentration of $NaNO_2$. In this case, using the data from Fig. 5, the permittivity of $NaNO_2$ particles at the phase transition point is found to be 10^5, whereas the permittivity of pressed polycrystalline $NaNO_2$ is $\simeq 100$. The fact that $NaNO_2$ in artificial opals exhibits a giant permittivity was mentioned in [11], but the authors of that paper did not offer any data demonstrating instability of $NaNO_2$ in pores.

The observed temporal evolution of sodium nitrite in nanopores, which manifests itself in the phase transition temperature, the NMR line position, and the permittivity tending (after heating) to the values typical of a bulk sample, suggests that $NaNO_2$ nanoparticles loaded in pores acquire some specific features. These features are possibly related to an increase in the amplitude of atomic vibrations above the ferroelectric phase transition point for $NaNO_2$ in porous glass, an effect revealed recently in neutron scattering experiments [19].

It should be stressed that the temporal evolution of sodium nitrite embedded in the molecular framework of SBA-15 is not due to $NaNO_2$ escaping from the pores under heating. To check this experimentally, we performed additional studies of the permittivity of $NaNO_2$ loaded in pores of silica gel (average pore size 2.4 nm), whose particles measured about 3 nm, and observed a temporal evolution similar to that obtained in the case of SBA-15. The results of the measurements are presented graphically in Fig. 6.

5. CONCLUSIONS

We have conducted ^{23}Na NMR and dielectric measurements of $NaNO_2$ embedded in the molecular framework of SBA-15 over a broad temperature interval, which revealed gradual variations in the phase transition temperature, the NMR line position, and the permittivity caused by sample heating above T_c.

As-prepared $NaNO_2$ nanoparticles were found to exhibit a substantial shift (reaching –18 K) of the ferroelectric phase transition temperature as compared to that for a bulk sample, a noticeable decrease in the

NMR line shift, and a strong increase in the permittivity at the phase transition point. After several successive heating–cooling thermocycles, these properties of sodium nitrite in pores approached those of the bulk sample. No such evolution with time has thus far been observed in small ferroelectric particles in porous matrices.

ACKNOWLEDGMENTS

The National Science Council of Taiwan (project no. 92-2811-M-006-014) is gratefully acknowledged for its support.

REFERENCES

1. J. F. Scott and C. A. Paz de Aranjo, Science **246**, 1400 (1989).
2. *Ferroelectric Ceramics*, Ed. by N. Setter and E. L. Colla (Birkhause, Basel, 1993).
3. I. Yamashita, H. Kawaji, T. Atake, Y. Kuroiwa, and A. Sawada, Phys. Rev. B **68**, 092104 (2003).
4. Y. Drezner and S. Berger, J. Appl. Phys. **94**, 6774 (2003).
5. T. Yu, Z. X. Shen, W. S. Toh, J. M. Xue, and J. Wang, J. Appl. Phys. **94**, 618 (2003).
6. B. Jiang and L. A. Bursill, Phys. Rev. B **60**, 9978 (1999).
7. C. L. Wang, Y. Xin, X. S. Wang, and W. L. Zhong, Phys. Rev. B **62**, 11423 (2000).
8. P. L. Zhang, W. L. Zhong, and J. F. Hu, Solid State Commun. **116**, 249 (2000).
9. E. V. Charnaya, O. S. Pogorelova, and C. Tien, Physica B (Amsterdam) **305**, 97 (2001).
10. E. V. Charnaya, S. A. Ktitorov, and O. S. Pogorelova, Ferroelectrics **297**, 29 (2003).
11. S. V. Pankova, V. V. Poborchii, and V. G. Solovev, J. Phys.: Condens. Matter **8**, L203 (1996).
12. Yu. A. Kumzerov and S. B. Vakhrushev, in *Encyclopedia of Nanoscience and Nanotechnology*, Ed. by H. S. Nalwa (Am. Sci., Los Angeles, CA, 2003).
13. S. Kohiki, S. Takada, A. Shimizu, K. Yamada, H. Higashijima, and M. Mitome, J. Appl. Phys. **87**, 474 (2000).
14. S. Jun, S. H. Loo, R. Ryoo, M. Kruk, M. Jaroniec, Z. Liu, T. Ohsuma, and O. Terasaki, J. Am. Chem. Soc. **122**, 10712 (2000).
15. J. K. Jung, O. H. Han, and S. H. Choh, Solid State Commun. **110**, 547 (1999).
16. N. Okubo, M. Igarashi, and R. Yoshizaki, Z. Naturforsch. A **51**, 277 (1966).
17. T. Gohda, M. Ichikawa, T. Gustafsson, and I. Olovsson, Phys. Rev. B **63**, 014101 (2000).
18. L. Pandey and D. G. Hughes, J. Phys.: Condens. Matter **4**, 6889 (1992).
19. A. V. Fokin, Yu. A. Kumzerov, N. M. Okuneva, A. A. Naberezhnov, S. B. Vakhrushev, I. V. Golosovsky, and A. I. Kurbakov, Phys. Rev. Lett. **89**, 175503 (2002).

Translated by G. Skrebtsov

Physics of the Solid State, Vol. 46, No. 12, 2004, pp. 2306–2310. Translated from Fizika Tverdogo Tela, Vol. 46, No. 12, 2004, pp. 2229–2232.

POLYMERS AND LIQUID CRYSTALS

Electrical and Luminescence Properties of a Poly(amidoamine) Dendrimer Containing Naphthalimide

A. V. Kukhto*, É. É. Kolesnik*, A. N. Lappo, A. E. Pochtenny**, and I. K. Grabchev*****

** Institute of Molecular and Atomic Physics, National Academy of Sciences of Belarus, pr. F. Skoriny 70, Minsk, 220072 Belarus*

e-mail: kukhta@imaph.bas-net.by

*** Belarussian State Technological University, Minsk, 220050 Belarus*

e-mail: root@bstu.unibel.by

**** Institute of Polymers, Bulgarian Academy of Sciences, Sofia, 1113 Bulgaria*

e-mail: grabchev@polymer.bas.bg

Received February 3, 2004; in final form, April 20, 2004

Abstract—The electrical and luminescence properties of a poly(amidoamine) (PAMAM) dendrimer containing naphthalimide are investigated. The influence of adsorbed oxygen on the electrical conductivity of thermally evaporated organic films is analyzed using cyclic thermal desorption. The results obtained are interpreted within a model of two-level hopping electron transfer according to which one of the two systems of energy levels corresponds to intrinsic states of electrons in PAMAM molecules and the other system is associated with the states of electrons in adsorbed oxygen molecules. The use of the cyclic thermal desorption method in combination with the proposed model makes it possible to estimate the localization length of electrons numerically and to determine the states involved in hopping electron transfer. It is demonstrated that the studied compound in the solid state possesses a high luminescence power over a wide spectral range. © *2004 MAIK "Nauka/Interperiodica".*

1. INTRODUCTION

In recent years, organic compounds of different classes have been extensively used in electronic devices [1]. Particular interest has been expressed by researchers in dendrimers, because these materials are very promising for use in electroluminescent structures [2], sensors [3], and light-harvesting antennas [3]. Dendrimer molecules consist of a core, conjugated dendrons, and surface groups. Consequently, compounds based on dendrimers can exhibit a great variety of functional and electronic properties [3]. In particular, dendrimer compounds are characterized by a high solubility and weak intermolecular interactions and can be used for manufacturing high-quality films. Moreover, molecules of these compounds possess a high quantum yield of fluorescence. In this work, we investigated the electrical, spectral, and luminescence properties of a poly(amidoamine) (PAMAM) dendrimer containing 1,8-naphthalimide groups in the peripheral part. The procedure of synthesizing this compound was described earlier in [4, 5]. The molecular structure is depicted in Fig. 1. The core of the PAMAM molecule exhibits strong electron-donating properties due to the presence of nitrogen atoms with a lone electron pair, whereas the peripheral part of this molecule is characterized by electron-seeking properties. Grabchev *et al.* [4] observed photoinduced electron transfer in these molecules, which can have a profound effect on electrical conductivity.

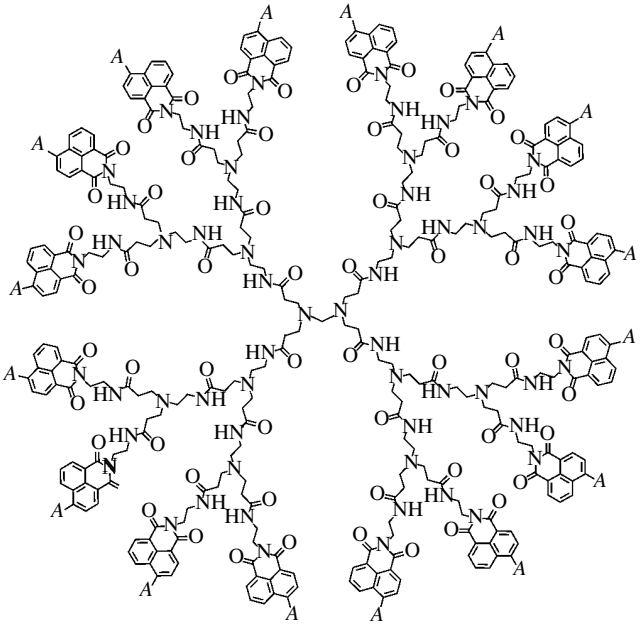

Fig. 1. Molecular structure of the studied compound. Designation: A = $NH(CH_2)_5CH_3$.

1063-7834/04/4612-2306$26.00 © 2004 MAIK "Nauka/Interperiodica"

2. SAMPLE PREPARATION AND EXPERIMENTAL TECHNIQUE

For our experiments, 50-nm-thick films of the PAMAM compound were prepared on a VUP-5 apparatus through thermal evaporation under vacuum with subsequent deposition of the evaporation products onto substrates.

The electrical measurements were performed using glass substrates whose surfaces were covered with a transparent layer prepared from a mixture of indium and tin oxides. Moreover, a multilayer structure consisting of sequentially deposited layers of the studied material and an upper silver electrode 20 nm thick was grown on the glass substrate. The layers were deposited in one vacuum cycle. The deposition rate did not exceed 1 nm/s.

The optical absorption spectra were measured on a Cary 500 Scan UV–VIS–NIR spectrophotometer (Varian Ltd.). The fluorescence spectra were recorded on an SFL-1211A spectrofluorimeter (Solar TII). The temperature dependences of the electrical conductivity of the PAMAM compound were measured on a V7É-42 electrometer (Belvar, Minsk) in air and under vacuum with a residual pressure of 10^{-2} Pa. The electrical measurements were carried out using cyclic thermal desorption [6]. In essence, this method is as follows. The electrical conductivity of many organic compounds depends on the concentration of adsorbed oxygen molecules. This concentration decreases upon heating of an organic sample. Upon heating of the sample under vacuum to a specified temperature, the concentration of molecular oxygen in the sample decreases to a particular value. By cooling the sample under vacuum from this temperature, we can measure the temperature dependence of the electrical conductivity at a constant oxygen concentration in the sample. Sequential heating of the sample to increasingly higher temperatures and measurement of the temperature dependences of the electrical conductivity during cooling from these temperatures make it possible to obtain a set of temperature dependences of the conductivity for different concentrations of adsorbed oxygen molecules in the same sample. The temperature dependence of the electrical conductivity G for PAMAM films can be described by the relationship

$$G = G_0 \exp\left(-\frac{E_a}{kT}\right), \quad (1)$$

where E_a is the activation energy for electrical conduction.

3. RESULTS AND DISCUSSION

The absorption and fluorescence spectra of PAMAM films and ethanol solutions of the PAMAM compound are shown in Fig. 2. As for the majority of π-conjugated organic compounds, the absorption and fluorescence spectra of the films and solutions under investigation do not radically differ from each other. This indicates that their individual properties are retained in the solid state. The naphthalimide fragments exhibiting luminescence properties in the blue–green spectral region are emitting chromophores [7]. In naphthalimide derivatives, the lower excited state is a charge-transfer state. For the studied compound, the specific interactions in the solid phase are more pronounced than those in the liquid phase. This can be judged from the fact that the fluorescence spectrum of the film is broader and is shifted toward the long-wavelength range as compared to the spectrum of the solution. It should also be noted that, in the solid state, the PAMAM compound retains a high luminescence power and exhibits a fluorescence spectrum over a wide range of wavelengths.

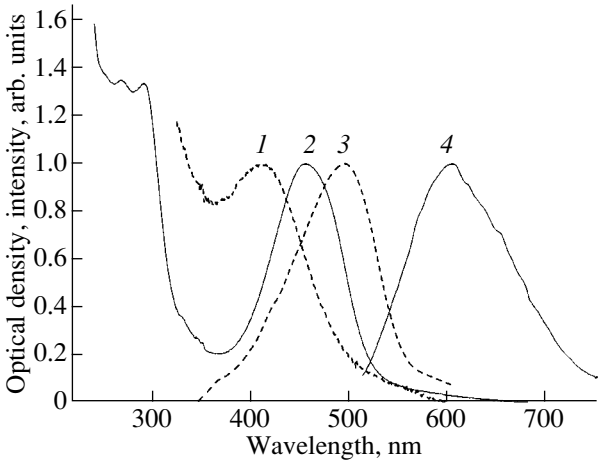

Fig. 2. (*1, 2*) Absorption and (*3, 4*) fluorescence spectra: (*1, 3*) ethanol solutions of the PAMAM compound (10^{-6} mol/l) and (*2, 4*) PAMAM films.

Taking into account the mirror symmetry rule and using the absorption and fluorescence spectra of the studied compound, we found that the lowest unoccupied molecular orbital is located at an energy of 2.4 eV. The barrier to electron injection, which is determined as the difference between the work function and the energy of the lowest unoccupied molecular orbital, amounts to 2.1 eV for both electrodes. Note that the barrier to electron injection can change by 0.5 eV or more due to the inhomogeneities formed in the film upon deposition [8].

The temperature dependences of the electrical conductivity of the PAMAM films measured using the cyclic thermal desorption method in air are depicted in Fig. 3. The set of temperature dependences of the electrical conductivity measured with a gradual increase in the temperature of the PAMAM films from 40 to 75°C was used to determine the preexponential factor G_0 and the activation energy for electrical conduction E_a in relationship (1) for different concentrations of adsorbed oxygen molecules.

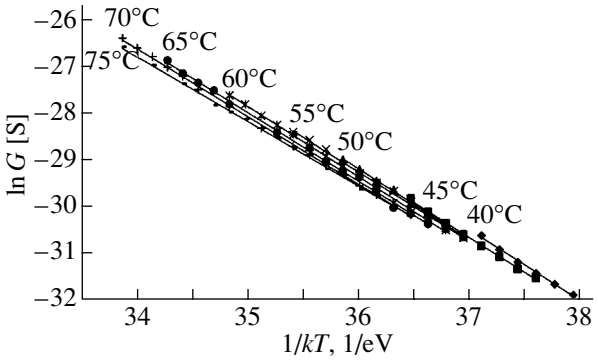

Fig. 3. Experimental temperature dependences of the electrical conductivity of the PAMAM films in air.

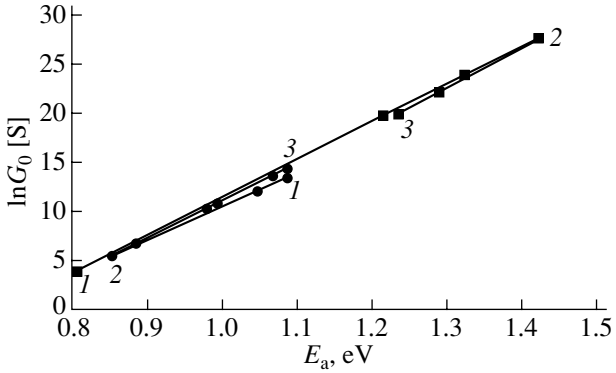

Fig. 4. Correlation between the activation energy and the preexponential factor in the expression describing the temperature dependence of the electrical conductivity of the multilayer structure based on PAMAM according to the results of measurements under high vacuum (circles) and in air (squares).

The results obtained can be interpreted in terms of the relationship between the preexponential factor G_0 and the activation energy E_a. This relationship accounts for the compensation effect (the Meyer–Neldel rule). The Meyer–Neldel rule asserts that the logarithm of the preexponential factor G_0 in relationship (1) describing the electrical conductivity G as a function of temperature T increases linearly with an increase in the activation energy:

$$\ln G_0 = A + BE_a, \tag{2}$$

where A and B are constants.

Figure 4 shows a correlation between the activation energy and the preexponential factor in the expression describing the temperature dependence of the electrical conductivity of the multilayer PAMAM structure according to the results of measurements under high vacuum and in air.

The dependence $\ln G_0(E_a)$ constructed from the results of the measurements of the PAMAM film under high vacuum is characterized by two portions, namely, portion *1–2* and portion *2–3* (see Fig. 4). In portion *1–2*, the preexponential factor increases with an increase in the activation energy. In portion *2–3*, the preexponential factor decreases with a decrease in the activation energy. Point *1* is obtained at a minimum temperature of 40°C. Points *2* and *3* correspond to temperatures of 65 and 75°C, respectively. It should be noted that, at a temperature of 75°C, the concentration of adsorbed oxygen molecules reaches a maximum and no evaporation of the sample is observed. The dependence $\ln G_0(E_a)$ constructed according to the results of measuring the PAMAM film in air is also characterized by two portions (Fig. 4). In portion *1–2*, the preexponential factor decreases with a decrease in the activation energy. In portion *2–3*, the preexponential factor increases with an increase in the activation energy. In this case, too, point *1* is obtained at a minimum temperature of 40°C. Points *2* and *3* correspond to temperatures of 50 and 75°C, respectively. At 75°C, no evaporation of the sample is observed.

The experimental data obtained in this work made it possible to evaluate the localization length of electrons. According to the results of the measurements performed in air and under high vacuum, the localization lengths of electrons were estimated at 0.61 and 1.13 Å, respectively. The localization length of electrons characterizes the height of the potential barrier between the localized states. The smaller the localization length, the higher the potential barriers separating the localized states and, correspondingly, the deeper the electron energy levels providing charge carrier transfer. For comparison, the localization length of electrons is equal to 8.9 Å for copper phthalocyanine and 1.2 Å for perylene pigment.

In order to interpret the results obtained, we used a model of two-level hopping electron transfer [9], according to which one of the two systems of energy levels corresponds to intrinsic states of electrons in PAMAM molecules and the other system is associated with the states of electrons in adsorbed oxygen molecules. These two systems of energy levels differ in the localization length of electrons. The localization length of electrons in the intrinsic states is designated by a_1, and the localization length of electrons in the impurity states is denoted by a_2 ($a_2 > a_1$).

The electrical conductivities G_1 and G_2 for the aforementioned two systems of electron energy levels can be written in the form

$$\begin{aligned} G_1 &= (G_{03})_1 \exp\left(-\frac{\alpha}{a_1 n_1^{1/3}} - \frac{E_{a1}}{kT}\right), \\ G_2 &= (G_{03})_2 \exp\left(-\frac{\alpha}{a_2 n_2^{1/3}} - \frac{E_{a2}}{kT}\right), \end{aligned} \tag{3}$$

where $(G_{03})_1$ and $(G_{03})_2$ are constants dependent on the localization length of electrons in the intrinsic and

impurity states, respectively; $\alpha = 1.73$ is the three-dimensional percolation constant; n_1 and n_2 are the concentrations of centers of electron localization in the intrinsic and impurity states, respectively; and E_{a1} and E_{a2} are the activation energies for intrinsic and impurity conduction, respectively. The activation energies E_{a1} and E_{a2} can be determined from the relationships

$$E_{a1} = \frac{1.61e^2 n_1^{1/3}}{4\pi\varepsilon_0\varepsilon}, \quad E_{a2} = \frac{1.61e^2 n_2^{1/3}}{4\pi\varepsilon_0\varepsilon}, \qquad (4)$$

where ε_0 is the permittivity of free space and ε is the relative permittivity.

The concentrations of centers of electron localization in the intrinsic and impurity states are related by the expression

$$n_1 + n_2 = n = \text{const}, \qquad (5)$$

because the impurity energy levels are formed through splitting off from the band providing electron transfer in a material free from impurities. Therefore, the electrical conductivity in the material containing impurities can be represented by the formula

$$G = G_1 + G_2. \qquad (6)$$

In this case, the temperature dependence of the electrical conductivity is adequately described by relationship (1) and the experimentally observed activation energy in this relationship can be calculated from the expression

$$E_a = -\frac{\partial(\ln G)}{\partial(1/kT)}. \qquad (7)$$

By using this expression with due regard for relationships (3)–(6), we obtain the formula

$$E_a = \frac{E_{a1}G_1 + E_{a2}G_2}{G_1 + G_2}. \qquad (8)$$

Consequently, the preexponential factor in the expression describing the temperature dependence of the electrical conductivity can be calculated from the relationship

$$G_0 = G\exp\left(\frac{E_a}{kT}\right). \qquad (9)$$

When interpreting the experimental results in the framework of the proposed model of two-level hopping electron transfer, it can be assumed that the presence of several portions in the dependences $\ln G_0(E_a)$ obtained from the measurements in air and under high vacuum (Fig. 4) corresponds to two mechanisms of electrical conduction, namely, conduction through the intrinsic states of electrons in PAMAM molecules and conduction through the impurity states of electrons in adsorbed oxygen molecules.

The experimental dependences of the activation energy on the relative impurity concentration $x = n_2/n_1$ and the corresponding dependences calculated in the framework of the proposed model [9] are compared in Fig. 5. Analysis of these dependences revealed the following features: (i) charge transfer predominantly occurs through a combined system of intrinsic and impurity states at small relative concentrations $x < 0.02$, (ii) a crossover to electrical conduction through the impurity states is observed at larger values of x, and (iii) charge transfer proceeds through the intrinsic states at $x > 0.5$. For the PAMAM film, there are points lying in all three concentration ranges. The calculations were performed for the parameters $n_1 + n_2 = 9 \times 10^{27}$ m^{-3}, $a_1 = 0.09$ nm, $a_2 = 0.1$ nm, and $\varepsilon = 1$. Permittivity was chosen equal to unity because the mean distance between the centers of electron localization in organic dyes is relatively small. This circumstance makes it impossible to use the macroscopic parameters of field screening.

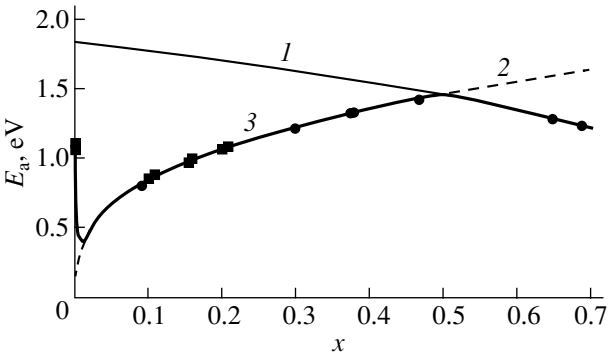

Fig. 5. Dependences of the activation energy on the relative concentration of adsorbed oxygen according to the results of measurements in air (circles) and under high vacuum (squares). Curves represent the results of calculations from relationships (7) and (8) for (*1*) intrinsic conduction, (*2*) impurity conduction through the electron states of adsorbed oxygen, and (*3*) conduction through a combined system of the intrinsic and impurity states.

Thus, the excellent agreement between the calculated and experimental dependences of the activation energy on the relative concentration of adsorbed oxygen allows us to draw the conclusion that electrical conduction in PAMAM films is associated with the hopping transfer of electrons. Depending on the concentration of adsorbed oxygen, this transfer can proceed either through the intrinsic states of electrons in PAMAM molecules or through the states of electrons in adsorbed oxygen molecules.

ACKNOWLEDGMENTS

This work was supported in part by the Belarussian Ministry of Education (project no. GB23-119) and the Belarussian Foundation for Basic Research (project no. F03MS-048).

REFERENCES

1. A. V. Kukhto, Zh. Prikl. Spektrosk. **70**, 151 (2003).
2. T. D. Anthopoulos, J. P. J. Markham, E. B. Namdas, I. D. W. Samuel, S.-C. Lo, and P. L. Burn, Appl. Phys. Lett. **82**, 4824 (2003).
3. K. Inoue, Prog. Polym. Sci. **25**, 453 (2000).
4. I. Grabchev, X. Qian, V. Bojinov, Y. Xiao, and W. Zhang, Polymer **43**, 5731 (2002).
5. I. Grabchev, V. Bojinov, and J.-M. Chovelon, Polymer **44**, 4421 (2003).
6. A. E. Pochtenny, D. I. Sagaĭdak, G. G. Fedoruk, and A. V. Misevich, Fiz. Tverd. Tela (St. Petersburg) **38**, 2592 (1996) [Phys. Solid State **38**, 1422 (1996)].
7. V. V. Gruzinskiĭ, A. V. Kukhto, É. É. Kolesnik, G. Kh. Shakkakh, and R. A. Minakova, Zh. Prikl. Spektrosk. **64**, 603 (1997).
8. A. V. Kukhta, E. E. Kolesnik, N. A. Shipitsa, and A. L. Zharin, in *Abstracts of the 4th International Conference on Electroluminescence of Molecular Materials and Related Phenomena* (Cheju, Korea, 2003), p. 68.
9. A. E. Pochtenny and A. V. Misevich, Pis'ma Zh. Tekh. Fiz. **29** (1), 56 (2003) [Tech. Phys. Lett. **29**, 26 (2003)].

Translated by O. Borovik-Romanova

Physics of the Solid State, Vol. 46, No. 12, 2004, pp. 2311–2316. Translated from Fizika Tverdogo Tela, Vol. 46, No. 12, 2004, pp. 2233–2237.

FULLERENES AND ATOMIC CLUSTERS

Photoemission Resonance and Its Quenching during Destruction of the Molecular Structure of a C_{60} Fullerite under Synchrotron Radiation

V. M. Mikoushkin*, V. V. Shnitov*, Yu. S. Gordeev*, S. L. Molodtsov, and D. V. Vyalykh****

** Ioffe Physicotechnical Institute, Russian Academy of Sciences, ul. Politekhnicheskaya 26, St. Petersburg, 194021 Russia*
e-mail: V.Mikoushkin@mail.ioffe.ru

*** Institut für Oberflächen- und Mikrostrukturphysik, Technische Universität Dresden, Dresden, D-01062 Germany*

Received April 26, 2004

Abstract—The photoelectron spectra of a C_{60} fullerene condensate are investigated. Under conditions where the photoionization (HOMO–ε1) and Auger (KVV*) transitions are at resonance, the intensity of molecular lines in the photoelectron spectra increases by a factor of several tens. It is found that even insignificant destruction of the molecular structure of fullurenes under synchrotron radiation leads to quenching of the observed resonance. The quenching of the resonance manifests itself in a decrease in the intensity of the molecular lines in the photoemission spectra. The revealed effect can be used to determine the degree of radiation-induced modification of fullerenes. © *2004 MAIK "Nauka/Interperiodica".*

1. INTRODUCTION

Investigation of the fragmentation and modification of fullerenes is an important problem from the standpoint of research into the fundamental properties of these new physical objects, which are intermediate between molecules and solids. Considerable progress toward an understanding of the mechanisms of ion- and electron-induced fullerene fragmentation has been made in recent years [1–6]. However, the interaction of fullerenes with radiation is still not clearly understood. Even the question of the possible transformation of the fullerene structure under radiation remains open. In particular, it has been established that the fragmentation of C_{60} fullerenes is a result of multiphoton excitation in a strong laser field [7, 8]. However, no fragmentation of isolated fullerene molecules upon single-photon absorption of synchrotron radiation has been revealed even for large excitation cross sections of valence electrons in the range from the excitation threshold to the photon energy $h\nu$ = 35 eV [9]. A different situation arises when fullerene molecules form a condensate (fullerite) in which the molecules are bound by van der Waals forces. Modification of the fullerite is observed under soft ultraviolet radiation from mercury discharge sources [10]. The transformation of the atomic structure is associated with the formation of chemical bonds between adjacent molecules, which, in turn, can form dimers and polymer chains. In our recent work [11], we found that the C_{60} fullerite undergoes a modification due to the destruction of fullerene molecules upon exposure to synchrotron radiation. This manifests itself in a change both in the location and intensity of the lines in the photoelectron and Auger spectra and in the shape of the valence-electron spectra, which become similar to the spectra of amorphous carbon. The observed process is characterized by a low efficiency, because the shape of the spectral lines changes only after prolonged exposure of the samples to intense polychromatic synchrotron radiation.

The purpose of the present work was to reveal a physical effect that would be sensitive to modification of the C_{60} fullerite. The solution of this problem will make it possible to devise a method for elucidating the mechanisms responsible for the modification and fragmentation of the fullerite and to elucidate prospects for using this material as a photoresist in dry lithography [12]. It is evident that the resonance effect can ensure high sensitivity. For this reason, we chose resonant photoelectron spectroscopy with synchrotron radiation as a tool for studying the processes of interest and photoemission resonance (associated with the interference between the amplitudes of direct photoemission and autoionization) as the object of our investigation. It was established that, under resonance conditions, the photoemission cross section for valence electrons of the C_{60} fullerite increases by a factor of several tens. As could be expected, even insignificant destruction of the molecular structure and the corresponding molecular state should lead to a considerable decrease in the intensity of the resonance peak. It is this effect that was observed in our experiments under exposure of the fullerite to synchrotron radiation.

2. EXPERIMENTAL TECHNIQUE

The experiments were performed on the Russian–German synchrotron beamline at the BESSY II storage

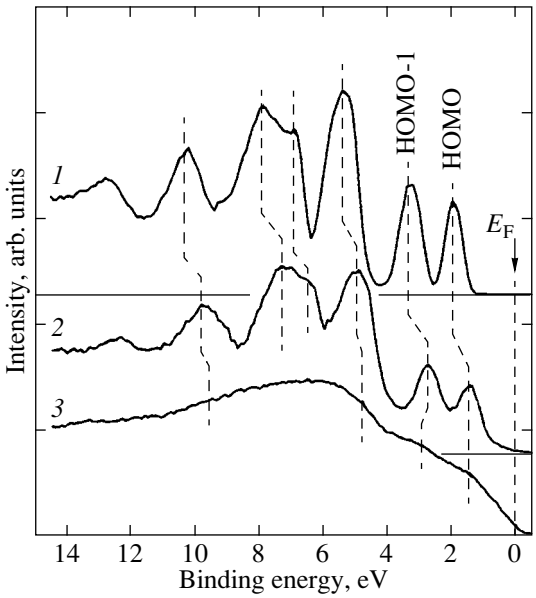

Fig. 1. Valence-band photoelectron spectra of (*1*) the as-prepared C_{60} fullerite ($Q = 0$), (*2*) the fullerite exposed to polychromatic synchrotron radiation ($Q > 0$), and (*3*) amorphous carbon. The spectra were excited by photons with energy $h\nu = 120$ eV.

ring (Berlin). Under all operating conditions, the energy spread of the synchrotron beam at the entrance of the analytical chamber did not exceed 30 meV. Films of the C_{60} fullerite were grown through the evaporation of fullerene molecules onto a conducting silicon substrate at room temperature in a preparation chamber of the spectrometer in the course of the experiment. The thickness of fullerite films was approximately equal to ten nanometers.

In this work, we measured the photoelectron spectra of the occupied valence band states (HOMO) and the near-edge x-ray absorption fine structure (NEXAFS) spectra, which provided information on the local density of unoccupied states (LUMO). The modification of the fullerite upon exposure to an intense polychromatic synchrotron beam ("zero-order" radiation) was checked against the photoelectron (HOMO) spectra excited by photons with an energy $h\nu = 120$ eV. In the photoabsorption experiments, the energy of monochromatic synchrotron radiation was varied over a wide range ($h\nu = 280$–320 eV), which covered the energies of excitation of C 1*s* core electrons into π^* and σ^* unoccupied states in the valence band and the continuum. In the resonant photoemission experiments, the valence-band photoelectron spectra were thoroughly investigated in the vicinity of the photon energy $h\nu = 284$ eV. This energy corresponds to resonance of the HOMO-1–ε1 photoemission of valence electrons and the C $1s$–π^*2p_z photoexcitation of core electrons into the lowest unoccupied state (LUMO). The photoelectron spectra were measured on a CLAM4 hemispherical analyzer operating in a constant relative resolution mode. This mode provided a high sensitivity of the spectrometer with sufficient resolution, which, in all the experiments, was less than 150 meV, i.e., less than the natural width of the lines under investigation.

3. MODIFICATION OF THE C_{60} FULLERITE UNDER SYNCHROTRON RADIATION

Analysis of the valence-band photoelectron spectra of the fullerite before and after exposure to an intense polychromatic synchrotron beam (zero-order radiation) revealed radiation-induced destruction of the C_{60} fullerene molecules [11]. This destruction manifests itself in a change in the photoelectron spectra. Figure 1 shows the photoelectron spectra of the pure as-prepared fullerite (spectrum *1*, dose $Q = 0$), the fullerite exposed to synchrotron radiation (spectrum *2*, $Q > 0$), and amorphous carbon (spectrum *3*) prepared under bombardment of the fullerite with argon ions in the same experiment. The photoelectron spectra of the as-prepared fullerite exhibit molecular peaks against a low-intensity quasi-continuous background. The spectrum of amorphous carbon is actually the quasi-continuous background. During exposure of the fullerite to synchrotron radiation, the intensity of the molecular peaks decreases and the background intensity increases; i.e., the photoelectron spectrum of the fullerite becomes more similar to the spectrum of amorphous carbon. The amorphization is accompanied by a shift of the molecular peaks toward the Fermi level (E_F), whose position was determined from the energy corresponding to the edge of the valence-band spectrum of amorphous carbon. An increase in the intensity of the photoelectron spectrum of the modified fullerite in the vicinity of the Fermi level indicates that the density of states near the energy E_F increases and that the band gap disappears.

It is obvious that the amorphization of the fullerite is caused by the destruction of fullerene molecules. A similar transformation of the electronic structure was observed earlier during amorphization of the fullerite upon electron impact [4–6]. Hence, in the case under consideration, it is reasonable to assume that the modification proceeds through a similar mechanism. This mechanism involves the excitation of valence electrons and the formation of intermolecular chemical bonds. In turn, this leads initially to polymerization of the fullerite and then (with an increase in the number of intermolecular chemical bonds) to destruction of the fullerene molecules. Moreover, complete or partial ejection of C_2 fragments becomes possible due to heating of the nuclear system of the fullerene as a result of the electron–phonon interaction. The appearance of extended electronic states in the vicinity of the Fermi level owing to the destruction of the fullerene molecules leads to an increase in the conductivity and the relaxation energy. The relaxation energy characterizes the response of the electronic system to the formation of a vacancy. An increase in the relaxation energy results in a decrease in the binding energy of electrons, which is responsible

for the shift in the molecular peaks. The difference between the observed modification of the fullerite under synchrotron irradiation and the aforementioned electron-induced modification lies in the fact that, in the former case, the electronic system is excited by both photons and photoelectrons.

4. STRUCTURE OF THE DENSITY OF UNOCCUPIED STATES AND ITS TRANSFORMATION UNDER SYNCHROTRON RADIATION

Revealing resonance effects sensitive to modification of the fullerite requires knowledge of the structure of unoccupied states that can be filled with C 1*s* core electrons in order to provide an autoionization channel of the resonant photoemission of the valence electrons. This information was derived from the NEXAFS spectra, i.e., from the dependences of the photoabsorption cross section on the energy of absorbed photons near the photoabsorption threshold [13–16]. Figure 2 depicts the NEXAFS spectrum of the fullerite film (spectrum *1*, $Q = 0$) near the threshold of the "C 1*s*–unoccupied state" transition ($h\nu = 280$–320 eV). The spectrum exhibits a number of peaks against a quasi-continuous background. These peaks correspond to maxima in the density of unoccupied states of C_{60} molecules below and above the edge of the continuous spectrum. The highest intensity is observed for the LUMO (t_{1u}, π^*2p_z, V^*) peak attributed to the lowest unoccupied molecular state. The excitation energy of this peak $h\nu = 284.1$ eV appears to be somewhat lower than the energy $h\nu = 284.5$ eV, which was determined in [14–16] for thick and thin fullerite films on aluminum and gold. The energy difference (0.4 eV) can be associated with both the difference in the properties of the prepared films and the error in determining the photon energy. As will be shown below, such an insignificant energy difference is of fundamental importance for the resonant photoemission.

Apart from the NEXAFS spectrum of the initial film, Fig. 2 shows the NEXAFS spectrum of the fullerite exposed to intense zero-order synchrotron radiation (spectrum *2*, $Q > 0$) and the spectrum of amorphous carbon (spectrum *3*). In the course of irradiation, we discovered an important experimental fact: the intensity of the peaks assigned to the unoccupied states in the valence band drastically decreases with an increase in the number of structural transformations. This is especially true for the LUMO peak observed at the lowest energy. Therefore, the destruction of the molecular structure of the fullerite is accompanied by a decrease in the amplitude of the "C 1*s*–LUMO" transition, which contributes to the autoionization amplitude of the resonant photoemission of valence electrons and, hence, should lead to a decrease in the photoemission cross section.

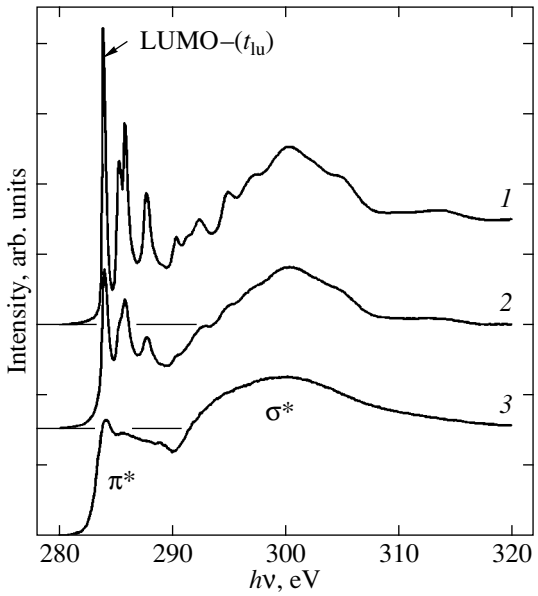

Fig. 2. NEXAFS (photoabsorption) spectra of (*1*) the as-prepared C_{60} fullerite ($Q = 0$), (*2*) the fullerite exposed to polychromatic synchrotron radiation ($Q > 0$), and (*3*) amorphous carbon.

5. PHOTOEMISSION RESONANCE AND ITS QUENCHING IN FULLERITES UNDER SYNCHROTRON RADIATION

As is known (see, for example, [16]), the condition for photoemission resonance is coincidence between the energies of the direct photoemission transition of a valence electron to the continuum (HOMO–ε1 or *V*–ε1 transition) and the transition to the intermediate autoionization state (C 1*s*–*V** transition) in which the Auger decay (KVV* transition) brings about the formation of the same final state as the direct transition. The interference between the amplitudes of these transitions results in an increase in the photoionization cross section of valence electrons when the amplitude of the transition to the free state and, hence, the autoionization amplitude are sufficiently large. This effect manifests itself in an increase in the intensity of the photoelectron spectra. The valence-band spectra of the fullerite under the conditions of photoresonance ($h\nu \sim 284.5$ eV) were previously obtained in studies of the charge transfer processes and the properties of thick and thin C_{60} films on aluminum, gold, and xenon condensate substrates [14–16]. However, those studies did not answer the question as to how much the intensity of the spectrum of the fullerite can increase at resonance.

Figure 3 illustrates the evolution of the general photoelectron spectra of the fullerite during the passage though resonance, i.e., with an increase in the x-ray photon energy from the energy below the excitation threshold of C 1*s* core electrons (spectrum *1*, $h\nu = 280$ eV) to the energy of the first resonance (spectrum *2*, $h\nu \sim 284$ eV) and above (spectrum *3*, $h\nu = 300$ eV). The

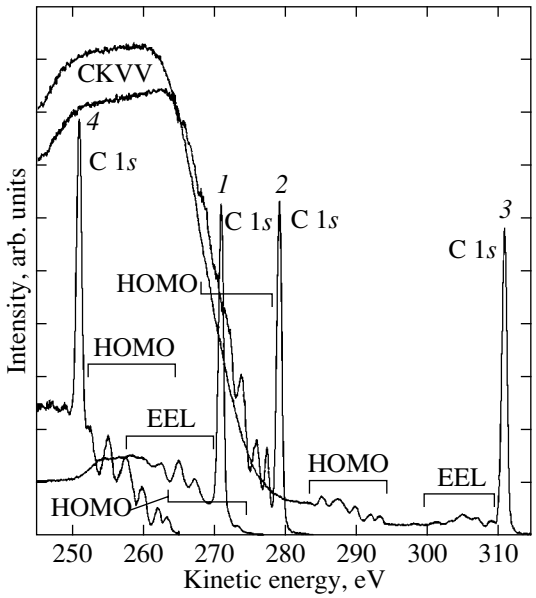

Fig. 3. Photoelectron and Auger spectra of the as-prepared C_{60} fullerite measured at different photon energies. $h\nu$ = (*1*) 280.0, (*2*) 284.1, (*3*) 300.0, and (*4*) 270.0 eV.

photon energy of the first resonance corresponds to the excitation of C 1*s* electrons into the first unoccupied molecular state (LUMO, t_{1u}, π^*2p_z or V^*). Spectrum *3* is associated with the transition of C 1*s* electrons to considerably higher unoccupied states that are formed by σ^* electrons and located above the vacuum level (Fig. 2). It can be seen from Fig. 3 that, at photon energies below the excitation threshold of the first resonance (spectrum *1*, $h\nu$ = 280 eV), the spectrum does not exhibit a broad CKVV Auger peak, and the molecular lines of valence electrons (HOMO) have a very low intensity, as can be judged from the peak of the highest occupied state. (Intense lines in the range under consideration belong to the EEL spectrum.) The autoionization leads to the appearance of the Auger peak and to an increase in the intensity of the molecular lines, which at resonance are satellites in the Auger spectrum (Fig. 3, spectrum *2*). An increase in the photon energy above the threshold (Fig. 3, spectrum *3*) results in a shift of the molecular peaks toward the high-energy range of electrons as compared to the Auger peak and in a weakening of the effect by approximately one order of magnitude. The weakening of the effect is associated not with the 1.5-fold lower density of σ^* states but primarily with the fact that electrons in these continuum states are localized at larger distances from atoms and spend a shorter time in their neighborhood. Therefore, the excited electrons, for the most part, play the role of "observers" rather than participants of the Auger process. Unfortunately, the synchrotron beam emerging from a monochromator always contains photons with doubled energy due to the second-order diffraction. As a consequence, the photoelectron spectrum involves the high-energy satellite peak of C 1*s* core electrons. In the range of the photoemission resonance, i.e., near the threshold of the formation of inner vacancies, this satellite peak is superposed on the valence-band (HOMO) spectrum and complicates its analysis (Fig. 3). This disadvantage of the method can be only partially eliminated by specially adjusting the monochromator of the synchrotron beamline. The considerable contribution from the second-order diffraction was also observed in [14–16]. Moreover, the interpretation of the spectra is complicated by the EEL structure caused by the excitation of the HOMO–LUMO electronic transitions with C 1*s* photoelectrons.

The general spectra shown in Fig. 3 demonstrate one more intricate effect. In the range where the photon energies differ significantly from the resonance energy and which is located 14 eV below the threshold of the first possible inelastic transition of the C 1*s* core electron to the lowest unoccupied state (LUMO), the intensity of the photoelectron spectrum (Fig. 3, spectrum *4*, $h\nu$ = 270 eV) is considerably higher than the intensity of the spectrum associated with the direct photoionization. The magnitude of the observed effect suggests that this effect exhibits resonant nature and is characterized by an additional amplitude. However, the photon energy in this case is high enough only for the C 1*s* core electron to be transferred to the occupied states of the valence band (HOMO). Such a transition is impossible. This contradiction can be resolved by making allowance for the channel of the virtual formation of vacancies in the occupied states due to virtual excitation of valence electrons (the HOMO–LUMO transition). Then, the process proceeds according to a standard scheme of resonant photoemission. The efficiency of the channel is indirectly confirmed by the high probability of exciting the HOMO–LUMO transition (see the EEL portion in Fig. 3). This suggests a strong correlation of the molecular states under consideration. Another possibility of inducing resonant excitation is associated with the reflection of the photoionized C 1*s* electron from the valence shell with complete energy transfer to a valence electron that leaves the atom to find itself in a state identical to the state involved in direct photoionization.

Therefore, the general spectra (Fig. 3) indicate that there are two ranges of resonant enhancement of the photoelectron spectra. Further analysis will be performed in the traditional range associated with the excitation of core electrons into the first unoccupied state. Let us consider the detailed valence band (HOMO) spectrum in a narrow binding energy range adjacent to the Fermi level (Fig. 4). Figure 4 depicts the spectrum measured at the photon energy ($h\nu$ = 284.1 eV) which almost coincides with the energy of the transition of core electrons to the first unoccupied state (C 1*s*–LUMO transition). Moreover, this figure shows two spectra measured at photon energies below and above the resonance energy, namely, at photon energies 0.5 eV lower and 0.8 eV higher than the energy of the

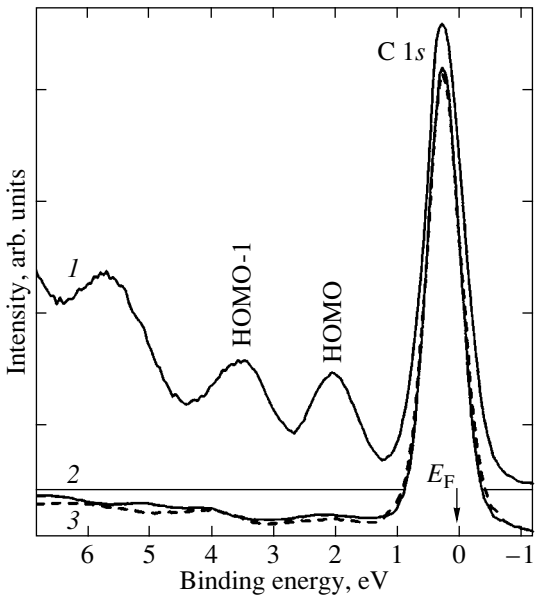

Fig. 4. Valence-band photoelectron spectra of the as-prepared C_{60} fullerite ($Q = 0$) measured at (*1*) the resonance photon energy ($h\nu = 284.1$ eV), (*2*) the photon energy below the resonance energy ($h\nu = 283.6$ eV), and (*3*) the photon energy above the resonance energy ($h\nu = 284.9$ eV).

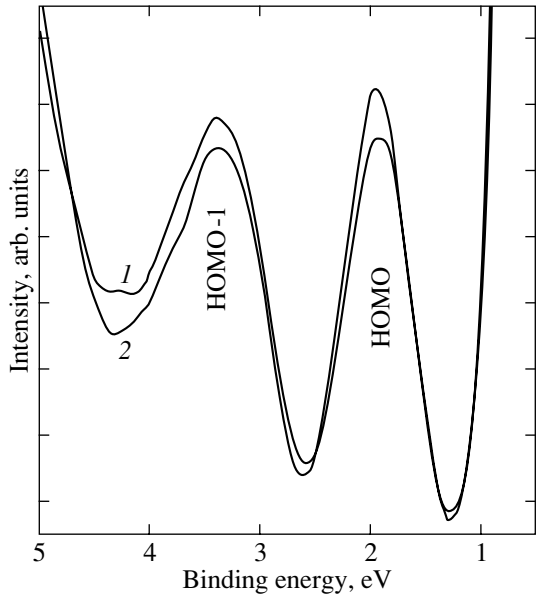

Fig. 5. Fragments of the valence-band (HOMO-1, HOMO) photoelectron spectra of the C_{60} fullerite measured (*1*) before ($Q = 0$) and (*2*) after ($Q > 0$) irradiation by photons with energy $h\nu = 284.1$ eV.

C 1*s*–LUMO transition. It can be seen from Fig. 4 that the molecular lines in the photoelectron spectrum at resonance are enhanced by a factor of more than 20. The C 1*s* core photoelectron line of the second-order diffraction is dominant in the spectra presented in Fig. 4. For this reason, we chose a narrower spectral range covering the HOMO and HOMO-1 molecular peaks for further investigation.

The main result obtained in the present work is illustrated in Fig. 5, which shows how the fragment of the valence-band photoelectron spectrum measured at photoemission resonance changes during exposure of the fullerite film to monochromatic synchrotron radiation with energy $h\nu = 284.1$ eV. Spectra *1* and *2* correspond to the unirradiated ($Q \sim 0$) and irradiated ($Q > 0$) films, respectively. As can be seen from Fig. 5, the irradiation leads to a considerable decrease (by 13%) in the intensity of the molecular peaks. It is evident that the quenching of the resonance is due to the destruction of the molecular structure of the fullerite and the corresponding destruction of the first unoccupied (LUMO) state. The magnitude of the observed effect can be evaluated as follows: the comparable decrease in the intensity of the molecular lines measured far from the resonance (at $h\nu = 120$ eV) is achieved only at radiation doses that are two orders of magnitude higher than the dose accumulated in the resonance experiment. Therefore, the observed effect can be used to characterize very subtle processes associated with the modification and fragmentation of fullerenes and fullerites.

6. CONCLUSIONS

Thus, it was established that, under synchrotron radiation, the C_{60} fullerite undergoes a modification due to the destruction of individual fullerene molecules. This process manifests itself in a change in the shape of the photoelectron spectra (which become similar to the spectra of amorphous carbon) and quenching of the photoemission resonance. Under conditions of photoemission resonance, the intensity of the molecular lines in the photoelectron spectra of the fullerite increases by a factor of several tens. It was demonstrated that, upon exposure of the fullerite to synchrotron radiation with even very low doses, the quenching of the resonance results in a decrease in the intensity of the molecular lines in the photoemission spectra. The inference was made that the observed effect can be used as a highly sensitive tool for determining the degree of modification and fragmentation of fullerenes and fullerite.

ACKNOWLEDGMENTS

We would like to thank A.S. Vinogradov for many pieces of helpful advice regarding the performance of photoemission resonance experiments.

This work was supported by the BESSY II, the International Association of Assistance for the promotion of cooperation with scientists from the New Independent States of the Former Soviet Union (project INTAS nos. 2136, 03-51-4706), the Russian Academy of Sciences within the framework of the "Low-Dimensional Quantum Structures" program, the Ministry of

Science and Technology of the Russian Federation within the framework of the "Physics of Solid-State Nanostructures" program, and the Netherlands Organization for Scientific Research (NWO, project no. 047.003.012).

REFERENCES

1. E. E. B. Campbell and F. Rohmund, Rep. Prog. Phys. **63**, 1061 (2000).
2. O. Hadjar, R. Hoekstra, R. Morgenstern, and T. Schlathölter, Phys. Rev. A **63**, 033201 (2001).
3. B. Dünser, M. Lezius, P. Scheier, H. Deutsch, and T. D. Märk, Phys. Rev. Lett. **74**, 3364 (1995).
4. V. M. Mikushkin and V. V. Shnitov, Fiz. Tverd. Tela (St. Petersburg) **39** (1), 187 (1997) [Phys. Solid State **39**, 164 (1997)].
5. Yu. S. Gordeev, V. M. Mikushkin, and V. V. Shnitov, Fiz. Tverd. Tela (St. Petersburg) **42** (2), 371 (2000) [Phys. Solid State **42**, 381 (2000)].
6. V. V. Shnitov, V. M. Mikushkin, V. V. Bryzgalov, and Yu. S. Gordeev, Fiz. Tverd. Tela (St. Petersburg) **44** (3), 428 (2002) [Phys. Solid State **44**, 444 (2002)].
7. H. Hohmann, C. Callegari, S. Furrer, D. Grosenick, E. E. B. Campbell, and I. V. Hertel, Phys. Rev. Lett. **73**, 1919 (1994).
8. S. Hunsche, T. Strczewski, A. l'Huillier, A. Persson, C.-G. Wahlström, B. van Linden van den Heuvell, and S. Svanberg, Phys. Rev. Lett. **77** (10), 1966 (1996).
9. I. V. Hertel, H. Steger, J. de Vries, B. Weisser, C. Menzel, B. Kamke, and W. Kamke, Phys. Rev. Lett. **68**, 784 (1992).
10. Y. Wang, J. M. Holden, A. M. Rao, P. C. Eklund, U. D. Venkateswaran, D. Eastwood, R. Lidberg, G. Dresselhaus, and M. S. Dresselhaus, Phys. Rev. B **51** (7), 4547 (1995).
11. Yu. S. Gordeev, V. M. Mikoushkin, V. V. Shnitov, and S. L. Molodtsov, in *Abstracts of XXIII International Conference on the Physics of Electronic and Atomic Collisions (XXIII ICPEAC)* (Stockholm, 2003).
12. V. V. Shnitov, V. M. Mikoushkin, and Yu. S. Gordeev, Microelectron. Eng. **69**, 429 (2003).
13. V. M. Mikoushkin, V. V. Shnitov, V. V. Bryzgalov, Yu. S. Gordeev, S. L. Molodtsov, D. V. Vyalich, and S. Danzenbächer, BESSY Annual Report (2003).
14. A. J. Maxwell, P. A. Brühwiler, A. Nilsson, N. Mårtensson, and P. Rudolf, Phys. Rev. B **49** (15), 10717 (1994).
15. A. J. Maxwell, P. A. Brühwiler, D. Arvanitis, J. Hasselström, and N. Mårtensson, Phys. Rev. Lett. **79**, 1567 (1997).
16. P. A. Brühwiler, O. Karis, and N. Mårtensson, Rev. Mod. Phys. **74** (3), 703 (2002).

Translated by O. Borovik-Romanova

Physics of the Solid State, Vol. 46, No. 12, 2004, pp. 2317–2322. Translated from Fizika Tverdogo Tela, Vol. 46, No. 12, 2004, pp. 2238–2243.

FULLERENES AND ATOMIC CLUSTERS

Ab initio Study of Novel Crystals Based on Fullerene C_{60} and Carbynes

S. V. Lisenkov*, L. A. Chernozatonskiĭ*, and I. V. Stankevich**

**Emanuel Institute of Biochemical Physics, Russian Academy of Sciences, ul. Kosygina 4, Moscow, 119991 Russia*
e-mail: lisenkov@sky.chph.ras.ru, cherno@sky.chph.ras.ru
***Nesmeyanov Institute of Organoelement Compounds, Russian Academy of Sciences, Moscow, 119991 Russia*
e-mail: stan@ineos.ac.ru

Received May 11, 2004

Abstract—The density-functional theory is used to predict the existence of new carbon structures consisting of C_{60} fullerenes connected by linear carbon chains with different numbers of atoms. The stability and the electronic structure of 1D, 2D, and 3D forms of these structures are studied. It is shown that there are two basic forms of such compounds depending on the parity of the number of atoms in the interfullerene chain. The polyhedral fragments of the structures considered are shown to consist only of sp^2 carbon atoms. All crystals are semiconductors with the band gap lying in the interval 1.17–1.36 eV. *© 2004 MAIK "Nauka/Interperiodica".*

1. INTRODUCTION

Many years have passed since the first calculations of the structure of the C_{60} molecule [1] and its subsequent discovery [2]; however, these surprising polyhedral-frame compounds called fullerenes still attract the attention of scientists. It is known that fullerene C_{60} is used to synthesize various carbon nanostructures and their derivatives. As examples, we cite polymer C_{60} compounds, endohedral fullerene complexes [3], structures of the "peapod" type [4, 5], etc. The possible creation of transistors based on a single fullerene molecule was predicted in [6].

A few years after the discovery of C_{60}, it was established that the pure C_{60} crystalline phase is a molecular crystal [3]. It has been found that, under the action of pressure (<10 GPa) and temperature (<1000 K), the crystal transforms into various structures consisting of polymerized C_{60} molecules [7–9], namely, crystalline phases of linear chains (quasi-one-dimensional (1D) structures) and quasi-two-dimensional (2D) polymerized structures, in which C_{60} fullerenes are covalently bonded by four-membered cycles formed as a result of the "2 + 2" reaction of cycloaddition. In 2D structures, the molecules form two different phases, rhombohedral and orthorhombic. At high pressures (≥10 GPa) and temperatures (≥1000 K), superhard phases have been observed [10, 11], whose structures consist of 3D-polymerized C_{60} molecules [12, 13]. Recently, quantum-chemical calculations of the equilibrium geometry, electronic spectrum, and elastic moduli of some 3D-polymeric fullerene structures have been performed [14, 15].

In [16], the semiempirical PM3 method and the Hartree–Fock HF/6-G21 method were used to calculate the equilibrium geometry of the C_{60} + C[N] + C_{60} clusters ("dimers") and C_{60} + C[N] + C_{60} + C[N] + C_{60} clusters ("trimers") containing N = 2–5 carbon atoms, and 1D, 2D, and 3D structures on the basis of C_{60} + C[2] polymers were constructed. To calculate the geometrical parameters of such structures, the method of molecular mechanics in cluster approximation was used. It should be noted that all polyhedral fragments of these systems contained pairs of sp^3 carbon atoms, since such calculations showed that joining a carbon chain to atoms of one of the double bonds in C_{60} results in the formation of a threefold cycle with a pair of sp^3 atoms as its base. For example, a 1D structure was given by a quasi-one-dimensional C_{60} + C[2] chain. In a quasi-2D structure, each fullerene was bonded with four or six neighboring C_{60} molecules by chains of carbon atoms. Structures of the 3D type (crystals) consisted either of quasi-1D chains or of quasi-2D lattices bonded by van der Waals forces.

In this study, using the density-functional theory (DFT) [17], we calculated the geometrical structure, stability, and electronic structure of each phase of such compounds with two to six carbon atoms in a chain by optimizing both the atomic coordinates and the cell parameters. It is shown that a new structural configuration can exist (in contrast to [16], none of the optimized structures contains sp^3 hybridized atoms at the junction of a fullerene and a carbon chain), and its semiconductor properties are predicted.

The article is organized as follows. In Section 2, we describe details of the calculations, and in Section 3, the results are discussed.

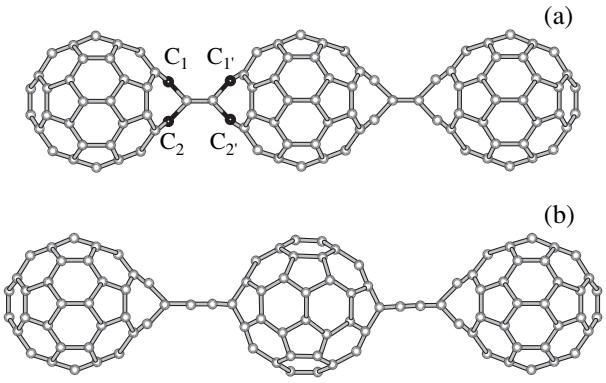

Fig. 1. Trimers consisting of C_{60} fullerenes connected by (a) two- and (b) three-atom carbon chains. In calculations, the initial approximation corresponded to tetrahedrally coordinated carbon atoms C_1, C_2 and $C_{1'}$, $C_{2'}$ in the C_{60} fullerenes (denoted by solid circles) [16].

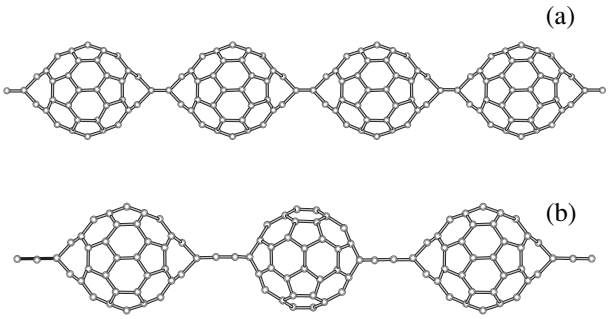

Fig. 2. Fragments of periodic quasi-1D structures with different numbers of carbon atoms: (a) C_{60} + C[2]–1D structure and (b) C_{60} + C[3]–1D structure.

2. DETAILS OF THE CALCULATIONS

The calculations were performed by the density-functional method [17] using the SIESTA program [18]. We note that the equilibrium geometry and electronic properties of fullerenes and nanotubes calculated using this program [19–22] agree well with the experimental data. Calculations were performed in the generalized gradient approximation using the parametrization suggested by Perdew, Burke, and Ernzerhof [23]. Nonlocal norm-conserving pseudopotentials developed by Troullier and Martins [24] in the Kleinman–Bylander form [25] were applied for the description of the electrons of the atomic core. In all calculations, the DZP basis and 150 Ry for energy cutoff were used. The optimization procedure for the atomic configuration was performed until the forces acting on the atoms became smaller than 0.04 eV/Å. Test calculations were performed for the atomic and electronic structure of both graphite and fullerene C_{60}. The calculated C–C bond lengths in C_{60} (1.42 and 1.47 Å) are in very good agreement with the experimental data (1.40 and 1.46 Å, respectively), and the total energy per atom of C_{60} (0.38 eV/atom with respect to the total energy per atom of graphite) was also in good agreement with experiment (0.39–0.43 eV/atom [26]). Moreover, in this approximation, the difference of HOMO–LUMO energies for a C_{60} molecule was 1.64 eV, in good agreement with the experimental value of 1.6–1.8 eV.

The unit cell parameters and the atomic coordinates were optimized using the conjugate gradient method. In optimizing the geometry, different numbers of *k* points in the Brillouin zone were used. For the structures with an even number of atoms between fullerenes, we used 25 to 48 *k* points. For the structures containing odd number of atoms in a linear chain between fullerenes, the calculation was performed only at the Γ point. The accuracy of this approximation was tested for diamond with various values of the cell parameters. It was established that, for a unit cell parameter exceeding 15 Å, the results of the calculations did not change as the number of *k* points in the calculation was increased. Since the unit cell parameters of the structures under study with an odd number of atoms between the fullerenes exceed 25 Å, it is sufficient to use only the Γ point. We used the Monkhorst–Pack method [27] to generate *k* points.

3. SIMULATION RESULTS AND DISCUSSION

First, we optimized the geometry of clusters consisting of two (dimers) or three C_{60} molecules (trimers) connected by a chain consisting of two to six carbon atoms. Generally, a junction of the carbon chain to atoms of one of the double bonds of C_{60} results in the formation of a three-membered cycle [16] based on a C_1–C_2 bond between two sp^3 atoms (Fig. 1). Therefore, as the initial approximation, we chose the structures with four-coordinated C_1 and C_2 atoms forming bonds of these three-membered cycles. After the geometry was optimized, the interatomic C_1–C_2 and $C_{1'}$–$C_{2'}$ distances in these structures were equal to 2.31 Å. Such structures, which have no sp^3-hybridized atoms, are shown in Fig. 1. They appear to have a lower energy (by 0.10–0.16 eV/atom) than the initial structures. Therefore, in what follows, we consider only fullerene compounds that do not contain C_1–C_2 bonds (Figs. 1–3). For these structures, we introduce the notation C_{60} + C[*N*]–*K*D, where *N* is the number of carbon atoms in a chain connecting two fullerenes and *K* is the structure dimensionality (equal to 1 for quasi-1D structures, 2 for quasi-2D structures, and 3 for a crystal).

Optimization of the geometry of all structures showed that the most stable configuration of a trimer with an even number of atoms in a chain between fullerenes is the structure of the symmetry group D_{2h} (Fig. 1a). The most stable configuration of a trimer of C_{60} fullerenes with an odd number of atoms between the fullerenes is that in which one fullerene is rotated through 90° with respect to another (Fig. 1b). The coordinates obtained for the atoms in the trimers were used

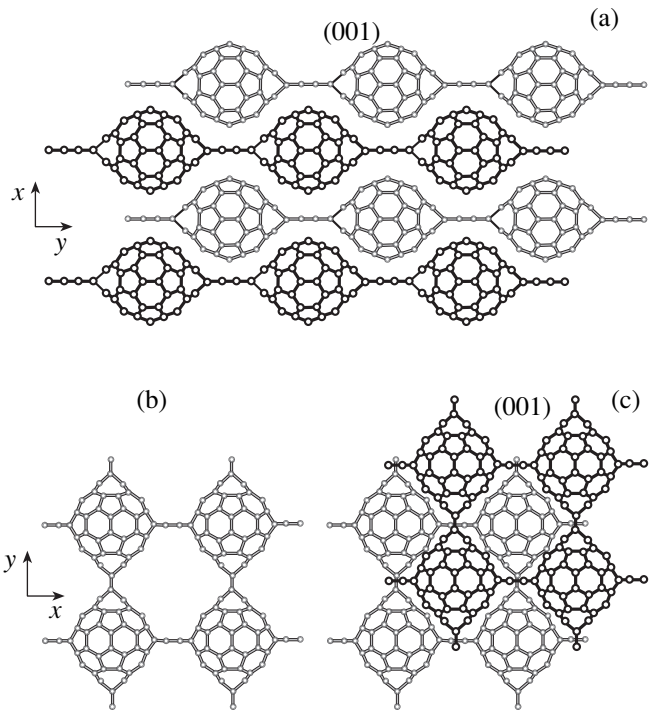

Fig. 3. 3D and 2D forms of polymeric compounds of C_{60} fullerenes and carbyne chains: (a) the (001) plane of the molecular crystal (orthorhombic lattice, *Immm* symmetry group) consisting of C_{60} + C[4]–1D chains with four carbon atoms; (b) a fragment of the C_{60} + C[2]*p*–2D planar structure (quasi-2D "tetragonal" lattice, *Imm* symmetry group) with two atoms between C_{60} fullerenes; and (c) a fragment of the C_{60} + C[2]*p*–3D crystal consisting of the planar polymers shown in (b). Solid and open circles correspond to the atoms of the structures located in the neighboring (001) and (001/2) planes, respectively.

as initial data for simulating 1D structures and molecular crystals formed by them. Figures 2 and 3 show fragments of 1D and 3D structures of such compounds, as well as the structures formed by 2D-bonded fullerenes.

3.1. Chain Structures with an Even Number of Atoms between Fullerenes

In the case of quasi-1D chains with an even number of carbon atoms between fullerenes, we considered three structures whose unit cells contained 62, 64, and 66 atoms. In optimizing the geometry, we used 30, 26, and 24 *k* points, respectively. A fragment of the C_{60} + C[2]–1D structure is shown in Fig. 2a. The next stage was calculation of the electronic spectra. Figure 4 shows a fragment of the one-electron spectrum of the C_{60} molecule in the region of energies close to the HOMO–LUMO region. The electronic band structure of the C_{60} + C [2]–1D compound is shown in Fig. 4b. It is seen in Figs. 4a and 4b that the presence of chains of carbon atoms that covalently bond fullerenes gives rise to very narrow allowed bands and a band gap E_g = 1.17 eV; the band gap is smaller than the energy difference $E_{HOMO–LUMO}$ for a C_{60} molecule (1.64 eV). Thus, the structure considered is a semiconductor with an indirect gap between the valence and conduction bands.

Next, we simulated the structure of molecular crystals (a bulk centered orthorhombic lattice) consisting of the quasi-1D chains described above. Such crystals form an orthorhombic lattice with the *Immm* symmetry group. A fragment of one of them, namely, of the C_{60} + C[4]–3D crystal, is shown in Fig. 3a. Its electronic spectrum is plotted in Fig. 5. It is seen that this crystal is a semiconductor with a band gap E_g = 1.33 eV. Calculations showed that C_{60} + C[*N*]–3D molecular crystals (*N* = 2, 4, 6) are semiconductors with band gaps E_g lying in the range 1.19–1.36 eV. These values differ only slightly from the band gap of the quasi-1D isolated C_{60} + C[*N*]–1D chain. Rather narrow conduction and valence bands (E_c, E_v ~ 0.38 eV) indicate that the interaction between the chains in such crystals is weak.

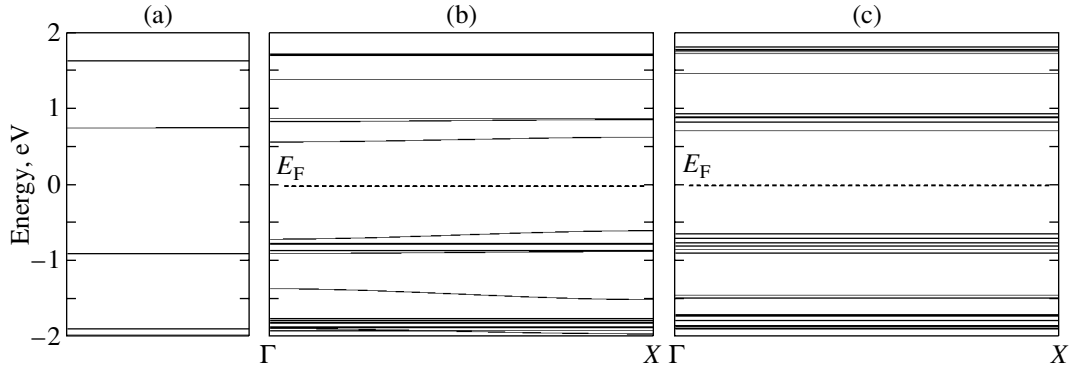

Fig. 4. (a) One-electron spectrum of the C_{60} molecule and (b, c) the electronic band structure of (b) C_{60} + C[2]–1D and (c) C_{60} + C[3]–1D chains. The energies are measured from the Fermi level E_F.

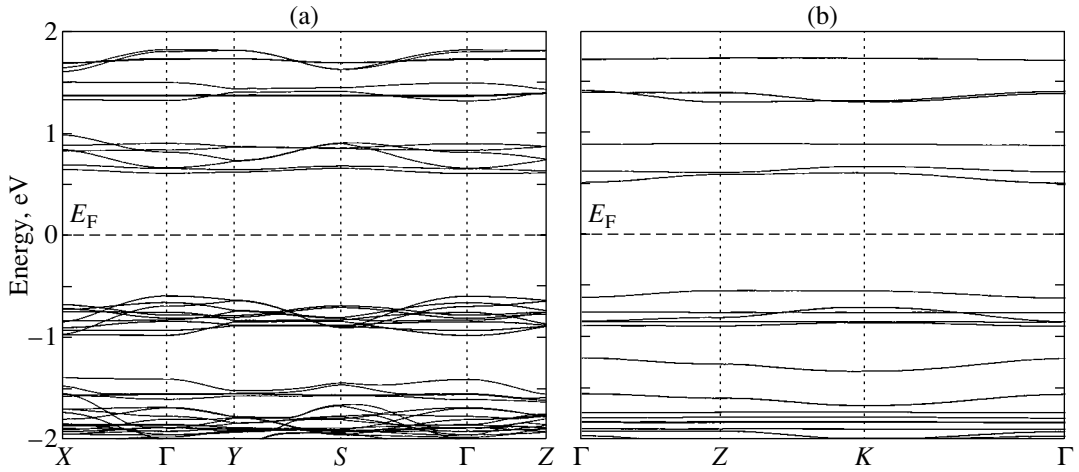

Fig. 5. Electronic band structures of (a) a molecular C_{60} + C[4]–3D crystal and (b) a 2D C_{60} + C[2]*p*–2D crystal. The energies are measured from the Fermi level E_F.

3.2. Chain Structures with an Odd Number of Atoms between Fullerenes

We simulated quasi-1D structures formed by C_{60} fullerenes connected by chains with an odd number of atoms (three and five). The unit cells in this case contain 126 and 130 atoms. Only the Γ point was used to optimize the geometry for both structures. The simulation showed that the obtained 1D structures are also semiconductors, just as in the case of chains with an even number of atoms. The band gap E_g is 1.32 eV for C[3] and 1.33 eV for C[5]. A fragment of the C_{60} + C[3]–1D quasi-1D chain is shown in Fig. 2b, and its electronic band structure is plotted in Fig. 4c. In contrast to the C_{60} + C[2]–1D chain (Fig. 4b), the spectrum of C_{60} + C[3]–1D has narrower allowed bands (E_c, E_v ~ 0.001 eV). This fact indicates that the presence of a third atom in the carbon chain weakens the interaction between fullerenes.

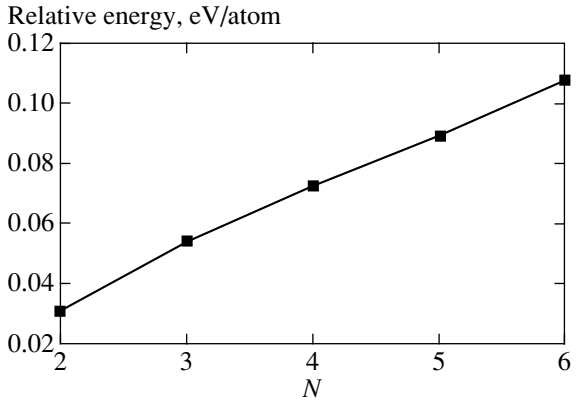

Fig. 6. Total energy per atom (measured from the total energy per atom for the C_{60} molecule) as a function of the number of carbon atoms *N* in carbyne chains in quasi-2D polymeric C_{60} + C[*N*]–1D structures.

Calculations for molecular crystals consisting of 1D fullerene chains (an orthorhombic lattice with the *Immm* symmetry group) with an odd number of atoms between the fullerenes showed that such molecular crystals are also semiconductors with band gaps E_g equal to 1.31 and 1.34 eV for C[3] and C[5], respectively.

Thus, we may conclude that, irrespective of the number of carbon atoms between C_{60} fullerenes, all crystalline 3D structures investigated are semiconductors with band gaps E_g lying in the range 1.19–1.36 eV. In Fig. 6, the total energy per atom (with respect to the energy of the C_{60} molecule) for quasi-1D fullerene chains is plotted as a function of the number N = 2–6 of carbon atoms connecting the neighboring fullerenes. Since the dependence of the total energy of quasi-1D linear chains C_{60} + C[*N*]–1D on *N* is linear (Fig. 6), it is obvious that a two-atom carbon chain connecting C_{60} fullerenes has the lowest energy.

3.3. Planar Structures with an Even Number of Atoms between Fullerenes

We calculated the equilibrium geometry of the C_{60} + C[2]–2D structure (a 2D pseudotetragonal lattice, the *Imm* symmetry group) formed by C_{60} fullerenes connected by two-atom chains (C_{60} + C[2]*p*–2D) (Fig. 3b) and its energy spectrum. The calculation showed that this structure is also a semiconductor with a band gap E_g = 1.16 eV, the smallest among the band gaps of the structures considered (see table). In Fig. 5b, we plot the energy bands of the planar C_{60} + C[2]*p*–2D compound. Based on this compound, we constructed and optimized the structure of the molecular C_{60} + C[2]*p*–3D crystal (Fig. 3c). Analysis of the electronic spectrum showed

Main parameters (lattice constants, band gap E_g, total energy per atom E with respect to that of the C_{60} molecule) for 1D, 2D, and 3D fullerene structures, the unit cell volume V, and the ratio ρ_N/ρ_0 of the density of the C_{60} + C[N]–3D structures to the C_{60} molecular-crystal density equal to 1.72 g/cm^3

Structure	a, Å	b, Å	c, Å	E_g, eV	E, eV/atom	V, Å^3	ρ_N/ρ_0
C_{60} + C[2]–1D	–	–	11.347	1.17	0.031	–	–
C_{60} + C[3]–1D	–	–	25.565	1.32	0.054	–	–
C_{60} + C[4]–1D	–	–	14.083	1.33	0.073	–	–
C_{60} + C[5]–1D	–	–	31.024	1.33	0.089	–	–
C_{60} + C[6]–1D	–	–	16.801	1.37	0.105	–	–
C_{60} + C[2]*p*–2D	–	11.111	11.476	1.16	0.058	–	–
C_{60} + C[2]*p*–3D	11.343	11.374	11.612	1.23	0.027	1498.1	0.987
C_{60} + C[2]–3D	10.456	11.407	16.746	1.19	0.033	1997.3	0.741
C_{60} + C[3]–3D	10.312	16.446	25.613	1.31	0.051	2171.9	0.692
C_{60} + C[4]–3D	10.277	14.089	16.118	1.34	0.072	2333.8	0.654
C_{60} + C[5]–3D	10.196	16.018	31.171	1.34	0.085	2545.5	0.609
C_{60} + C[6]–3D	10.131	14.892	16.004	1.36	0.101	2414.5	0.652

that this crystal is also a semiconductor with a band gap E_g = 1.23 eV.

The results of the calculations are given in the table, in which the main parameters obtained are listed: the parameters of the unit cell, the band gap E_g, the total energy per atom measured with respect to that of the C_{60} molecule, and the ratio of the density ρ_N of the C_{60} + C[N]–3D structures to the density ρ_0 of the molecular C_{60} crystal. The structures that contain connecting two-atom carbon chains appeared to have the lowest energy. The total energies per atom of such structures of different dimensionalities have the following values: 0.031 eV/atom for C_{60} + C[2]–1D, 0.058 eV/atom for C_{60} + C[2]*p*–2D, 0.033 eV/atom for C_{60} + C[2]–3D, and 0.027 eV/atom for C_{60} + C[2]*p*–3D. It follows from these data that the C_{60} + C[2]*p*–3D crystal has the lowest energy among the planar polymers.

The ratio ρ_N/ρ_0 characterizes the packing density of 3D structures measured with respect to that of the C_{60} molecular crystal. The C_{60} + C[5]–3D crystal having density $\rho_5 = 0.609\rho_0$ appeared to be the most loosely packed. The loose packing of the structure should facilitate its doping by atoms of other elements, for example, metal (*M*) or hydrogen molecules. Doping can substantially change the electronic structure of the crystals considered. In particular, because the conduction band is narrow, doping can produce a new compound with superconducting properties, just as in the case of M_3C_{60} compounds [3]. However, verification of these assumptions requires special calculations.

4. CONCLUSIONS

Thus, in the framework of the DFT method, the possible existence of new 1D, 2D, and 3D forms of carbon structures that consist of C_{60} fullerenes connected by linear chains of carbon atoms has been predicted and theoretically justified. We have found two stable forms of such structures depending on whether the number of atoms in the chains connecting the C_{60} fullerenes is even or odd. We have shown that the structures described above are semiconductors with band gaps $E_g \sim 1.2$–1.3 eV, which are comparable to the band gap of the crystalline silicon (E_g = 1.17 eV) and are 1.2 to 1.3 times smaller than the band gap of the molecular C_{60} crystal. Direct transitions between the valence and conduction bands in the crystals considered can stimulate their applications in IR optoelectronic devices.

ACKNOWLEDGMENTS

The authors are grateful to É.I. Isaev for helpful remarks and his help in the simulation.

The calculations were performed by one of the authors (S.V.L.) at the Joint Supercomputer Center of Russia and in part at the Computer Center of the Moscow State University.

This work was supported by the program of the Ministry of Science and Education of the Russian Federation “Promising Directions in the Physics of Condensed Matter” (direction “Fullerenes and Atomic Clusters”) and the Russian national program “Low-Dimensional Quantum Structures.”

REFERENCES

1. D. A. Bochvar and E. G. Gal’pern, Dokl. Akad. Nauk SSSR **209**, 610 (1973) [Sov. Phys. Dokl. **18**, 239 (1973)].
2. H. W. Kroto, J. R. Heath, S. C. O’Brien, and R. F. Smalley, Nature **318** (6042), 162 (1985).

3. M. S. Dresselhaus, G. Dresselhaus, and P. C. Eklund, *Science of Fullerenes and Carbon Nanotubes* (Academic, San Diego, 1996).
4. H. W. Smith, M. Monthioux, and D. E. Luzzi, Nature **396** (6709), 323 (1998).
5. D. J. Hornbaker, S.-J. Kahng, S. Misra, B. W. Smith, A. T. Johnson, E. J. Mele, D. E. Luzzi, and A. Yazdani, Science **295**, 828 (2002).
6. H. Park, A. K. L. Lim, E. H. Anderson, A. P. Alivisatos, and P. L. Mceuen, Nature **407** (6800), 57 (2000).
7. M. Nuñez-Regueiro, P. Monceau, and J.-L. Hodeau, Nature **355** (6357), 237 (1992).
8. M. Nuñez-Regueiro, L. Marques, J.-L. Hodeau, O. Bethoux, and M. Perroux, Phys. Rev. Lett. **74** (2), 278 (1995).
9. *Fullerene Polymers and Fullerene Polymer Composites*, Ed. by P. C. Eklund and A. M. Rao (Springer, 2000), Springer Ser. Mater. Sci., Vol. 38.
10. L. A. Chernozatonskii, N. R. Serebryanaya, and B. N. Mavrin, Chem. Phys. Lett. **316** (3–4), 199 (2000).
11. N. R. Serebryanaya, V. D. Blank, V. A. Ivdenko, and L. A. Chernozatonskii, Solid State Commun. **118** (4), 183 (2001).
12. L. Marques, M. Mezouar, J.-L. Hodeau, M. Nuñez-Regueiro, N. R. Serebryanaya, V. A. Ivdenko, V. D. Blank, and G. A. Dubitsky, Science **283** (5408), 1720 (1999).
13. V. D. Blank, S. G. Buga, N. R. Serebryanaya, V. N. Denisov, G. A. Dubitsky, A. Ivlev, B. N. Mavrin, and M. Yu. Popov, Phys. Lett. A **205** (2–3), 208 (1995).
14. S. Okada, S. Saito, and A. Oshiyama, Phys. Rev. Lett. **83** (10), 1986 (1999).
15. S. Okada and A. Oshiyama, Phys. Rev. B **68** (23), 235402 (2003).
16. A. R. Sabirov, I. V. Stankevich, and L. A. Chernozatonskiĭ, Pis'ma Zh. Éksp. Teor. Fiz. **79** (3), 153 (2004) [JETP Lett. **79**, 121 (2004)].
17. P. Hohenberg and W. Kohn, Phys. Rev. **136** (3), 864 (1964).
18. J. M. Soler, E. Artacho, J. D. Gale, A. Garcia, J. Junquera, P. Ordejón, and D. Sanchez-Portal, J. Phys.: Condens. Matter **14** (11), 2745 (2002).
19. P. Ordejón, E. Artacho, and J. M. Soler, Phys. Rev. B **53** (16), R10441 (1996).
20. A. Rubio, D. Sanchez-Portal, E. Artacho, P. Ordejón, and J. M. Soler, Phys. Rev. Lett. **82** (17), 3520 (1999).
21. E. Burgos, E. Halac, R. Wehlt, H. Bonadeo, E. Artacho, and P. Ordejón, Phys. Rev. Lett. **85** (11), 2328 (2000).
22. P. Ordejón, Phys. Status Solidi B **217** (1), 335 (2000).
23. J. P. Perdew, K. Burke, and M. Ernzerhof, Phys. Rev. Lett. **77** (18), 3865 (1996).
24. N. Troullier and J. L. Martins, Phys. Rev. B **43** (3), 1993 (1991).
25. L. Kleinman and D. M. Bylander, Phys. Rev. Lett. **48** (20), 1425 (1982).
26. H. S. Chen, A. R. Kortan, R. C. Haddon, M. L. Kaplan, C. H. Chen, A. M. Mujsce, H. Chou, and D. A. Fleming, Appl. Phys. Lett. **59** (23), 2956 (1991).
27. H. J. Monkhorst and J. D. Pack, Phys. Rev. B **13** (12), 5188 (1976).

Translated by I. Zvyagin